Multi-wavelength Investigations of Solar Eruptive Phenomena

A thesis submitted for the degree of

Doctor of Philosophy

by

Upendra Kumar Singh Kushwaha

(Roll No. 11330010)

Under the Supervision of

Dr. Bhuwan Joshi

Reader

Udaipur Solar Observatory

Physical Research Laboratory, Udaipur, India.

DEPARTMENT OF PHYSICS

INDIAN INSTITUTE OF TECHNOLOGY GANDHINAGAR

2016

to

my parents

Declaration

I declare that this written submission represents my ideas in my own words and where others' ideas or words have been included, I have adequately cited and referenced the original sources. I also declare that I have adhered to all principles of academic honesty and integrity and have not misrepresented or fabricated or falsified any idea/data/fact/source in my submission. I understand that any violation of the above will be cause for disciplinary action by the Institute and can also evoke penal action from the sources which have thus not been properly cited or from whom proper permission has not been taken when needed.

Upendra Kumar Singh Kushwaha

Roll No: 11330010

Date: February 23, 2016

CERTIFICATE

It is certified that the work contained in the thesis titled "**Multi-wavelength Investigations of Solar Eruptive Phenomena**" by **Upendra Kumar Singh Kushwaha (11330010)**, has been carried out under my supervision and that this work has not been submitted elsewhere for a degree.

Dr. Bhuwan Joshi

Reader

Udaipur Solar Observatory

Physical Research Laboratory

Udaipur 313001, India

Date: February 23, 2016

Acknowledgements

I am most indebted to Dr. Bhuwan Joshi, my PhD adviser, for his continuous motivation, invaluable support, intellectual guidance, and help of various kinds. He helped in my study to large extent from basic data analysis and image processing to independent thinking and scientific writing. His aspiration to carryout outstanding research work has always been a source of inspiration for me. I am deeply grateful to Prof. P. Venkatakrishnan for his continuous encouragement and generous support throughout my research endeavor. I have enjoyed talking to him about work and other matters on several occasions.

I am also grateful to Dr. Astrid Veronig for her suggestions and constructive comments to improve the quality of work carried out in this thesis. She is a passionate scientist, and I learned many things from her through discussions over emails.

I express my sincere gratitude to the Doctoral Student Committee (DSC) members, Prof. Shibu K. Mathew and Dr. Ramitendranath Bhattacharya for their useful comments and suggestions during my IITGN review reports. I am also grateful to my thesis experts, Prof. Nandita Srivastava and Prof. P. Janardhan for reviewing my thesis and help in improving the quality of the thesis.

I would also express my gratitude to Prof. J. N. Goswami, former Director; and Prof. Utpal Sarkar, Director; for providing necessary facilities to carryout research work at PRL. I must thank PRL academic committee, for reviewing my progress in research time-to-time and providing constructive input for further improvements. I thank the faculty members of USO, Prof. Ashok Ambastha, Dr. Brajesh Kumar and Dr. Raja Bayanna for their generous helps and encouragements. I am also thankful to the faculty members of PRL in particular, Prof. R. Ramesh, Prof. A. K. Singhal, Dr. Jitesh R. Bhatt, Dr. Namit Mahajan, Dr. Varun Sheel, Dr. R. Rangarajan, Dr. Bijaya Sahoo, Dr. J. S. Ray, and Dr. Vinai Kumar Rai for teaching various courses during my PhD course work. In addition, I would also like to thank the library and computer centre staff for efficiently maintaining the facilities.

I would like to thank all of the team members of RHESSI, TRACE, AIA/SDO, HMI/SDO, NoRH, GOES, EUVI/STEREO, MDI/SOHO, LASCO/SOHO, KSO, and Culgoora Radio Observatory for providing the valuable data which has been utilized in this thesis.

I take this opportunity to thank my seniors, Dr. Sanjiv Tiwari, Dr. Ram Ajor Maurya, Dr. Rohan Eugene Louis, Dr. Anand D. Joshi, Dr. Vema Reddy Panditi and Dr. Suruchi Goel; to my batch mates, Aadhi, Avdesh, Arko, Anjali, Bhabya, Dinesh, Damodar, Dilip, Debasis, Gulab, Gaurav Tomar, Gaurav Sharma, Grish Chakravarty, Gangi, Lekshmy, Lata, Midhun, Monojit, Naveen, Nigam, Priyanka, Rajeev, Tanmoy, Uma, Wageesh, Yashpal; and my juniors, Alok, Sanjay, Rahul and Hemant for their company and help in different aspects throughout thesis work. I would like to give special thanks to Amzad, Arun Awasthi, Sunil, Sushant, Amrendra, Chinmay, Kaushik, Shidhartha, Shashi, Fazlul for their friendly guidance and helps in various manners. I thank my other friends at PRL, Arun Pandey, Jagat, Girish, Kuldeep, Pankaj, Apurva, Ashim, Newton, and many other JRFs, SRFs, PDFs and PAs. I extend my thanks to Rahul Sharma and Sudarshan Jain for their support of various kinds.

Thanks to all other staff members of USO, Mr. Mukesh M. Saradava, Mr. Raju Koshy, Mr. Rakesh Jaroli, Mr. Naresh Jain, Late Mr. Sudhir Kumar Gupta, Ms. Rammya Bireddy, Mr. Nurul Alam, Mr. Pinakin Shikari, Mr. Laxmilal Suthar, Mr. Dalchand Purohit, and Mr. Jagdish Singh Chauhan for their help and support in various ways during my stay at USO.

I am also thankful to all the family members at USO colony, Mrs. Usha Venkatakrishnan, Mrs. Saraswati, Mrs. Mahima, and Mrs. Bharti for providing the homely environment with invitations for lunch and dinners on various occasions.

I am very much privileged to express my sincere thanks to all my M.Sc. and B.Sc. teachers from University of Allahabad, for their nice teaching and making me eligible to get into research.

Finally, I owe my deepest gratitude to my parents who has given me the freedom necessary to concentrate on my research. I am also thankful to other family members, in particular, grandparents, uncles, aunties, siblings, and cousins for their wholehearted love. I must say, that being away from home, I have missed innumerable opportunities to be with family members, but they have always been by my side all the while.

Upendra Kumar Singh Kushwaha

Abstract

Solar eruptive phenomena correspond to various kind of transient activities occurring in the solar atmosphere in the form of flares, prominence eruptions and coronal mass ejections. They mostly originate from solar active regions which consist of complex magnetic structures extending from the deeper sub-photospheric layers, crossing through the photosphere to the coronal heights. An eruptive flare typically spreads across all the atmospheric layers of the Sun and involves substantial mass motions and particle acceleration. Multi-wavelength observations are thus crucial to probe the underlying physical processes occurring at different layers and regions at and above the photosphere.

In this thesis, I have studied some key aspects of solar eruptive phenomena such as solar flare, prominence eruption, coronal implosion, failed eruption, and sigmoid-to-arcade evolution. These investigations have employed contemporary multi-wavelength solar observations with superior resolution. The imaging and spectroscopic capabilities of Reuven Ramaty High Energy Solar Spectroscopic Imager (RHESSI) have been extensively utilized to investigate the thermal and non-thermal energy release processes associated with different stages of the eruptive phenomena. Complementary to RHESSI X-ray measurements, we have combined solar observations at Extreme Ultraviolet (EUV), Ultraviolet (UV), Microwave (MW), optical, and radio wavelengths to investigate the complex physical processes occurring at different atmospheric layers of the Sun during the eruptive events.

We study two spectacular prominence eruptions and associated flare activities which occurred in active regions NOAA 10656 on 2004 August 18 (event I) and NOAA 11548 on 2012 August 18 (event II) with the motivation to identify the prominence destabilization through the observations of pre-eruption phase and pre-flare activity. The violent eruption of the prominences is accompanied by major flares. We also explore the signatures of magnetic reconnection in the

corona and discuss the thermal and non-thermal effects driven by prominence eruption during their eruptive phase. During event I, three localized episodes of energy release were observed in the vicinity of the filament before the eruption that produced intense heating along with non-thermal emission. The prominence eruption was accompanied with an X1.8 flare during which multiple HXR bursts were observed up to 100–300 keV energies. We have noted striking HXR coronal source at 50–100 keV energy band that was formed at the time of detachment of the prominence from the source region. From the location, timing, strength, and spectrum of HXR emission, we conclude that the prominence eruption was driven by distinct events of magnetic reconnection occurring in the current sheet below the erupting prominence. During event II, we observed multitude of coronal activities in the form of a blowout jet, rapid evolution of a flux rope above the prominence, and events of episodic energy release. Out of these activities, the flux rope exhibited the most dramatic evolution, characterized by splitting and rotation along with localized brightenings during its outward expansion. The prominence underwent catastrophic loss of equilibrium with the onset of an M1.8 flare, suggesting large-scale energy release by magnetic reconnection. During the impulsive phase of the flare, a plasmoid eruption was observed below the apex of erupting prominence at multiple EUV channels. The temporal, spatial and kinematic correlations between erupting prominence and plasmoid imply that the magnetic reconnection supported the fast ejection of prominence in the lower corona.

Flare research has been dominated by the study of eruptive flares because of their large-scale structure and long duration. On the other hand, it is rather challenging to investigate energy release processes in confined flares due to their rapid evolution in a compact region that impose severe observational constraints. Now with the availability of observations at unprecedented temporal, spatial, and spectral resolutions from RHESSI and SDO, we have made an effort to investigate the triggering mechanism and magnetic reconnection scenario in a confined M4.0

flare in AR NOAA 11302 on 2011 September 26. From this case study, we infer some important conclusions about the evolution of flare loops and thermal/non-thermal emissions within the confined environment of active region corona. This event was associated with a magnetic transient which was observed ∼1 minute prior to the flare onset at the early flare location within the inner core region. The spectral, temporal, and spatial properties of magnetic transients suggest that the sudden changes in the small-scale magnetic field have likely triggered the flare by destabilizing the highly sheared pre-flare magnetic configuration.

We have studied a confined eruption (or failed eruption) of a flux rope which occurred in AR NOAA 10646 on 2004 July 14. After striking pre-flare phase, we observed a major M6.2 flare during which a large flux rope and associated prominence material underwent confined eruption. A major highlight of the pre-flare phase lies in the observation of large-scale contraction in overlying coronal loops for a span of ∼30 minutes during which the overlying loops underwent an altitude decrease of ∼20 Mm (40% of the initial height) during pre-flare phase. The impulsive phase of the flare is characterized by multiple non-thermal peaks during which very high plasma temperature (T ∼30 MK) and substantial non-thermal characteristics were observed. The time-evolution of thermal energy exhibits a good correspondence with the variations in cumulative non-thermal energy which suggest that the energy of accelerated particles efficiently converted to hot flare plasma implying validation of the Neupert effect in terms of flare energetics.

Finally, we have presented a multi-wavelength investigation of a sigmoid-to-arcade development in AR 11719 on 2013 April 11. The study aims to explore several crucial aspects involved during the process of solar eruption right from the formation stage of coronal EUV sigmoid to the post-eruption phase of the source region. The evolution of sigmoid was observed at 94 Å images which implies that the structure comprised of very high temperature plasma. The sigmoid eruption was accompanied with a large M6.5 two-ribbon flare which is characterized by a prolonged rise phase of $\sim$21 minutes. We have especially emphasized morphological and spatial evolution of flare sources during the prolonged rise phase and discussed their observational disparities with the standard flare model.

Contents

List of Figures

List of Tables

Chapter 1

Introduction

1.1 Solar eruptive phenomena

Solar eruptive phenomena correspond to various kind of transient activities occurring in the solar atmosphere in the form of flares, prominence eruptions and coronal mass ejections. The advancements in solar observing capabilities, especially from space, have greatly enhanced our understanding about these phenomena. The synthesis of multi-wavelength data has revealed that different forms of the eruptive phenomena are manifestations of a single physical process involving the disruption of coronal magnetic field. The investigations of source region characteristics of solar eruptions are crucial to widen our knowledge about space weather and Sun-Earth relationship.

1.1.1 Solar flares

The most striking explosive form of solar eruptive phenomena are solar flares. A solar flare is a sudden, brief and powerful outburst, releasing an energy from 10^{28} to 10^{34} ergs on time scales of seconds to several tens of minutes. Such short-lived solar flares release their energy within active regions which is the magnetized atmosphere in, around and above sunspots, and vary in intensity and frequency of

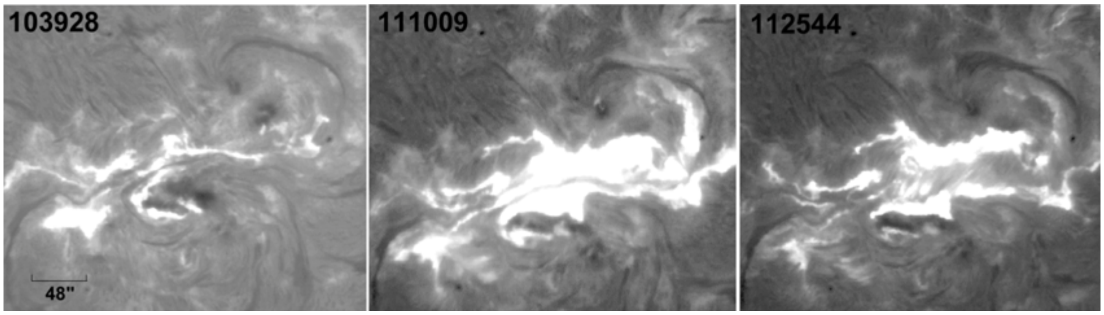

Figure 1.1: Evolution of historical 4B/X17 flare observed on 2003 October 28 in active region NOAA 10486. The Hα filtergrams were taken from Udaipur Solar Observatory (USO). The time (in UT) of each filtergram is annotated at top-left corner in *HourMinSec* format. Figure from Ambastha (2007).

occurrence with the 11-year solar activity cycle. Flares typically spread across all atmospheric layers and involve substantial mass motions and particle acceleration.

Although first reported from the observations of visible sunlight, by Carrington (1859) and Hodgson (1859), flares usually produce only minor perturbations in the integrated or white light. In contrast, the flaring radio and X-ray emission is frequently several thousands of times more energetic than the Sun's normal radiation at these wavelengths. This invisible radiation indicates the presence of energetic electrons, accelerated to very high speeds approaching that of light, and gas heated to temperatures of about 10 million degrees. The most intense, high energy radiation of solar flares, X-rays and γ-rays, comes from magnetic loops in solar active regions.

Flare classification

– **Hα classification:** Typically the Hα spectral line, at a wavelength of 6563 Å is used for solar flare patrol. A filter with a passband of 1/4 to 1/2 Å (0.25 – 0.50 Å) is commonly used for this application. To be classified as a flare, the chromospheric brightening must exceed an area threshold and a brightness threshold. For Hα observations, the brightness threshold is 150% of the chromospheric background, and the area threshold is ten millionths of the visible solar hemi-

Table 1.1: Optical classification of solar flares.

Importance class	Area (A) at disk center	
	in millionths of a solar hemisphere*	in square degrees
S	$A < 100$	< 2.0
1	$100 \leqslant A < 250$	$2.1 \leqslant A < 5.1$
2	$250 \leqslant A < 600$	$5.2 \leqslant A < 12.4$
3	$600 \leqslant A < 1200$	$12.5 \leqslant A < 24.7$
4	$A \geqslant 250$	$A \geqslant 24.8$

$*$ one millionth of the solar atmosphere $\approx 3.03 \times 10^6$ km^2

sphere[1]. A brightening which has less than 150% of chromospheric background (even though it may have more than ten millionths area) is termed a plage fluctuation. A small brightening which exceeds 150% of chromospheric background but less than 10 millionths hemispheric area is termed a point brightening. A typical major flare in Hα often appears as two extended, parallel ribbons which move apart with the progression of the flare (see Figure 1.1).

The Hα observations of solar flares leads to a classification scheme based on their extent and brightness in Hα. In this scheme, flares are classified with a character (S = subflare, or 1, 2, 3, or 4 for the successive larger flares) that denotes the flare size and a letter (f = faint, n = normal, b = bright) corresponding to subjective estimate of the intensity of emission (Table 1.1).

– **GOES classification:** Another classification scheme of solar flares based on soft X-ray observations of the Sun by series of Earth-orbiting GOES satellites has come into common usage since about 1970. In this scheme, the size of flare is given by the peak intensity (on a logarithmic scale) of the emission. The flares are classified with a letter (A, B, C, M, or X) corresponding to the power of 10 (-8, -7, -6, -5, -4, respectively) of the peak 1–8 Å flux in units of W m^{-2} and a number (1–9) that acts as a multiplier (see Table 1.2). Generally, flares smaller than C1 can only be detected during a solar cycle minimum when the

[1] http://www.ips.gov.au/Educational/2/4/2

Table 1.2: Soft X-ray classification of solar flares.

Importance	peak flux at 1–8 Å (W m^{-2})
A	10^{-8} to 10^{-7}
B	10^{-7} to 10^{-6}
C	10^{-6} to 10^{-5}
M	10^{-5} to 10^{-4}
X	10^{-4} and above

X-ray background is low. Flares occasionally exceed class X9 in intensity; they are simply referred to as X10, X11 etc. events (e.g., historical X17 flare on 2003 October 28; Mandrini et al. 2006).

Confined versus eruptive flares

The very early observations of solar flares in soft X-ray (SXR) wavelengths from the Skylab mission in 1973–1974 established two morphologically distinct classes of flares: confined and eruptive events (Pallavicini et al. 1977). The confined flares are characterized by brightenings in a single magnetic loop or flux tube and remains apparently unchanged in shape and position throughout the event thus also referred as simple loop, compact or point flares (e.g., see left panel of Figure 1.2). The loop may have a structure consisting of several (or a continuum of) loops and may cause a simple brightening in Hα at the feet of the loop. Simple-loop flare vary considerably in size, and we may see brightened arches that involve emissions from adjoining coronal regions, as well as short-lived brightenings of tiny X-ray bright points not detectable at all in the chromosphere. Generally, confined flares are short duration and impulsive in nature that are not associated with CMEs. The second category comprises the long duration events (LDE) which are eruptive in nature (e.g., see right panel of Figure 1.2). These are much larger and more dramatic than a confined flare and generally occurs along a polarity inversion line (PIL) in the photospheric magnetic field and are observed in Hα on the disc as two bright ribbons expanding outward from the PIL (see Figure 1.1). Frequently,

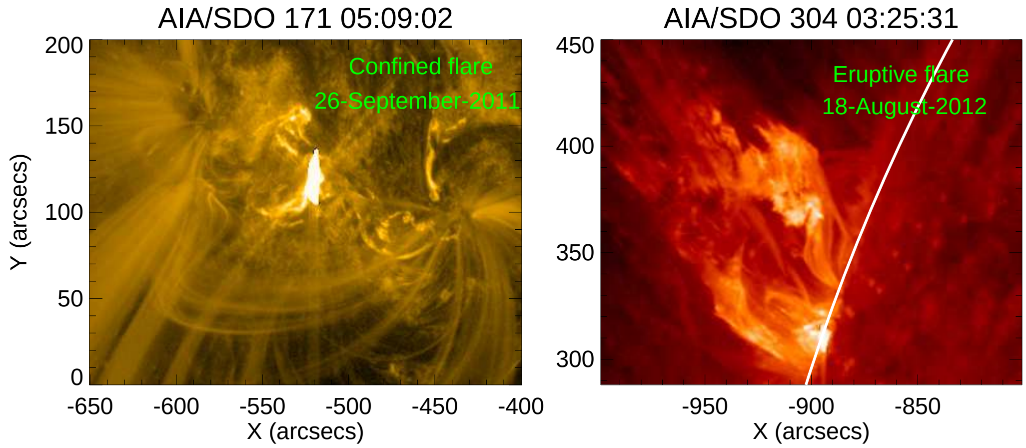

Figure 1.2: Examples of confined and eruptive flares. Left panel shows AIA 171 Å image of a M4.0 confined flare observed in active region NOAA 11302 on 2011 September 26. Right panel presents AIA 304 Å image of an eruptive M1.8 flare observed in active region NOAA 11548 on 2012 August 18.

eruptive flares are seen to be connected by a rising arcade of so-called "post-flare" loops (see Figure 1.3). Two-ribbon flares are strongly associated with CMEs.

1.1.2 Prominences

Prominences are relatively cool, dense objects that are embedded in the hotter corona and are commonly observed above the solar limb in emission in Hα line (Figure 1.5). The term "prominence" is used in describing a variety of such cool objects ranging from relatively stable structures (with life times of several hours to several days) to relatively transient structures (with life times of a few hours or less). When seen projected against the solar disk, prominences appear in absorption in Hα as dark features called "filaments". Although prominences and filaments are known to be the same structures, they were originally identified as distinct objects. We use the terms "filament" and "prominence" interchangeably in general contexts (Gilbert et al. 2001).

Traditionally, prominences are observed in the first line of the Balmer series of the hydrogen, famously known as the Hα line, with wavelength 6562.8 Å. When

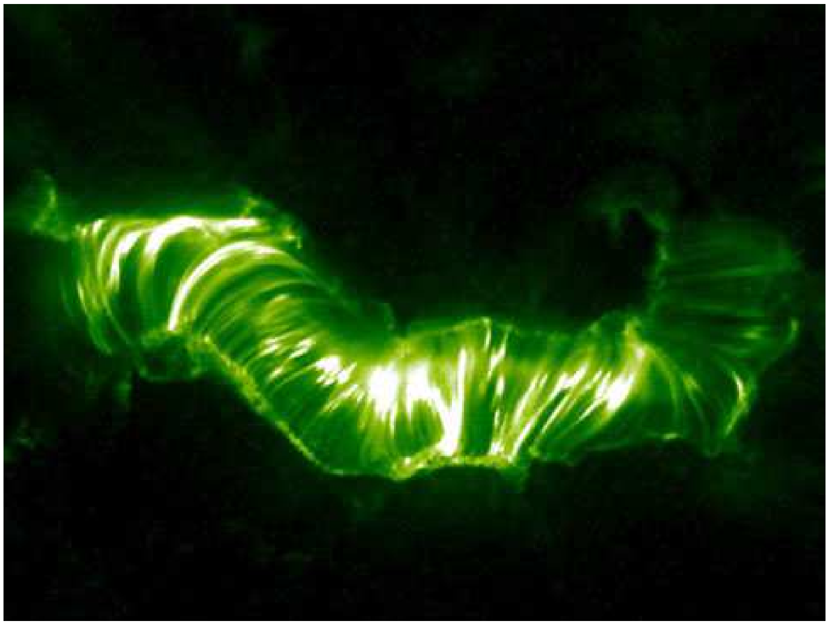

Figure 1.3: TRACE EUV post-flare loops of the famous 'Bastille Day Flare' observed on 2000 July 14 at 195 Å. Figure is adapted from http://soi.stanford.edu/results/SolPhys200/Schrijver/images/T195_20000714_105955.gif.

seen against the solar disc, filaments absorb all of the light in the Hα line, and re-emit it. However, the amount of light the filament re-emits in the direction of the observer is very small compared to light in the same wavelength band coming from rest of the solar disc. As a result, the filament appears dark on the disc (Zirin 1988). However, when seen against the dark sky, the light emitted by prominences towards the observer is more than that scattered by the tenuous corona, due to which they appear bright. Their temperature ranges from 5000–8000 K, while the number density ranges from 10^{16}–10^{17} m^{-3}. For a comparison, we note that temperature and density of the surrounding solar atmosphere are roughly 10^6 K and 10^{15} m^{-3}, respectively. Apart from Hα, filaments are also observed in the He I infrared line at 10830 Å. For more than past 15 years though, filaments are also observed in several extreme ultraviolet (EUV) wavelengths, like 195 Å and 304 Å. This has allowed the researchers to explore hitherto unseen aspects of prominence evolution, especially their eruptions.

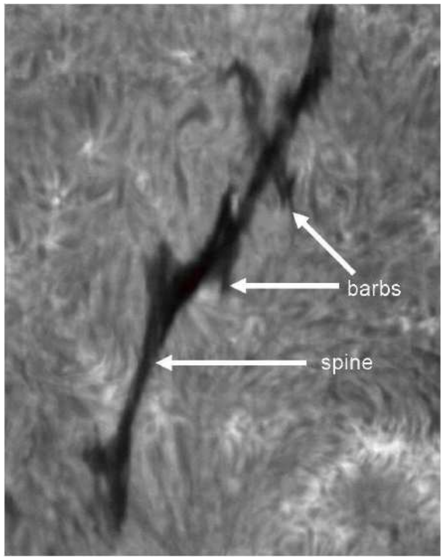

Figure 1.4: An image of a filament with its spine and barbs are marked and identified by arrows.

Physical characteristics

The prominences are commonly classified as “active region”, “intermediate”, and “quiescent” prominences to delineate basic variations in prominence characteristics. It should be noted that majority of prominences of all types show two common structural components: spine and barbs (Martin 1998). The spine corresponds to the major axis of the structure (particularly evident in long filaments seen on the disk) and is the highest part of the prominence. The barbs are the appendages along the sides of filament which extends from spine (Figure 1.4).

– **Active region prominences:** Active region (AR) prominences occur adjacent to sunspots, typically over PILs in associated plage regions. The key structures in the AR prominences are long thin threads that occur in groups of relatively horizontal “bundles”. The bundles are generally not straight and can exhibit upward or downward curvature. Thread lengths are typically 5–30 Mm with typical thicknesses of 350–650 km in Hinode/SOT images (Okamoto et al. 2007). AR prominences are the most eruptive of prominences with typical time between eruptions or major “activation” events measured in hours. In comparison, intermediate and quiescent prominence erupt on time scales of days or weeks.

– **Intermediate prominences:** Intermediate prominences form outside of active regions, typically in the mid-latitude regions between remnant plage regions that have been sheared by differential rotation to form elongated PILs, sometimes extending for 500 Mm or more. Intermediate prominences do not usually occupy the entire PIL, occurring in shorter segments of order 100 Mm in the extended filament channel. Like AR prominences, intermediates are composed of a multitude of threads having thickness of ∼300–500 km. However, intermediate prominence threads are shorter in length and occur in upward-arcing "dips", at least when seen at the limb along some sight lines (prominence appearance is highly dependent on the angle of the line-of-sight to the local prominence axis at the limb) (see Berger 2014).

Intermediate filaments exhibit the same activation events as AR structures but with lower frequency. Intermediate filament eruptions typically involve only individual segments with neighboring segments often remained unaffected.

– **Quiescent Prominences:** Quiescent prominences are typically found in high latitude regions ($>50^{\circ}$) far from active regions, are generally shorter in latitudinal extent, and associated with weaker photospheric fields. Quiescent prominences are the tallest prominences, sometimes extending 50 Mm or more above the limb (Figure 1.5). All quiescent prominences have overlying coronal cavities, however, the cavity may not be visible in typical EUV filtergrams for some sight angles.

Typical quiescent prominence structures in visible light passbands are long, predominantly quasi-vertical threads. These threads are thicker and more complex than active or intermediate prominence threads. Typical threads thickness is 500–700 km in Hinode/SOT observations with lengths on the order of 10–20 Mm (Berger et al. 2008). However, when seen on the disc, quiescent filament threads appear much thinner and more horizontal than limb prominence threads (see e.g., Lin et al. 2005).

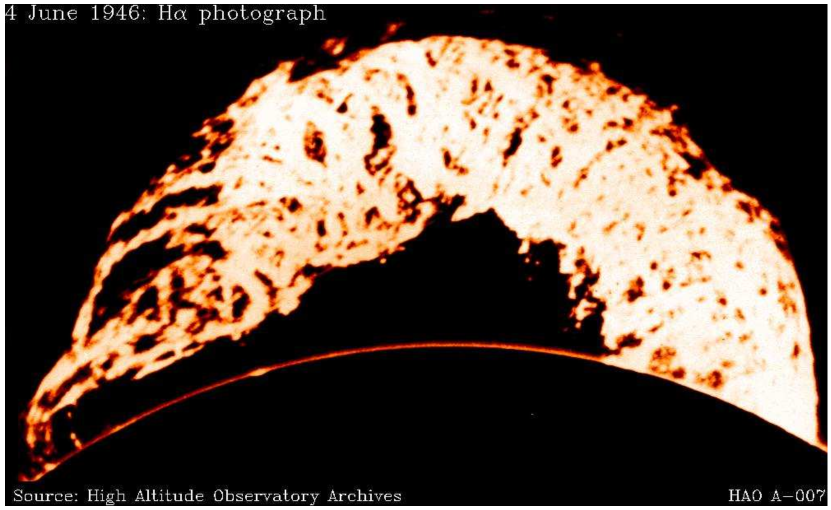

Figure 1.5: A very famous gigantic prominence, nicknamed as the granddaddy, observed in Hα on 1946 June 4 from the High Altitude Observatory (HAO). Figure adapted from http: *//casswww.ucsd.edu/archive/public/tutorial/Sun.html*

Eruptive prominence

Most of the prominences complete their lifetimes on the Sun in the form of eruptions (Filippov and Den 2001). A prominence is said to attain its eruptive phase when it becomes unstable and rises, parts of it become fainter and eventually disappear, and the rest of its mass may fall back and join the formation of a new prominence. It is widely accepted that the eruption is accomplished with the sudden release of the stored magnetic energy in the corona (Low 1981; Forbes 2000). However, the cause responsible for a sudden destabilization is still not known precisely. Observations reveal that prominence eruptions follow a variety of ways. Raadu et al. (1987) have termed prominences that rise slowly over a long period of time as *disparition brusques* (DBs). Prominences during their eruption have been reported to exhibit a helical nature by several researchers (Vrsnak et al. 1988, 1991; Srivastava et al. 1991). CMEs associated with eruptive prominences (EPs) are also known to show a helical structure (Dere et al. 1999; Ali et al. 2007; Kumar et al. 2012). The activation of prominences may also be caused due to the subtle pre-flare activity that starts several hours prior to their eruptive phase

(Chifor et al. 2006, 2007; Joshi et al. 2011). The pre-flare activity mostly occurs in the form of localized and distinct events of energy release, in the vicinity of the quasi-stationary prominence.

Contemporary studies show that prominences exhibit a wide range of eruptive activity behavior including dramatic activation with the filament mass remaining confined to the low corona (e.g., Ji et al. 2003; Alexander et al. 2006; Mrozek 2011), the eruption of part of the observed filament structure (Tang 1986; Gilbert et al. 2000; Gibson et al. 2002; Pevtsov 2002), and the almost complete eruption of all the prominence mass (Plunkett et al. 2000).

To elucidate the relation between the filament mass and corresponding supporting magnetic structure, Gilbert et al. (2007) proposed observational definitions of "full", "partial", and "failed" eruptions. A "full" eruption is defined to occur when the entire magnetic structure erupts while containing the bulk (approximately 90% or more) of the pre-eruptive filament mass (i.e., the mass escapes without draining or settling back to the surface). "Failed" eruptions are defined by the dynamical evolution of the filament, which displays an initially eruptive-like acceleration persisting for a relatively short duration prior to a period in which the filament decelerates, reaching a maximum height as the mass in the filament threads drains back toward the Sun (Mrozek 2011). In the other words, in a "failed" eruption, none of the lifted filament mass nor the supporting magnetic structure escapes the solar gravitational field, although this does not preclude localized dynamic activity, heating and flare production (Alexander et al. 2006). "Partial" eruptions are more complicated to define observationally, since the coupling of the filament mass and its supporting magnetic structure create a couple of different sub-categories in this class. The first type of partial eruption occurs when the entire magnetic structure erupts containing either some or none of its supported pre-eruptive filament mass. The second type of partial eruption occurs when the magnetic structure itself partially escapes containing either some or none of the filament mass.

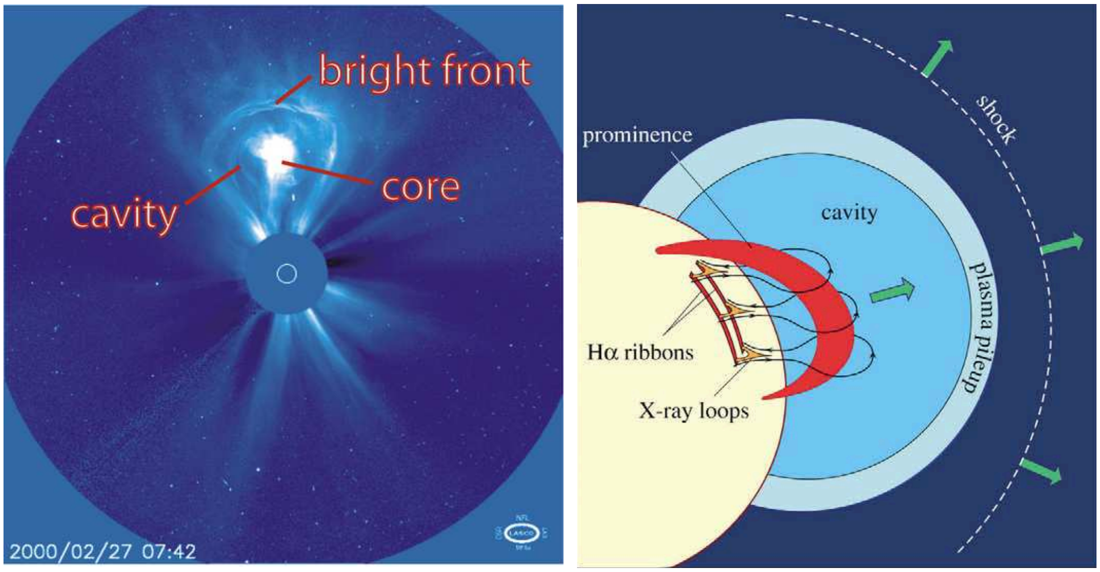

Figure 1.6: Left panel: An example of a classical three-part CME. The core, cavity and bright front are indicated (Riley et al. 2008). Right panel: A standard model for a "three-part" CME or eruptive flare (Forbes 2000).

.

1.1.3 Coronal mass ejection (CMEs)

Coronal mass ejections are one of the most spectacular manifestations of solar activity, in which vast amount of magnetic flux ($\sim 10^{21-23}$ Mx) and solar plasma ($\sim 10^{15-16}$ g) are ejected from the low corona into interplanetary space (Gosling 1990). Because of their large structure and high energetics, CMEs are thought to be important for reconfiguring the large-scale fields of the solar corona over the solar cycle (Low 2001). CMEs also play a major role in Sun-Earth connection.

Basic characteristics of coronal mass ejections

CMEs exhibit a variety of shapes and sizes with many topological variations (Reviews by Hundhausen 1999; Harrison 2001; Hudson et al. 2006; Gopalswamy 2006). Many CMEs have a classical "three-part" structure: a bright leading arc followed by a darker, low density cavity and bright core of dense material (Figure 1.6). The leading arc can appear as a sharply defined single loop or highly structured loop system. The bright leading edge is due to plasma that piles-up ahead of the eruption. With the expansion of the loop system, one often finds a cavity behind it which shows that the loop system is leading a region of depleted density. However, the magnetic field in the cavity region is probably higher. For many CMEs, the ascending feature of a prominence or filament is seen within the cavity which erupts as a part of the CME event. Many CMEs appear to rise from the pre-existing coronal helmet streamers that can persist in the corona for days to about a month. The streamer can show signs of the impeding ejection by displaying a gradual 'swelling' one to several days before ejection. The ejection itself can disrupt the steamer which may form again afterwards.

Estimates of the apparent speeds of the leading edges of CMEs range from about 30 to over 2500 km s^{-1} with an average value of $\sim$300–500 km s^{-1} (Yashiro et al. 2004). The gravitational escape speed near the base of the corona can be estimated to be about 550 km s^{-1}. The majority of CMEs show constant speed or modest acceleration at speeds below the gravitational escape speed. Even for speeds at the extreme low end of the observed range of speeds very few display deceleration. The relative absence of deceleration suggests that CMEs are generally driven by magnetic and pressure forces that either cancel or overwhelm gravity once CMEs are in motion (Low 2001, and references their in). The mass of the CME can be estimated by measuring the excess brightness of a given image relative to a pre-event image. Many estimates have put a typical CME mass at about 10^{15-16} g. The kinetic and potential energies of a CME can be determined from the inferred masses and velocities. The total mechanical energy of a major CME computed in this manner is of the order 10^{31-32} ergs. However, mass and energy calculations may have large uncertainties because of the assumption that CME material is located in the plane of the sky.

Source regions of coronal mass ejections

The association of prominence or filament eruption with the CMEs is well recognized. Statistical investigations indicate that 75% of CMEs contain prominence

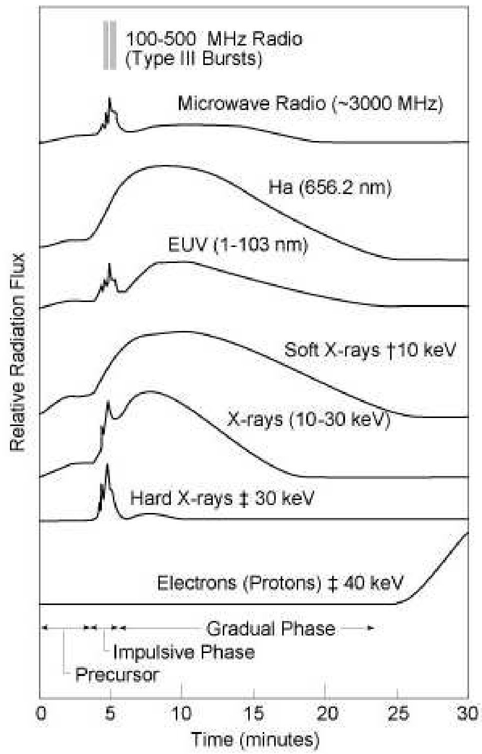

Figure 1.7: A schematic representation of the different phases of a typical solar flare as observed in electromagnetic radiation and particle motion. Figure from Kane et al. (1974).

or filament material, with or without flare, as a part of ejection. The prominence can rise as a single entity within the CME but many events show partial prominence eruption under the CME (Harrison 2001). Many CMEs are observed to involve solar active regions. For such events, the ejection process can be associated with flare activity (Low 2001). Observations reveal that three-part CMEs are associated with chromospheric Hα two ribbon flares or long duration X-ray events in the corona (Kahler 1992; Hundhausen 1999). The study of relationship between the relative timings of flare onsets and CME onsets shows that the flare onset can occur well before, in coincidence with or after the CME onset. Further, the location of a CME associated flare can be anywhere under or near the span of CME. Frequently a flare is observed at one of the legs of the CME. Based on many observations of CME characteristics associated with prominences and/or flares, one can draw the conclusion that associated flare and prominence activity occur as a result of process which also led to the mass ejection, but neither the flare nor the prominence eruption cause the CME. For the same reasons, the

CME cannot generate the flare (Harrison 2001).

The coronal dimming observed in X-ray and in the EUV is an other important signature of CMEs which shows a change in density due to depletion of emitted material in the region of interest (Hudson and Webb 1997). Another interesting feature associated with the eruptions are the EUV waves. These waves are best seen in the running difference images at 195 Å observed by EIT instrument aboard SOHO. Thompson et al. (1999) interpreted them as fast mode MHD waves, similar to the Morton wave observed in Hα.

1.2 Evolutionary aspects of eruptive flares

1.2.1 Time evolution

A flare is a multi-wavelength phenomena. Therefore, in order to have a complete understanding of its temporal evolution, we need to look at the time profiles observed at different wavelengths (see Figure 1.7). However, it has been observed that there could be subtle activities at the flare location before its onset. In the following, we discuss different aspects of flare evolution.

Pre-flare activity and precursor phase

The pre-flare activity refers to the very earliest stage of flare which is elusive to recognize even in soft X-rays (SXRs) (Joshi et al. 2011). The activities in this initiation phase can be seen at longer wavelength such as Hα, ultraviolet (UV), and extreme ultraviolet (EUV). The observations of subtle changes in the configuration of EUV loops and localized brightenings during this early phase can provide important clues about the triggering mechanism of the eruption (Chifor et al. 2007; Joshi et al. 2011). It has been suggested that the pre-flare brightening may occur as a result of slow magnetic reconnection and provide a trigger for the subsequent large-scale eruption (Moore et al. 2001; Chifor et al. 2007).

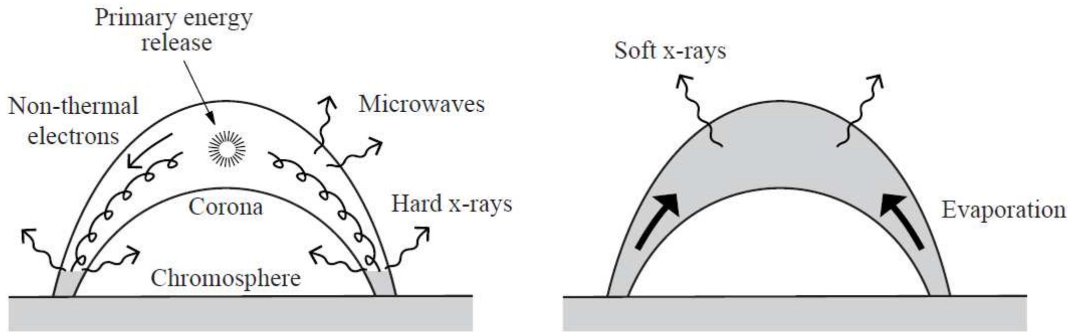

Figure 1.8: Non-thermal thick-target model showing the production of microwave, hard X-ray and Soft X-rays. Figure from Priest and Forbes (2002).

Many flares show slow and gradual enhancement in SXRs before the onset of the impulsive energy release, referred to as the X-ray precursor phase (Tappin 1991). This early phase mainly corresponds to small-scale brightening in UV to SXR wavelengths (Chifor et al. 2007; Kim et al. 2008; Joshi et al. 2011). The precursor flare brightening mostly occurs in the neighborhood of the main flare location (Fárník et al. 1996). However, usually precursor and main flare locations do not exactly coincides (Fárník and Savy 1998; Warren and Warshall 2001). Some studies recognize the precursor phase brightenings as the evidence for distinct, localized instances of energy release which play a significant role in destabilizing the magnetic configuration of active region leading to eruption and large-scale magnetic reorganization (Chifor et al. 2007; Joshi et al. 2011).

Impulsive phase

The primary energy release takes place during the impulsive phase which lasts from tens of seconds to tens of minutes. This phase is marked by emission in hard X-rays (HXR), non-thermal microwave (MW) and in some cases also γ-rays and white-light continuum, showing evidence of strong acceleration of both electrons and ions. These radiations are further supplemented by strong enhancement of emissions in chromospheric lines (e.g., Hα), UV and EUV. The impulsive phase is mainly characterized by the flare signatures at chromospheric layers where the feet of magnetic loops are rooted at the both side of polarity inversion line. Morphologically, flare brightenings at this region are termed as "footpoints" or "ribbons" detected in HXRs and Hα observations, respectively (see right panel of Figure 1.9). With the upward expansion of the arcade of loops, the two parallel flare ribbons (or HXR footpoints) separate from each other during the impulsive phase and later. The HXR emission from the footpoints of the flaring loops is traditionally viewed in terms of the thick-target bremsstrahlung process in which the X-ray production at the footpoints of the loop system takes place when high-energy electrons accelerated in the coronal reconnection region, come along the guiding magnetic field lines and penetrate the denser transition region and chromospheric layers (Figure 1.8) (Brown 1971; Syrovatskii and Shmeleva 1972).

Gradual phase

The gradual phase of a solar flare is best described by SXR time profile. During the impulsive onset of HXR emission, the SXR gradually builds up in strength and peaks a few minutes after the impulsive emission. This implies that the long-lived and gradual SXR emission is a delayed effect of the impulsive onset of HXR radiation. This phase is characterized by the formation of loops (and arcade of loops in large flares) which emits in SXRs and EUV, indicating the presence of hot plasma ($\sim$10–20 MK) inside them. The process of filling of hot plasma in coronal loops is termed as "chromospheric evaporation" (right panel of Figure 1.8) (Neupert 1968; Lin and Hudson 1976; Milligan et al. 2006a,b; Nitta et al. 2012). The chromospheric plasma is rapidly heated and compelled to spread out in the coronal loops primarily by the energy deposition of energetic electrons accelerated at the magnetic reconnection site in the corona (Lin and Hudson 1976; Veronig et al. 2010). Thermal conduction from the corona may also play a role in heating the chromospheric plasma (Antiochos and Sturrock 1978; Warren and

Warshall 2001; Battaglia et al. 2009). The flare loop system exhibits a gradient in temperature with outermost loops being the hottest (Forbes and Acton 1996).

1.2.2 Sigmoid-to-arcade evolution

Sigmoids are distinct, coronal structures which are often associated with the source region of coronal mass ejections (Rust and Kumar 1996; Manoharan et al. 1996). They appear as forward or inverse S-shaped large features composed of hot coronal plasma and frequently observed in coronal images taken in soft X-ray (Sterling et al. 2000; Gibson et al. 2002) and hot EUV energy channels (Zarro et al. 1999; Vemareddy and Zhang 2014). The central portion of these structures is approximately aligned with the filament channel. Hudson et al. (1998) suggests that a large fraction (seven out of eleven) of the soft X-ray source regions of halo CMEs have pre-flare sigmoid shape. By studying Yohkoh/SXT movies for the years 1993 and 1997, Canfield et al. (1999) found that sigmoidal regions are significantly more likely to be eruptive than non-sigmoidal regions. Typically they transforms into arcades or cusped loops as the eruption progresses (Sterling et al. 2000; Pevtsov 2002; Gibson et al. 2004). A sigmoid indicates a highly sheared, non-potential coronal magnetic field and might be an important precursor of a CME. The "sigmoid-to-arcade" development suggests the eruption and subsequent reconnection of strong magnetic field lines associated with the CME system (Sterling et al. 2000).

1.2.3 CSHKP model

The most commonly quoted reconnection model for flares is the so-called CSHKP model (Figure 1.10) (Carmichael 1964; Sturrock 1966; Hirayama 1974; Kopp and Pneuman 1976). Carmichael (1964) was the first to suggest that flare loops and ribbons could be understood as a consequence of the relaxation of the magnetic field lines stretched by the ejection of plasma into interplanetary space. Because

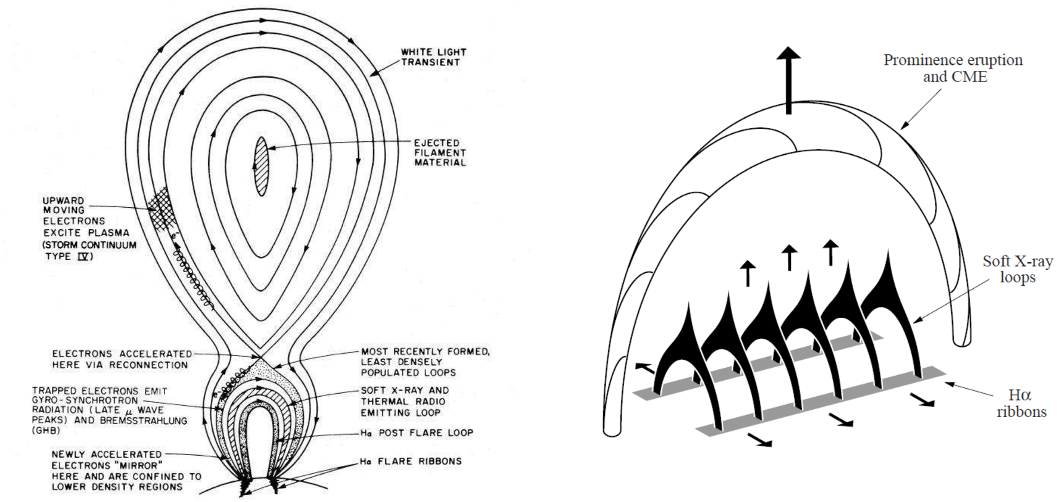

Figure 1.9: Magnetic topology of a gradual or eruptive flare (left panel) (Cliver et al. 1986), some key observational features of an eruptive flare (right panel) (Priest and Forbes 2002).

the field lines of closed magnetic loops are well anchored at their footpoints in the photosphere, they become highly extended when the plasma at the top of the loop is ejected during an eruption. The field lines stretched in this way are said to be "open", and they relax to form smaller closed loops through the process known as magnetic reconnection. Models of this process show that the reconnection process also releases sufficient magnetic energy to account for the radiative and kinetic energy observed during an eruption (Sturrock 1972; Hirayama 1974; Kopp and Pneuman 1976). The rise of the loop system is explained by the fact that the reconnection site continually moves upward as more and more magnetic field lines reconnect. The picture automatically accounts for the apparent motions of the flare ribbons without the existence of any actual plasma flow in the two ribbons (right panel of Figure 1.9). It also explains why the hottest X-ray loops are at the top of the loop system. The common point in four pioneering papers of CSHKP model is only that magnetic reconnection occurs in a vertical current sheet above a closed loop. There is no agreement on the mechanism of current sheet formation in these papers.

The overall behavior of a large two ribbon flare is shown in Figure 1.9 (left

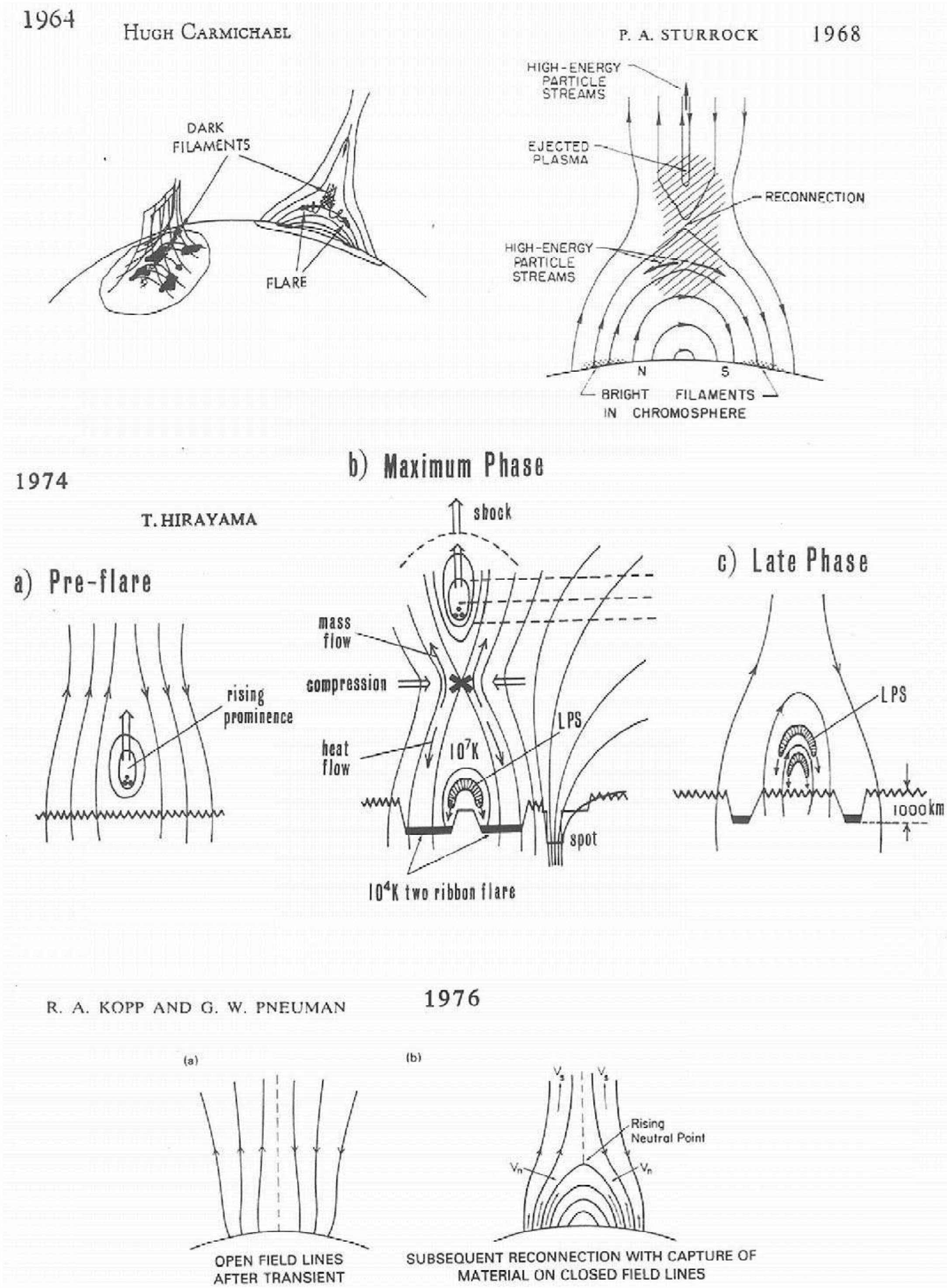

Figure 1.10: The basic coronal magnetic configuration first proposed for eruptive flares by Carmichael (1964), later improved by Sturrock (1966), Hirayama (1974), and lastly by Kopp and Pneuman (1976). Figure from Lin et al. (2003).

panel). First, a sheared or twisted coronal arcade containing a prominence rises slowly during the pre-flare phases. Then at flare onset there is a rapid eruption and the production of fast particles and flare loops, presumably due to the onset of reconnection below the rising arcade. A similar process can occur outside an active region when a large quiescent prominence and its overlying helmet structure erupt to give a coronal mass ejection. The MHD of the process may well be the same as in an eruptive two-ribbon flare from inside an active region. Since the magnetic field strength outside an active region is much lower, eruptive speeds and electric fields are much smaller, therefore fewer non-thermal effects are produced.

1.2.4 Plasmoid-induced-reconnection model

Yohkoh satellite discovered X-ray plasmoid ejections from compact impulsive flares (Shibata et al. 1995; Ohyama and Shibata 1997, 1998), Shibata (1996, 1997), proposed the plasmoid-induced-reconnection model, by extending the classical CSHKP model. In this model, the plasmoid ejection plays a key role in triggering fast reconnection (Figure 1.11). According to this model, the plasmoid play two crucial roles in triggering fast reconnection:

• A plasmoid can store energy by inhibiting reconnection. The magnetic reconnection would follow only after the plasmoid ejection from the current sheet. If a larger plasmoid is ejected, a larger energy release will occur.

• A plasmoid can induce strong inflow into the reconnection region. Let us consider the situation where a plasmoid suddenly rises at velocity $V_{plasmoid}$. Since the plasma density does not change much during the eruption process, the inflow must develop toward the X-point to compensate the mass ejected by the plasmoid. The inflow speed can be estimated from the mass conservation law (assuming incompressibility, for simplicity); $V_{inflow} \sim V_{plasmoid}\ L_{plasmoid}/L_{inflow}$ where $\mathrm{L}_{plasmoid}$ and L_{inflow} ($\geqslant L_{plasmoid}$) are the typical sizes of the plasmoid

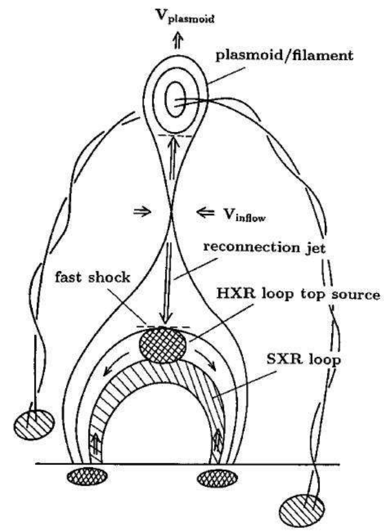

Figure 1.11: A schematic representation of plasmoid-induced-reconnection model proposed by Shibata (1996).

and the inflow. In this model, the impulsive phase corresponds to the interval when $L_{inflow} \sim L_{plasmoid}$, i.e., $V_{inflow} \sim V_{plasmoid}$. Since the reconnection rate is determined by the inflow speed, the ultimate origin of fast reconnection in this model is the fast ejection of the plasmoid. If the plasmoid ejection (or outflow) is inhibited in some way, the fast reconnection would soon cease (Shibata 1999b).

Shibata (1996, 1997) further proposed that the plasmoid-induced-reconnection model is also applicable to smaller flares, such as microflares and X-ray jets. The key point is that the plasmoid formation and ejection is a scale invariant process and so it can occur even in a very small flare.

1.3 Theories of solar eruptions

The contemporary models of solar eruption assume that the energy released during eruptions is stored in the coronal magnetic field prior to the eruption, and that a loss of stability or equilibrium of coronal magnetic field leads to the energy release and eruption (Lin et al. 2005). These models transfer energy from the convection zone over a long time scale. The continual emergence of new flux from the convection zone and the movements of the footpoints of closed coronal field lines causes stresses to build up in the coronal field . Eventually, these stresses exceed a threshold beyond which a stable equilibrium can no longer be maintained, so the coronal field erupts. The models are based on the mechanism of accumulating energy in the coronal magnetic field, so they are thought of as the *storage model* (Priest and Forbes 2000)

In the following subsections, we discuss a few representative *storage models* of CMEs. In accordance with the approach of Klimchuk (2001), we describe various models in three classes: *mass loading*, *tether release*, and *tether straining* models (Figure 1.12).

1.3.1 Mass loading

The basic mechanism involved in *mass loading* models is illustrated in Figure 1.12 (top panel). Here a spring is being compressed by a heavy weight. If the weight is shifted to the side, the spring will suddenly uncoil, releasing much of the stored energy. Models that exploit this basic concept to explain solar eruptions are called *mass loading* models.

In *mass loading* models, it is presumed that the pre-eruption field is metastable allowing build up of sufficient free energy by mass loading before the onset of eruption. The substantial mass necessary for adequate compression can come in two possible form: higher-than-normal density coronal material distributed over a large volume, or extensively dense prominence material confined to a small volume. It has been suggested by Low (1996, 1999) and others that prominences play a fundamental role in the CME process. Several observations of the prominence eruptions, however, put constraint on the *mass loading* models. Here we find two main difficulties: (1) Many CMEs do not show any associated prominences in their source regions. (2) In a few cases when the CME is associated with prominence eruption, it has been observed that most of the prominence

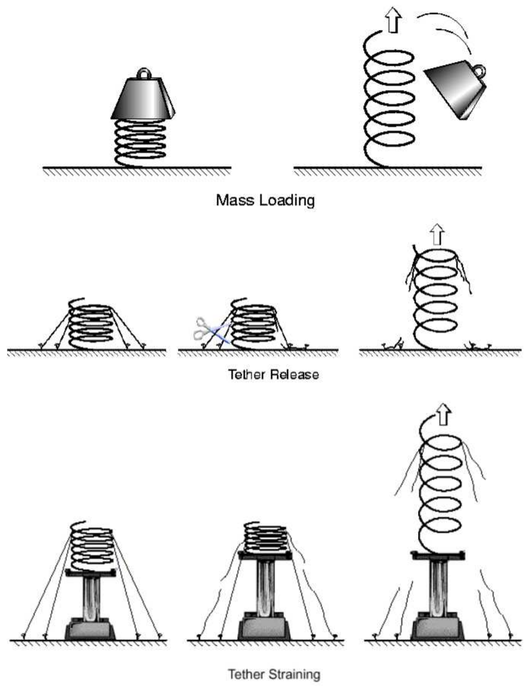

Figure 1.12: Physical (mechanical) analogues of three different CME models. Figure from Klimchuk (2001).

mass appears to rise rather than fall (Gilbert et al. 2000). In view of this, it can be concluded that mass loading by prominences can explain at most a subset of CMEs. Klimchuk (2001) has summarized advantages and limitations of various mass loading models of CME (e.g., Chou and Charbonneau 1996; Guo and Wu 1998; Low 1999).

1.3.2 Tether release

The flux ropes and filaments during the pre-eruptive conditions involve a balance between the upward force of magnetic pressure and the downward force of magnetic tension. The field lines that provide tension are sometimes called tethers. As illustrated by Klimchuk (2001), an analogy of such a system can be represented by ropes that hold the compressed spring in place (middle panel of Figure 1.12). Now a slow and systematic release of tethers would result greater strain on the remaining tethers. Eventually the strain becomes so great that the teth-

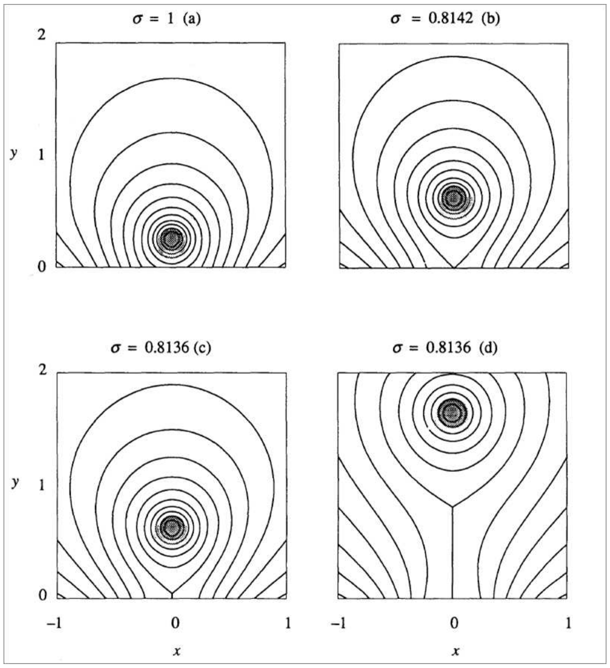

Figure 1.13: An example to the tether release process. Figure from Isenberg et al. (1993).

ers start to break. This proceeds catastrophically, and the spring uncoils in an explosive fashion. A few examples of CMEs models where *tether release* mechanism works are van Ballegooijen and Martens (1989); Forbes and Isenberg (1991); Isenberg et al. (1993); Lin et al. (1998) etc. Here, we present model of Forbes and Isenberg (1991) to illustrate how *tether release* works. It consists of an infinitely long flux rope and overlying arcade. Figure 1.13 shows a projection of the field onto a vertical plane orthogonal to the main axis. The arcade field lines act as the tethers that prevent the flux rope from rising. Their footpoints are slowly brought together by a converging flow imposed at the photosphere. When the footpoints meet at the neutral line, they connect to form a new circular field line at the perimeter of the flux rope, disconnected from the photosphere (see Figures 1.13(a)–(c)). After enough of the arcade field lines have been converted to flux rope field lines, force balance is no longer possible, equilibrium is lost, and the flux rope abruptly rises (Figure 1.13(d)).

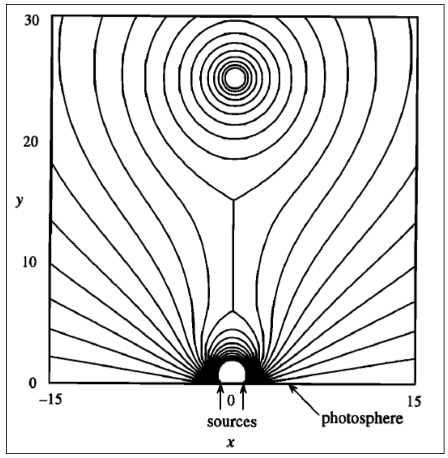

Figure 1.14: Magnetic reconnection at a vertical current sheet underneath the erupting flux rope. Figure from Lin and Forbes (2000).

The reconnection necessary for full eruption has an important observational consequence. It produces closed loops underneath the erupting flux rope. They form a new arcade that steadily grows with time as more and more reconnected flux accumulates. Many such arcades are observed in association with CMEs, but whether their timing, size, and location are consistent with the model predictions is not so clear (Hundhausen 1999).

1.3.3 Tether straining

Similar to *tether release* model, *tether straining* model also recognizes a slow evolution of flux rope toward its eruption. In *tether release*, the total stress is approximately constant in time but is distributed over fewer and fewer tethers. In tether straining, the number of tethers is constant but the total stress increases. In Figure 1.12 (bottom panel), we have shown the analogue representation of *tether straining* processes as depicted by Klimchuk (2001). In this illustration, the spring now sits on a platform that is slowly lifted. Ropes attached to the ground hold the top of the spring at a fixed height. As the spring becomes compressed, the strain on the ropes increases until they finally break, releasing the spring. The examples of *tether straining* model include sheared arcade models of Mikic and Linker (1994); Choe and Lee (1996); Antiochos et al. (1999) and Amari et al. (1996) and flux rope models of Forbes and Priest (1995); Wu et al. (1995) and Wu et al. (2000). Here, we briefly describe two representative models of this class, namely, *breakout* model of Antiochos et al. (1999) and *flux rope* model of Forbes and Priest (1995).

Breakout model (Antiochos et al. 1999)

This model fundamentally exploit the quadrupolar magnetic structure, with four distinct flux systems that are color coded blue (central arcade), green (two side arcades), and red (overlying field). Shearing motions imposed near the equator stretch the inner field lines of the central arcade in an east-west direction which are shown as thicker blue lines (Figure 1.15) (see Karpen et al. 2012). The enhanced magnetic pressure associated with the shear causes the core of the central arcade to inflate. Red field lines and unsheared (thin) blue field lines are the tethers which counter this tendency. As the system becomes more and more stressed, the magnetic X-point above the central arcade distorts, closing like a pair of scissors to form a horizontal region of enhanced electric currents (the red and blue field lines are oppositely directed). Once the stress is sufficiently great and the current layer sufficiently thin, the adjacent red and blue field lines reconnect to become green field lines that pull away from the X-point. With fewer tethers to resist, the central arcade bulges more, and a runaway eruption ensues.

Flux rope model (Forbes and Priest 1995)

The basic configuration of this model is that all the photospheric flux is concentrated in two point sources as shown in Figure 1.14. A converging flow is imposed at the photosphere to brought these sources closer but not allowed them to meet, hence the reconnection is not possible at this stage. However, the converging flows lead to buildup of magnetic pressure underneath the flux rope as the point sources are brought closer together. This increases the strain on the tethers, and

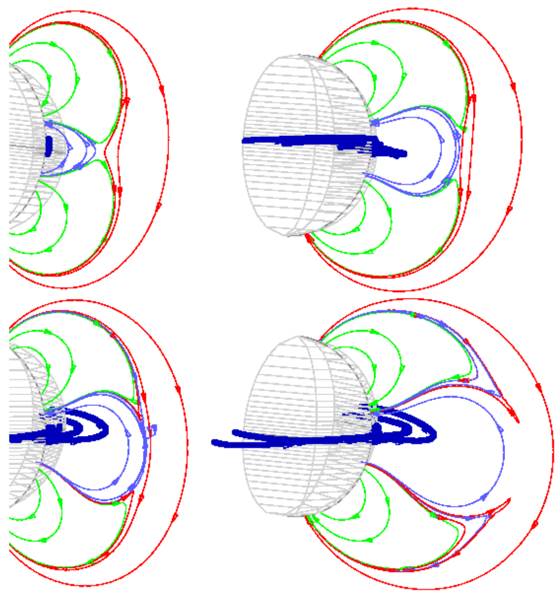

Figure 1.15: Breakout CME model showing the evolution of a quadrupolar system in which the inner part of the central arcade are sheared by antiparallel footpoint motions near the neutral line (equator). The field bulges slowly until the red and blue lines start to reconnent, and a fast eruption initiated (Antiochos et al. 1999; Karpen et al. 2012). Figure is addopted from http: *//solarmuri.ssl.berkeley.edu/ hhudson/cartoons/thepages/Antiochos.html*

equilibrium is eventually lost. The flux tube abruptly rises, a vertical current sheet is formed, and reconnection allows the eruption to proceed.

1.4 Motivation and organization of the thesis

During a flare, thermal and non-thermal emissions are originated at different energy levels, simultaneously from various regions of the active region. An eruptive flare typically spreads across all the atmospheric layers of the Sun and involves large-scale reorganization of coronal loop configuration across the polarity inversion line. To probe the complex physical processes involved in triggering and subsequent energy release in solar flares, we have carried out effective utilization of multi-wavelength and multi-instrumental measurements of the Sun in this thesis. In the following, I outline contexts and objectives of my work.

- We have undertaken extensive multi-wavelength studies of a few representative events of different categories, viz., confined and eruptive flares. These comprehensive investigations provide valuable insights on complex energy release processes occurring simultaneously at different layers of solar atmosphere with various temporal, spatial and energy scales. The new observations would be examined in the framework of scopes and limitations of standard flare model.

- A major objective of our work is to acquire observational signatures of magnetic reconnection and locate the site of particle acceleration and energy deposition by effectively combining HXR, MW, EUV, UV, and optical measurements.

- In this thesis, a comprehensive study of HXR spectra of solar flares has been undertaken with the motivation to investigate plasma heating to tens of millions of degree Kelvin and characterize temporal and spatial evolution of non-thermal electrons.

- To understand the triggering mechanism of solar eruptions, we emphasize observations of pre-flare activity and precursor phase of solar flares. Further, measurements of magnetic flux evolution through the photosphere during pre- to post- eruption phases can provide insights about the favorable conditions that lead to solar flares.

In this thesis, attempts have been made to investigate the key aspects of solar eruptive phenomena such as prominence eruptions, confined flares, coronal implosion, confined eruptions, and sigmoid-to-arcade evolution. For this purpose, we have selected a few representative solar events well observed at HXR energies by RHESSI. To explore the energy release processes simultaneously at different heights of solar atmosphere and energy scales, we investigate EUV, UV, optical, and radio observations taken from various space and ground based instruments in conjunction with X-ray measurements.

Based on the work carried out to accomplish the aforementioned objectives, this thesis is organized into seven chapters. A brief summary of the work presented in each chapters is given below.

Chapter 1: ***Introduction***

In this chapter, we have provided a detailed discussion on different aspects of solar eruptive phenomena in a manner that is relevant to the work presented in this thesis. This chapter includes descriptions on structures of active region corona, multi-wavelength flare emissions, and mechanisms of solar eruptions.

Chapter 2: ***Observations and data analysis***

This chapter contains the details of multi-wavelength observations taken from ground and space based telescopes. The techniques and tools used in analyzing multi-wavelength imaging data along with various algorithms for X-ray image reconstruction and spectral fittings are described. The major data sources for this thesis are: Reuven Ramaty High Energy Spectroscopic Imager (RHESSI), Solar Dynamic Observatory (SDO), Transition Region And Coronal Explorer (TRACE), and Nobeyama Radioheliograph (NoRH).

Chapter 3: ***Evolutionary phases of solar eruptive prominences and associated multiple flare activity***

In this chapter, we study spectacular eruptions of two active region prominences which occurred in active region NOAA 10656 on 2004 August 18 and NOAA 11548 on 2012 August 18 at west and east limbs of the Sun respectively. A major objective of this study is to identify the process of prominence destabilization through the observations of pre-eruption phase of the active region and pre-flare activity. By synthesizing the multi-wavelength measurements during the eruptive phase of the prominences, we explore the signatures of magnetic reconnection in the corona and discuss the thermal and non-thermal effects driven by the prominence eruption.

Chapter 4: ***Confined flare in AR 11302 and associated magnetic transients***

Majority of confined flares exhibit rapid evolution and compact morphology. Unlike the eruptive flares, where large-scale reconnection is driven by flux ropes or filament eruptions, we do not have clear idea about triggering of reconnection in confined flares. To understand the triggering mechanism and multi-wavelength aspects of energy release in such flares, we present a case study of a confined M4.0 flare from NOAA 11302 on 2011 September 26. Observations at unprecedented temporal, spatial, and spectral resolution from SDO and RHESSI enabled us to explore the possible triggering and energy release processes of this flare despite its very impulsive behavior and compact morphology. From this case study, we infer some important conclusions about the evolution of flare loops and thermal/non-thermal emissions within the confined environment of active region corona. Another novelty of this analysis lies in the identification and assessment of magnetic transients that developed just prior to the flare onset.

Chapter 5: ***Dynamical evolution of coronal loops and energy release during a confined flux rope eruption in AR 10646***

In this chapter, we study coronal events that occurred in active region NOAA 10646 on 2004 July 14 over a span of one and half hours. After striking pre-flare phase, we observe a major M6.2 flare during which a large flux rope and associated prominence material underwent confined eruption. In this study, we present observations of large-scale contraction of overlying EUV coronal loops, observed for an extended period of ∼30 minutes during the pre-flare phase. Such a large-scale contraction of coronal loops has been reported for the first time. By analyzing the multi-wavelength observations of the pre-flare phase, we attempt to compare the observed phenomena of loop contraction with coronal implosion scenario predicted by Hudson (2000). In this chapter, we have further performed detailed RHESSI X-ray spectroscopy to estimate thermal and non-thermal energies released during the M6.2 flare.

Chapter 6: ***Multi-wavelength study of a sigmoid-to-arcade evolution in AR NOAA 11719***

In this chapter, we present a comprehensive multi-wavelength analysis of sigmoidal active region NOAA 11719 on 2013 April 11. We discuss the dramatic evolution of this active region over a period of ten hours during which EUV sigmoid structure was formed by the interaction of systems of coronal loops. With the expansion of twisted flux ropes, the sigmoid underwent an activation phase and subsequently erupted. The evolution of sigmoid was observed at 94 Å images which implies that the structure comprised of very high temperature plasma (∼6 MK). During the eruption, we observed a large two-ribbon M6.5 flare which is characterized by a prolonged rise phase of ∼21 min. We have especially emphasized morphological and spatial evolution of flare sources during the early rise phase and discuss how these observations put constraint on standard flare model.

Chapter 7: ***Summary and prospects***

This chapter provides the summary of the work done highlighting the major findings in the above chapters and the scope for the future work.

Chapter 2

Observations and data analysis

2.1 Introduction

The solar eruptive phenomena mostly originate from solar active regions which consist of complex magnetic structures extending from the deeper sub-photospheric layers, crossing through the photosphere to the coronal heights. During an eruptive flare, the primary energy release takes place in the corona. Soon afterward, the flare spreads across all the atmospheric layers of the Sun and produce radiative signatures from plasma heated at multi-temperature and particles accelerated to high energies (Lin et al. 2003; Fletcher et al. 2011). Thus, a detailed study of solar transients require a thorough investigations of multi-wavelength measurements which is obtained from various space and ground-based instruments.

In this thesis, we have presented comprehensive analyses of X-ray observations of the Sun taken by Reuven Ramaty High Energy Solar Spectroscopic Imager (RHESSI). All the events reported in different chapters of this thesis were well observed by this instrument. We have extensively utilized imaging and spectroscopic capabilities of RHESSI to investigate the thermal and non-thermal energy release processes associated with different stages of the eruptive phenomena. Complementary to RHESSI X-ray measurements, we have combined solar observations at EUV, UV, Optical, Microwave, and Radio wavelengths to deduce the multi-wavelength perspective of the energetic processes. The other major data sources for this thesis are: Solar Dynamic Observatory (SDO), Transition Region And Coronal Explorer (TRACE), and Nobeyama Radioheliograph (NoRH). In particular, for imaging at UV and EUV wavelengths, TRACE data was extremely useful for solar events occurred in pre-SDO era. In this chapter, we provide a brief description of these instruments along with details of their data and analysis techniques.

2.2 Reuven Ramaty High Energy Solar Spectroscopic Imager (RHESSI)

The Reuven Ramaty High Energy Solar Spectroscopic Imager (RHESSI; Lin et al. 2002), launched on February 5, 2002, is a Small Explorer (SMEX) mission of National Aeronautics and Space Administration (NASA). It was designed to explore the basic physics of particle acceleration and explosive energy release in solar flares, through imaging and spectroscopy of hard X-ray/γ-ray continua emitted by energetic electrons, and of γ-ray lines produced by energetic ions. RHESSI provides full Sun observations with very high spatial and spectral resolutions. The basic instrumental characteristics of RHESSI satellite are given in Table 2.1.

2.2.1 RHESSI imager

RHESSI imaging is based on a Fourier-transform technique using a set of 9 Rotational Modulation Collimators (RMCs, grid pairs). Each RMC consist of two widely-spaced, fine-scale linear grids, which temporally modulate the photon signal from sources in the field of view as the spacecraft rotates about an axis parallel to the long axis of the RMC (for a schematic view see Figure 2.1). Each grid is a planar array of equally-spaced, X-ray-opaque slats separated by transparent slits

Table 2.1: RHESSI instrumental characteristics (Lin et al. 2002).

Energy range	3 keV to 17 MeV
Energy resolution (FWHM)	1 keV up to 100 keV 3 keV up to 1 MeV 5 keV up to 17 MeV
Angular resolution	$2''.3$ up to 100 keV $7''$ up to 400 keV $36''$ up to 1 MeV
Temporal resolution	2 s for detailed image, tens of ms for basic image
Field of view (FOV)	Full Sun ($\sim 1^{\circ}$)
Detectors	9 germanium detectors (7.1 cm dia. $\times$ 8.5 cm), cooled to $<$ 75 K with sterling-cycle mechanical cooler
Imager	9 pair of grids, with pitches from 34 microns to 2.75 mm, and 1.55 m grid separation

(Figure 2.2). The slits of each pair of grids are parallel to each other and their pitches (p) are identical so that the transmission through the grid pair depends on the direction of the incident X-rays. The modulation can be measured with a detector placed behind the RMC. The modulation pattern over half a rotation for a single RMC provides the amplitude and phase of many spatial Fourier components over a full range of angular orientations but for a small range of spatial source dimensions. Multiple RMCs, each with different slit widths, can provide coverage over a full range of flare source sizes.

Several image reconstruction algorithms (e.g., BACK PROJECTION, CLEAN, FORWARD FITTING, PIXON, etc.) are available in the RHESSI software which models the spatial distribution of photons by employing the observed modulated time profiles, spacecraft roll position as well as pointing. In our work, we have mainly used CLEAN and PIXON algorithms for image reconstruction. Here, we provide only a brief description about BACK PROJECTION, CLEAN and PIXON algorithms. More detailed description for all the image synthesis algorithms is given in Hurford et al. (2002).

– **BACK PROJECTION:** This is the most straightforward and basic method of image reconstruction. Back projection basically projects each detected photon back from the detector through the slits of the grid pairs to all possible locations for its origin on the Sun. This creates a probability map made up of parallel ridges aligned with the slit orientation at that time. The spacing between ridges is equal to twice the FWHM resolution of the sub-collimator. This back projection is repeated for each detected photon and the resulting probability maps are summed to form the so-called dirty map. This is simple and fastest algorithm for RHESSI image reconstruction but it provides poor quality images with sidelobes. The size of sources are also not reliable. Therefore, this algorithm is not much suitable when precise measurements of source location and size are required.

– **CLEAN:** CLEAN is an iterative algorithm based on the assumption that the image can be well represented by a superposition of point sources. This algorithm first finds the pixel with the highest flux in the dirty map created by the BACK PROJECTION algorithm and then assigns a point source with a fixed fraction of that flux at that pixel location in a new map of CLEAN components. It then subtracts that same fractional flux from the dirty map but spread out according to the Point Spread Function (PSF) centered on that pixel. This process is repeated by taking the pixel with highest flux in the new dirty map, the so-called residual map. Followed to this, iteratively the image is cleaned until either the number of iteration exceeds its limit or residual map leads to negative maximum. CLEAN is a relatively fast algorithm to reconstruct X-ray images and provides a reasonable estimation of HXR emitting region. Therefore, this algorithm is highly preferred for image processing.

– **PIXON:** The PIXON algorithm used for the reconstruction of images from

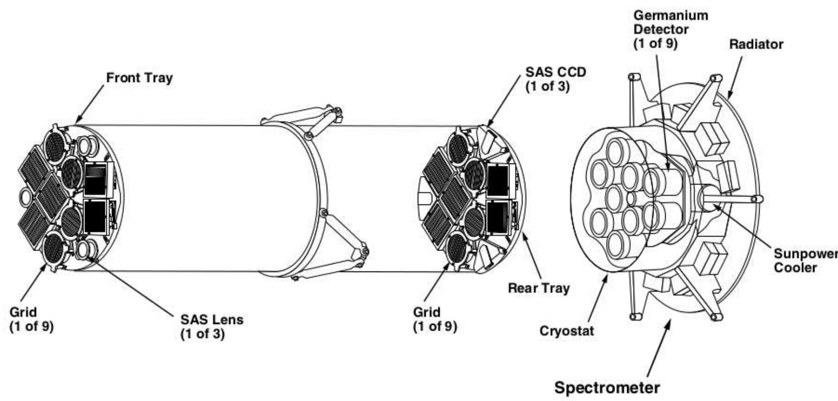

Figure 2.1: A schematic view of RHESSI imager. The principal components of RHESSI consists of two identical sets of nine grids mounted on front and rear grid trays. A corresponding set of nine cooled germanium detectors is mounted behind the rear grids. The solar aspect system (SAS) consists of three lenses mounted on the front grid tray which focus optical images onto SAS CCDs on the rear grid tray. Figure from Hurford et al. (2002).

RHESSI data is an adaptation of the program successfully used to analyze data from Yohkoh/HXT (Metcalf et al. 1996). Unlike CLEAN, which models the source as a collection of point sources, this algorithm seeks a superposition of circular sources or pixons of different sizes and parabolic profiles that best reproduces the measured modulations from the different detectors. The goal is to construct the image with the fewest degrees of freedom (the fewest pixons) that is consistent with the observations (i.e., the image predicts the modulated count rates with a value of chi-square per degree of freedom acceptably close to one). This technique is generally thought to provide the most accurate image photometry but the image processing with this algorithm is extremely slow. Therefore, this algorithm is highly useful to reconstruct precise images of extended source for specific times during a flare.

2.2.2 RHESSI spectrometer

The RHESSI spectrometer package is composed of nine cryogenically cooled coaxial germanium detectors (GeD)(Smith et al. 2002). A very important fact

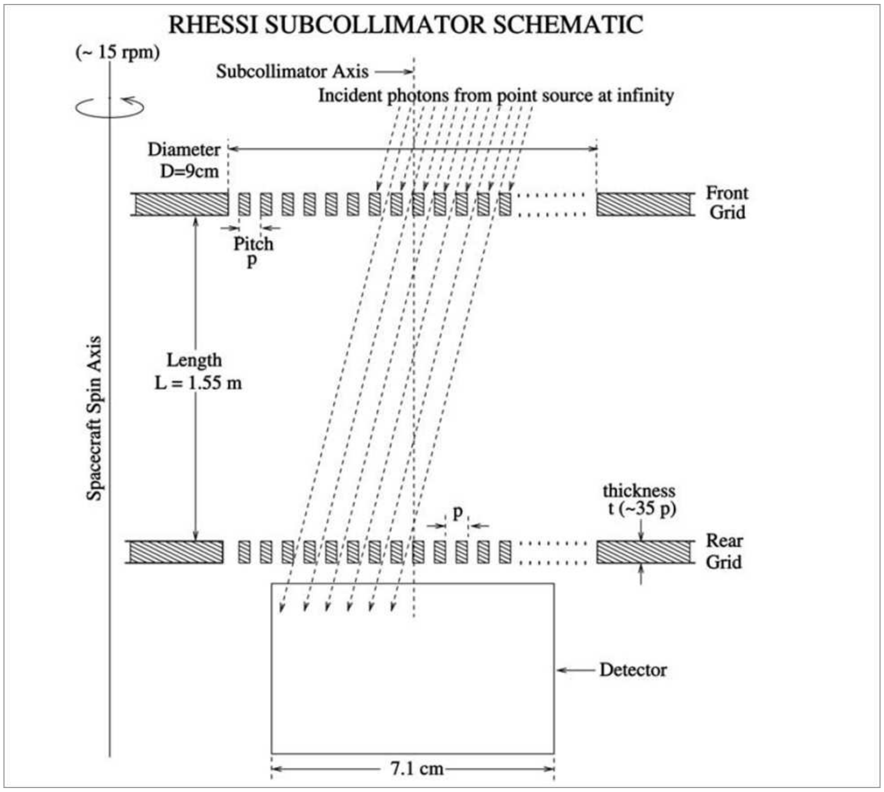

Figure 2.2: A schematic view of the RHESSI subcollimators. Figure from Hurford et al. (2002).

about the super-cooled ultra-pure germanium at cryogenic temperatures is that no electron-hole pairs in the conduction band is produced other than when a hard X-ray or gamma-ray photon interacts in the crystal which enables the release of many energetic electrons which create free pairs. If there is a high electric field ($\sim$1000 V cm^{-1}) across the crystal, the electrons and holes will be pulled to each electrode, creating a current pulse that can be amplified and digitized by suitable electronics.

RHESSI spectrometer is uniquely designed for achieving high-spectral resolution which allows for the accurate measurement of even extremely steep power-law spectra. The RHESSI GeD design provides energy coverage from 3 keV to 17 MeV with a single mechanically robust detector. For this purpose, hyper-pure (n-type) coaxial germanium material (7.1 cm dia. $\times$ 8.5 cm long) was used.

Table 2.2: TRACE temperature response (Handy et al. 1999).

Wavelength (Å)	Emission	Bandwidth (Å)	Temperature (K)
171	Fe IX/X	6.4	$1.6–20 \times 10^5$
195	Fe XII/XXIV	6.5	$5.0–20 \times 10^5$,
			$1.1–2.6 \times 10^7$
284	Fe XV	10.7	$1.25–4.0 \times 10^6$
1216	H I Ly α	84	$1.0–3.0 \times 10^4$
1550	C IV	30	$6.0–25 \times 10^4$
1600	UV cont, C I, Fe II	275	$4.0–10 \times 10^3$
1700	Continuum	200	$4.0–10 \times 10^3$
5000	White light	broad	$4.0–6.4 \times 10^3$

The inner electrode is segmented into two contacts that collect charge from two electrically independent detector segments, to provide the equivalent of a ∼1.5 cm thick planar GeD in front of a ∼7 cm thick coaxial GeD. The front segment thickness is chosen to stop photons up to ∼250 keV. The photons with energies from ∼250 keV to 17 MeV, including all nuclear γ-ray lines, stop primarily in the thick rear segments alone, with smaller fractions stopping in the front segment, thus depositing energy in both the front and rear segments.

The RHESSI spectroscopy is performed through OSPEX (Object Spectral Executive) which is an object-oriented interface for X-ray spectral analysis of solar data. It is the next generation of SPEX (Spectral Executive) written by R. Schwartz in 1995. It takes count rate spectra as its input then defines the time intervals for analysis, determines and subtract the background, decides on the functional form to assume for the photon spectrum, and uses the instrument response function to produce photon flux spectra.

2.3 Transition Region And Coronal Explorer (TRACE)

TRACE (Handy et al. 1999) was a NASA SMEX mission designed to investi-

Table 2.3: TRACE instrumental characteristics (Handy et al. 1999).

Primary diameter	30 cm
Effective focal length	8.66 m
Field of view (FOV)	$8'.5 \times 8'.5$
Resolution	$1''$
CCD detector	Array of 1024×1024 pixels
Pixel size	21 μm ($0''.5$)

gate the connections between fine-scale magnetic fields and the associated plasma structures on the Sun. It was launched on April 2, 1998 into a Sun-synchronous polar orbit and remained operational till June 21, 2010.

TRACE features a Cassegrain telescope with a 30 cm aperture and a field of view (FOV) of $8'.5 \times 8'.5$. It was designed to take solar images at multiple wavelengths with spatial resolution of $1''$ ($0''.5$ pixel^{-1}) and at very high temporal cadence of less than one minute. Normal incidence multilayer optics capable of observing from the photosphere to the corona enable TRACE to follow the evolution and dynamics of the solar atmosphere at selected temperatures over the range of 6000 K–10 MK. The TRACE temperature response at different wavelengths is listed in Table 2.2 and its instrumental characteristics in Table 2.3.

The pointing information of TRACE is not as accurate as a full disk imager (e.g., SOHO) where the solar limb provides a reference. In addition, the thermal bending of the TRACE guide telescope also leads an unknown variation in the pointing of at least few arcseconds (Fletcher et al. 2001; Alexander et al. 2006). Therefore, care must be taken while comparing images taken by TRACE and other instruments.

It is believed that pointing information of SOHO is quite accurate. SOHO provides full disk images of the Sun at white light (WL) and EUV channels. The cross-correlation methods are available to correct TRACE pointing by aligning TRACE images with respect to nearly-simultaneous SOHO images at the same wavelength (Gallagher et al. 2002; Metcalf et al. 2003). In this thesis, we have

Table 2.4: The primary ions observed by AIA (Lemen et al. 2012).

Channel (Å)	Primary ion(s)	Region of atmosphere	Char. log(T)
4500	Continuum	Photosphere	3.7
1700	Continuum	Temperature minimum, photosphere	3.7
304	He II	Chromosphere, transition region	4.7
1600	C IV + cont.	Transition region, upper photosphere	5.0
171	Fe IX	Quiet corona, upper transition region	5.8
193	Fe XII, XXIV	Corona and hot flare plasma	6.2, 7.3
211	Fe XIV	Active region corona	6.3
335	Fe XVI	Active region corona	6.4
94	Fe XVIII	Flaring corona	6.8
131	Fe VIII, XXI	Transition region, flaring corona	5.6, 7.0

used cross-correlation algorithm of Gallagher et al. (2002) for correcting TRACE pointing information.

2.4 Solar Dynamics Observatory (SDO)

The Solar Dynamics Observatory (SDO; Pesnell et al. 2012), launched on February 11, 2010 is the first mission under NASA's Living With a Star (LWS) program. The scientific objective of SDO is to understand how the Sun's magnetic field is generated and structured, and how this stored magnetic energy is converted and released into the heliosphere and geospace in the form of solar wind, energetic particles, and variations in the solar irradiance. It comprises three instruments: Atmospheric Imaging Assembly (AIA), Helioseismic and Magnetic Imager (HMI), and Extreme Ultraviolet Variability Experiment (EVE). In this thesis, we have extensively used observations from both AIA and HMI instruments. In the following subsections, we provide a brief description of these instruments.

2.4.1 Atmospheric Imaging Assembly (AIA)

The Atmospheric Imaging Assembly (AIA; Lemen et al. 2012) aboard SDO is designed to provide a multi-wavelength view of solar atmosphere with unprecedented temporal and spatial resolutions. It takes multiple simultaneous high-

Table 2.5: The AIA instrument characteristics (Lemen et al. 2012).

Diameter of primary mirror	20 cm
Field of view	$41' \times 41'$ (along detector axes)
	$46' \times 46'$ (along detector diagonal)
Pixel size/Resolution	$0''.6$ (12 μ)/$1''.5$
CCD detector	Array of 4096 $\times$ 4096 pixels
Cadence	8 wavelengths in 10 s to 12 s
Typical exposure times	0.5 to 3 s

resolution full-disk images of the corona and transition region up to 0.5 $R_\odot$ above the solar limb with $1''.5$ ($0''.6$ pixel^{-1}) spatial resolution and 12 s temporal cadence. The characteristic temperatures of various EUV channels of AIA cover a range from 6×10^4 K to 2×10^7 K. Therefore, AIA enables us to observe the changing topology of the magnetic field structures even as the coronal plasma changes its temperature.

The AIA instrument consists of four generalized Cassegrain telescopes that are optimized to observed narrow band passes in the EUV and UV in order to observe solar emissions from the transition region and corona (see Table 2.4). Each f/20 telescope has a 20 cm primary mirror and an active secondary mirror. The key parameters of AIA are given in Table 2.5. Each telescope field of view is approximately $41'$ circular diameter.

2.4.2 Helioseismic and Magnetic Imager (HMI)

Helioseismic and Magnetic Imager (HMI; Schou et al. 2012) is an instrument aboard SDO which is designed to study oscillations and the magnetic field at the solar surface, or photosphere. It provides full-disk, Doppler, intensity, and magnetic images with spatial resolution of $\sim 1''$ ($0''.5$ pixel^{-1}) and temporal cadence of 45 s of the solar photosphere, allowing studies of the sources and evolution of activity within the solar interior. HMI consists of a refracting telescope of 14 cm clear aperture, a polarization selector, an image stabilization system, a narrow band tunable filter and two 4096 pixel CCD cameras with mechanical shutters

Table 2.6: HMI specifications (Schou et al. 2012).

Central wavelength	6173.3 Å ± 0.1 Fe I line
Filter bandwidth	76 mÅ ± 10 mÅ
Field of view	2000″
Angular resolution	Better than 1″.5
Detector resolution	0″.50 ± 0″.01 pixel^{-1}
Dopplergram cadence	<50 s
Camera image cadence	<4 s
Timing	<1 μs stability, <100 ms absolute

and control electronics (see Table 2.6 for the instrument specifications).

HMI samples the neutral iron line at six wavelength positions symmetrically around the line center (6173 Å) at rest. The line-of-sight (LOS) observables, produced every 45 seconds, are Doppler velocity at the solar surface, LOS magnetic field strength, Fe I line width, line depth, and continuum intensity. They are calculated using 12 filtergram images, taken at six wavelengths and two polarizations, viz., the left- and right- circular polarizations (LCP and RCP) (Couvidat et al. 2012). Using these LCP and RCP profiles at each pixel, an algorithm is applied to derive full-disk maps of the LOS components of the magnetic and velocity field with a 45 s cadence (Couvidat et al. 2012).

2.5 Nobeyama Radioheliograph (NoRH)

Nobeyama Radioheliograph (NoRH; Nakajima et al. 1994; Hanaoka et al. 1994; Takano et al. 1997) is an imaging solar radio telescope at Nobeyama Solar Radio Observatory (NSRO) of the National Astronomical Observatory of Japan (NAOJ). It consists of 84 parabolic antennas with 80 cm diameter, sitting on lines of 490 m long in the east/west and of 220 m long in the north/south directions. The array configuration is optimized to observe the whole Sun with high spatial and temporal resolution and a high dynamic range of images (Table 2.7). At 17 and 34 GHz frequencies, NoRH provides MW images with spatial

Table 2.7: NoRH instrumental characteristics (Takano et al. 1997).

Frequency	17 GHz (right and left circular polarization), 34 GHz (only intensity)
Field of view	Solar full disk
Spatial resolution	$10''$ (17 GHz), $5''$ (34 GHz)
Temporal resolution	0.1 s (event), 1 s (steady)

resolution of $10''$ and $5''$ respectively.

2.6 GOES soft X-ray data

The Geostationary Operational Environmental Satellite (GOES) is a series of spacecraft developed by NASA for National Oceanic and Atmospheric Administration (NOAA). The X-ray Sensors (XRS) onboard GOES provides uninterrupted observations of solar X-ray fluxes. GOES XRS measurements have been made since 1970. On each satellite, there are two sensors which provide solar X-ray fluxes for the wavelength bands of 0.5–4 Å and 1–8 Å. For GOES XRS, the data sampling rate depends on the satellite generation. For GOES 13–15, the data accumulation time is 2.048 s and both the channels take data simultaneously. The GOES 12 through 15 spacecraft further carry a sophisticated X-ray telescope called the Solar X-ray Imager (SXI) to image the solar corona, heated at million degree Kelvin. We have used GOES XRS measurements to investigate the temporal evolution of solar flares and associated phenomena.

In summary, this thesis is an attempt to effectively combine multi-wavelength data at a wide range of wavelengths to understand the physical processes occurring during solar eruptions. Apart from the major data resources described above, we have also taken data for limited usage and specific scientific purposes from other instruments. These supplementary data sources are: Kanzelhöhe solar observatory (KSO) for Hα filtergrams; Extreme Ultraviolet Imager (EUVI) on board Solar TErrestrial RElations Observatory (STEREO) for EUV images;

Large Angle and Spectrometric Coronagraph (LASCO) on board Solar and Heliospheric Observatory (SOHO) for CME white light images; Culgoora Solar Observatory for radio dynamic spectrum; etc. We have provided brief description and citations of these instruments at appropriate sections of the thesis.

Chapter 3

Evolutionary phases of solar eruptive prominences and associated multiple flare activity

3.1 Introduction

Prominences, or, equivalently, filaments are relatively cool, dense objects of chromospheric material suspended in the hotter corona by magnetic fields. When these structures erupt, both the prominence material and magnetic field are expelled together. Decades of observations reveal that prominence eruptions are often associated and physically related to solar flares and coronal mass ejections (CMEs). Therefore, the study of prominence activity not only forms a very interesting topic of research in itself, but also offers an opportunity to understand the physics of associated flares and CMEs.

In view of their locations and physical characteristics, prominences are classified in different categories viz., active region, intermediate, and quiescent (section 1.1.2). Out of these classes, the active region prominences undergo the most dynamic evolution. These are low lying and rapidly evolving structures, forming in the newly emerged magnetic fields of an active region. The activation and eruption of active region prominences are frequently associated with flaring activities. In such cases, location, timing and, strength of flare emissions at X-ray energies is expected to provide important clues about crucial physical processes, such as, site of magnetic reconnection, particle acceleration, heating, etc. (Ding et al. 2003; Ji et al. 2003; Moon et al. 2004; Alexander et al. 2006; Liu and Alexander 2009; Liu et al. 2009c; Vemareddy et al. 2012).

Examination of subtle activity near the filament and morphological changes within the filament during the pre-eruption phase has been considered very important to the investigation of the physical conditions of the solar atmosphere that lead to rapid energy release and large-scale eruption (Fárník et al. 2003; Chifor et al. 2007; Joshi et al. 2011). However, due to the limited sensitivity of detectors, a detailed X-ray imaging analysis is often not possible to obtain during this phase of mild energy release. We still do not have a clear idea about the association between short-lived magnetic reconnection events that occur in the pre-eruption phase and the main flare that involves large-scale magnetic reorganization. In this regard, it is very important to explore the pre-flare phase in order to determine the location/height of the reconnection sites as well as the non-thermal characteristics of energy release.

The relationship between filament rise and associated radiative signatures (i.e., flare or pre-flare activity) has been the subject of several recent studies (Liu et al. 2009c; Joshi et al. 2011; Sterling et al. 2011; Joshi et al. 2013). These studies reveal that, in general, the active region filament eruption undergoes two phases of evolution: a slow rising activation phase which is dominated by thermal emission (flare preheating phase), and eruptive phase during which impulsive flare emission is observed. With the availability of high-resolution EUV images at multiple channels from TRACE and AIA/SDO, the case studies of prominence eruptions have become quite promising. These observations, when combined with multi-band X-ray time profiles and images from RHESSI, are expected to provide

Table 3.1: List of prominence eruptions studied in this chapter.

S.N.	Date	Observing period (UT)	Active region	Flare class (Time in UT)	Location
Event I	2004 August 18	16:00–18:00	10656	X1.8 (17:30–17:45)	S14W91
Event II	2012 August 18	02:45–04:00	11548	M1.8 (03:20–03:45)	N20E90

crucial insights to explore the underlying physical processes that constrain the theoretical simulations.

A very important objective toward the investigations of the source region characteristics of solar eruptions is to address their triggering mechanisms (Manoharan and Kundu 2003; Joshi et al. 2007; Sterling et al. 2011). Several models and magnetic configurations have been proposed to explain the possible mechanisms that lead to the onset of eruptive flares (Moore and Roumeliotis 1992; Antiochos et al. 1999; Moore et al. 2001; Linker et al. 2003; Karpen et al. 2012, etc.). The "flux cancellation model" exhibits that the dissipation of magnetic flux at the surface reduces the magnetic tension force of the overlying field that confines a flux rope so that the upward magnetic pressure dominates at some point of the evolution leading to the eruption of the flux rope (Linker et al. 2003). The "tether cutting model" is fundamentally based on a single, highly sheared magnetic bipole, with the earliest reconnection occurring deep in the sheared core region (Moore et al. 2001). In the "breakout model" the fundamental topology of the erupting system is multi-polar. Here the eruption is initiated by reconnection at a neutral point located in the corona, well above the core region (Antiochos et al. 1999). In this manner, the tether cutting model is built on the concept of an "internal reconnection" while the breakout model is suggestive of an "external reconnection" (Sterling et al. 2001). In observations, the identification of the suitable triggering mechanism for a solar eruption needs a thorough examination

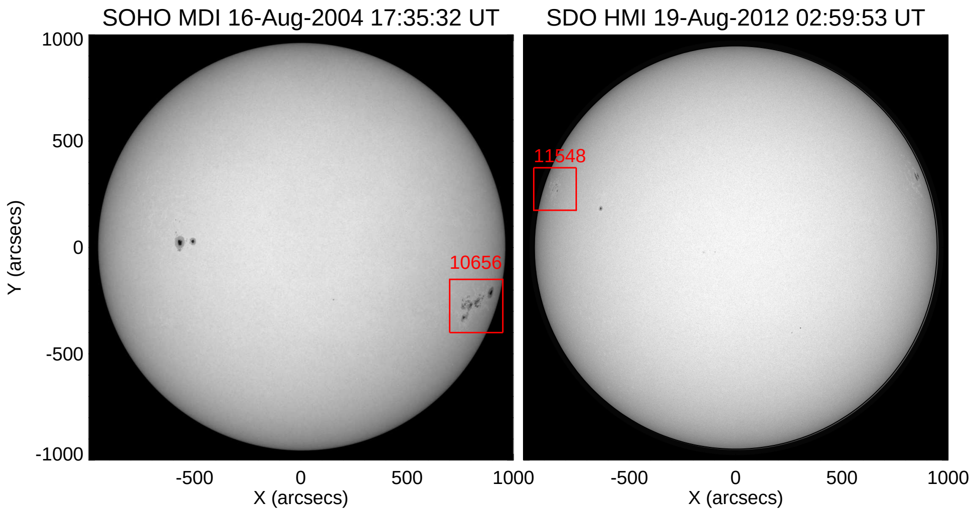

Figure 3.1: Left panel: MDI/SOHO white light (WL) image showing the location of active region NOAA 10656 on the solar disk which produced the prominence eruption and multiple flare activity on 2004 August 18 (Event I; Table 3.1). Right panel: HMI/SDO WL image showing the location of active region NOAA 11548 on the solar disk which was the source region of the prominence eruption and associated flaring activities on 2012 Agust 18 (Event II; Table 3.1). Since both the active regions were very close to the limb on the day of events, for better visualisation, we have shown full disk images at a differences of 1–2 days from the day of reported activities.

of the activities near the activation site and surrounding regions even before the start of filament's activation. These activities may not always be associated with the noticeable radiative signatures but can represent important features related to the dynamical evolution of pre-eruption corona.

This chapter contains comprehensive study of spectacular eruptions of two active region prominences which occurred in active region NOAA 10656 on 2004 August 18 and NOAA 11548 on 2012 August 18 at west and east limbs of the Sun respectively (see Table 3.1). The locations of these active regions on solar disk are shown in Figure 3.1. One of the objective of this study is to identify the process of prominence destabilization through the observations of pre-eruption phase of the active region and pre-flare activity. By synthesizing the multi-wavelength measurements during the eruptive phase of the prominences, we explore the signatures

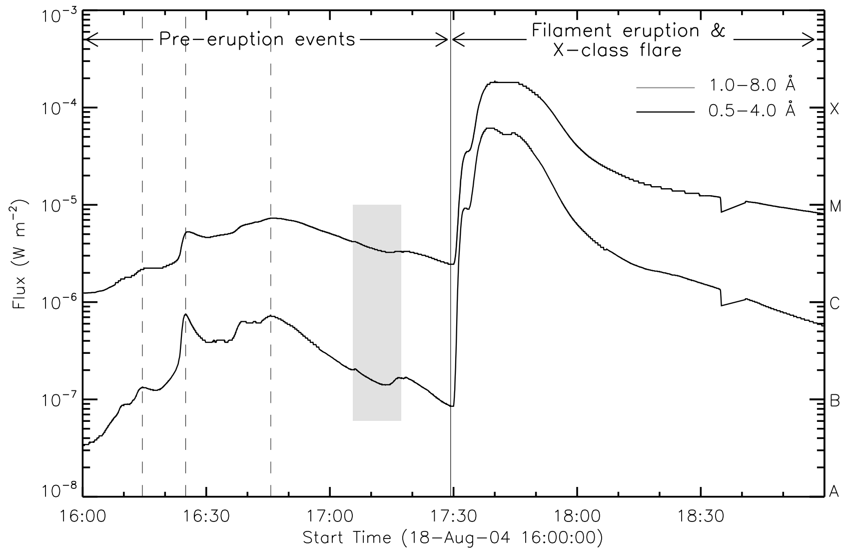

Figure 3.2: Soft X-ray flux from the Sun observed by the GOES satellite in the 0.5–4 Å and 1–8 Å wavelength bands with a time cadence of 3 s between 16:00 and 19:00 UT. The vertical solid line differentiates the pre-eruption phase from the eruptive X1.8 flare. The vertical dashed lines during the pre-flare interval indicate three sub-peaks at 16:14:30, 16:25:00, and 16:45:39 UT during which EUV images reveal three localized instances of energy release (denoted as pre-events I, II, and III; see Table 5.1). The gray shaded region in the light curves correspond to the interval during which the filament exhibited fast morphological evolution.

of magnetic reconnection in the corona and discuss the thermal and non-thermal effects driven by the prominence eruption.

3.2 2004 August 18 prominence eruption in AR 10656

3.2.1 Overview of multiple flare activity

The prominence eruption under investigation is associated with multiple flare activity during its activation and eruptive phases. Therefore, we first discuss the evolution of GOES soft X-ray flux during the entire period of prominence

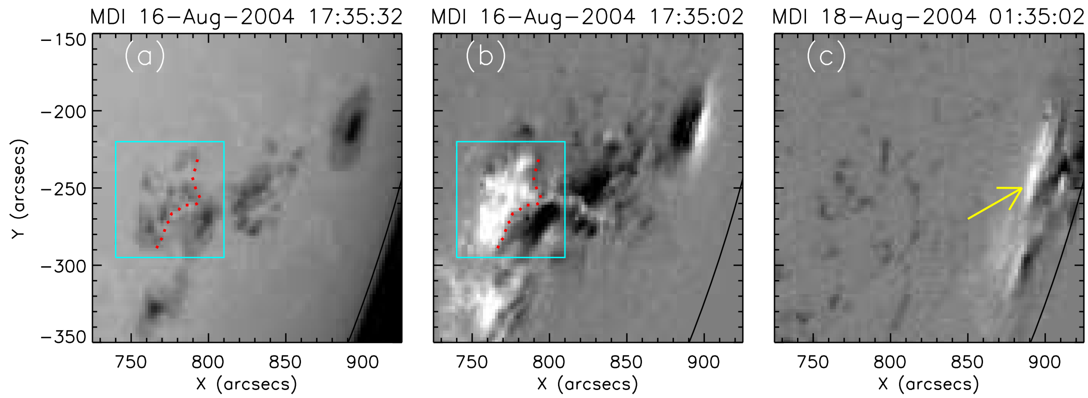

Figure 3.3: SOHO/MDI observations of NOAA AR 10656. Since the active region was very close to the solar limb at the time of activity, we show a white light image and magnetogram taken two days prior to the event in panel (a) and (b), respectively. Close inspection of the region of interest (enclosed by a box) indicates a complicated magnetic polarity distribution on the surface. An estimate of the magnetic polarity inversion line is shown by the dotted line. The magnetogram of the active region on the day of events under study is shown in panel (c) and the activity site is marked by an arrow.

evolution. In Figure 3.2, we show GOES flux profiles in the 0.5–4 Å and 1–8 Å wavelength bands between 16:00 and 19:00 UT on 2004 August 18. From this light curve, one can clearly distinguish two phases of the flux evolution. The first phase extends from 16:00 to 17:30 UT and is characterized by a gradual rise and fall of the GOES flux. We note that three impulsive sub-peaks are superimposed on the gradually varying SXR flux during this phase at 16:14:30, 16:25:00, and 16:45:39 UT, indicated in Figure 3.2 by vertical dashed lines. A careful examination of the GOES flux with EUV images taken by TRACE reveals that these sub-peaks represent localized events of energy release in the vicinity of a filament (detailed discussion is presented in section 3.2.4). Further, we note that these three sub-peaks are more pronounced in the high energy channel of GOES (i.e., 0.5–4 Å band) with the second one as the most impulsive. Hereafter, these sub-peaks are called pre-events I, II, and III as they correspond to the energy release prior to the eruption. The second phase corresponds to a major eruptive flare of class X1.8 between 17:30 and 19:00 UT during which the filament erupts as part of a CME.

3.2.2 Structure of the active region

On 2004 August 18, active region NOAA 10656 was very close to the west limb of the Sun, with a mean position at S14W90. The white light images taken from the Michelson Doppler Image (MDI; Scherrer et al. 1995) on board Solar and Heliospheric Observatory (SOHO) indicate that, at the time of the events, the leading part of the active region was behind the solar limb. Therefore, to get a better understanding of the magnetic configuration of the activity site, we show a white light image and a magnetogram taken by SOHO/MDI two days before the reported event in Figure 3.3(a) and (b). We note that the active region had a complex $\beta\gamma\delta$ magnetic configuration with sunspot clusters of negative and positive polarities as the leading and trailing sunspot groups, respectively. The region of interest lies in the trailing part of the active region (marked by a box in Figures 3.3(a) and (b)). We find that the active region is spatially complex. However, it is also apparent that the activity site does not exhibit a lot of mixing of polarities, so an approximate polarity inversion line (PIL) can be drawn (indicated in Figures 3.3(a) and (b) by the red dotted line). The events occurred near the PIL, and the activity site is marked by an arrow in Figure 3.3(c). From these longitudinal magnetograms, we conclude that the flaring region is mainly associated with a bipolar distribution of magnetic fields at the photosphere.

3.2.3 RHESSI X-ray light curves

RHESSI observations for the pre-eruption phase are available from 16:00 to 16:40 UT (Figure 3.4). The light curves in different energy bands (viz. 6–12, 12–25, and 25–50 keV) are constructed by taking average count rates from front detectors 1, 3–6, 8 and 9 in each energy band. We note that the RHESSI count rates between 16:10 and 16:20 UT are contaminated by particle event (i.e., the

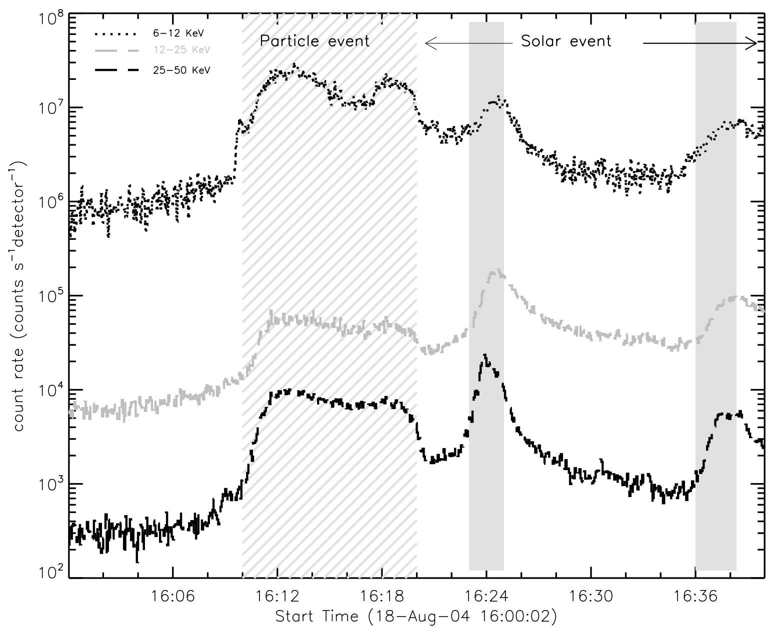

Figure 3.4: RHESSI time profiles of the pre-eruption events with a time cadence of 4 s. The cross-hatched region indicates the time intervals during which RHESSI observations are contaminated by a particle event. In order to present different RHESSI light curves with clarity, the RHESSI count rates are scaled by factors of 1/80, 1/5, and 1 for the energy bands 6–12, 12–25, and 25–50 keV, respectively. The gray shaded areas denote the time intervals, in which the X-ray spectra were computed and shown in Figure 3.14

RHESSI detectors were hit by high-energy particles trapped in Earth's radiation belts). This interval covers only the first sub-peak of the GOES profile, during which the level of SXR flux was relatively low. The second sub-peak, which is the most impulsive one, was nicely covered by RHESSI up to the 25–50 keV energy band. The third flare was partially observed by RHESSI between 16:35 and 16:40 UT as the spacecraft entered in the South Atlantic Anomaly (SAA).

In figure 3.5, we present RHESSI and GOES X-ray light curves during the eruptive X1.8 flare. The examination of GOES profiles clearly indicates that the flare emission is associated with two distinct phases (marked in Figure 3.5 as phases I and II). The first phase is characterized by a rapid rise and a gradual decline of SXR flux between 17:30:00 and 17:33:30 UT. The flux further enhances

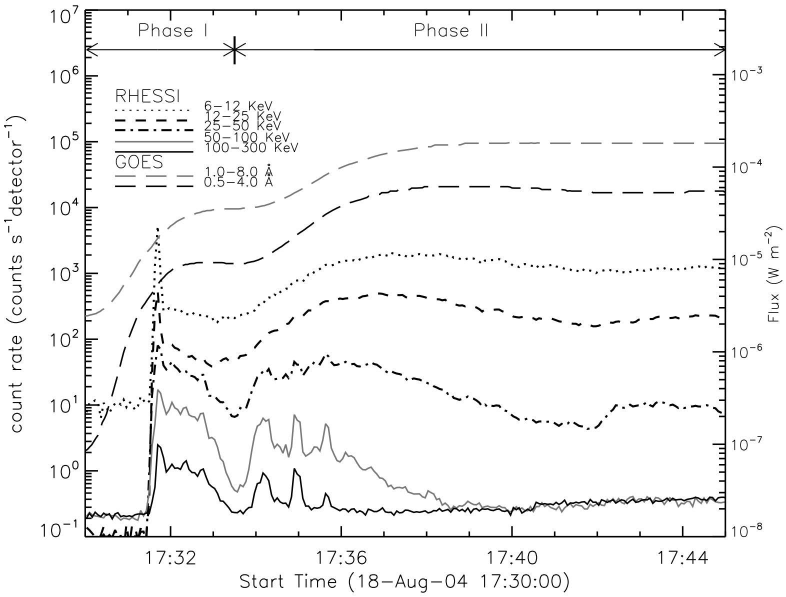

Figure 3.5: RHESSI time profiles during the filament eruption and associated X1.8 flare with a time cadence of 4 s. In order to present different RHESSI light curves with clarity, RHESSI count rates are scaled by factors of 1, 1/20, 1/30, 1/40, and 1/60 for the energy bands 6–12, 12–25, 25–50, 50–100, and 100–300 keV, respectively. For comparison, the SXR flux in two wavelength channels observed by GOES are also plotted. We identify two phases in the evolution of the X-ray flux. We note prolonged non-thermal emission during phase I while phase II is characterized by three HXR bursts, which are observed up to 100–300 keV.

after 17:33:30 UT and maximizes at ∼17:40 UT which marks the overall maximum of the event. It is noteworthy that the first phase is associated with intense and prolonged high energy emission up to 100–300 keV. On the other hand, hard X-ray (HXR) emission during the second phase occurred in the form of three distinct HXR bursts, which are clearly identified in all the HXR channels above 25 keV.

3.2.4 Multi-wavelength imaging

During the period of the reported events, TRACE was monitoring the active region mostly with its EUV channel at 195 Å. However, during the filament

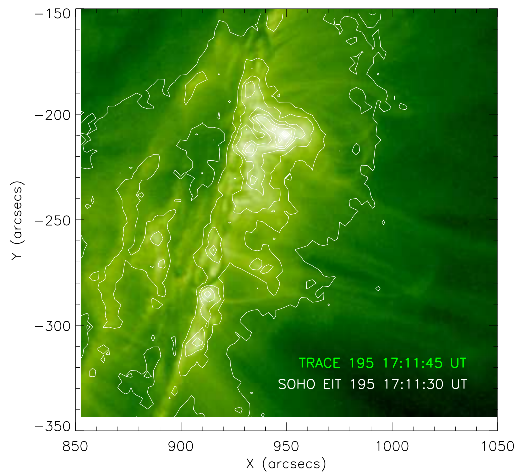

Figure 3.6: An illustration of the alignment of nearly co-temporal TRACE and SOHO/EIT 195 Å images.

eruption, TRACE also provided a few UV images at 1600 Å wavelength. The TRACE 195 Å filter is mainly sensitive to plasmas at a temperature around 1.5 MK (Fe XII), but during flares it may also contain significant contributions of plasmas at temperatures around 15–20 MK (due to an Fe XXIV line; Handy et al. 1999). The TRACE 1600 Å channel is sensitive to plasma at temperatures between (4–10) $\times$ 10^3 K and represents a combination of UV continuum, C I, and Fe II lines (Handy et al. 1999). The brightest and most rapidly varying features in the TRACE 1600 Å channel are likely to emit in the C IV lines as well (Handy et al. 1998).

To reconstruct RHESSI images, we have primarily used CLEAN algorithm (Hurford et al. 2002). During the X1.8 flare, we also present X-ray images reconstructed by computationally expensive PIXON algorithm (Metcalf et al. 1996) to show precisely the location of X-ray emission during some of the crucial stages of the eruption. PIXON algorithm provides more accurate image photometry than CLEAN algorithm and is considered the best method to image extended sources in the presence of compact sources (Aschwanden et al. 2004). The images are reconstructed by selecting front detector segments 3–8 (excluding 7) with 20 s integration time.

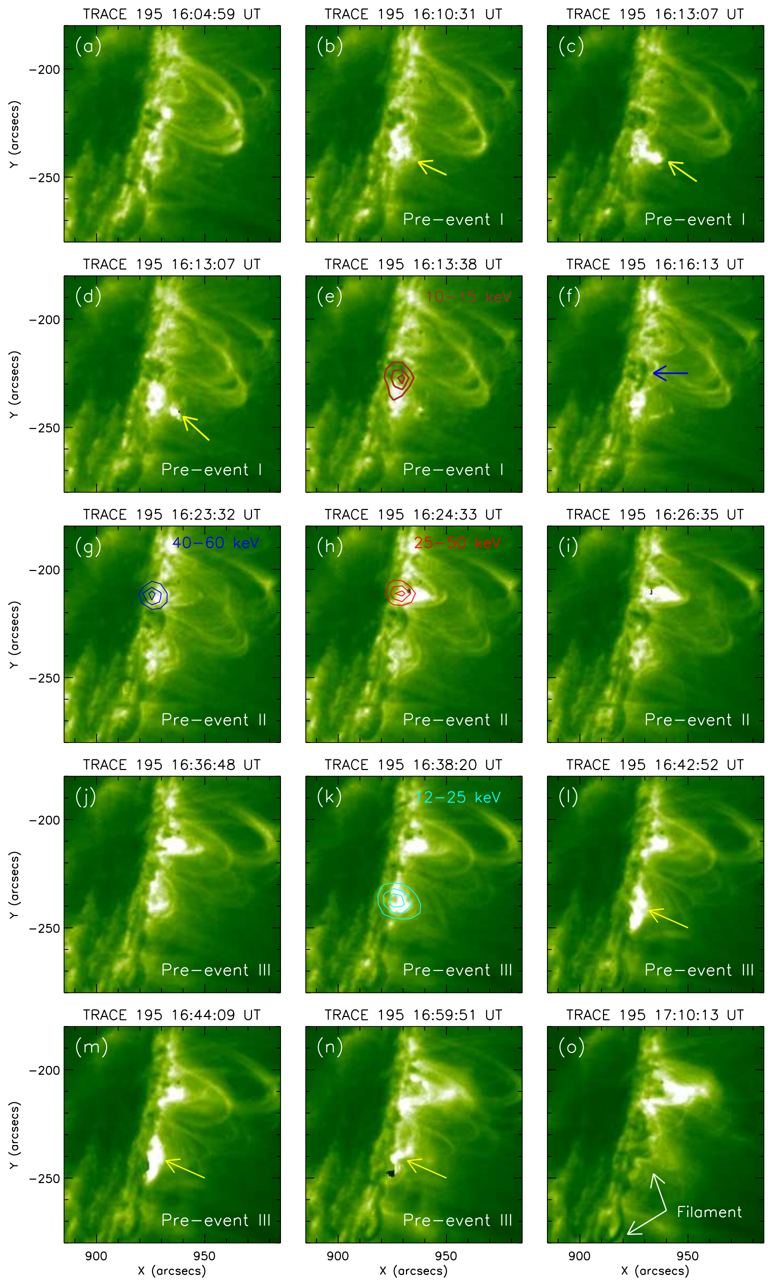

Figure 3.7: Sequence of TRACE 195 Å images showing three successive flares during the pre-eruption phase (i.e., pre-events I, II, and III) corresponding to the three sub-peaks indicated in the GOES profile. We note the intense brightening at the looptop (panel (b)) and formation and ejection of plasmoid (marked by arrows in panels (b)–(d)) during pre-event I. Following pre-event I, the filament rises (indicated in panel (f) by black arrow). Pre-event II is very impulsive during which HXR sources up to 40–60 keV is observed (panels (g)–(i)). Pre-event III is marked by successive brightening in two low-lying loops (marked by arrows in panels (l)–(n)). The contour levels for RHESSI images are 70%, 85%, and 95% of the peak flux in each image.

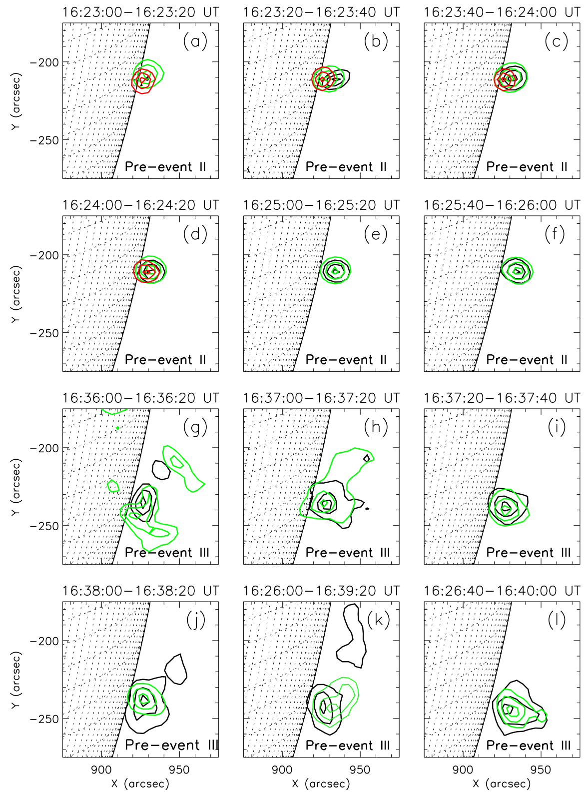

Figure 3.8: Evolution of RHESSI X-ray sources during pre-events II and III in 6–12 keV (black), 12–25 keV (green), and 25–50 keV (red) energy bands. RHESSI images are reconstructed with the CLEAN algorithm. The contour levels are 60%, 80%, and 95% of the peak flux in each image.

Our analysis includes the identification of spatial distribution of the hard X-ray emission derived from RHESSI measurements with respect to the filament evolution observed in (E)UV wavelengths from TRACE. However, pointing information of TRACE is often not good enough to obtain the precise co-alignment between TRACE and RHESSI images (see section 2.3). In order to correct the TRACE pointing, we have co-aligned near-simultaneous TRACE and SOHO/EIT images observed at same wavelength (i.e., 195 Å) using the method of Gallagher et al. (2002)[1]. This method is quite suitable for near-limb events where solar features in white light images do not appear very prominent (see e.g., Liu et al. 2009a). We found that the TRACE pointing was offset by $2''.7 \pm 0''.2$ in the X direction and $6''.8 \pm 0''.3$ in the Y direction (Figure 3.6.)

[1]http://www.tcd.ie/Physics/people/Peter.Gallagher/trace-align/index.html

Pre-eruption events

The availability of TRACE 195 Å images at high time cadence (∼30 s) during most of the pre-eruption phase (16:00 and 17:22 UT) enables us to examine the minute changes in the activity site. In Figure 3.7, we present a few representative TRACE 195 Å images. In the beginning (∼16:00 UT), the active region was relatively quiet (see Figure 3.7(a)). We find that a bright system of loops existed in the northern part of the active region, while its southern part lacked such coronal structures. Also, it is noteworthy that the active region did not exhibit very large, complex overlying field lines in EUV images despite its extended structure. This indicates a relatively simplified coronal structure in the active region.

After ∼16:07 UT, an intense brightening occurred at the southern side of the loop system (see Figure 3.7(b)), marking the onset of the first event of the pre-eruption phase (or "pre-event I"). The brightening was occurred until 16:22 UT with the maximum SXR intensity up to C2.2 at 16:14:30 UT. The flaring area grew rapidly and intense emission was produced at the looptop. At ∼16:12 UT, a blob-like structure (i.e., plasmoid) was formed at the looptop, which became detached from the flaring loops (plasmoid is marked by arrows in Figures 3.7(b)–(d)). The plasmoid showed the upward motion that can be clearly observed up to ∼16:15 UT. A very important feature that we note in this interval is the emergence of a filamentary structure (part of a long filament) just after pre-event I (indicated by an arrow in Figure 3.7(f)). We also note that the event occurred at the southern leg of this rising filament. Although the RHESSI observations during this interval were contaminated by a particle event, we could still reconstruct 10–15 keV X-ray images at the peak time (i.e., 16:13:40 UT). The X-ray source was observed to be co-spatial with intense flare loops (see Figure 3.7(e)).

At ∼16:23 UT, we note the start of pre-event II in the form of a sudden brightening near the second (i.e., northern) leg of the filament. The intensity and area of the flare showed a very fast rise and decay between 16:23 and 16:30

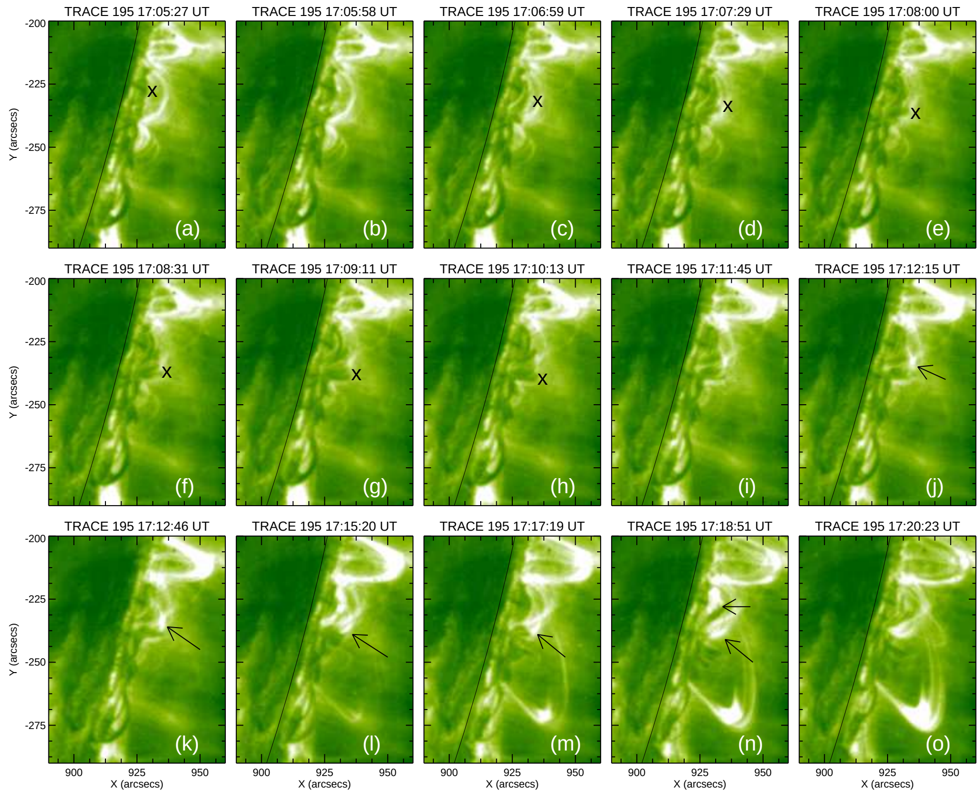

Figure 3.9: Sequence of TRACE 195 Å images showing the activation of filament after the pre-eruption events. The filament exhibits slow rise and rapid morphological evolution between 17:05 UT and 17:19 UT. This interval is marked by gray shaded region in Figure 3.2. The rise of filament is shown by placing a cross (‘×’) at the top. Note brightenings occurring below the apex of the prominence from ∼17:12 UT onwards (marked by arrows in panels (j)–(n)).

UT, implying an event of confined category. The impulsive GOES profile that peaked at 16:25:00 UT marked an event of class C6.7, while the maximum flux of HXR emission was observed earlier (16:23:50 UT in the 25–50 keV energy band). From EUV images, we note that there is a rapid expansion of height in the loop system in the corona during ∼16:23–16:27 UT. The volume and intensity of the loop system displayed a fast decline thereafter. The RHESSI observations reveal HXR source in 40–100 keV energy band, which is located near the base of an expanding loop system (see Figures 3.7(g) and (h)).

The SXR flux again strengthened after ∼16:35 UT and maximized at 16:45:39 UT, which corresponds to pre-event III of class C7.3 or the overall maximum of

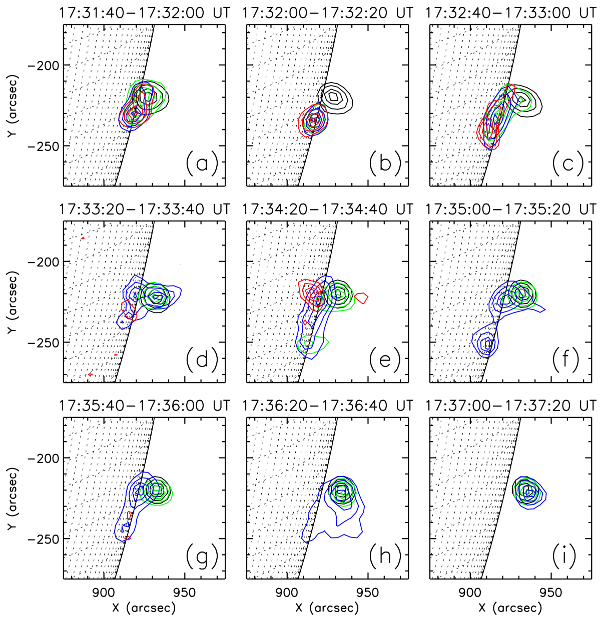

Figure 3.10: Evolution of RHESSI X-ray sources during eruptive X1.8 flare (see Figure 3.2) in 12–25 keV (black), 25–50 keV (green), 50–100 keV (blue), and 100–300 keV (red) energy bands. RHESSI images are reconstructed with the CLEAN algorithm. The contour levels are 55%, 70%, 85%, and 95% of the peak flux in each image.

SXR profile during the pre-eruption phase (see Figures 3.7(j)–(m)). This event occurred at the southern side of the filament, and part of it is co-spatial with pre-event I. Compared to the two events described earlier, this event presented a very different morphological evolution. Initially (i.e., at ∼16:35 UT), a single low-lying loop system brightened up and expanded. This was followed by the brightening of another adjacent small loop system at the southern side of existing flaring loops (marked by arrows in Figures 3.7(l)–(n)).

The coupled structure of two loop systems was visible up to ∼16:57 UT. These EUV observations are consistent with GOES profile that displayed broad maximum phase followed by gradual decline. RHESSI partially observed this phase up to ∼16:40 UT. We find that X-ray sources are observed in $\lesssim$ 25 keV energy bands from ∼16:36 UT onward. The X-ray emission sources are spatially correlated with the flaring loops observed in EUV images (see Figure 3.7(k)).

In Figure 3.8, we show the evolution of X-ray sources in different energy bands during the pre-events II and III. As discussed in sections 3.2.1 and 3.2.3, pre-event II was very impulsive. It is noteworthy that the X-ray sources are compact in all the energy bands (i.e., 6–12, 12–25, and 25–50 keV) throughout this event (see first and second rows of Figure 3.8). Due to the compactness of flaring region as well as proximity to the limb (see also Figures 3.7(g)–(i)), it is hard to resolve the emission sources corresponding to the looptop and footpoint regions. However, in the decay phase (see Figures 3.8(e) and (f)), when high energy HXR source vanishes, we can recognize distinct looptop emission in the form of upward moving 6–12 keV and 12–25 keV sources. In Figures 3.8(g)–(l), we present RHESSI X-ray images in 6–12 keV and 12–25 keV energy bands in the early phase of pre-event III. In the beginning, the source structure in both energy bands is broad. Especially from 12–25 keV energy band images (Figure 3.8(g)), we can clearly see an extended source with two centroids that likely represent emission from the looptop and footpoint locations. The extended source structure also indicates presence of hot plasma in larger volume and is consistent with the structure of the flaring region observed in EUV images. In the later stages, both X-ray sources move upward with the high energy source (12–25 keV) always located at higher altitudes in comparison to low energy source (6–12 keV).

Activation of prominence

After the pre-eruption events, the filament undergoes a very important stage of morphological evolution. This phase was observed between 17:05 and 17:19 UT, i.e., just after the pre-event III (indicated by gray shaded region in Figure 3.2). We present a sequence of TRACE 195 Å images in order to show a closer and clearer view of filament activation in Figure 3.9. The growth of filament is shown by placing a cross (‘×’) at the top of the rising filament. From a linear fit to height-time data, we estimate speed of rising filament as $\sim$12 km s^{-1}. After $\sim$17:11 UT, we observe a localized brightening (indicated by arrows in Figures 3.9(j)–(n)) which is located at the top of a twisted flux rope, but below the apex of the filament. This brightening grows in successive images. We note another localized brightening below the rising filament at $\sim$17:18 UT (indicated by another arrow in Figure 3.9(n)). Due to unavailability of TRACE observations between 17:22 and 17:34 UT, we are unable to track the later phase of filament activation. RHESSI observations during this phase are also not available.

Prominence eruption and X1.8 flare

TRACE observations of the event are available after 17:34 UT, i.e., ∼4 minutes after the onset of the flare (GOES start time ∼17:30 UT). By this time the eruption of filament had already begun (see Figures 3.11(b) and (h)). However, RHESSI observations are available from the beginning of the event (from 17:31 UT onward). In Figure 3.10, we present evolution of HXR sources in four energy bands (i.e., 12–25, 25–50, 50–100, and 100–300 keV). We note that the HXR emission at 12–25 keV (black contours) is associated with a compact, single coronal source throughout the flare which also exhibits "standard" upward movement. The HXR sources at higher energies (>25 keV) reveal complicated evolution. We observe onset of very high energy HXR emissions (25–50, 50–100, and 100–300 keV) from the very early stages (Figures 3.10(a)–(c)) which are mainly from the footpoint regions. This is followed by a very important phase during which high-energy coronal HXR sources are observed. In particular, there are instances when HXR emission up to 50–100 keV becomes very prominent from coronal regions besides footpoint locations (see Figures 3.10(d) and (f)). We further note that at these times, coronal HXR emission is from an extended region. During the later stages, only coronal HXR emission is detected (Figures 3.10(h) and (i)). We also note that the 50–100 keV HXR coronal source was observed until 17:38 UT. In the post flare phase, HXR coronal sources are observed only up to 25 keV energies.

In Figure 3.11, we present a few representative TRACE 1600 Å (panels (a)–(f)) and 195 Å (panels (g)–(l)) images. We have overplotted co-temporal RHESSI X-ray PIXON images at 12–25 keV and 50–100 keV energy bands in selected panels to compare the location of HXR coronal and footpoint sources with respect to

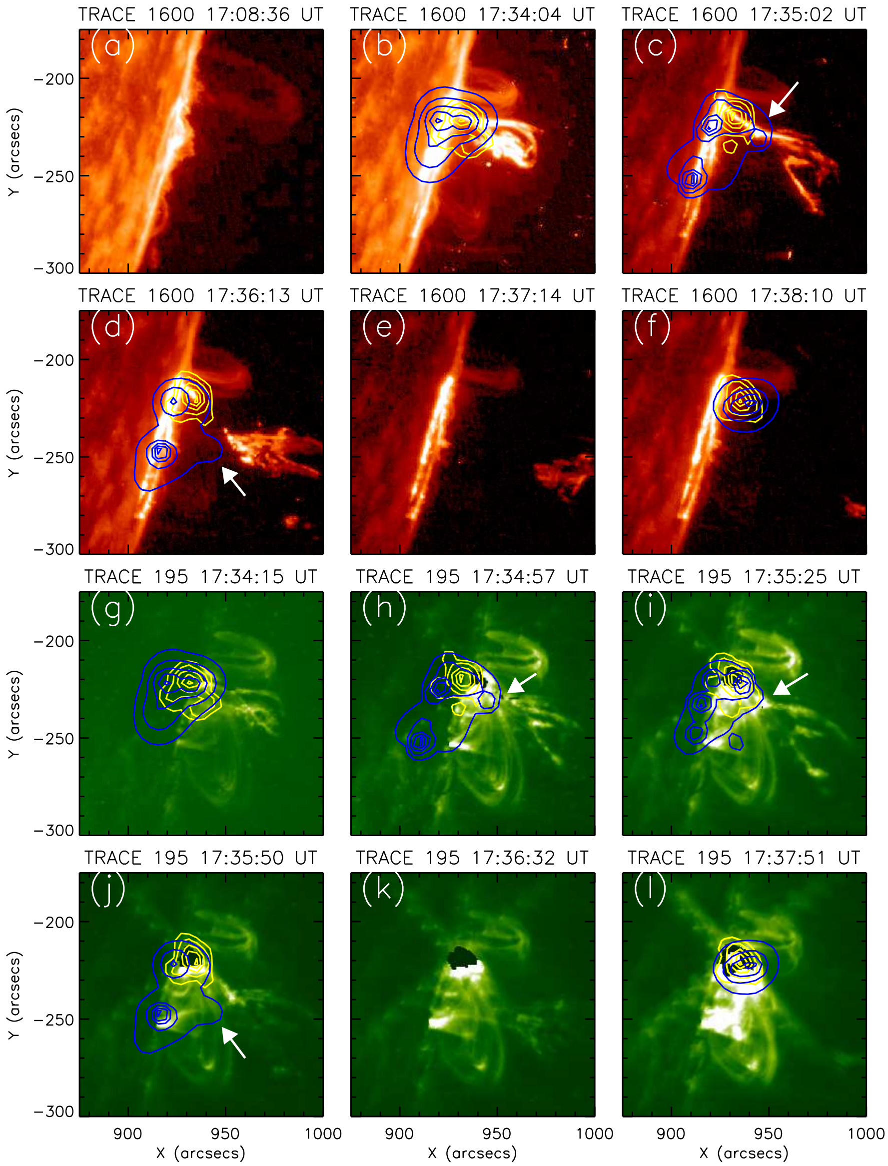

Figure 3.11: A few representative images taken by TRACE in 1600 Å and 195 Å channels during eruptive X1.8 flare (see Figure 3.2) overlaid by co-temporal RHESSI X-ray images in 12–25 keV (yellow) and 50–100 keV (blue) energy bands. It is noteworthy that 50–100 keV HXR coronal source lies over an elongated, bright (E)UV structure formed below the erupting prominence (marked by arrows in panels (c), (h) and (i)). We also note 50–100 keV HXR emission from an extended region in the corona during the phase of detachment of the prominence from the solar source region (marked by arrows in panels (d) and (j)). The RHESSI images are reconstructed with PIXON algorithm. The contour levels for RHESSI images are 10%, 25%, 50%, 75%, and 95% of the peak flux in each image.

the phases of erupting filament. With the start of TRACE observations at 17:34 UT, we observe expansion and stretching of a flux rope which rapidly evolved into a 'Y-shaped' structure (Figures 3.11(b) and (c)). We observe intense brightening along the leg of the erupting structure in the form of an elongated bright structure (Figure 3.11(c)). This bright feature is also seen in 195 Å images (see Figures 3.11(h) and (i)). It is noteworthy that the HXR coronal sources at 50–100 keV energy band lie over this elongated bright (E)UV structure (marked by arrow in Figures 3.11(c) and (h)). In the next frames during 17:35–17:36 UT (see Figures 3.11(d) and (j)), we find the detachment of the stretched flux rope from the solar source region and its upward propagation. From a linear fit to height-time measurements of the erupting filament observed at 1600 Å images, we estimate the speed of erupting filament as $\sim$270 km s^{-1}. We note that during the detachment of the flux rope, HXR emission at 50–100 keV is observed from an extended source covering footpoint as well as coronal regions (see Figures 3.11(d) and (i)). During this phase, RHESSI light curves indicate three consecutive HXR bursts (Figure 3.5). After the eruption, we observe a closed post-flare loop system with HXR emission from the coronal loops (see Figures 3.11(f) and (l)).

3.2.5 RHESSI X-ray spectroscopy

We have studied the evolution of RHESSI X-ray spectra during the pre-eruption phase as well as the eruptive X1.8 flare. We first generated a RHESSI spectrogram with an energy binning of 1/3 keV for energy range of 6–15 keV and 1 keV for energies >15 keV. We only used the front segments of the detectors, and excluded detectors 2 and 7 (which have lower energy resolution and high threshold energies, respectively). The spectra were deconvolved with the full detector response matrix (i.e., off-diagonal elements were included; Smith et al. (2002)). Spectral fits were obtained using a forward-fitting method implemented in the OSPEX code. OSPEX allows the user to choose a model photon spectrum, which is multiplied with the instrument response matrix and then fitted to the observed count spectrum. The best-fit parameters are obtained as output. We used the bremsstrahlung and line spectrum of an isothermal plasma and a power-law function with a turnover at low X-ray energies. The negative power-law index below the low-energy turnover was fixed at 1.5. In this manner, there are five free parameters in the model: temperature (T) and emission measure (EM) for the thermal component, and power-law index (γ), normalization of the power law, and low-energy turnover for the non-thermal component. From these fits, we derive the temperature and EM of the hot flaring plasma as well as the power law index for the non-thermal component.

We computed spatially integrated, background subtracted RHESSI spectra accumulated for 20 s integration time during pre-events II and III (this time interval is indicated by gray colored strips in Figure 3.4). A few representative spectra during this interval are shown in Figures 3.12(a)–(f). We find that during pre-event II, the X-ray emission exhibited a very fast spectral evolution with the peak HXR emission between 16:23 and 16:24 UT. Due to fast spectral evolution of the flare, we decided to select the maximum energy value for fitting by comparing the flux during the flare with that of the background level for each time interval. This can be achieved by selecting the fitting option Auto-Set-Max in OSPEX software. The maximum value of energy used for fitting is indicated by a dashed line in each spectrum shown in Figures 3.12(a)–(c). The lower energy value for fitting was selected as 6 keV. In Figures 3.12(d)–(f), we show a few representative RHESSI spectra derived during the early part of the event III. The spectra were fitted in the energy range of 6–30 keV. In Figures 3.12(g)–(i), we show a few representative RHESSI spectra derived during X1.8 flare. The spectra were fitted in the energy range of 6–150 keV. Time evolution of various spectral parameters (temperature (T), emission measure (EM), and power-law index (γ)) obtained from fits to the RHESSI spectra, integrated over consecutive 12 s intervals, is shown is Figure 3.14.

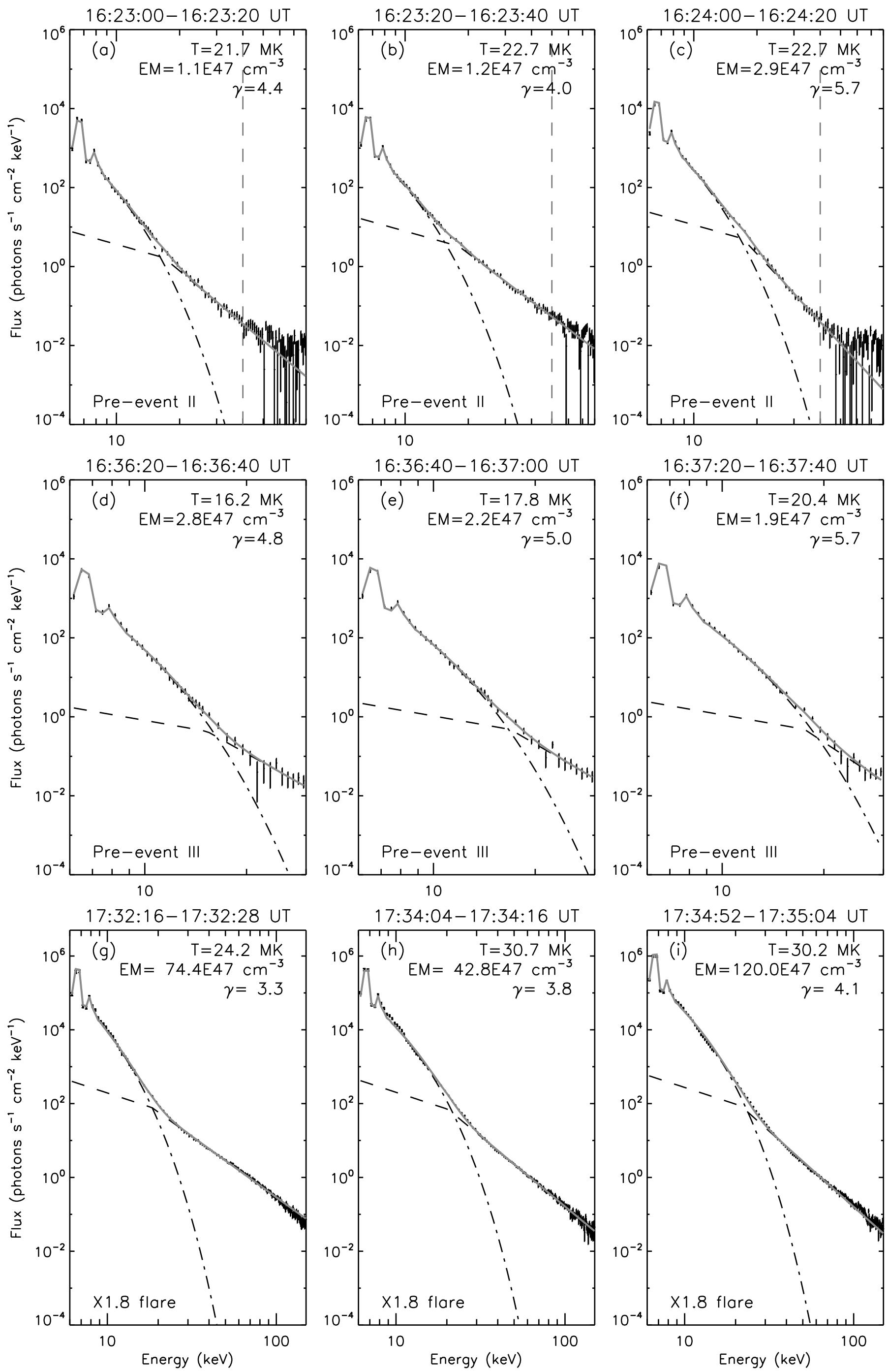

Figure 3.12: RHESSI X-ray spectra derived during various time intervals covering the pre-eruption events II and III (first and second rows respectively) and X1.8 eruptive flare (last row) together with applied fits. The spectra were fitted with an isothermal model (dashed-dotted line) and a functional power law with a turnover at low energies (dashed line). The gray (solid) line indicates the sum of the two components. The maximum energy used for fitting each spectrum during pre-event II is denoted by a vertical dashed line (in top row only).

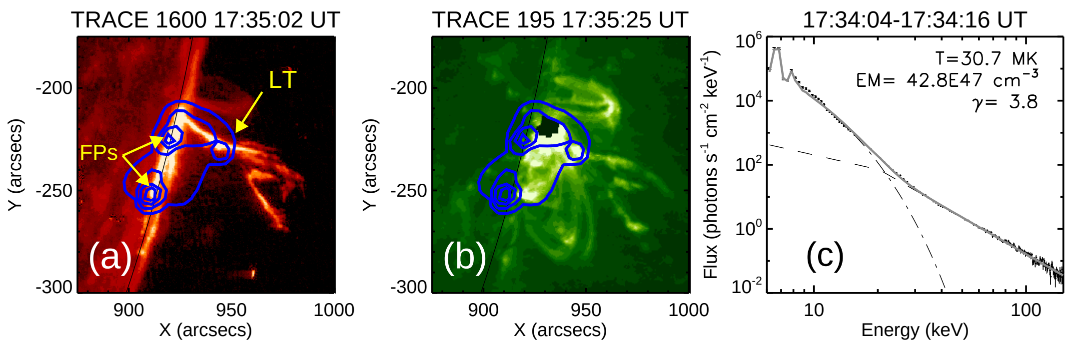

Figure 3.13: Panels (a) and (b): TRACE 1600 Å and 195 Å images overlaid by RHESSI contours in 50–100 keV (blue) energy band showing the detachment of prominence from the source region. Two foot points (FPs) and a coronal loop top (LT) sources are clearly detected and indicated by arrows in panel (a). Panel (c): HXR spectra during this phase showing high plasma temperature and significant non-thermal characteristics.

3.2.6 Results and discussion

We have presented a multi-wavelength study of four successive flares that occurred during the evolutionary phases of a prominence eruption in NOAA AR 10656 on 2004 August 18 over a period of 2 hr. Three class C flares occurred before the eruption, and the last event was a major X1.8 eruptive flare. The pre-eruption events occurred in the vicinity of the filament and were localized in nature. The filament became unstable and eventually erupted, producing an X-class flare. Table 3.2 presents an observational summary of flare activity and associated eruptive phenomena. We discuss the prominence eruption along with associated flare activity in terms of two evolutionary stages.

Pre-eruption phase

The pre-eruption phase is characterized by three localized flares (i.e., pre-events I, II, and III) along with the heating, activation, and rise of the filament. Pre-event I exhibited intense brightening of a low-lying loop system observed within a very confined volume (see Figures 3.7(b)–(e)). However, this small flare is remarkable because of its association with a plasmoid ejection. The formation of the plasmoid

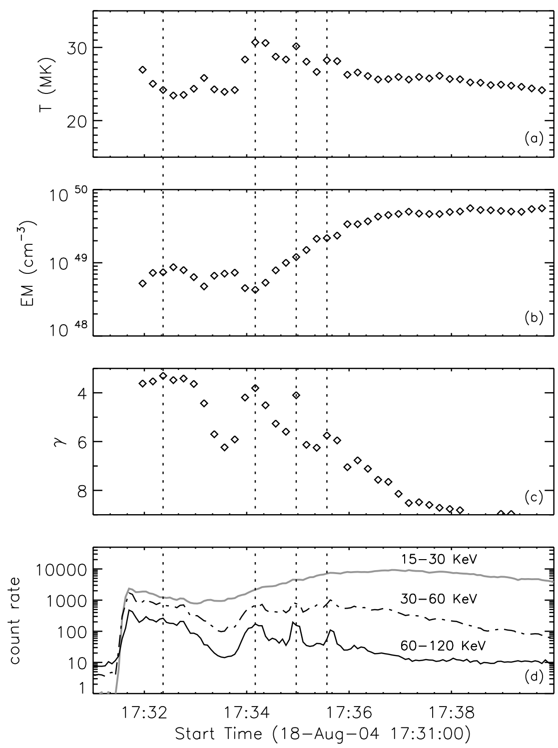

Figure 3.14: Temporal evolution of various spectroscopic quantities derived from RHESSI X-ray spectral fits of consecutive 12 s integration times for X1.8 flare. From top to bottom: plasma temperature, emission measure, photon spectral index, and RHESSI count rates in the 15–30 keV, 30–60 keV, and 60–120 keV energy bands. Dashed vertical lines indicate important phases of flare evolution during which spectra showed strong non-thermal characteristics.

at the top of the flare loops and its upward motion are readily visible from EUV images. Another significant observation is the presence of the 10–15 keV HXR LT source at the flare maximum, indicating intense plasma heating. The upward moving blob of hot plasma along with the HXR LT source provides evidence for the magnetic reconnection. It is likely that the ejection of plasma and magnetic fields, observed as plasmoid, is caused by weaker overlying magnetic fields and lower density above the flare loops. Plasmoid ejection is believed to be intimately connected to the magnetic reconnection (Karlický 2014). We emphasize that the rise of filament began after this small flare, which occurred at its southern leg, suggesting a casual relation between the flare event and filament rise. It is likely that the magnetic reconnection caused a weakening of overlying field lines, making the expansion of filament possible.

Pre-event II corresponds to the very rapid variation of the GOES flux that lasted for only $\sim$7 minutes. This highly impulsive and compact event took place at the northern leg of the filament (see figures 3.7(g)–(i)). Despite the impulsiveness of the event, we clearly identified that the peak of the HXR flux in 25–50 keV at 16:23:50 UT occurred before the thermal SXR peak in 1–8 Å at 16:25:00 UT. The timing of the peaks of the HXR and SXR fluxes suggests that high energy HXR emission is associated with processes that are intimately linked with the primary energy release (i.e., magnetic reconnection), while the SXR flux with a delayed maximum is attributed to the thermal emission from hot flare loops. The series of co-spatial EUV and X-ray images readily confirm this picture. The EUV images reveal fast expansion of a loop system within a confined yet elongated region. We note that HXR emission was clearly observed up to 60 keV above the background level. It is noteworthy that X-ray spectra during the peak timings indicate hot plasma ($\sim$23 MK) with lower emission measure values (see Figures 3.12(a)–(c)), indicating intense plasma heating within a confined environment. At this point, the HXR spectrum reveals strong non-thermal characteristics at energies >15 keV with a photon spectral index of $\gamma \sim 4$. It is remarkable that in such a short-lived and confined event, we clearly recognize a *soft-hard-soft* spectral evolution, providing evidence of particle acceleration (Benz 1977; Grigis and Benz 2004; Joshi et al. 2011).

Compared to the previous events, pre-event III, showed a very different morphological evolution. The TRACE EUV observations suggest that this event is associated with the successive brightening of two systems of low-lying loops, which are located side by side (see Figures 3.7(j)–(n)). The partially available RHESSI observations indicate the emission from coronal loops along with an upward movement of the LT source, an important feature of the standard flare model (Joshi et al. 2007). RHESSI X-ray spectroscopy analysis reveals lower values of temperature and emission measure during this event compared to pre-event II.

During the time between events I and III, the evolution of the filament was very slow. However, we emphasize that the filaments's slow evolution in the pre-eruption phase is temporarily and spatially associated with flaring activity.

Table 3.2: Observational summary of activities during pre-eruption phase and eruptive X1.8 flare.

Phases	GOES interval in UT (peak time)	Activity	
		TRACE (EUV)	RHESSI
Pre-event I (C2.2)	16:07–16:22 UT (16:14 UT)	Localized brightening along with plasmoid ejection at southern leg of the filament, prominence slowly rises	Contaminated by particle event, compact source in 10–15 keV
Pre-event II (C6.7)	16:23–16:30 UT (16:25 UT)	Confined flare at the northern leg of the filament	HXR source up to 50–80 keV detected with significant non-thermal emission ($\gamma \simeq$4.0)
Pre-event III (C7.3)	16:35–17:05 UT (16:45 UT)	Sequential brightening in two low-lying loops followed by arcade formation	Partially observed up to ∼16:40 UT, mostly thermal emission from the looptop up to ∼30 keV
Filament activation	17:05–17:19 UT	Rise of prominence along with localized brightenings	Not available
Filament eruption and X1.8 flare	17:30–19:00 UT	Prominence eruption, formation of bright elongated coronal structure below the erupting prominence	Multiple HXR bursts with strong non-thermal HXR emission, high-energy coronal HXR sources

We observe more significant morphological changes associated with the rising filament after the pre-eruption events (see Figure 3.9). The changes started to occur just after pre-event III and were continuously observed during the rest of the pre-eruption phase. During this interval, the filament exhibited a continuous rise with a speed of ~12 km s^{-1}. Before the main eruption, we find brightenings within the twisted filament channel, which is also reflected in GOES observations as a small bump at ~17:18 UT (Figure 3.2). The localized brightenings at two different locations below the apex of the prominence are likely caused by heating due to magnetic reconnection (Chifor et al. 2007). We further note that as the brightening increased, the filament appeared less structured, probably due to the change from absorption of EUV radiation to emission caused by the fast heating of plasma within the filament (Filippov and Koutchmy 2002).

Prominence eruption and X1.8 flare

This phase is marked by the onset of the X1.8 flare, during which the activated filament underwent a transition into the dynamic phase and erupted. This phase is characterized by a fast rise of the prominence (~270 km s^{-1}) and strong HXR non-thermal emission. The evolution of the HXR flux during the X-class flare is very interesting. It displayed four distinct episodes of flux enhancements; the first peak was very broad (labeled phase I; see Figure 3.5) and gradual, while the other three peaks were impulsive (labeled phase II; see Figure 3.5). More importantly, these peaks were observed at very high energies of up to ~100–300 keV. During phase I of the prolonged HXR emission (17:31 UT–17:33 UT), the X-ray emission above ~20 keV followed hard power law with a photon spectral index ~3.5 (Figure 3.14). The spectra continued to be harder throughout this phase. The spectra increased in hardness again during the next three HXR bursts (indicated by vertical dashed lines in Figure 3.14). We note a very important phase of prominence eruption in (E)UV observations between the second and third HXR peaks (at ~17:35 UT). With the rapid expansion of the prominence, intense brightening is observed in (E)UV images below the erupting structure (Figure 3.11(c) and (h)). It is remarkable that this important stage of prominence eruption is spatially and temporarily associated with high-energy HXR emission in the form of an extended coronal HXR source observed in the 50–100 keV energy band (Figure 3.11). In order to pinpoint this crucial stage of prominence evolution, we further highlight combined (E)UV and X-ray observations in Figure 3.13. We note that the temperature rose to very high values (with a maximum value of ∼31 MK at 17:34 UT) during the HXR bursts that occurred between 17:34 and 17:36 UT. This period of high plasma temperature coincides with the appearance of an elongated bright (E)UV structure which is co-spatial with an extended HXR coronal source, showing intense emission from loop top (LT) and footpoint (FP) regions (see Figure 3.13). This stage of multiple HXR bursts concluded with the final detachment of the prominence from the solar source region, with the closed post-flare loops remaining on the solar limb. We also note that the thermal emission dominates during the decay phase with a slow rise in emission measure.

After the first HXR burst (∼17:32–17:33 UT), we observe strong HXR coronal emission at energies $\geq$25 keV (Figures 3.5(d)–(i)), which was detected until the late phases of the flare. Moreover, HXR images at 50–100 keV clearly indicate coronal emission between 17:35 and 17:38 UT. Such a high energy coronal HXR emission has recently been detected in several flares by RHESSI during their different evolutionary phases (Veronig and Brown 2004; Krucker et al. 2008; Joshi et al. 2009, 2011). However, the physical mechanism for this strong non-thermal source in the tenuous corona is still not clearly understood.

3.2.7 Summary and conclusions

The observations of multiple flare activity associated with the phases of prominence eruption from AR NOAA 10656 provide us with an unique opportunity to understand some of the aspects of the eruption processes, namely, the role of the pre-eruption magnetic reconnection, triggering mechanism, particle acceleration, and large-scale reconnection during the main phase of the eruption, which are summarized as follows.

1. Our observations imply that pre-eruption events essentially represent discrete episodes of magnetic reconnection that play an important role in filament evolution toward eruption. The evidence for localized magnetic reconnection and particle acceleration is observed in the form of plasmoid ejection, HXR emission, and *soft-hard-soft* evolution of the HXR spectra. The sequence of activities suggest that the localized and short-lived episodes of magnetic reconnection that occurred in the vicinity of the filament, would tend to weaken the overlying magnetic structure. Here it is important to note that the decrease of overlying magnetic field is a crucial factor that permits the process of successful eruption of an unstable flux rope (Török et al. 2004; Török and Kliem 2005). Observations presented here reveal an early quasi-static, slowly evolving phase of the filament before the onset of more dynamic activation phase. The activation phase of filament associated with slow rise and heating has been recognized as an important precursor before the eruption (Sterling and Moore 2005; Liu et al. 2008; Sterling et al. 2011).

2. These observations also reveal that initiation of the eruption is essentially linked with the EUV/X-ray emissions originating at the lower corona and/or chromospheric heights rather than reconnection occurring in higher coronal loops, above the prominence. The HXR emission also suggests that the pre-eruption reconnection occurred close to the leg of the prominence. The heating of the rising prominence during its activation phase essentially resembles the precursor phase brightenings that are generally observed a few to tens of minutes prior to a large flare in the form of enhancements of soft X-ray and EUV emissions (Magara and Shibata 1999). From these observations we infer that the mechanism leading to pre-eruption flares and precursor emission caused the onset of filament activation and eruption. Our present interpretation of the initiation of the prominence eruption is consistent with the *tether-cutting* mechanism (Moore and Roumeliotis 1992). The onset of the X1.8 flare marks the fast rise phase of the filament. Sterling and Moore (2005) suggested that the transition to the fast-rise phase would occur when the low-lying reconnection that initiated the slow-rise phase inflated the overlying filament-carrying fields enough that they became unstable and violently erupted, perhaps due to an MHD instability or due to runaway tether cutting.

3. The filament eruption was accompanied by an X1.8 flare. The flare is marked by four distinct HXR peaks up to 100–300 keV energies. We observed strong and prolonged non-thermal HXR emission right at the flare onset, evidencing an extended phase of particle acceleration (see e.g., Joshi et al. 2012, and references therein) related to the early stages of filament eruption. We therefore interpret that the initial ejection of filament is associated with the formation of a current sheet underneath which then reconnects to cause the subsequent eruption and non-thermal emission (see e.g., Alexander et al. 2006). RHESSI and TRACE observations during the next three HXR bursts are consistent with this interpretation which reveal a thin, elongated, and bright structure in (E)UV images co-spatial with 50–100 keV extended coronal HXR sources. Within the scope of standard flare model, we believe that the extended coronal HXR emission associated with bright, thin (E)UV structure is a direct consequence of magnetic reconnection in the current sheet formed below the erupting prominence. This is further supported by the fact that at this very interval, the temperature attained the highest value of $\sim$31 MK. These three impulsive HXR bursts clearly showed *soft-hard-soft* spectral evolution suggesting distinct events of particle acceleration associated with the early phase of CME initiation. The appearance of strong HXR coronal as well as footpoint emissions during the impulsive phase imply rapid dissipation of magnetic energy in the current sheet as a result of increase in the rate of magnetic reconnection (see e.g., Sui and Holman 2003).

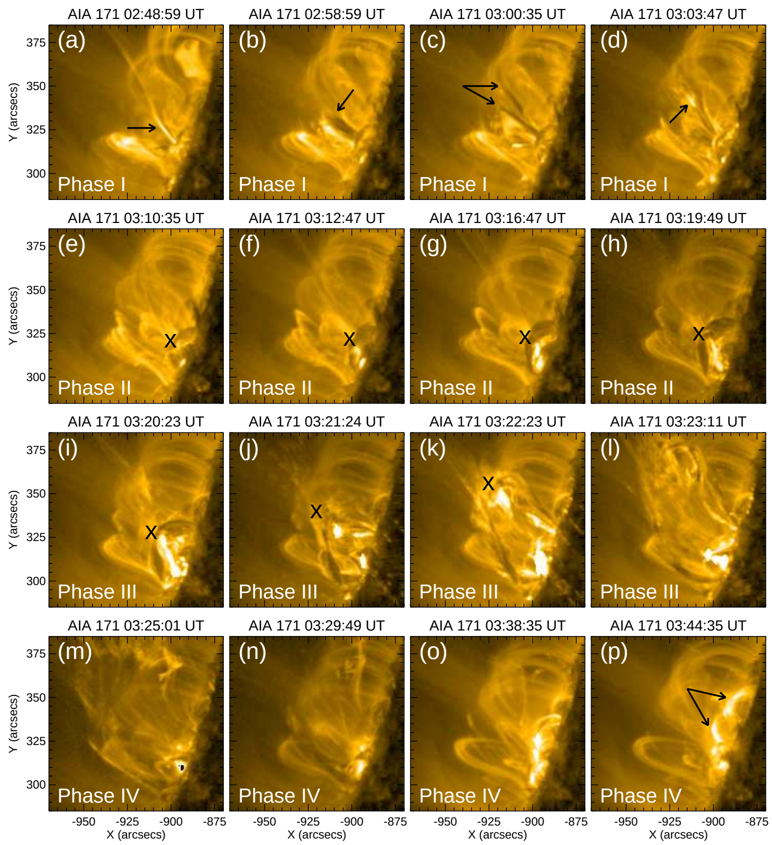

Figure 3.15: Series of AIA 171 Å images showing the overall eruption scenario which is divided in four phases (see Table 3.3). Several important features are identified during the various phases which are annotated in this figure. Phase I: Arrows indicate a blowout jet (panel (a)), fast rise and evolution of a flux rope (panels (b)–(d)); Phase II and III: The prominence apex (marked by cross (×)) during its slow and fast rise phases (panels (e)–(k)); Phase IV: Arrows indicate an arcade of post-flare loops following the eruption (panel (p)).

3.3 2012 August 18 prominence eruption in AR 11548

3.3.1 Phases of prominence eruption

The active region NOAA 11548 was at the east limb of the Sun on 2012 August 18. The examination of this active region between 02:45 and 03:45 UT displays a host of dynamical activities which are eventually connected to the activation and spec-

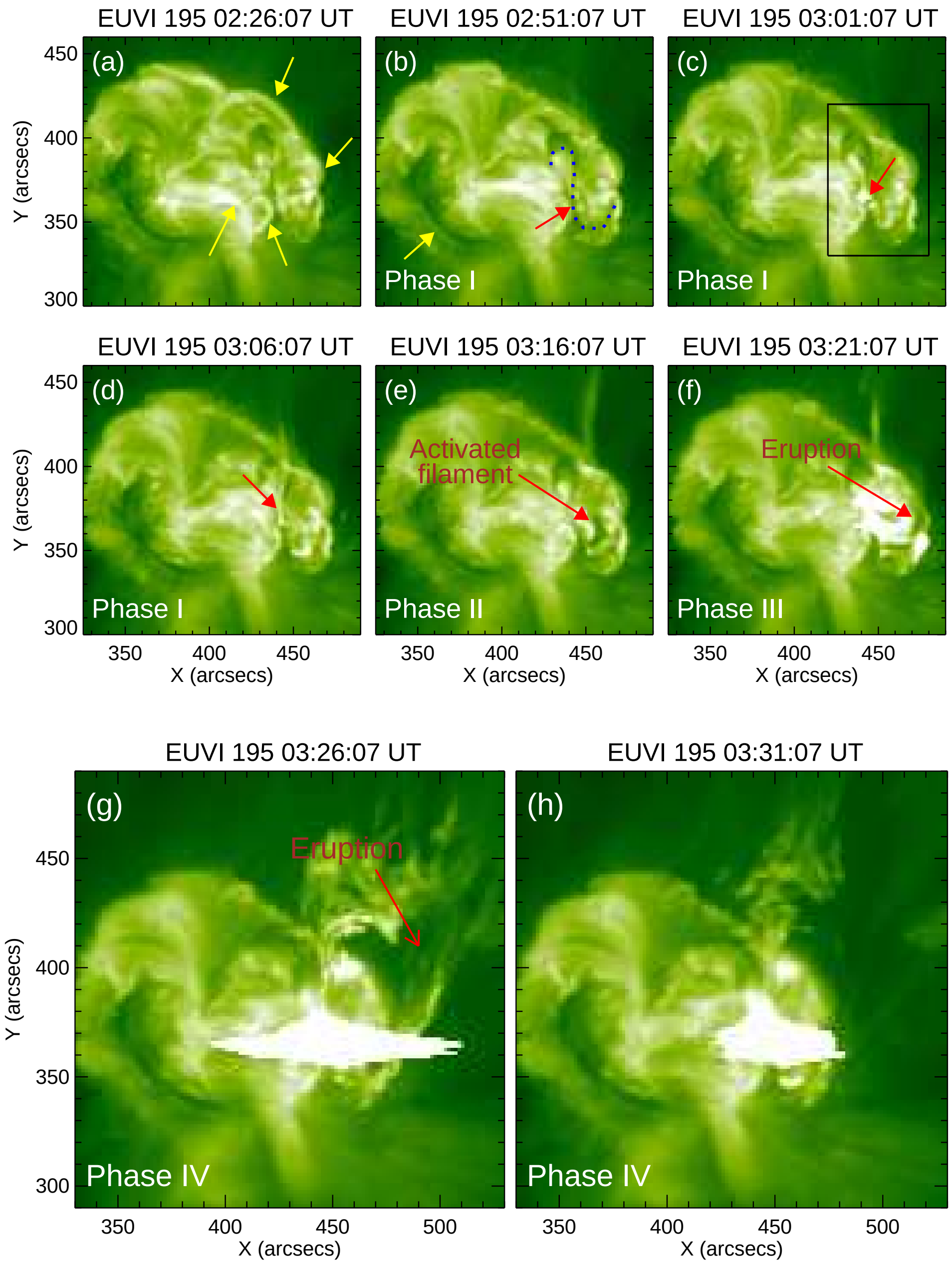

Figure 3.16: Representative images taken by EUVI/SECCHI on board STEREO-B. The region of interest is shown inside the box in panel (c). In panel (c), we mark the prominence which underwent activation and subsequent eruption by dotted line while another prominence belonging to this active region (shown by yellow arrow) remains quiet throughout these observations. We note that the site of prominence activity is connected to other parts of active region by multiple loop systems (some such loops are marked by arrows in panel (a)) which suggests that multiple flux systems close to polarity inversion line are involved in the eruption process. In panels (d)–(g), we show sequence of dynamical activities occurring near the prominence during its pre-eruption and activation phases.

tacular eruption of a prominence. By a careful investigation of the active region during this period along with light curves at different X-ray and EUV channels, we divide the whole activity in four phases which are summarized in Table 3.3. In Figure 3.15, we show some representative images captured by 171 Å channel of AIA to depict four evolutionary phases of the prominence eruption.

The phase I (02:45–03:10 UT) corresponds to activities during the pre-eruption period (Figure 3.15(a)–(d)). The sequence of images clearly show that the corona above the activity site (i.e., the site of prominence rise) was quite dynamical during phase I. We particularly highlight two important developments during this phase. First, a dynamic well-collimated stream of plasma appeared during ∼02:47–02:54 UT, which extends higher into the corona (marked by arrow in Figure 3.15(a)). Based on the morphological and kinematic evolution of this structure at multi-wavelengths, we recognize this as a blowout jet (Moore et al. 2010, 2013). We find that this blowout jet produces stronger emission and more dynamical evolution at cooler EUV lines (e.g., 304 Å). With the decay of this structure, we see the rapid rise of a flux rope which initially appeared to be a single, wide structure (marked in Figure 3.15(b)). The flux rope split into two parts as it grew in the corona while their lower portions are always connected (marked in Figure 3.15(c)). This flux rope appeared in absorption (i.e., dark structure) evidencing this to be at a lower temperature than the ambient corona. It is remarkable that the bifurcated structure continuously rotated (likely underwent untwisting) along their common base.

After about ∼30 minutes of dynamical activities in the corona (i.e., phase I), the prominence activation started and it underwent a slow rise during the phase II (03:10–03:20 UT; Figure 3.15(e)–(h)). The EUV images reveal that brightening started below the rising prominence at 03:12 UT which continuously built up with the increase of prominences height. The rise of prominence is shown by placing a cross (×) symbol at the apex of the prominence in different panels of Figure 3.15. The height-time plot of the rising prominence is given in Figure 3.20 which shows

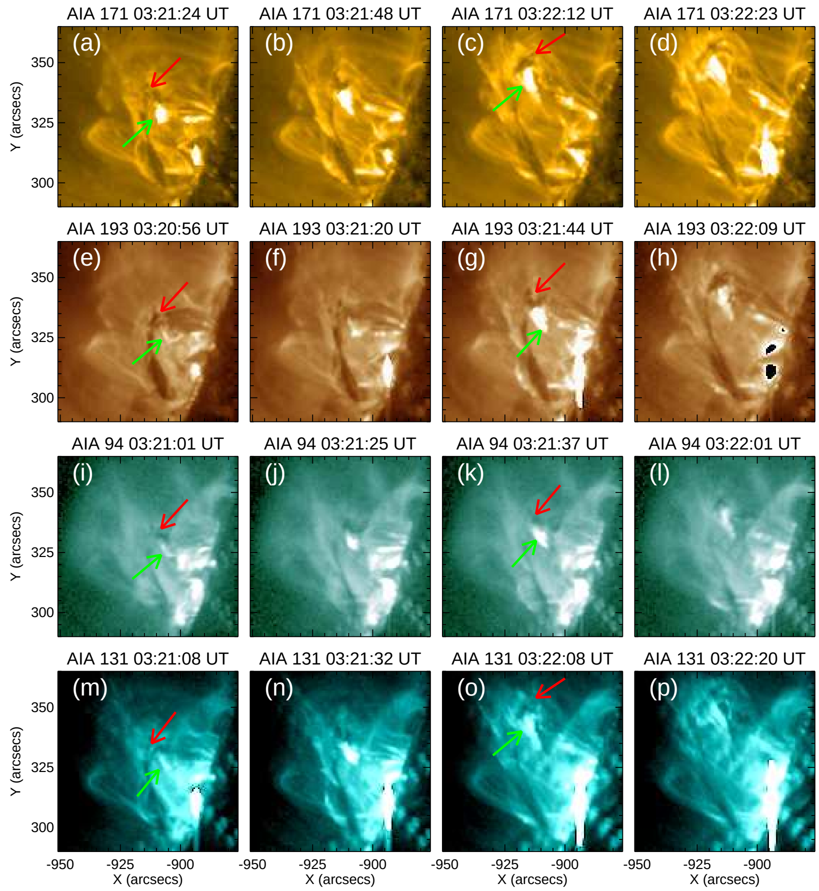

Figure 3.17: Representative AIA images taken at different EUV channels showing the eruption of prominence (i.e., fast expansion; phase III). In these images, we can clearly distinguish fast eruption of the plasmoid (green arrows) below the fast rising prominence (red arrows). Note that the plasmoid ejected in the direction of the apex of prominence.

that the prominence expanded with a speed of $\sim$12 km s^{-1} during this phase.

The prominence was set to fast rising (eruptive) motion during phase III (03:20–03:25 UT; Figure 3.15(i)–(l)). During this phase the prominence erupted with a speed of $\sim$149 km s^{-1}. The source region, however, exhibited intense brightening for several minutes after the complete eruption of prominence from AIA field of view and a growing arcade of post-flare loops appeared (phase IV; Figure 3.15(m)–(p)). we also note that the eruption of this prominence was associated with a CME.

3.3.2 Coronal structures of active region

After defining the phases of prominence evolution in the preceding section, we explore the morphology of coronal loops of the active region and its evolution with the prominence activation and eruption. Since the active region are located just at the limb as per SDO observations, we have analyzed Extreme Ultraviolet Imager (EUVI; Wuelser et al. 2004) observations to understand on-disk perspectives of the active region. EUVI is a part of the Sun-Earth-Connection Coronal and Heliospheric Investigations (SECCHI; Howard et al. 2007) instrument suite on board NASA's STEREO mission. In Figure 3.16, we provide a series of EUVI images at 195 Å covering different phases of this activity. Images presented here correspond to STEREO-B observations which had an angular separation of -115° with respect to Earth (in heliocentric coordinates) on the day of event[2]. The EUVI images have a resolution of $1''.6$ pixel^{-1}. The activity site is marked by a box in Figure 3.16(c).

Although EUVI has coarse temporal resolution (5 min) but this data is extremely useful to understand the magnetic configuration of the activity site. We find that the activity site is connected to other parts of active region by large bright loops. We mark four most noticeable loops in Figure 3.16(a) that have likely participated in the eruption of the prominence under investigation while the prominence is marked by dotted lines in Figure 3.16(b). The early pre-flare signatures in the form of localized brightening is seen at the middle of the filament (Figure 3.16(c)). There is another filament channel in this active region (marked by yellow arrow in Figure 3.16(b) which does not take part in the eruption and remains undeflected throughout. The images show other important features, such as, pre-flare brightening (Figure 3.16(c)), streams of hot plasma ejection (Figure 3.16(d)), prominence activation and source region brightenings (Figures 3.16(e)–(f)) and finally prominence eruption (Figures 3.16(g)–(h)) which

[2]http://$stereo-ssc.nascom.nasa.gov/cgi-bin/make\_where\_gif$

are well consistent with the observations taken at multiple EUV channels of AIA.

The EUVI data confirms the occurrence of multiple dynamical activities in the vicinity of a twisted filament channel before its activation. The presence of large EUV coronal loops connecting the activity site to distant parts of the active region suggests that multiple flux systems existed close to the polarity inversion line (PIL) which is delineated by the prominence itself.

3.3.3 Prominence's fast rise and plasmoid ejection

During the eruptive phase of the prominence (i.e., phase III), the images at several EUV wavelengths (that represent plasma at different temperatures) reveal very crucial features that required special attention. In Figure 3.17, we present multi-wavelength view of this phase at four channels of AIA, viz., 171 Å (log(T)=5.8), 193 Å (log(T)=6.2, 7.3), 94 Å (log(T)=6.8), and 131 Å (log(T)=5.6, 7.0).

After the onset of fast eruption of the prominence at ∼03:20 UT (described in section 3.3.1, we observe intense brightening below the rising prominence which is different from the source region brightening (Figure 3.15(i)). We notice a bright structure got detached from the source region as the prominence further rose (∼03:21 UT) and the structure continuously moved upward in the corona in consort with the prominence eruption (Figure 3.17). This feature is seen at different AIA channels which reveals that it represents eruption of a blob of plasma at high temperature, i.e., a plasmoid. The plasmoid is always located below the rising prominence and clearly seen till ∼03:23 UT. In Figure 3.20, we plot the altitude evolution of this plasmoid from AIA 171 Å images. We find that the plasmoid underwent a fast ejection with a speed of 177 km s^{-1}.

3.3.4 Episodic energy release and M1.8 eruptive flare

During the pre-eruption, activation, and eruptive phases of the prominence, we observe brightenings at different regions of corona (see Figure 3.15 and section

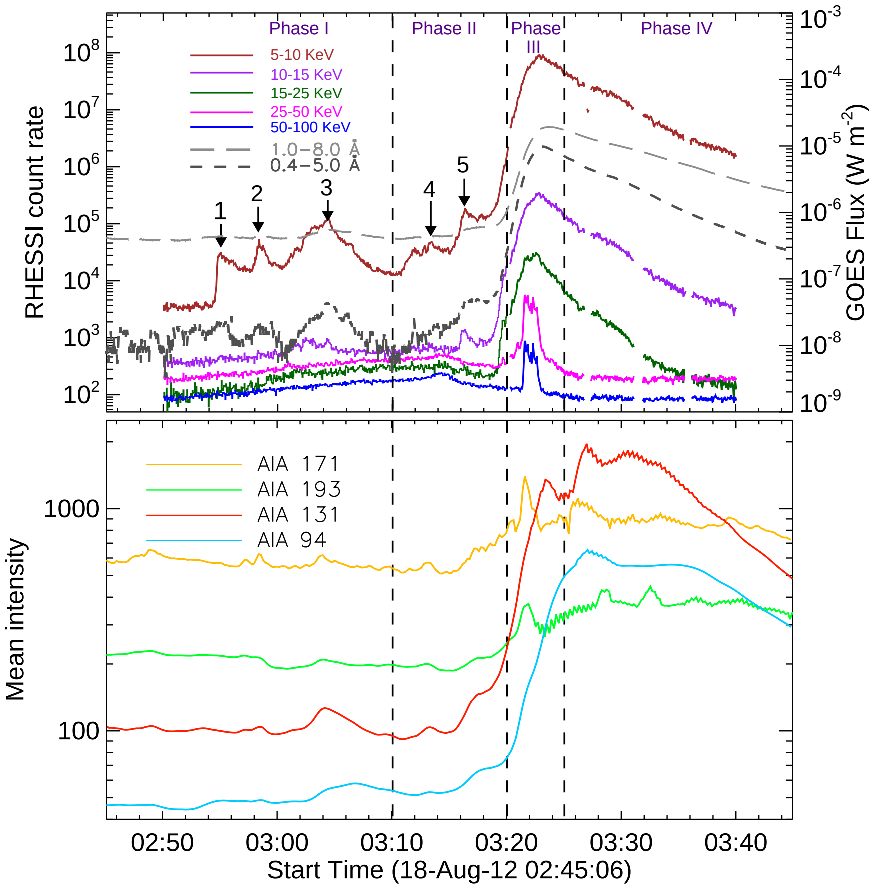

Figure 3.18: Top panel: X-ray time profiles observed by GOES and RHESSI. The RHESSI light curves are constructed by measuring the photon count rates in 5–10, 10–15, 15–25, 25–50 and 50–100 keV energy bands with a time cadence of 4 s. Bottom panel: The EUV light curves at four wavelengths. These light curves denote the mean intensity of the activity sites derived from successive AIA images observed at 12 s cadence.

3.3.1). These brightenings correspond to events of energy release at different temporal and spatial scales. Therefore in order to understand the characteristics of energy release processes, we present different light curves of the flaring region in Figure 3.18.

The top panel of Figure 3.18 provides X-ray light curves obtained from GOES (1–8 Å and 0.5–4 Å) and RHESSI (5–10, 10–15, 15–25, 25–50, and 50–100 keV) observations. In the bottom panel, we show EUV light curves in four channels (171, 193, 94, and 131 Å). We also mark different evolutionary phases of the

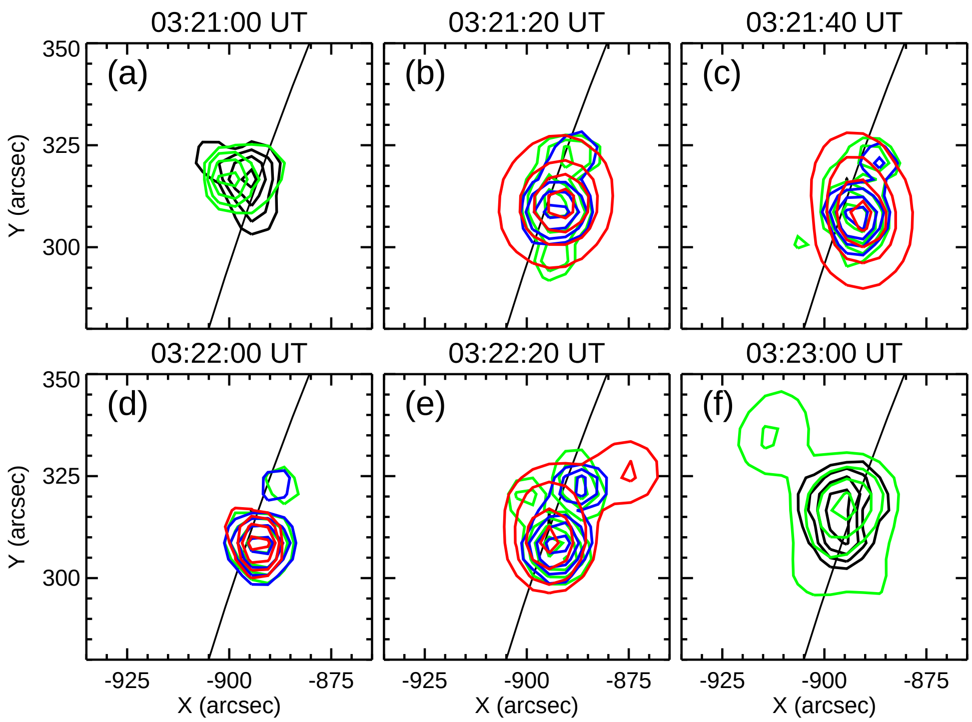

Figure 3.19: Temporal evolution of HXR sources in 12–25 keV (black), 25–50 keV (green), 50–100 keV (blue), and 100–200 keV (red) during the imporatnt stages of flare impulsive phase. The contour levels for both HXR images are set as 20%, 35%, 55%, and 85% of the peak flux of each images.

prominence (Table 3.3) in this plot for a comparison.

A comparison between light curves and EUV images suggests that various peaks during the pre-eruption phase (phase I) indicate intermittent and localized episodes of coronal energy release. It is noteworthy that these pre-flare events are highly distinguishable in X-ray light curve of RHESSI (5–10 keV) and higher energy band of GOES (0.5–4 Å). Following the onset of slow rise of prominence (phase II), the process of continuous energy release is set below the prominence with gradual increase in intensity which resembles with precursor flare brightening. The eruptive phase of prominence (phase III) is characterized by impulsive increase in the intensity of emission (i.e., impulsive phase of M1.8 flare) implying the onset of large-scale magnetic reconnection. At X-ray bands, impulsive phase is recognized up to $\sim$200 keV energies. After the complete expulsion of the

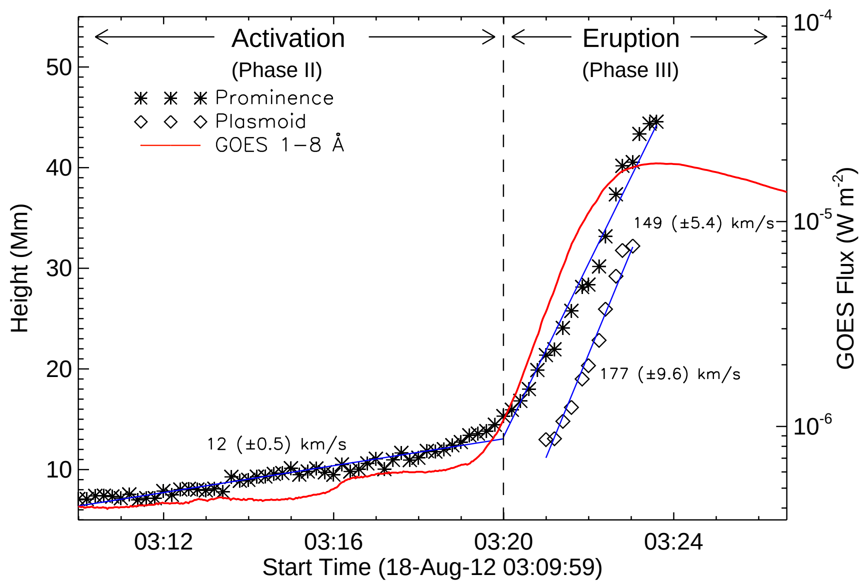

Figure 3.20: Height-time plot of the prominence derived from AIA 171 Å images. We have also shown the height-time plot for the plasmoid eruption (derived from AIA 171 Å images) which was observed below the apex of prominence during its eruptive phase. The comparison of prominence height-time plot with GOES 1–8 Å light curve (red curve) indicates that the SXR flux enhanced slowly during the activation phase while it increased impulsively during the eruptive phase.

prominence, the X-ray light curves indicate decay phase of the flare. However, the EUV light curves show a prolonged emission after the flare's impulsive phase due to the bright emission from post-flare loop arcade.

3.3.5 Spatial and spectral evolution of X-ray emission

RHESSI observed the Sun continuously during the various phases of this prominence activity right from the pre-eruption phase (∼03:00 UT) till the end of the M-class flare. We also note that the RHESSI measurements during this whole period are contaminated by X-rays from a particle event[3] (i.e., the RHESSI detectors were hit by high-energy particles trapped in the Earths radiation belts). However, the particle rates are low that remain mostly constant throughout the

[3]http://hesperia.gsfc.nasa.gov/hessidata/metadata/2012/08/18/

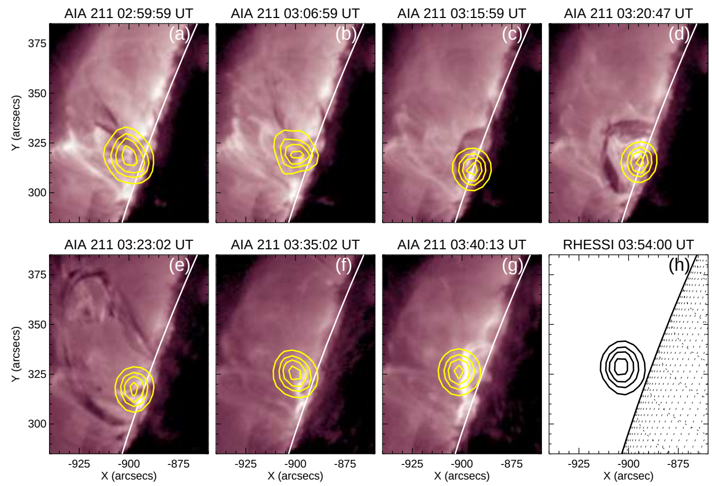

Figure 3.21: A few representative images showing the locations of RHESSI CLEAN images in 6–12 keV (yellow) energy band with respect to prominence evolution in AIA 211 Å images (panels (a)–(g)). The contour levels for X-ray images are 60%, 75%, 85%, and 95% of the peak flux of each images.

observations. Further, the reconstruction of images at different energy band up to 200 keV (Figure 3.19) provides very clear images of source structure and evolution which indicate that particle event (which mostly effects observations at higher energy bands) does not affect the RHESSI measurements much.

RHESSI X-ray light curves (5–10 and 10–15 keV; Figure 3.18(a)) clearly show that there is a significant emission at soft X-ray energies during the pre-eruption phase (phase I) from the active region corona with distinct and episodic emission peaks (marked as 1, 2, and 3) with the third one as the strongest and the broadest. The X-ray intensity further built up after the onset of prominence activation (phase II or precursor emission) and two prominent peaks can be identified at this phase (marked as 4 and 5) which are superimposed on the continuously rising flux level. Following peak 5, the X-ray flux, in all energy bands (5–10, 10–15, and 15–25 keV) underwent an impulsive increase in emission, attaining the maximum of M1.8 flare at $\sim$03:22 UT. We further note that the impulsive peaks at high energy HXR bands (i.e., 25–50 and 50–100 keV) are broad and structured with rapid intensity fluctuations.

The RHESSI images during pre- as well a post- eruption phases clearly indicate soft X-ray loop sources which are overplotted on EUV images at 211 Å to indicate its location with respect to other ongoing activities (Figure 3.21). A careful examination of series of 6–12 keV RHESSI images reveals that prior to the eruptive phase of the prominence, the LT source appeared at varying heights in the corona with a general trend of decrease in altitude. The LT source changed its direction of motion with the eruptive phase of the prominence (phase III; ∼03:20 UT onward) and begin to exhibit the 'standard' upward movement. In Figure 3.22, we quantitatively present the altitude evolution of 6–12 keV X-ray source from 03:00 to 03:54 UT. The source altitude is derived by measuring the centroids of X-ray emission along its main axis of motion. We find that, in general, altitude of LT source decreases during 03:00 UT to 03:16 UT with a speed of ∼4 km s^{-1}. With the onset of eruptive phase, the LT source moved upward with a speed of ∼16 km s^{-1} till 03:30 UT which slowed down ∼7 km s^{-1} thereafter.

The spatial evolution of X-ray sources at various energy bands, viz., 12–25 (black), 25–50 keV (green), 50–100 (blue), and 100–200 keV (red), during the impulsive phase of M1.8 flare is shown in Figure 3.19. The RHESSI images are reconstructed using PIXON algorithm with the natural weighing scheme using front detector segments 3–8 (excluding 7). We note a pair of distinct centroids at 50–100 keV and 100–200 keV energy bands that likely indicate emissions from conjugate footpoints of the flare loop systems. It is striking to note a HXR coronal source at 25–50 keV that underwent rapid altitude evolution (Figures 3.19(e) and (f)). This HXR coronal source appeared for a brief interval (∼2 min) and evolved along the trajectory of the EUV plasmoid eruption (section 3.3.3 and Figure 3.17). However, unlike to EUV plasmoid, it could not be followed to higher altitudes, presumably due to decrease in the density of corona.

In Figure 3.23, we present temperature (T) and emission measure (EM) derived from GOES. The plot also show T and EM derived from RHESSI spectroscopy for a few selected time intervals. For RHESSI analysis, we first generated a RHESSI spectrogram with an energy binning of 1/3 keV from 6 to 15 keV and 1 keV from 15 to 100 keV, and 5 keV from 100 to 200 keV energies. We only used front segments of the detectors, and excluded detectors 2 and 7. The spectra were deconvolved with the full detector response matrix. We have carefully chosen appropriate background intervals during the pre-eruption phase when the contribution of both background solar flux and particle event (non-solar event) are present. Depending upon the observed count rates, different background intervals were carefully chosen for different energy ranges: 02:51:00–02:53:30 UT for 6–12 keV and 03:08:32–03:10:20 UT for >12 keV. As noted earlier, the particle event was of low intensity and exhibited mild variations during the observing period (see section 3.3.5). For reference, we present a few representative spatially integrated, background subtracted RHESSI spectra in Figure 3.23. The spectra look quite reasonable within the observing limitations.

We note that during the pre-eruption phase, the temperature reaches to $\sim$10 MK while during the impulsive phase the plasma is heated to $\sim$25 MK (Figure 3.24(a)). The EM remains low prior to the eruptive phase (Figure 3.24(b)) which indicates that events of localized heating took place during this interval. With the impulsive phase of event, the EM also rises.

3.3.6 Results and discussion

Pre-eruption activity and activation phase of the prominence

The sequence of activities associated with the prominence eruption on 2012 August 18 clearly demonstrate that this eruption was associated with multiple phases. Here we note that these multiple phases are defined in terms of the dynamical evolution of prominence while the X-ray and EUV light curves (and corresponding images) present crucial information about energy release processes during these phases. We believe that different peaks in the light curve provide basic information about the timescales that operate during the coronal energy

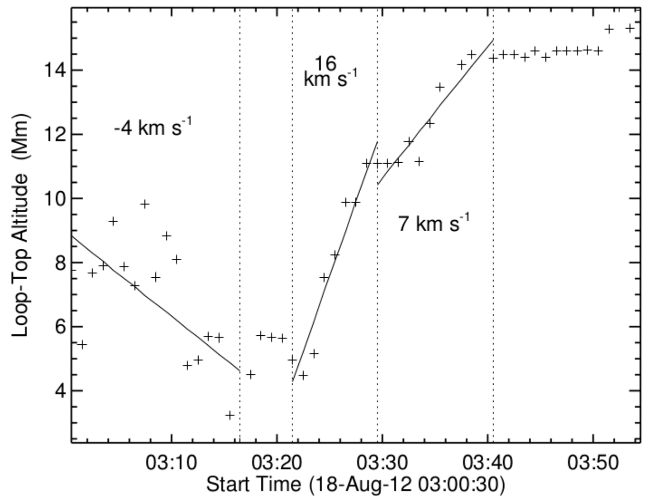

Figure 3.22: Altitude evolution of thermal 6–12 keV sources representing hot coronal loops during phases of the prominence activation and eruption. We note that LT source appeared at varying heights in the corona with a general trend of decrease in altitude. The 'standard' upward motion of X-ray loop source is observed only after ∼03:20 UT, i.e., with the impulsive phase of flare emission following the fast eruption of the prominence.

release. From a light curve, we also recognize whether the energy release occurs as intermittent events or a continuous (prolonged) process. Further, the energy release during a flare, as evidenced from a light curve, can exhibit diverse forms: small, slow and gradual (precursor phase of flare), large and rapid (impulsive phase), or large and gradual (decay phase of large eruptive events).

First we discuss the energy release events during the pre-eruption phase (phase I). There are three events during this phase (identified as 1, 2, and 3 in Figure 3.18). The third event is by far the largest and presents gradual rise and fall while the earlier two events lasted for a shorter time period with smaller flux enhancements. All these events present intermittent energy release processes with RHESSI light curves indicating a sequential increase in peak intensity for successive events. Peaks 2 and 3 are also identified in EUV light curves (Figure 3.18) although the enhancement in the flux level during the peak varies from one to another wavelength. The multi-wavelength data analyzed in the preceding sections clearly demonstrate that these energy release events of shorter time-scales

Table 3.3: Summary of various phases associated with prominence activation and eruption. Note that various phases of the prominence eruption are marked in EUV and X-ray time profiles shown in Figure 3.18 and representative images taken by AIA at 171 Å channel are presented in Figure 3.15

Phases/characteristics	Time	Observations
Phase I: Pre-eruption coronal activity	02:45–03:10 UT	Dynamical activities in the corona: Streams of hot plasma and eruption of a cool flux rope associated with localized brightening, intermittent energy release in X-ray (5–10 keV) and EUV, thermal X-ray emission, prominence remained stationary during this phase.
Phase II: Prominence activation	03:10–03:20 UT	Slow rise of prominence with a speed of $\sim$12 km s^{-1}, gradual increase of thermal X-ray and EUV emissions, EUV brightening is mostly confined underneath the prominence.
Phase III: Prominence eruption and M1.8 flare	03:20–03:25 UT	Prominence was set to fast rising motion with speed of $\sim$149 km s^{-1} and eventually erupted, multi-band EUV observations of plasmoid eruption below the erupting prominence, impulsive energy release in the source region leading to M1.8 flare.
Phase IV: Flare decay and post flare loops	03:25–03:45 UT	Formation of post-flare loops and arcades in the source region, slow decay of flare soft X-ray and EUV radiations.

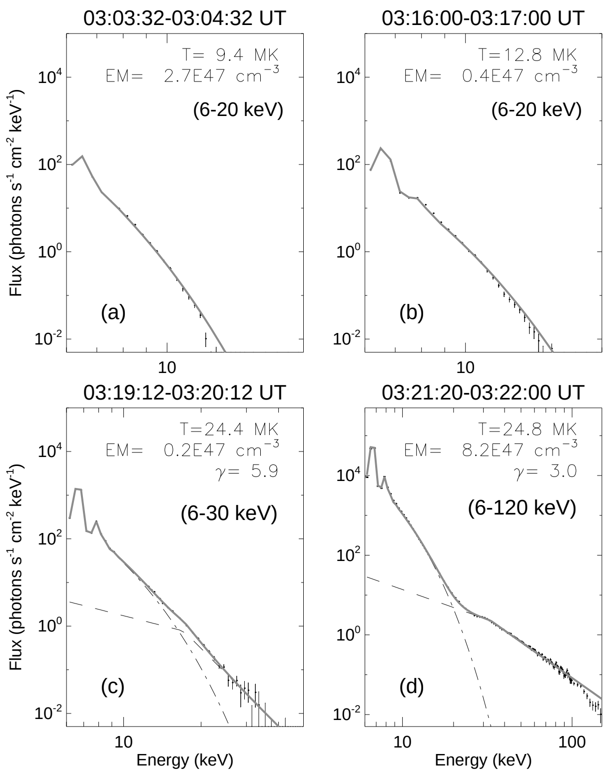

Figure 3.23: RHESSI X-ray spectra derived during selected intervals. The spectra shown in panels (a) and (b) are fitted with an isothermal model and correspond to the interval prior to the eruptive phase of the prominence. Panels (c) and (d) display spectra during the eruptive phase of the prominence and associated M1.8 flare. These spectra are fitted with a combination of isothermal model (dashed-dotted line) and power-law (dashed line) with gray line indicating the sum of the two components. The energy ranges chosen for fitting are shown on each panels.

occurred in the vicinity of a pre-existing prominence that subsequently underwent an activation phase. More importantly, these intermittent events are associated with dynamical phenomena in the active region corona, namely, a blowout jet and dramatic eruption of a flux rope (Figures 3.15(a)–(c)). During the evolution of the flux rope, we observe localized brightening within the flux rope as it undergoes rotation and upward expansion (Figure 3.15(d)). The coronal jets are believed to involve interchange magnetic reconnection, i.e, reconnection between closed and open flux. In active regions, the open field corresponds to field lines with one remote footpoint located very far from the locally closed domain (Shimojo

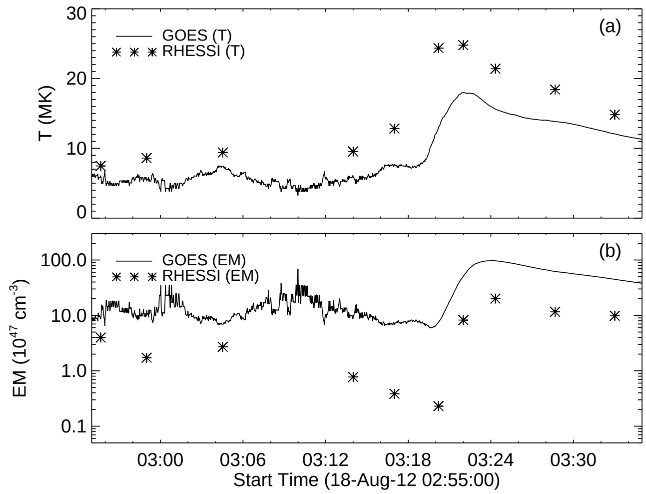

Figure 3.24: Evolution of temperature (T) and emission measure (EM) in panels (a) and (b) respectively which are derived from GOES and RHESSI X-ray measurements.

and Shibata 2000; Schmieder et al. 2013). The timing and location of sequence of pre-eruption activities indicate a probable connection between discrete events of energy release and subsequent activation of the prominence. In many earlier studies, discrete and localized X-ray brightenings have been reported that occur several minutes prior to the filament activation and associated flares at sites closer to the filament (Chifor et al. 2007; Joshi et al. 2013). Such small-scale energy release is often termed as pre-flare activity. Previous studies further suggest that the pre-flare activity represents early signatures of filament destabilization.

We note that during this pre-eruption phase, the X-ray emission was observed at varying altitudes in corona with a general trend of decrease in altitude (Figures 3.22 and 3.21). More importantly, altitude variation of the looptop source is associated with a distinct pre-flare event of coronal energy release (event 3) of phase I during which X-ray emission exhibits a gradual rise and decline (Figure 3.18). In view of this temporal consistency, we speculate that the observed variations in X-ray emission centroids represent shift in the position of magnetic reconnection site in the corona. Certainly this kind of X-ray source evolution is not consistent with the standard flare model in which the X-ray loop sources move successively upward in the corona. These observations reveal complex magnetic configuration of pre-eruption corona where pre-flare energy release took place. The altitude decrease of X-ray looptop source during solar flares has been reported in earlier studies (Sui and Holman 2003; Sui et al. 2004; Joshi et al. 2007; Veronig et al. 2006). However, compared to present case, the earlier observations indicate a more systematic downward motions of the X-ray looptop source. Further, in contrast to above mentioned studies, where X-ray sources underwent altitude decrease during the early impulsive phase of solar flares, we found altitude decrease of X-ray source during the modest energy release characterized by the pre-flare activity. In view of these differences, we speculate that the altitude decrease of X-ray source reported in this study is probably of different kind from the previously observed descending motions of X-ray sources.

The filament activation starts with the onset of phase II. The filament slowly rises with a speed of $\sim$12 km s^{-1} (Figure 3.22). The X-ray light curves of this phase clearly reveal a continuous rise of SXR flux (see RHESSI 5–10 keV and GOES 1–8 Å profile; Figures 3.18 and 3.22). This flux enhancement is superimposed by two peaks (marked as peaks 4 and 5) with peak 5 being noticeable at higher energies also (i.e., 10–15 keV profile). Although both phase I and phase II are associated with events of episodic energy release, the synthesis of multi-wavelength data suggests different characteristics of energy release phenomena. The phase I is characterized by varieties of coronal activity above the prominence and corresponding intermittent coronal EUV brightenings. Further, it is noted that during phase I, RHESSI sources indicate X-ray emission from relatively higher altitudes. On the other hand, once the prominence is set to upward expansion (i.e., onset of phase II), we do not notice significant coronal activities above the prominence and the X-ray and EUV emissions are observed continuously underneath the prominence. These observations imply that the gradual rise of SXR emission during phase II is likely the consequence of magnetic reconnection as predicted by the standard flare model although the X-ray light curves clearly reveal the energy release process to be small and gradual. Therefore, we interpret the energy release during phase II as a consequence of slow magnetic reconnection during prominence activation with slow rising motion.

The on-disk view of the active region observed from EUVI/SECCHI clearly reveal that the filament under investigation was highly twisted structure (Figure 3.16). We clearly find that the filament is surrounded/overlaid by complex system of coronal loops which together formed multi-polar flux system in the corona. It is to be noted that the multi-flux topology is one of the basic ingredients of breakout model of solar eruption. Recall that the energy release in the pre-eruption phase mainly occurred in the corona, well above the filament. Moreover, the dynamical emergence of a flux rope, its rotation, expansion and associated brightening in the corona should be recognized as a very critical part of the pre-eruption phase. The association of blowout jet, appearing prior to flux rope expansion, with the pre-eruption activity suggest that the multi-polar flux system of the active region contains large field lines with one remote footpoint located far from the locally closed domain. The filament activation (slow rise) begins after these coronal activities. In the breakout model, the magnetic reconnection in the breakout current sheet causes removal of overlying flux by transferring it to the adjoining regions. The resulting decrease in the downward tension causes the sheared field to expand faster (Antiochos et al. 1999). Several multi-wavelength observations of solar eruptions show qualitative agreement with the topology and expected dynamical evolution of the breakout model (Manoharan and Kundu 2003; Subramanian et al. 2003; Gary and Moore 2004; Sterling and Moore 2004; Sui et al. 2006a; Joshi et al. 2007; Lin et al. 2010). In particular, the radiative signatures of magnetic reconnections above the prominence during the early phases of eruption have been recognized as an observational evidence of breakout reconnection (e.g., Subramanian et al. 2003). By comparing our observations with breakout model, we conjecture that the expansion of sheared flux rope in the lower corona (see

Figures 3.15), above the quasi-stationary filament, is the consequence of ongoing breakout reconnection at higher coronal levels. Under this scenario, the onset of activation phase (slow rise of the prominence; phase II) would represent a stage when the constraining magnetic configuration had sufficiently weakened to allow the slow rise of the high density prominence. With the rise of prominence, a vertical current sheet would form underneath it and reconnection in this current sheet would correspond to flare brightening as proposed in the standard flare model which is well consistent with our observations. In view of this, we recognize a two-step process in the filament destabilization: the pre-eruption coronal activities are probably associated with the successive weakening of restraining overlying magnetic configuration which result in the outward expansion of core flux comprising the prominence. Following the rise of prominence, the standard flare reconnection would set underneath which will further contribute toward the detachment of the prominence from the source region.

3.3.7 Prominence eruption and M1.8 flare

After significant pre-flare activities, the prominence was set to complete loss of equilibrium during phase III (refer to Figure 3.18 and 3.2.4) and eventually erupted as a CME triggering impulsive energy release in the source region corresponding to an M1.8 flare. The X-ray observations of the impulsive phase of the flare reveal high temperature (T $\sim$25 MK) and significant non-thermal characteristics ($\gamma \sim 3$) indicating rapid plasma heating and acceleration of electrons to high energies (>100 keV). This phase is accompanied with the upward motion of X-ray looptop source. In the classical "CSHKP" model of eruptive (two-ribbon) flares, this rising motion of X-ray source reflects the progression of magnetic reconnection during which field lines rooted successively further apart from the magnetic inversion line reconnect (Joshi et al. 2007).

Intense brightening was observed from the source region right from early stage of prominence eruption. Soon afterwards, the source region brightening became more structure and a clear plasmoid appeared that underwent fast upward motion with the same direction of motion as the apex of erupting prominence. The plasmoid eruption is observed in several EUV channels including 94 Å and 131 Å images that corresponds to very high plasma temperature of 6×10^6 K. In the unified model of solar flares, proposed by Shibata (1996), it was recognized that the plasmoid eruption plays a crucial role in magnetic reconnection process. These evidences mostly came from flares observed from Solar X-ray Telescope (SXT) on board Yohkoh (see, e.g., Shibata et al. 1995; Ohyama and Shibata 1997, 1998; Nishizuka et al. 2010). Recently evidences of plasmoid eruption was also found from EUV observations at different wavelength channels taken from AIA (Takasao et al. 2012; Kumar and Cho 2013). From our observations, we note that the filament posed a large-scale structure comprising of dark material (i.e., cool and dense plasma) while the plasmoid was observed as a blob of hot plasma below the apex of prominence. It is noteworthy that during the impulsive phase of the flare the speeds of plasmoid ($\sim$177 km s^{-1}) and prominence eruption ($\sim$149 km s^{-1}) are of the same order. By exploring the temporal and spatial correlations between the erupting prominence and plasmoid ejection, we recognize a feedback relation between the kinematic evolution of the prominence and large-scale magnetic reconnection. Our observations imply that the onset of impulsive energy release (signifying fast reconnection below the outward moving prominence; see Figure 3.22) caused acceleration of plasmoid which subsequently supported the eruption of prominence in the lower corona.

3.3.8 Summary and conclusions

In this study, we try to address some important questions pertaining to triggering mechanism of solar eruptions and the process of prominence destabilization. Further, our study sheds some light about the role of magnetic reconnection towards the early evolution of erupting prominences.

1. The pre-eruption phase reveal significant dynamic activities in the corona, mostly above the apex of the prominence under investigation. During this phase, the prominence remains stable. The pre-eruption coronal activities include a blowout jet followed by the rotation and subsequent eruption of a dark flux rope. The blowout jet provides evidence for interchange magnetic reconnection that involve reconnection between closed and open flux systems of the active region (Pariat et al. 2015). These activities occur in conjunction with intermittent X-ray and EUV brightenings at different locations in corona. Apart from co-spatial X-ray and EUV brightenings at lower corona, we emphasize the EUV brightening that occurred at a higher coronal level during the rotation of the flux rope in pre-eruption phase. These complex activities are followed by prominence activation. The pre-eruption activities, coupled with the fact that the active region corona posses a highly complex structure of multiple coronal loop systems, can be qualitatively compared with model of solar eruptions. From this multi-wavelength study, we conclude that our observations of pre-eruption coronal activities described above support the breakout model of solar eruptions (Antiochos et al. 1999; Karpen et al. 2012).

2. The onset of prominence activation (i.e., slow rising phase) is accompanied by gradual increase of thermal X-ray and EUV emissions. The gradual rise of thermal emission corresponds to precursor phase of the flare and suggests a more intense plasma preheating . This could be attributed to the slow reconnection. The X-ray loop source continued to exhibit downward altitude shift until this phase. These observations reveal that the prominence destabilization is a multi-step process.

3. After dynamical activities in corona during which the prominence remained static and its subsequent slow activation, the prominence erupted resulting the impulsive emission of M1.8 flare. The onset of violent eruption of the prominence indicates a catastrophic loss of equilibrium. Here we present a remarkable observation in which a plasmoid ejection immediately chased the erupting prominence. During this phase, the X-ray loop source (which exhibited downward motion in the two earlier phases), changed its direction of motion and started moving upward, in consort with the magnetic reconnection scenario in the standard flare model. In view of these observations, we propose that the impulsive phase represents fast magnetic reconnection in long vertical current sheet that probably lie between the plasmoid (in higher corona) and X-ray coronal source (in lower corona). We further argue that the temporal, spatial and kinematic correlations between erupting prominence and plasmoid imply that the magnetic reconnection supported the fast ejection of prominence in the lower corona (e.g., Temmer et al. 2008, 2010).

3.4 Concluding remarks

The detailed study of eruption of active region prominences on 2004 August 18 (event I) and 2012 August 18 (event II) provides us valuable insights about the processes pertaining to quasi-stationary, slowly evolving, and eruptive phases of prominences. Both events are associated with active regions that were close to the solar limb but within the solar disk. The locations of prominences makes it possible to examine their height variations even during their slow evolution. These events were carefully selected in view of their extended coverage from RHESSI as we wanted to probe the association of X-ray emissions at thermal and non-thermal energies with the pre-eruption stages of the prominence evolution. Due to superior sensitivity of RHESSI detectors, it was possible to investigate temporal, spatial, and spectral properties of weak X-ray emission which originated from localized regions in the vicinity of prominence while it exhibited slow kinematic evolution.

The multi-wavelength studies presented in this chapter reveal that active region prominences undergo an extended quasi-static, slowly evolving phase before the onset of more dynamic activation phase. During this interval, multiple pre-flare activity was observed which were accompanied with brief yet significant episodes of HXR emission. The observations at EUV channels suggest localized brightening which are frequently co-spatial with X-ray sources. Further, the measurements of temperature (T) and emission measure (EM) suggest EUV brightenings to represent intense heating within the confined volume. Therefore, we recognize slow rise and intense heating of segments of prominences as an important precursor of its subsequent eruption. An important highlight of the study of event I is the small yet clear pre-flare X-ray emission that follows power-law function, suggesting the acceleration of electrons that are likely caused by the magnetic reconnection. In event I, the pre-eruption activities occurred at the level of quasi-static prominence or near its apex. On the other hand, event II displayed spectacular pre-eruption activities, mostly well above the prominence, in the form of coronal brightenings and jet phenomena. Understanding the spatial distribution of pre-eruption activities is of immense importance to understand the triggering mechanism of solar eruptions. We have compared, our observations of pre-eruption activities with the representative models of solar eruptions.

The eruption of prominences is associated with major flares. In particular, during event I, we noted striking HXR coronal source at 50–100 keV energy band that was formed while the prominence was getting detached from the solar source region, thus, marking the CME onset. During event II, we observed a plasmoid eruption at hot EUV channels during the early phase of prominence ejection which eventually evolved into the CME. These observations suggest that magnetic reconnection likely support the fast eruption of prominence in the lower corona.

Chapter 4

Confined flare in AR 11302 and associated magnetic transients

4.1 Introduction

Large database of solar flares acquired from the space borne soft X-ray imagers over the last few decades reveal that flares can broadly be classified in two morphologically distinct classes: confined and eruptive flares (section 1.1.1). The confined flares show brightening within a compact loop structure that lasts only for shorter duration (e.g., on the order of few minutes). They are usually modeled in terms of energy release within a single static magnetic loop and, therefore, also referred to as single loop or compact flares. The second category comprises the long-duration events (LDEs) in SXRs (e.g., tens of minutes to up to hours) that are eruptive in nature. Motions of large chromospheric flare ribbons and the formation of post flare loop arcades during LDE flares essentially reveal large-scale restructuring of coronal loops. After the advent of coronal mass ejection (CME) observations, it has been recognized that LDE flares are strongly associated with CMEs while confined flares lack CMEs. It is worth emphasizing that the temporal evolution of CME and flare signatures in eruptive events suggests

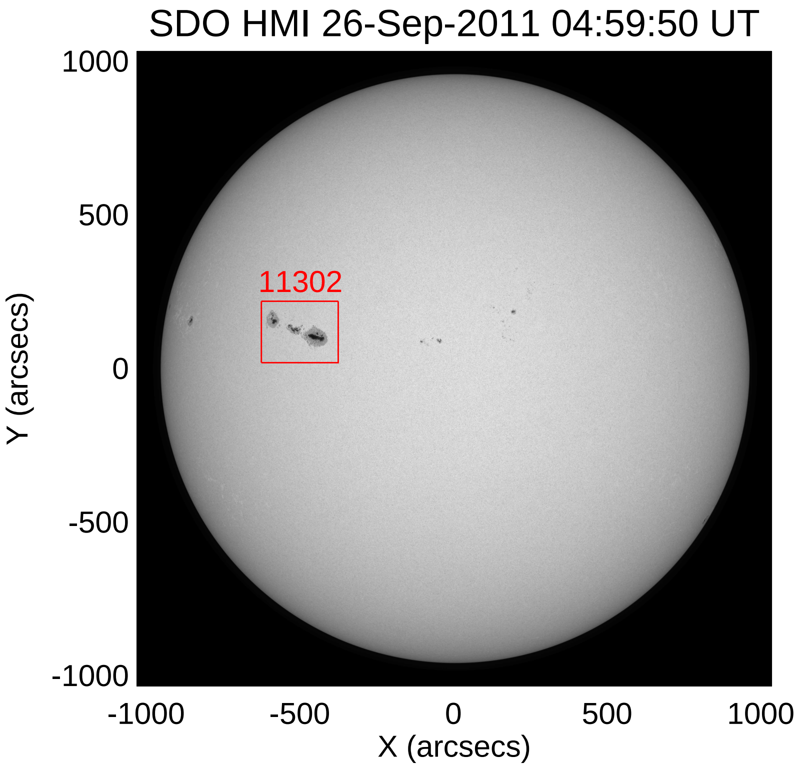

Figure 4.1: White light image of the full Sun taken by HMI/SDO on the day of event reported in this chapter. The active region 11302 is enclosed in a rectangular box.

that both phenomena have a strongly coupled relationship but not a cause-effect one (Zhang et al. 2001; Temmer et al. 2010). In fact there are instances where highly energetic X-class flares occur without associated CMEs (Wang and Zhang 2007; Thalmann et al. 2015).

It has been commonly observed that solar flares occur in closed magnetic field configurations associated with active regions. It is very likely that such closed magnetic structures will encompass one or more magnetic neutral lines in the photospheric magnetic flux. In a simplistic model, one can think of a bipolar magnetic configuration in terms of an inner region, called the core fields, and the outer region, called the envelop or overlying fields (Moore et al. 2001). The core fields are rooted close to the neutral line while the envelop fields are rooted away from it. Usually the core fields are strongly non-potential during pre-flare phase. The initial energy release occurs in the core region while the overlying fields act as a constraining force to prevent the eruption of core fields (see Wang and Zhang

2007).

The basic magnetic configuration during a flare is revealed by magnetic loops which can be quite complex in some cases. Observations also indicate that in some cases magnetic reconnection takes place between pre-existing loops and newly emerging flux (Hanaoka 1997). The multi-wavelength investigations of the evolution of coronal loops and changes in their connectivities during a flare provide important constraints on the role of magnetic reconnection during the restructuring of the magnetic configuration (Hanaoka 1996; Kundu et al. 2001; Sui et al. 2006b; Su et al. 2013). Understanding the physical conditions of the core region of a flare's magnetic environment can provide special insights into the underlying mechanism for impulsive energy release (Chandra et al. 2009).

Flare research has been dominated by the study of eruptive flares because of their large-scale structure and long duration. On the other hand, it is rather challenging to investigate the energy release processes in confined flares due to their rapid evolution in a compact region that imposes severe observational constraints. Now with the availability of solar observations from SDO and RHESSI having unprecedented observational capabilities in temporal, spatial, and spectral domains, it would be quite promising to perform an in-depth analysis of energetic confined flares despite their compact and abrupt nature.

From decades-long observations, it have been established that the fast evolution of an active region is associated with the occurrence of flares/CMEs (for a review, see van Driel-Gesztelyi and Culhane 2009). The emergence of new flux through the photosphere plays a crucial role in the rapid evolution of an active region. During the majority of large flares, significant changes in photospheric magnetic fields have been observed to occur at flaring site within 10 minutes of flare onset (Sudol and Harvey 2005). Wang et al. (2002) reported very striking evidence for changes in photospheric magnetic fields before the flare onset in the form of rapid disappearance of a small sunspot at the flaring site. It has also been reported by Kusano et al. (2012) that the evolution of small-scale magnetic

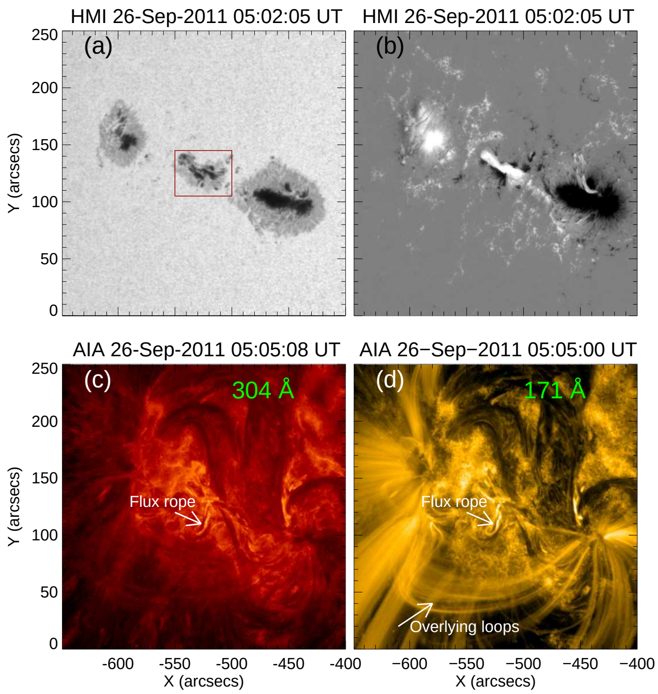

Figure 4.2: Multi-wavelength view of the active region NOAA 11302 on 2011 September 26. Panel (a): HMI white light picture of the active region presenting its elongated shape with three well-developed sunspot groups. The M4.0 flare is associated with the central sunspot group shown by a rectangular box. Panel (b): HMI magnetogram of the active region showing that the leading and following sunspot groups have negative and positive polarity magnetic flux, respectively. However, in between these two sunspot groups a small sunspot group has a complex mix polarity. Panel (c): AIA 304 Å image of NOAA 11302 just before the flare onset. A small flux rope is noted at the source region and is indicated by an arrow. Panel (d): AIA 171 Å image clearly shows that the source region was fully enveloped the overlying loop system that is marked by another arrow.

patches can disturb the coronal magnetic field through reconnection and produce a large-scale flare. Now with the availability of high time cadence longitudinal magnetograms from HMI on board SDO, it has became possible to precisely examine such magnetic field changes before and during flares.

In this chapter, we perform a detailed multi-wavelength study of a confined M4.0 flare that occurred on 2011 September 26. This flare was observed by SDO, RHESSI and NoRH. Although the event was short-lived and confined, it produced intense non-thermal emission in the hard X-ray (HXR) at energies up to 200 keV. The photospheric line of sight (LOS) magnetic field measurements reveal significant changes in the magnetic structure of the activity site before and during the event. In section 4.2, we analyze multi-wavelength data which essentially emphasize the link between various flare-associated phenomena from pre- to post- flare stages in different layers of the solar atmosphere. We provide a detailed analysis of magnetic flux evolution through the active region and flare associated magnetic transients in section 4.3. The discussion and conclusions are presented in section 4.4.

4.2 Multi-wavelength analysis of flare emission

4.2.1 Event overview

According to the solar region summary reports compiled by the Space Weather Prediction Center[1], an unnumbered active region was encroaching over the eastern limb on 2011 September 21 with an uncertain magnetic configuration. It was designated as NOAA 11302 with $\beta\gamma$ magnetic configuration on 2011 September 23. The active region developed from $\beta\gamma$ to a complex $\beta\gamma\delta$ configuration during September 25–26. NOAA 11302 was indeed a highly flare-productive active region which produced 2 X-class and 14 M-class flares within a week (i.e., during the period 2011 September 22–28). An impulsive M4.0 flare occurred between 05:06 UT and 05:14 UT on 2011 September 26 (see Figure 4.3) in NOAA 11302 when the average position of active region on solar disk was N13E34. The location of this active region on the solar disk is illustrated in Figure 4.1.

The multi-wavelength view of the active region NOAA 11302 is shown in Figure 4.2. The active region was comprised of three well-developed sunspot groups, as appeared in the HMI continuum image (see Figure 4.2(a)). The flaring site is enclosed by a rectangular box. The HMI magnetogram reveals that the leading

[1] $http://www.swpc.noaa.gov$

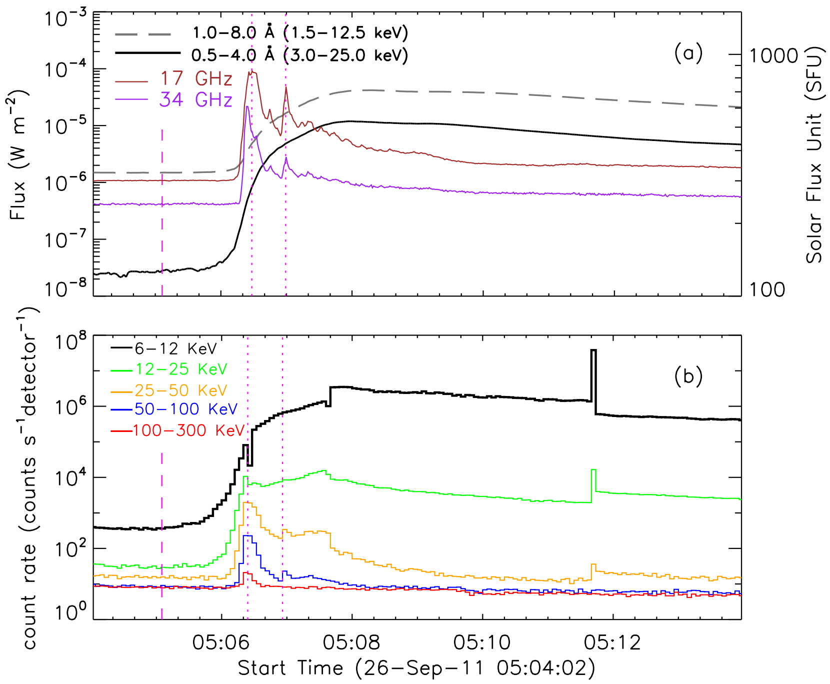

Figure 4.3: GOES soft X-ray flux profile, overlaid by NoRH microwave fluxes (top panel) and RHESSI X-ray light curves (bottom panel) of an M4.0 class flare on 2011 September 26. In order to present RHESSI light curves with clarity in different energy bands, count rates are scaled by factors of 1, 1/2, 1/5, 1/10, and 1/40 for the energy bands 6–12 keV (black), 12–25 keV (green), 25–50 keV (orange), 50–100 keV (blue), and 100–300 keV (red), respectively. The dashed vertical line marks the time at which flux cancellation begins in sub-region S1 (see Figure 4.13 (d)). Another two dotted vertical lines indicate consistent peaks in the HXR and MW light curves. The spikes seen in RHESSI light curves at 05:07:50 UT and 05:11:20 UT correspond to instrumental artifact due to the change in attenuator state.

sunspot group was dominated by strong positive polarity. However, the flare occurred in a mixed polarity region which lies in between the leading and trailing sunspot groups (see Figures 4.2(a) and (b)). Figures 4.2(c) and (d) present images of the active region in the 304 Å and 171 Å channels of AIA, respectively. We note a small flux rope in EUV images at the flare location which is marked by arrows in Figures 4.2(c) and (d). The observations in AIA 171 Å clearly indicate that the flaring site was enveloped by overlying coronal loops which are shown by an arrow (see Figure 4.2(d)).

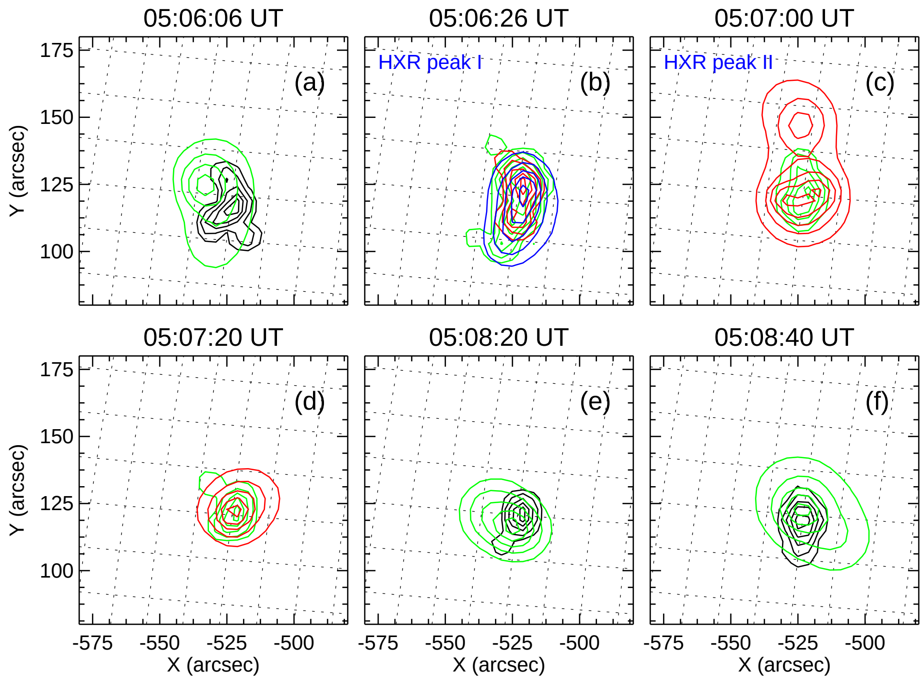

Figure 4.4: Evolution of HXR sources in 12–25 keV (black), 25–50 keV (green), 50–100 keV (red), and 100–200 keV (blue) energy bands. RHESSI images are reconstructed with the PIXON algorithm with an integration time of 20 s (mid-time is mentioned at the top of each panel). The contour levels for the images are set as 15%, 30%, 50%, 70%, and 90% of the peak flux for each image.

4.2.2 X-ray and MW observations

In Figure 4.3, we present X-ray and MW light curves of the flare in different energy bands. Figure 4.3(a) shows GOES X-ray time profiles (in 1–8 Å and 0.5–4 Å energy bands) and NoRH MW light curves (in 17 GHz and 34 GHz frequencies). According to GOES reports, the flare took place between 05:06 UT and 05:14 UT with a peak at ∼05:08 UT. We note that MW emissions at both frequencies (i.e., 17 GHz and 34 GHz) exhibit two distinct peaks at an interval of ∼32 s. The RHESSI light curves in five different energy bands are shown in Figure 4.3(b). The HXR emissions (>25 keV) show a prominent peak at 05:06:24 UT (peak I) which is well consistent with the first (strongest) MW bursts. Furthermore, we note that HXR light curves in 25–50 and 50–100 keV energy bands exhibit

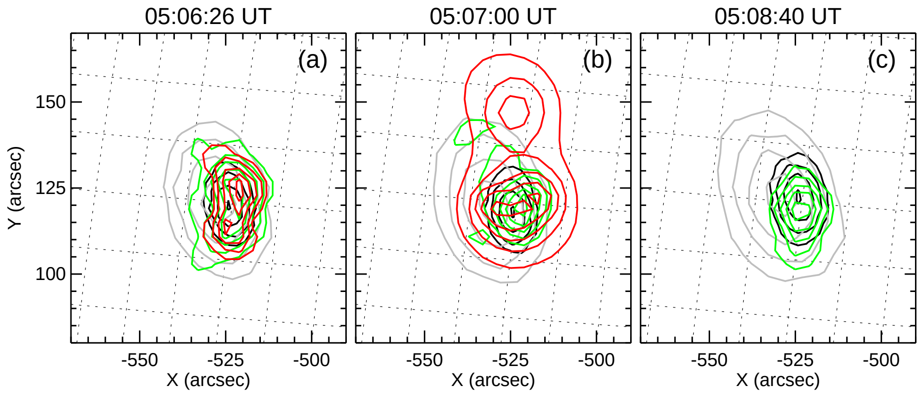

Figure 4.5: Spatial evolution of HXR sources (12–25 keV: green, 50–100 keV: red) with respect to the MW emission (17 GHz: gray, 34 GHz: black). The contour levels for RHESSI PIXON images are 15%, 30%, 50%, 70%, and 90% of peak flux for each image. For NoRH MW images, contour levels are set as 15%, 30%, 50%, and 85% of the peak flux.

a second peak (peak II), again showing consistency with the second MW bursts at 05:06:56 UT. These two consistent peaks in HXR and MW are marked by the dotted vertical lines (see Figure 4.3). On the other hand, the HXR emissions at lower energies (i.e., <25 keV) resemble GOES SXR profiles.

In Figure 4.4, we present a sequence of RHESSI X-ray images which show the spatial evolution of HXR source in different energy bands, viz., 12–25 keV (black), 25–50 keV (green), 50–100 keV (red), and 100–200 keV (blue). The RHESSI images are reconstructed using PIXON algorithm with the natural weighing scheme using front detector segments 3–8 (excluding 7). To reconstruct RHESSI images at high energies (50–100 keV and 100–200 keV), we also include front detector segments 1 and 2 to understand the source structure precisely. The sequence of images reveal that, except during peak II, the HXR sources present a compact morphology. It is important to note that the flare started with very high energy HXR emission (see 100–200 keV source in Figure 4.4(b)) and this epoch is marked as peak I in the HXR and MW light curves. At this time, although the HXR emitting region is very concentrated, we note three emission centroids at high

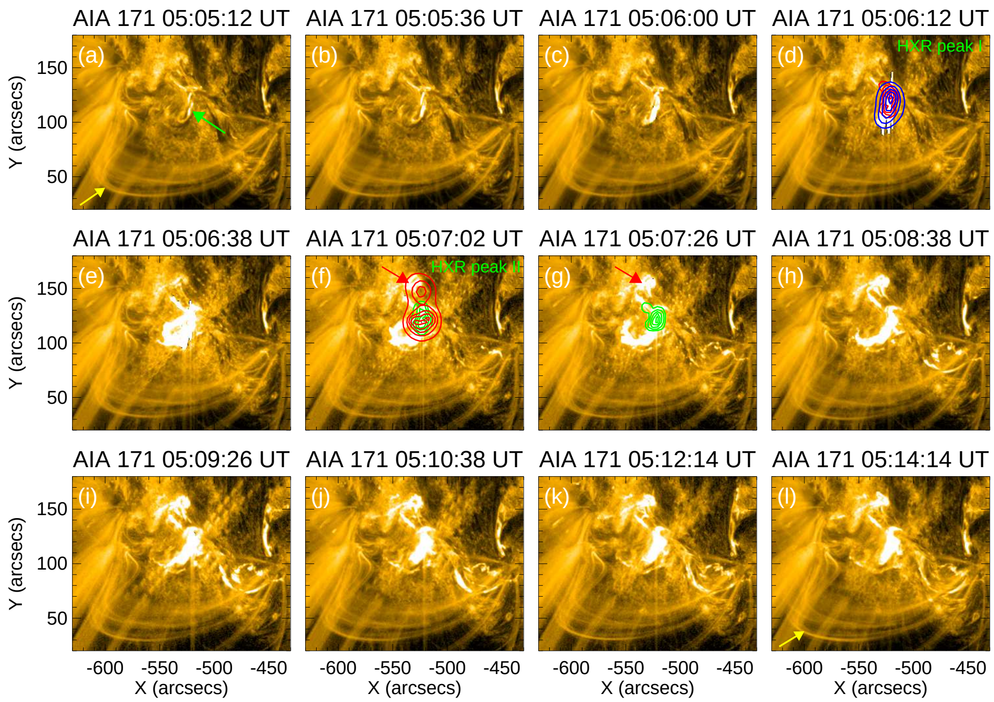

Figure 4.6: Sequence of AIA 171 Å images presenting flare evolution as well as it's magnetic loop environment of the flaring active region. A small J-shaped filament/flux rope is indicated by an arrow (green) in panel (a). Flaring site is fully enveloped by overlying loop systems, which are preserved throughout the event and marked by arrows (yellow) in panels (a) and (l). Red arrows in panels (f) and (g) indicate EUV brightening at a relatively distant location. The RHESSI PIXON images at different energy bands (i.e., 25–50 (green), 50–100 (red) and 100–200 keV (blue) are overplotted on some of the co-temporal 171 Å images. The contour levels for X-ray images are set as 15%, 30%, 50%, 70%, and 90% of peak flux for each image.

energies (>50 keV) within the compact volume (see also Figure 4.5). During the peak II, 50–100 keV HXR source exhibits significant morphological evolution with the appearance of a second HXR source at the northern side of the pre-existing source (Figure 4.4(c)). After peak II, HXR emission up to 50 keV was observed till 05:09 UT (Figures 4.4(e)–(f)).

In Figure 4.5, we plot MW sources at 17 GHz (gray) and 34 GHz (black) over co-temporal HXR images. It is evident that there is a single MW source at both frequencies throughout the flare evolution. We also find that the structure of

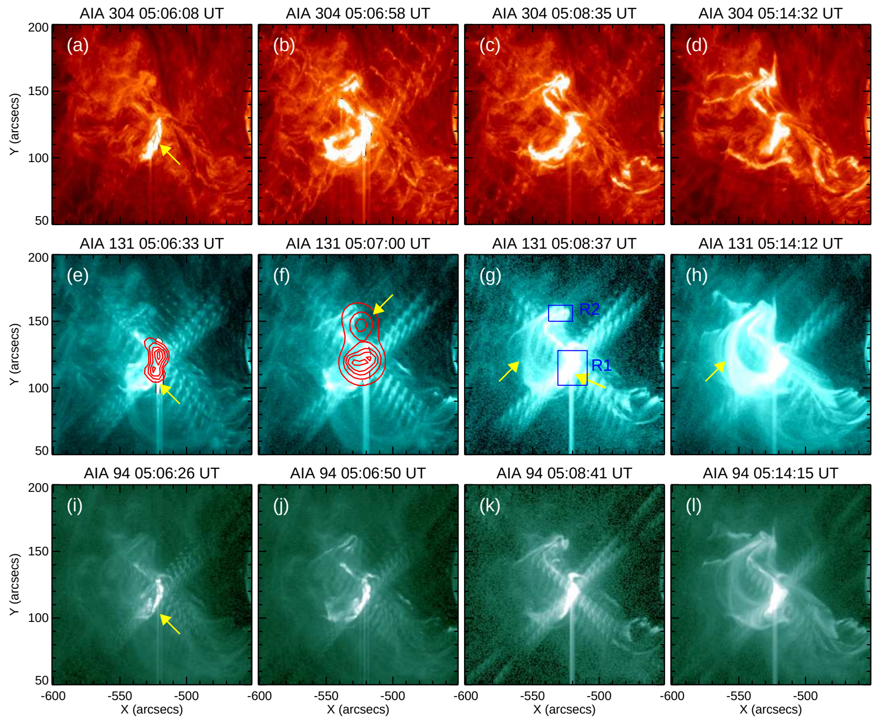

Figure 4.7: Multi-wavelength view of flaring region observed by SDO/AIA and RHESSI. The contours of RHESSI PIXON images at 50–100 keV (red) energy band are overplotted on some of the representative AIA images (panels (e) and (f)). The position of J-shaped flux rope and its underneath early flare brightening are indicated by arrows (panels (a) and (i)). A number of bright regions are seen at later stages (see panels (c) and (d)). A series of AIA 131 and 94 Å images are shown in middle and bottom rows respectively. Hot flaring loop systems are marked by arrows in panels (g) and (h), while their associated two distant footpoint locations are indicated by boxes in panel (g). The contour levels for the X-rays are set as 15%, 30%, 50%, 70% and 90% of peak flux for each image.

34 GHz source resembles more with high energy HXR source (i.e., 50–100 keV) except during peak II when the HXR source displayed emission from an extended region with two emission centroids.

4.2.3 UV, EUV, and Hα observations

We have thoroughly examined AIA observations taken in 171, 304, 131, 94, 1600, and 1700 Å band passes. During the flare activity, AIA takes images with different exposure times ranging from 0.1 to 2.9 s. To compensate for this, each AIA image was normalized to its respective exposure time.

In Figure 4.6, we present a sequence of AIA 171 Å (Fe IX; log(T)=5.7) images showing important stages of the flare evolution starting from pre-flare stages. The emission at this wavelength is originated in quiet corona and upper transition region. The X-ray images in different energy bands, i.e., 25–50 keV (green), 50–100 keV (red), and 100–200 keV (blue) corresponding to peak I, peak II, and decay phase are also overplotted in a few selected panels for a comparison. In the very beginning, we note a small 'J-shaped' absorbing structure (filament) in the low corona, which is marked by a green arrow (Figure 4.6(a)). The flare brightening occurs along this filament which rapidly increases (cf. Figures 4.6(b)–(e)). This early flare location is associated with strong non-thermal HXR emission during the peak I (Figure 4.6(d), see also Figures 4.4(b)). There is a rapid increase in brightness and volume of the flaring region after the peak I. During peak II, we observe intense EUV brightening at a new location (red arrow in Figure 4.6(f) and (g)) which is spatially correlated with the second HXR source (Figures 4.6(f) and 4.4(c)). Following peak II, flare brightening spreads in an extended region and the flare appears like a 'S-shaped' structure (e.g., Figure 4.6(h)). However, we note that there is no signature of the eruption from flaring region in spite of intense thermal and non-thermal emission, and the overlying loop structure remains intact (note constant structure of overlying loops which are marked by arrows (yellow) in Figures 4.6(a) and (l)).

In Figure 4.7, we present a series of images taken at three different EUV channels (i.e., 304, 131 and 94 Å) of AIA. The time sequence of AIA 304 Å (He II; log(T)= 4.7) images provide signatures of the flare evolution in chromosphere and transition region (top row of Figure 4.7). We note a rapid increase in the intensity of the flaring region following peak I, similar to the flare signatures in 171 Å. In the later stages, we observe several ribbon-like brightenings in the extended region (Figures 4.7(c) and (d)). In the middle and bottom rows of Figure 4.7, we present sequence of AIA 131 Å (Fe VIII, XXI; log(T)=5.6, 7.0)

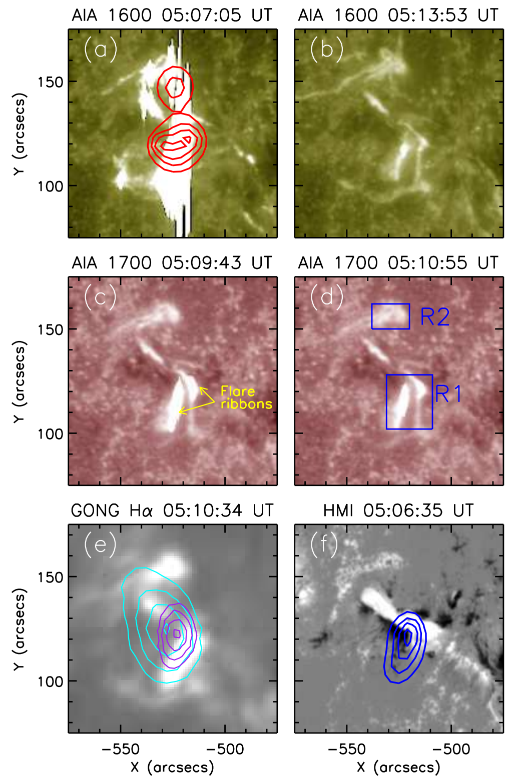

Figure 4.8: Top and middle rows: AIA observations at 1600 Å and 1700 Å channels. Co-temporal X-ray contours in 50–100 keV (red) are overplotted in panel (a). The main flare and remote flare bright locations are enclosed by rectangular boxes R1 and R2, respectively in panel (d). Panel (e): GONG Hα image overlaid by co-temporal NoRH MW contours at 17 GHz (cyan) and 34 GHz (purple). Panel (f): HMI magnetogram of active region overlaid by *RHESSI* HXR (100–200 keV (blue)) source showing the flare location with respect to photospheric magnetic structure.

and AIA 94 Å (Fe XVIII; log(T)=6.8) images showing the transition region and hot flaring corona. The images at these wavelengths provide crucial information on the connectivity of flaring loops and their complex structures. We note an impulsive brightening in short, low lying loops (marked in Figures 4.7(e) and (i) by arrows) which corresponds to peak I. We call this region as the *inner core region*. Following peak II, we observe the formation of a new loop system (marked by arrows in Figures 4.7(g)–(h)) that connects the early flare location (marked as R1; cf. Figure 4.7(g)) with a relatively remote region (marked as R2; cf. Figure 4.7(g)). This newly formed loop system essentially forms an *outer core region*. The magnetic structure of these two regions, i.e., R1 and R2, is further discussed in section 4.3 (see also Figure 4.11). The R1 region continued to show intense emission till the decay phase. The EUV images taken at 94 Å further confirm this scenario (Figures 4.7(i)–(l)).

In Figure 4.8, we present observations taken at 1600 Å (C IV +cont.; log(T)=5.0) and 1700 Å (continuum; log(T)=3.7) channels of AIA (top and middle panels). In the bottom panel of Figure 4.8, we show Hα images during the gradually decaying phase of the flare taken from Global Oscillation Network Group (GONG)[2]. Gong provides Hα images at a spatial resolution of $2''$ ($1''$ pixel^{-1}) and time cadence of 1 min. For a comparison, RHESSI HXR contours are also overplotted in AIA 1600 Å image shown in Figure 4.8(a). The observations at these wavelengths present the flare response at lower atmospheric layers such as temperature minimum photosphere (1700 Å), chromosphere (Hα), and upper photosphere and transition region (1600 Å). In UV images, we can clearly distinguish two well resolved flare ribbons at the location of the HXR source (Figures 4.8(b)–(d)). Like EUV images, UV observations also show emissions from regions R1 and R2 (Figure 4.8(d)). We also find that Hα and UV features match well, although poor spatial resolution of Hα images do not allow us to resolve Hα flare ribbons. In Figure 4.8(e), we plot MW 17 and 34 GHz sources over Hα images. We find that 17 GHz emission seems to be associated with hot flaring loops connecting regions R1 and R2. On the other hand, the 34 GHz source is mainly located within R1 region. In Figure 4.8(f), we present an HMI magnetogram of active region NOAA 11302 overlaid by RHESSI HXR (100–200 keV) source showing the flare location with respect to photospheric magnetic structure.

4.2.4 RHESSI X-ray Spectroscopy

In order to understand the heating of flaring plasma and non-thermal characteristics of accelerated electrons, we have studied the evolution of RHESSI X-ray spectra during the flare. For this analysis we first generated a RHESSI spectrogram with an energy binning of 1/3 keV from 6–15 keV, 1 keV from 15–100 keV and 3 keV from 100–200 keV energies. We only used the front segments of the detectors, and excluded detectors 2 and 7 (which have lower energy resolution

[2]http://gong.nso.edu/info/

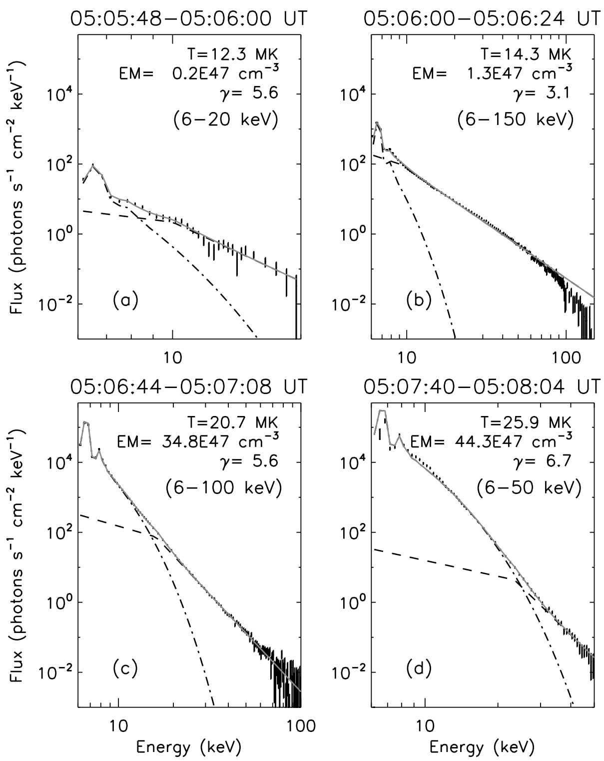

Figure 4.9: RHESSI X-ray spectra derived during the various stages of flare evolution. The spectra were fitted with an isothermal model (dash–dotted line) and a broken power law with a turnover at low energies (dashed line). The gray (solid) line indicates the sum of the two components. Each spectrum is accumulated over 24 s (except panel (a)) using all RHESSI front detector segments except 2 and 7 and the fitting energy range is indicated in each panel. For the spectra shown in panel (a), we have chosen 12 s integration time because prior to 05:05:48 UT, the non-thermal HXR emission was insignificant (cf. Figure 4.3).

and high threshold energies, respectively). The spectra were deconvolved with the full detector response matrix (i.e., off-diagonal elements were included; Smith et al. 2002).

In Figure 4.9, we illustrate spatially integrated, background subtracted RHESSI spectra for three selected intervals. Spectral fits were obtained using a forward-fitting method implemented in the OSPEX code. Since the flare exhibited very fast spectral evolution, the energy range for spectral fittings has been carefully selected for different intervals depending upon the flare and background counts.

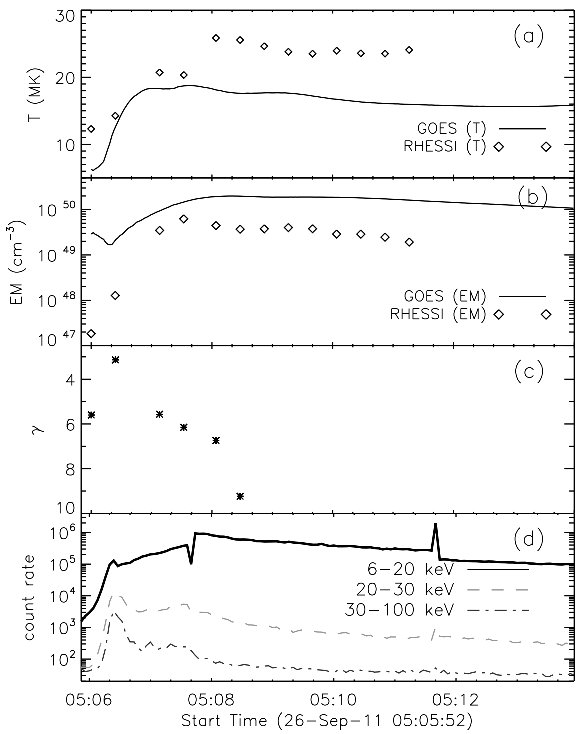

Figure 4.10: Temporal evolution of various spectroscopic quantities derived from RHESSI X-ray spectral fits of consecutive 24 s integration time. From top to bottom: plasma temperature (T), emission measure (EM), photon spectral index (γ), and RHESSI count rates in the 6–20 keV, 20–30 keV, and 30–100 keV energy bands. For comparison, we have also shown variations in T and EM obtained from the GOES satellite over the corresponding panels (a) and (b).

We used the bremsstrahlung and line spectrum of an isothermal plasma and a power-law function with a turnover at low X-ray energies. The negative power-law index below the low-energy turnover was fixed at 1.5. In this manner, there are five free parameters in the model: temperature (T) and emission measure (EM) for the thermal component, and power-law index (γ), normalization of the power law, and low-energy turnover for the non-thermal component. From these fits, we derive the T and EM of the hot flaring plasma as well as γ for the non-thermal component, which are plotted in Figure 4.10. We also provide T and EM estimations from the GOES measurements in Figure 4.10(a) and (b).

The RHESSI spectra indicate a very impulsive rise of HXR non-thermal emission. There was hardly any X-ray flux above background before 05:05:40 UT (see Figure 4.3). As one can clearly recognize, there is weak yet reliable X-ray flux up to 20 keV in the early impulsive phase (see Figure 4.9 (a)). It is noteworthy that although the HXR level is very low at this interval, the HXR spectrum can be well fitted with a power law index γ = 5.6 at energies ∼10 keV indicating early non-thermal characteristics. The spectra exhibit a very impulsive evolution and indicate strong non-thermal emission starting at very low energies ($\gtrsim$ 9 keV) from the next interval onward (Figures 4.9 and 4.10). It is quite evident from Figure 4.9(b) that the HXR spectrum follows a hard power law with a photon spectral index $\gamma = 3.1$ at the first HXR burst. At this time, HXR emission up to ~150 keV was observed above the background level (Figure 4.9 (b)). After the two HXR bursts, the steepness of power law distribution increased and contributions of thermal emission rapidly enhanced up to ~25 keV. The non-thermal HXR emission was not very significant after ~05:10 UT. The temperature profile indicates that the temperature was lowest around the first HXR peak (see Figures 4.10(a) and 4.9(b)). It increases after the HXR impulsive phase and peaked at ~05:08 UT with T ~26 MK. The plots of T and EM show a good consistency. We further note that the temperature calculated from the two GOES channels are lower than RHESSI measurements (e.g., GOES peak temperature is ~18 MK) but both shows similar trends. The differences between GOES and RHESSI estimations are likely caused due to the different sensitivity and response of the two instruments. However, this also points to the fact that the observed plasma is multi-thermal (e.g., Li and Gan 2005).

4.3 Structure and evolution of magnetic fields

4.3.1 Magnetic complexity and flux emergence

The active region NOAA 11302 exhibited a very interesting elongated structure consisting of three distinct sunspot groups and reported event is associated with the central part of the active region having mix magnetic polarities (see Figure 4.2(a) and (b)). In Figure 4.11, we present the time evolution of photospheric magnetic flux derived from SDO/HMI magnetograms through different areas of the active region. We use 3 min averaged data from HMI between 00:30 UT and

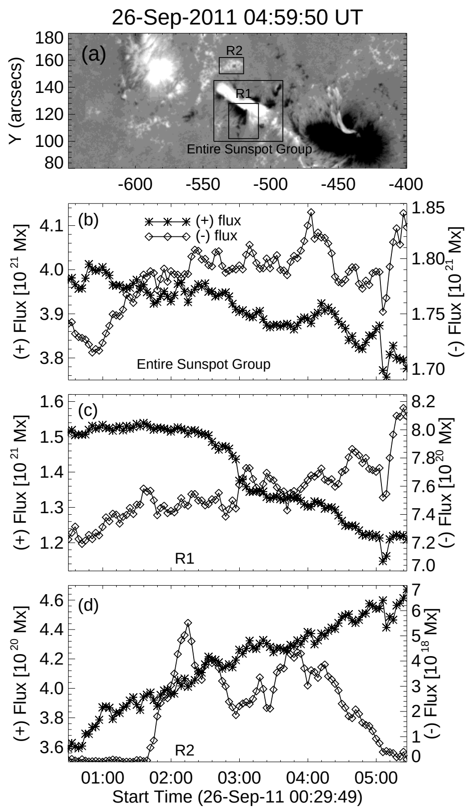

Figure 4.11: Evolution of magnetic flux through different regions associated with the flare site. These regions (i.e., entire sunspot group, R1, R2) are shown in panel (a). The magnetic flux of both positive and negative polarities have been computed through these regions which are plotted in panels (b)–(d).

05:30 UT to estimate the photospheric magnetic flux. In order to correct for the solar differential rotation, we have derotated all the images to a common reference time of 05:30 UT by using the SolarSoftWare routine drot_map.pro. The areas selected for the magnetic flux estimation include the entire sunspot group along with two smaller regions R1 and R2 which are indicated in Figure 4.11(a). We have previously discussed the spatial importance of regions R1 and R2 in (E)UV images (refer to Figures 4.7 and 4.8). The region R1 essentially corresponds to the early flare location which was also associated with the HXR emission during peak I. In our previous description, we have defined this region as the inner core region (see Section 4.2.3). The region R2 corresponds to the footpoint of a large flare loop system that connects the inner core region to a relatively remote location.

From the magnetic flux profile of the entire sunspot group (Figure 4.11(b)), we find that this region is dominated by the positive polarity although the order of magnitudes of positive and negative fluxes are same. The positive flux through

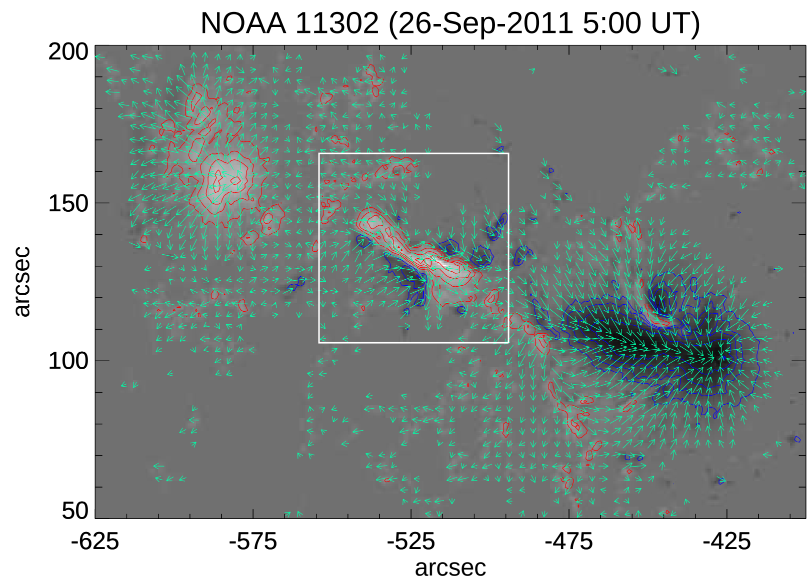

Figure 4.12: Vector map of NOAA AR 11302 obtained from HMI at 05:00 UT on 2011 September 26. Transverse vectors above threshold values are shown as green arrows. Red and blue contours are for positive and negative flux regions with the levels of ± 2000, ± 1500, ±1000 and ±500 Gauss. The box shows the region of interest where the flare took place.

this region was observed to decrease over the period of ∼5 hrs while the negative flux exhibits an increasing trend. In the inner core region (R1), we observe that the negative flux generally increases while the positive flux decreases over the observing period (Figure 4.11(c)). Further, the positive flux exhibits almost constant level till ∼02:30 UT. We find a very interesting variation of magnetic flux through R2 region (Figure 4.11(d)). It is quite important to note that R2 lies in a magnetically dispersed region of predominant positive polarity, away from the central sunspot group (Figure 4.11(a)). In this region, we find a continuous increase of positive magnetic flux. On the other hand, the negative flux profile exhibits irregular patterns in its evolution with relatively fast increase and decrease of the magnetic flux. We further note significant fluctuations in the evolution of negative flux between 2:00 and 2:30 UT. A careful examination of the magnetograms reveal that these fluctuations are caused by the appearance of moving magnetic features. It is important to note that the emergence of positive flux through R2 region and negative flux through R1 region are of similar scales, suggesting that the two regions are magnetically connected. EUV images after the peak II indeed show the existence of bright coronal loops that join the R1 and R2 regions (AIA 131 Å and 94 Å images in Figure 4.7(g), (h) and (l)).

In Figure 4.12, we show a vector magnetogram of the active region NOAA 11302 on 2011 September 26 at 05:00 UT obtained from HMI. The transverse vector fields are indicated by green arrows in the figure. The region associated with the flaring activity is shown inside a white box. The direction of transverse vectors between the negative polarity regions and positive polarity regions indicate that the magnetic field line are highly sheared. To quantify the non-potentiality of the field lines in the activity site, we compute the spatially averaged signed shear angle (SASAA; Tiwari et al. 2009), which represents the average deviation of the observed transverse vectors from that of the potential transverse vectors. Over the region of interest (shown inside the box in Figure 4.12), the SASAA has been estimated as $-\ 8^{\circ}.82$.

4.3.2 Emergence of transient magnetic bipole (TMB)

A careful examination of HMI magnetograms reveals the emergence of a spatially separated bipolar magnetic region within the inner core region which developed about $\sim$1 minute prior to the flare onset (see Figure 4.13). In Figure 4.13(b), we show a running difference image of magnetograms taken at the pre-flare phase. This difference image clearly displays the emergence of a magnetic bipole (shown by arrows). Here it is worth emphasizing that this transient magnetic bipole (TMB) appeared just before the flare onset and cannot be seen in earlier magnetograms (which are taken at a time cadence of 45 s). This implies that the emerging bipolar region evolved rather quickly and was separated, presumably due to a pre-existing highly sheared magnetic structure. We further note that the negative polarity region appears as an intrusion of magnetic flux in a larger region

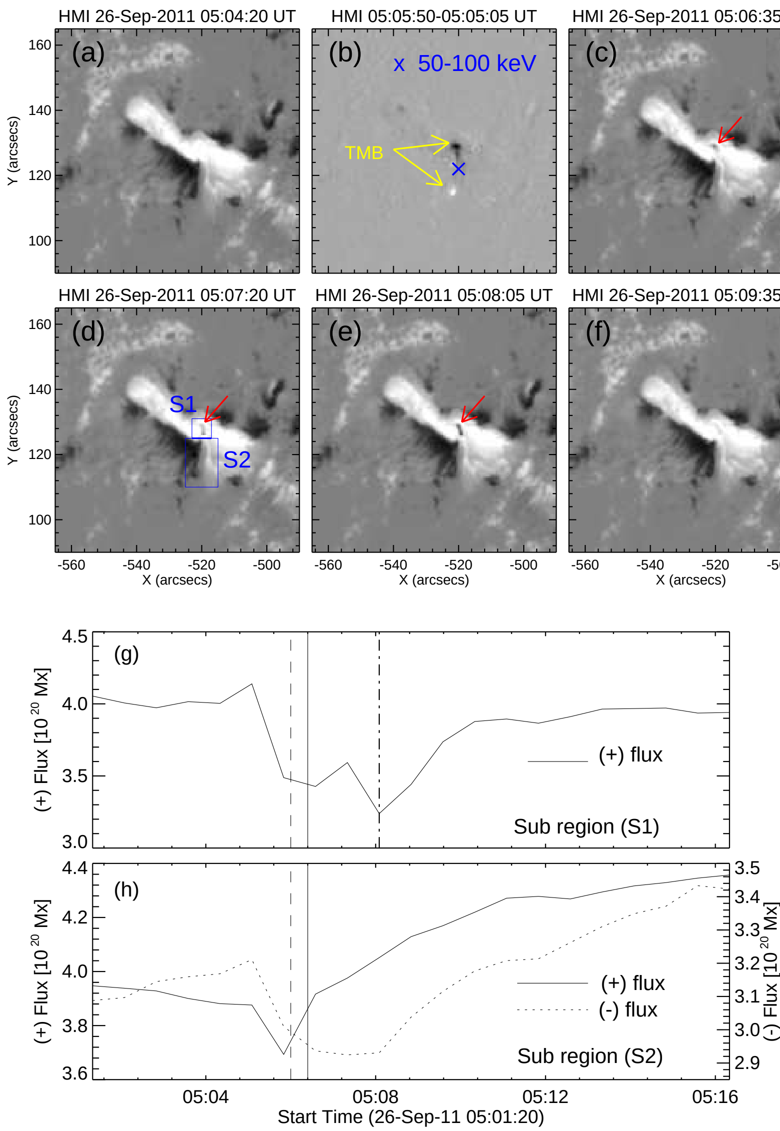

Figure 4.13: Sequence of HMI magnetograms of the flaring sunspot group, showing magnetic field evolution during the event. Panel (b) presents a difference image of two consecutive magnetograms of just before the flare onset time. The emergence of transient magnetic bipole (TMB) is indicated by a V-shaped arrow in panel (b). The "×" symbol marks the centroid of the X-ray source in 50–100 keV (blue). An intrusion of negative polarity flux into the positive polarity region is indicated by red arrow in panels (c)–(e). The two sub-regions of different sizes are selected for the quantitative study of flux evolution which are shown by rectangular boxes in panel (d). In the panels (g) and (h), we plot the flux profiles of sub-regions S1 and S2 respectively. Dashed and solid vertical lines mark the flare onset and peak of the impulsive phase. Dash-dotted line in panel (g) indicates the time when the positive flux cancellation through the sub-region S1 was maximum.

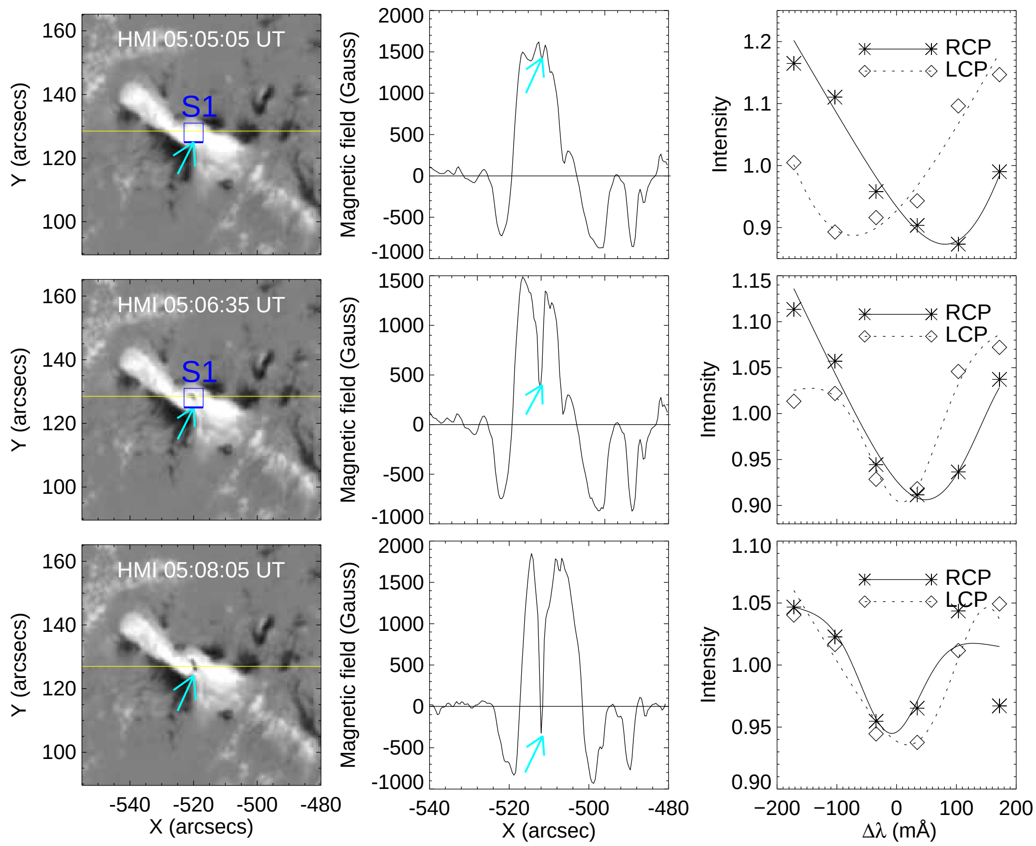

Figure 4.14: Left column: sequence of HMI magnetograms. Middle column: magnetic flux profiles along a horizontal line passing through sub region S1. Right column: HMI six-point spectra in both LCP and RCP components of Fe I line for the respective locations marked by arrows (cyan) in the left column.

dominated by positive polarity (marked by arrows in Figures 4.13(c)–(e)). For a quantitative analysis of the magnetic flux evolution, we have enclosed the negative flux region within a box S1 as shown in Figure 4.13(d). We have measured the positive and negative flux through the sub-region S1 for all the available magnetograms from 05:01 to 05:16 UT observed with a time cadence of 45 s. We find that with the appearance of the intrusion of the negative flux region at 05:05:05 UT, the positive flux through sub-region S1 started to decrease while the maximum cancellation of positive flux occurred at 05:08:05 UT (see Figure 4.13(g)). Here, it is important to note that the negative flux through S1 was nil during this interval except at 05:08:05 UT when the total negative flux through

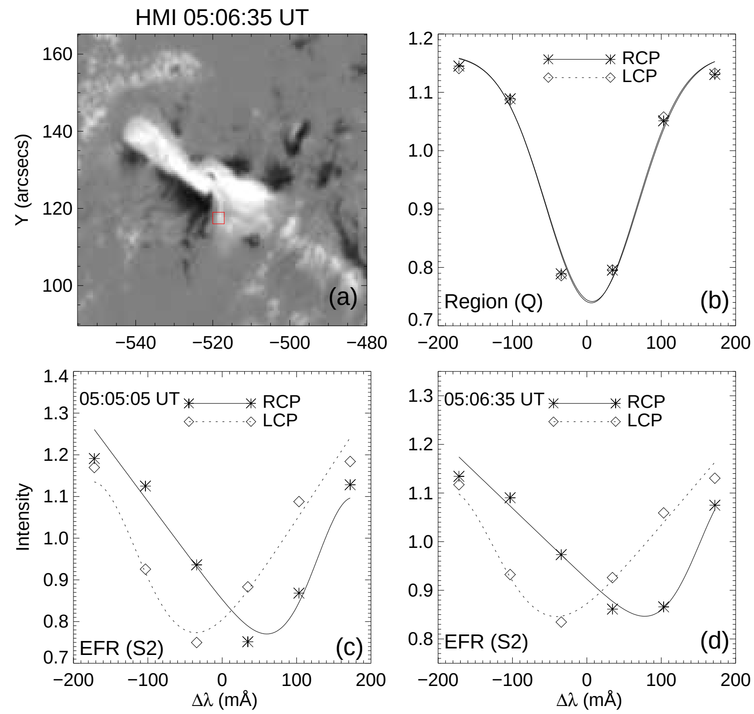

Figure 4.15: Top left: HMI magnetogram of activity site around the peak time of the event. The region selected for the spectral analysis is shown in panel (a) by a small box. Top right: LCP and RCP profiles for a quiet region (nil magnetic field). Bottom left: HMI six-point spectra for (+) EFR at the flare onset time (05:05:05 UT) in both LCP and RCP components. Bottom right: spectral profiles of same region at the peak time of the event (05:06:35 UT). The splitting between the centroid of the LCP and RCP profiles is ∼70 mÅ and the RCP profile shifted toward positive values. At this time the splitting between the centroid of LCP and RCP is ∼90 mÅ.

this region was 1.28×10^{18} Mx. Although the cause of the magnetic transient is unknown, we can speculate that the newly emerged negative flux was initially entirely depleted in canceling the pre-existing strong, large-scale positive flux. We note that the flux started decaying from 05:05:05 UT, i.e., at about 1 minute prior to the impulsive flare emission. The onset of the flux decay with respect to the triggering of flare can clearly be seen in Figure 4.3, where the dashed vertical line marks the time at which flux cancellation begins.

HMI magnetograms clearly indicate that the positive flux region has a relatively extended structure which is shown inside the rectangular box S2 (Figure

4.13(d)). The time profiles of magnetic flux evolution through S2 are plotted in Figure 4.13(h), which clearly indicates an increase in positive flux (and a corresponding decrease in negative flux) during the interval of this confined event. We note that following the flare's onset, the changes in the positive flux are irreversible while negative flux decline till the flare's impulsive phase and increases subsequently. We also find that the main HXR source is localized in between the TMB (Figure 4.13(b)).

4.3.3 Spectral behavior of TMBs

The emergence of TMB prior to the event is a very important phenomenon as it occurs in a localized region over relatively short timescales. Therefore, it is desirable to probe the characteristics of these small-scale magnetic structures more rigorously to provide a plausible interpretation of this phenomena in relation to the flare occurrence.

In Figure 4.14, we investigate the variations of magnetic flux in the negative emerging flux region. In the left column of Figure 4.14, we show a sequence of three representative HMI magnetograms in which a horizontal line is drawn that passes through the negative flux region. The magnetic flux profiles along these horizontal lines are plotted in the middle column of Figure 4.14. A comparison of these magnetic flux profiles clearly indicates a continuous cancellation of positive magnetic flux at the location of the negative polarity transient (the location of the transient is marked by arrows in right and middle columns of Figure 4.14). The plots in the right column of Figure 4.14 show HMI spectral profiles at the location of the magnetic transient. The spectral profiles show the variation of intensity at six wavelengths (±34.4, ±103.3, and ±172.0 mÅ) around the center of Fe I line at 6173.3 Å for left circular polarization (LCP) and right circular polarization (RCP). For reference, line profiles corresponding to a magnetically quiet region are shown in Figure 4.15(b), which obviously illustrate an overlap of LCP and RCP profiles. It is evident that with the cancellation (decrease) of positive flux, the two line profiles (i.e., LCP and RCP) shift systematically toward each other and eventually switch positions with the reversal of magnetic polarity (from the top to bottom panels of Figure 4.14). Similarly, the HMI spectral line profiles corresponding to the region of emerging positive flux region is presented in Figure 4.15.

4.4 Results and discussion

The active region NOAA 11302 had a peculiar elongated structure with three separated sunspot groups which altogether formed a $\beta\gamma\delta$ magnetic configuration. The M4.0 flare is associated with the central sunspot group. From HMI magnetograms, it is quite evident that this central region exhibited mixed distribution of polarities in the photosphere. Table 5.1 presents observational summary of various multi-wavelength phenomena associated with this event.

We note that the present event is an appropriate example of confined flare in that it was a short-lived event that occurred in the low corona and did not lead to a CME (see e.g., Wang and Zhang 2007). The absence of the ejection of any material from the flaring site is further evident from the fact that the overlying large magnetic loops, imaged in AIA 171 Å, remain unaltered following the flare. On the other hand, the flare is accompanied with very high energy HXR emission (up to 200 keV) and at the peak we detected an HXR source at 100–200 keV, evidencing an intense energy release in the form of non-thermal particles. Therefore, the absence of an eruption from such a high energetic flare implies that the core fields were not allowed to escape by the overlying fields despite the intense energy release. Wang and Zhang (2007) have made a systematic study of a set of X-class flares of eruptive and confined categories. Their results suggest that confined events occur closer to the magnetic center, while eruptive events tend to occur close to the edge of active regions. For a flare occurring at the

Table 4.1: Observational summary of activities before and during confined M4.0 flare.

Observation/ Activity	Time	Wavelength	Remarks
Emergence of magnetic flux	From ∼5 hr prior to the flare	Magnetogram	Flux emergence of negative and positive polarities in the inner and outer core regions associated with flare loop configuration respectively
Small J-shaped filament at the flare location	Pre-flare images (<05:06 UT)	EUV (e.g., 304, 171 Å)	Filament is seen as an absorbing feature
Appearance of transient magnetic bipole (TMB)	From pre-flare phase (05:05:05 UT) to end of impulsive phase	Magnetogram	∼1 minute prior to flare onset
Confined M4.0 flare in the vicinity of filament	Impulsive phase started at 05:06:00 UT with peak emission at 05:06:24 UT	HXR, MW and EUV	Two distinct non-thermal peaks at interval of 32 s, evidence for a two-step magnetic reconnection process
Impulsive phase	05:06–05:08 UT	HXR (>25 keV)	HXR emission up to 200 keV energies with $\gamma \sim 3$, mostly a single, compact HXR source except during peak II
Evolution of distinct inner and outer core regions of the flare loop system	05:06–05:10 UT	EUV	Large overlying loops of the active region remain intact

central part of an active region, like the present one, it is more likely that the core field region will have a stronger envelope of overlying fields which may act as a shield for the prevention of eruption (Török et al. 2004; Török and Kliem 2005).

The temporal evolution of HXR and MW emissions provide crucial evidence of the energy release processes. Both RHESSI and NoRH light curves reveal very abrupt rise of flare emission that peaked instantly and simultaneously in both HXR and MW channels. The increase in HXR flux at energies >25 keV is usually identified as the start of the impulsive phase of a flare which is suggestive of the injection of the non-thermal electrons into the flaring loop (see, e.g., Siarkowski et al. 2009; Joshi et al. 2012). In our observations we do not find any precursor or pre-flare enhancements in X-ray profiles before the impulsive phase. We further emphasize that the GOES low-energy channels also indicate an increase in X-ray flux with the beginning of the HXR impulsive phase. The rapid temporal evolution of X-ray and MW flux along with strong non-thermal characteristics of X-ray spectra ($\gamma \sim$3) indicate that this event is an "early impulsive flare" (Sui et al. 2006b). We further stress that at the peak of the impulsive phase the transition from thermal to non-thermal emissions took place at a very low energy (~9 keV) while the spectrum extended up to 150 keV. The lack of precursor phase (Joshi et al. 2011) clearly implies the absence of significant plasma pre-heating before strong particle acceleration. Due to the confined nature (i.e., non-eruptiveness) of this highly impulsive event, we interpret that the early non-thermal HXR and MW bursts are the consequence of abrupt energy release via spontaneous magnetic reconnection (see, e.g., Lee et al. 2003).

The impulsive phase lasted for <1 minute. It is important to note that, within this short phase, the HXR and MW time profiles displayed dual peaks at a separation of ~32 s. It should be noted that these two peaks differ in terms of spectral properties of the HXR emission as well as the morphology of the HXR source structure. (1) The thermal emission rapidly built up after the first HXR peak while non-thermal contribution significantly decreased (e.g., turnover from thermal to non-thermal energies increased from ∼9 keV to ∼15 keV). (2) At the first peak, the HXR emitting region was highly concentrated with multiple centroids and was observed up to 100–200 keV energies while the second HXR peak was relatively less energetic and a new 50–100 keV HXR source originated for a very brief interval that was well separated from the pre-existing HXR source location. These observations lead us to believe that the dual-peaked structure of the impulsive phase corresponds to the distinct events of electron acceleration in the corona (Grigis and Benz 2004; Kundu et al. 2009; Li and Gan 2005) as a result of a two-step magnetic reconnection process.

The combined multi-wavelength view of the flare imaged by SDO/AIA in several EUV and UV wavelengths provides a clear scenario of coronal energy release and its response at lower atmospheric layers. The observations taken in all the EUV channels reveal that the flare was initiated with a sudden brightening at a very localized region above/around a small filament. The co-spatiality of this localized EUV region (defined as *inner core region* in the previous section) with the high-energy HXR source (e.g., 100–200 keV) provide evidence for the strong particle acceleration at this location. It is worth mentioning that the HXR emission from the inner core region is highly concentrated and lasted until the decay phase of the flare. We further note that the HXR sources at lower, intermediate, and higher energies are nearly co-spatial and do not indicate significant spatial evolution. In the standard flare model, HXR emission is believed to originate from distinct locations of flaring loops, viz., footpoint and looptop regions (Krucker et al. 2008). In general, HXR emissions at lower energies originated from the coronal region while the high-energy part is associated from denser chromospheric layers where footpoints of the loops are anchored (see, e.g., Joshi et al. 2009, 2007). In our case, the overlapping of high- and low- energy sources possibly indicates that looptop and footpoint sources of a flaring loop are too close to each other to be resolved, i.e., at least one of the loops involved in the magnetic reconnection is a very short low-lying loop. This is further confirmed by UV images taken at 1600 and 1700 Å which show very closely situated flare ribbons formed following the initiation of magnetic reconnection. Closely separated flare ribbons would imply formation of short, simplified loops after the primary energy release. It is likely that due to small separation, conjugate HXR sources corresponding to the two ribbons are not distinguishable.

Peak II of the impulsive phase is associated with EUV brightening in a relatively remote location besides continuous emission from the inner core region. It is important to note the high-energy HXR emission (50–100 keV source) that originated from this remote flare location for a very brief interval. More importantly, we observed high-temperature EUV loops (e.g., 131 Å and 94 Å images) that connect this new source with the inner core region. The configuration and evolution of new loops form an *outer core region* which showed intense thermal emission after the impulsive phase. The formation of new loop system suggests a second stage of magnetic reconnection during which short loops in the inner core region interacted with larger coronal loops at relatively higher altitudes. Thus the sequential brightening of inner and outer regions of coronal field lines in the core region provide evidence for flare models involving the interaction of coronal loops (see e.g., Hanaoka 1996, 1997; Kundu et al. 2001). Although it is difficult to reconstruct the geometry of the loops for this event, the configuration of newly developed loop with respect to the inner core region suggests that the two interacting loop systems probably shared a common footpoint. Hanaoka (1997) proposed that in such a double-loop configuration, a flare can be caused by the interaction between an emerging loop and an overlying loop.

A crucial aspect of this study lies in exploring the phenomenon of flux emergence both at large and relatively smaller spatial and temporal scales. Large-scale changes in photospheric magnetic flux were observed from $\sim$5 hr prior to the flare. A continuous increase of negative flux was detected at the main flare location (R1; see Figure 4.11), while positive flux emergence occurred at a relatively remote location (R2; cf. Figure 4.11). Moreover, EUV observations clearly show the formation of a loop system that joins the R1 and R2 regions which provide clear evidence that the two regions are magnetically connected. The analysis of HMI vector magnetograms clearly reveal highly sheared magnetic structures in pre-flare phases with SASSA as $8^{\circ}.8$. It is likely that the continuous flux emergence would increase the shearing of field lines. Earlier studies have shown that SASSA $\gtrsim 8^{\circ}$ indicates that the active region is capable of driving major flares of M and X categories (Tiwari et al. 2010). The flux emergence along with enhanced magnetic shear is believed to be the fundamental process associated with the supply of magnetic free energy into the corona in the pre-flare stages (Wang et al. 2004; Zheng et al. 2012).

The emergence of a pair of magnetic transients of opposite polarity (called TMB in preceding sections) within the inner core region has important physical implications for recognizing the processes that lead to the destabilization of the magnetic structure and thereby causing the flare initiation. The role of small magnetic structures toward the flare triggering processes has been addressed in simulations in a recent study by (Kusano et al. 2012). Since TMB reported here appear about 1 minute prior to the flare onset, relating this feature with the flare triggering mechanism is justified. We stress that out of two magnetic transients, the negative polarity transients is highly distinctive due to its location and morphology (note the S1 region shown in HMI magnetograms in Figure 4.13). A patch of negative polarity intruded in a larger region of positive flux and exhibited a compact structure that remained stationary. In a recent study, Harker and Pevtsov (2013) reported a very similar magnetic feature which indicates small-scale changes in the magnetic field structure.

The HMI spectra of the TMB clearly indicate the shifting of LCP and RCP profiles in wavelength direction which suggest a systematic dominance of corresponding magnetic polarities from the pre-flare phase (Figures 4.14 and 4.15). Further the spectral profiles do not indicate any flare-induced anomaly, such as sudden deviation of the spectral line from absorption to emission (Maurya et al. 2012; Qiu and Gary 2003). These observations coupled with the fact that magnetic transients developed before the flare and located away from the HXR flare kernels provide evidence that these magnetic transients represent a real change in the magnetic field structure preceding the flare.

4.5 Summary and conclusions

In the literature of solar flares, there are limited works on multi-wavelength evolution of confined flares. Further, unlike eruptive flares, where large-scale reconnection is driven by flux ropes or filament eruptions, we do not have clear idea about triggering of reconnection in confined flares. Now thanks to high cadence E(UV) imaging from AIA/SDO and X-ray measurements from RHESSI, we are in a situation of providing concrete details of energy release in confined flares.

The confined M4.0 flare on 2011 September 26 analyzed in this chapter occurred at the core of active region NOAA 11302. From this case study, we infer some important conclusions about the evolution of flare loops and thermal/non-thermal emissions that should be compared with similar events in future studies. The flare light curves exhibit an abrupt rise of non-thermal emission with co-temporal HXR and MW bursts that peaked instantly without any precursor emission. This stage was associated with HXR emission up to 200 keV that followed a power law with photon spectral index (γ) $\sim$3. Another non-thermal peak, observed 32 s later, was more pronounced in the MW flux than the HXR profiles. Dual peaked structures in the MW and HXR light curves suggest a two-step magnetic reconnection process. EUV images exhibit a sequential evolution of the inner and outer core regions of magnetic loop systems while the overlying loop configuration remained unaltered. Combined observations in HXR, (E)UV, and Hα provide support for flare models involving the interaction of coronal loops.

A novelty of this analysis lies in the identification and assessment of magnetic transients that developed just prior to the flare onset. The spectral, temporal, and spatial properties of these magnetic transients reveal that these small-scale magnetic structures are real and physically linked with the impulsive flare onset that does not show any precursor emission. We therefore, suggests that the small-scale changes in the magnetic structure play a crucial role in the flare triggering process by disturbing the pre-existing sheared magnetic configuration. The interpretation of such magnetic transients developing prior to the flare onset is ambiguous, i.e., we cannot yet determine whether these features are associated with the real emergence of magnetic flux or structural changes in the magnetic configuration. Since magnetic transients reported here developed simultaneously as a pair of opposite polarity patches and the corresponding regions exhibit variations in the magnetic flux from the pre-flare to the end of impulsive phase, we cannot rule out the possibility that these magnetic transients resulted from the impulsive emergence of magnetic flux through the photosphere. To our knowledge, such rapidly evolving bipolar magnetic structures prior to the flare has been reported for the first time. For a better understanding of the role of small-scale magnetic structures toward the flare initiation process, a comprehensive survey of existing and upcoming high resolution solar data is required. In the future, we plan to probe the characteristics of magnetic transients in detail.

Chapter 5

Dynamical evolution of coronal loops and energy release during a confined flux rope eruption in AR 10646

5.1 Introduction

In the standard flare model (see Section 1.2.3), the initial driver of the flare process is a rising prominence (also called filament when viewed on the solar disk) formed in the chromosphere along the magnetic polarity inversion line (PIL) of solar active regions. In the early stages of a large eruptive flare, the core fields (i.e., the inner flux system rooted close to PIL) containing the prominence erupt which would result in the stretching of the envelope fields. With the evolution of the eruption process, the stretched field lines reclose via magnetic reconnection beneath the erupting filament (Lin et al. 2003). The extensive solar observations over the last decades, mainly from space borne telescopes, have revealed several important features of the multi-wavelength flare that have further strengthened the standard flare model and provided concrete observational inputs to understand the role of magnetic reconnection toward plasma heating and particle acceleration. These features include: occurrence of hard X-ray (HXR) footpoint (FP) and looptop (LT) sources, formation of Hα flare ribbons at the opposite polarity regions, rising arcade of the intense soft X-ray (SXR) loops, plasmoid ejections, upward motion of HXR LT source, and increasing separation of Hα flare ribbons along with HXR FP sources (see reviews by Moore and Roumeliotis 1992; Shibata 1999a; Benz 2008; Fletcher et al. 2011; Karlický 2014).

According to the standard flare model, filament activation is a crucial part of the flare process. Observations reveal several categories of the filament activation, viz. full, partial and failed (Gilbert et al. 2007). The full or partial eruptions are followed by flares and CMEs while the failed eruptions characterize those situations when a filament undergoes a successful activation in the beginning but finally fails to erupt from the corona. Full and partial eruption of filaments have been reported in numerous observations (Plunkett et al. 2000; Gilbert et al. 2001; Zhou et al. 2006; Liu et al. 2007; Tripathi et al. 2009). On the other hand, failed eruptions are observed less frequently and therefore form a less studied topic in solar physics. Their study provide an opportunity to investigate the interaction between the erupted plasma and magnetic fields with the overlying coronal loops (see e.g., Rust 2003; Kumar et al. 2011; Mrozek 2011; Netzel et al. 2012). The rate of decrease of overlying magnetic fields with their heights is considered to be a crucial factor that determines whether an erupting prominence will lead to a successful eruption or confine within the overlying coronal region (Török and Kliem 2005). Ji et al. (2003) and Alexander et al. (2006) studied a failed eruption of a filament during which multiple HXR sources were observed from the coronal as well as FP locations. The examination of the locations of coronal HXR sources with respect to the dynamical evolution of the filament is of high interest toward a better understanding of the energy release scenario in solar eruptions.

Sometimes prior to the filament activation and associated flares, small local-

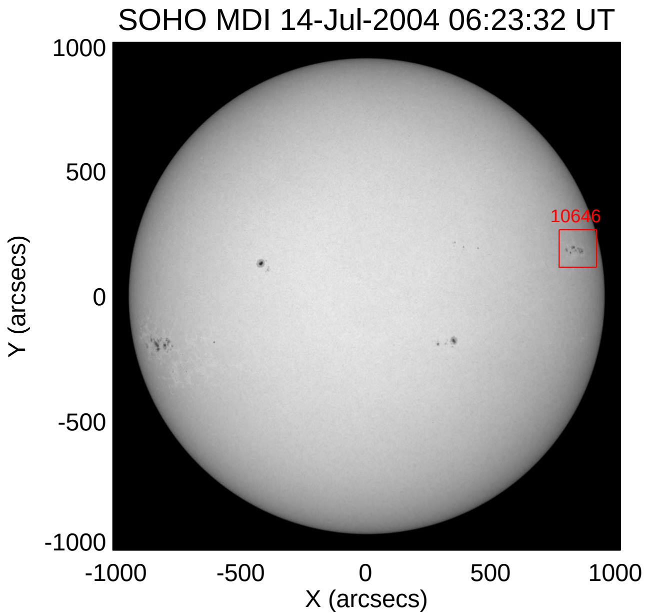

Figure 5.1: White light image of the full Sun taken by MDI/SOHO on the day of event reported in this chapter. The active region 10646 is enclosed within a rectangular box.

ized brightenings are observed to occur in the active region close to the site of the main flare (Kundu et al. 2004; Chifor et al. 2007; Joshi et al. 2013; Zhang et al. 2015). Such localized pre-flare brightenings are frequently observed as enhanced X-ray flux at low energies (e.g., GOES light curves) before the impulsive phase. It has been recognized that filaments undergo slow yet important changes during the pre-flare phase (Chifor et al. 2006, 2007; Joshi et al. 2011, 2013; Awasthi et al. 2014). Some studies also show crucial evidence of non-thermal X-ray emission during the early activation phase of solar eruptions (Fárník et al. 2003; Joshi et al. 2011). These investigations have provided clues to understand the processes occurring in the active region that eventually lead to filament destabilization and thus triggering the impulsive energy release. Therefore, while investigating the pre-flare phase, one should also carefully probe the state of overlying coronal loops besides the core region containing the filament.

In this chapter, we present observations of an M6.2 flare and its associated pre-flare activities observed in active region NOAA 10646 on 2004 July 14 between 04:30 UT and 06:00 UT that are associated with the confined eruption of a

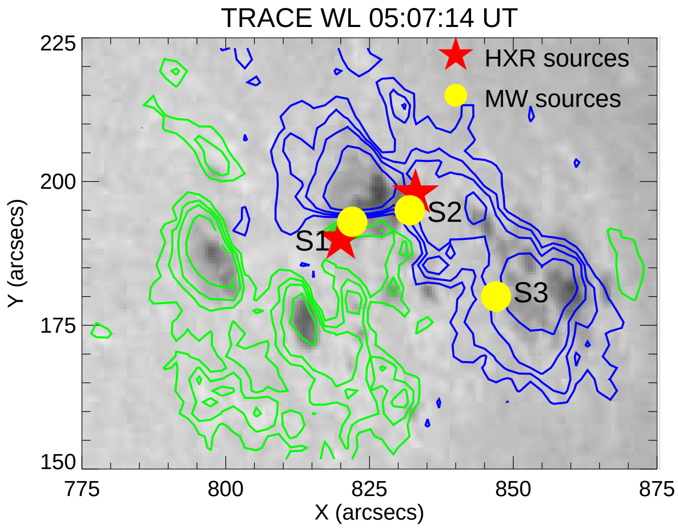

Figure 5.2: TRACE white light (WL) image overlaid by contours of co-temporal magnetogram taken from SOHO/MDI. The contour levels are ±100, ±200, ±300, ±500, ±800, ±1000 and ±1500 Gauss for positive polarity magnetic flux (blue) and negative polarity magnetic flux (green) respectively. The location of HXR and MW sources during the flare are indicated by star (★) and circle (•) respectively. We mark two conjugate emission centroids of HXR and MW sources observed during early impulsive phase of the M6.2 flare (see also Figures 5.9(b) and 5.11(b)) with S1 and S2 respectively. We further indicate a distant MW source by S3 (see also Figure 5.11(d)) which originated during the main impulsive phase (i.e., at 05:21 UT) and prevailed till the end of flare (∼05:30 UT). MW source S3 does not have any HXR counterpart.

filament (SOL2004-07-14). On the whole, this event was remarkable in several aspects. (1) We note significant pre-flare activity which is manifested in the form of large-scale contraction of overlying coronal loops. (2) Accompanying with the large-scale loop contraction, sequential brightening in the core region was observed which can clearly be recognized as three pre-flare events in the GOES X-ray profile. (3) A drastic increase in the speed of contraction is observed just ∼5 minute before the onset of the impulsive phase (i.e., during third pre-flare event). (4) During the impulsive phase, we observe multiple non-thermal peaks. The first stage of the impulsive phase marks the transition from signs of the magnetic implosion scenario (Hudson 2000) to the generally observed expansion of flaring coronal loops and the activation of filament.

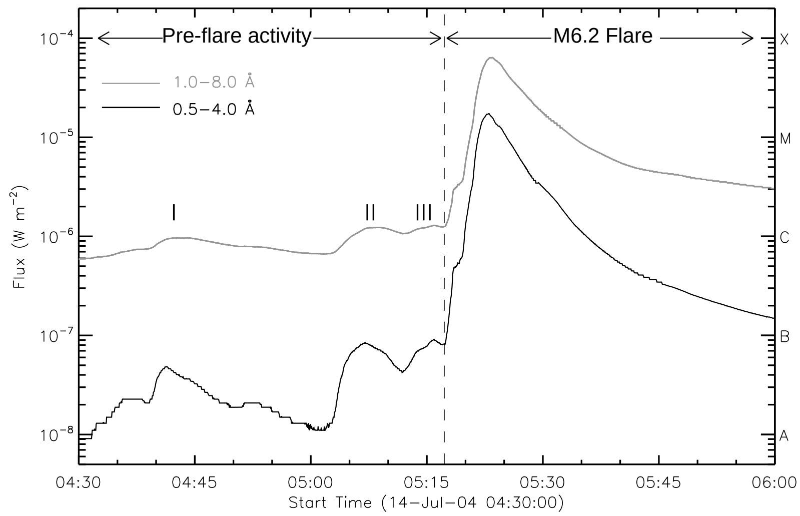

Figure 5.3: GOES soft X-ray flux profiles in 0.5−4 Å and 1−8 Å channels between 04:30 and 06:00 UT. The vertical–dashed line distinguish the pre-flare activity from the main M6.2 flare. The pre-flare phase (04:30 UT–05:17 UT) is characterized by multiple small peaks, which are more pronounced in GOES high energy channel (i.e., in 0.5–4.0 Å) and marked by I, II, and III.

In this work, we have analyzed data from TRACE, RHESSI, and NoRH. We present an overview of the multi-wavelength observations in section 5.2. We provide a detailed multi-wavelength diagnostic of this event in sections 5.3 and 5.4. In section 5.5, we discuss and interpret our observations. The summary and conclusion of the study is given in the final section.

5.2 Event overview: phases of flare evolution

On 2004 July 14, active region NOAA 10646 was situated close to the western limb at heliographic coordinates of N13W64 (see Figure 5.1). In Figure 5.2, we show a TRACE white light (WL) image overlaid by a SOHO/MDI line-of-sight (LOS) magnetic field map of NOAA 10646. We find that the active region consists of a set of sunspot groups with leading and trailing groups having positive and negative magnetic polarities respectively. The active region displayed a rather dispersed structure of sunspots with well separated magnetic polarities.

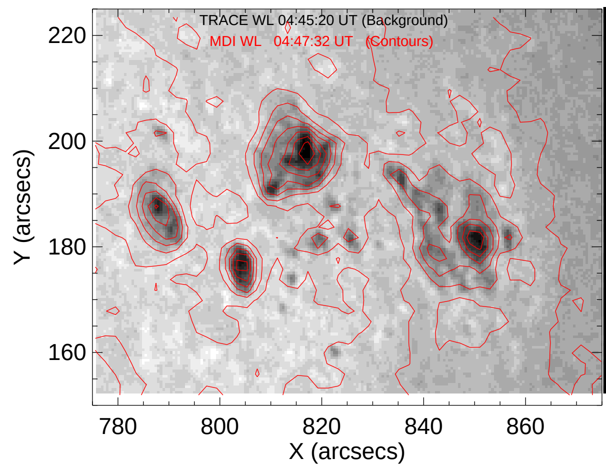

Figure 5.4: Illustration of the alignment of nearly co-temporal TRACE and SOHO/MDI white light images.

The active region NOAA 10646 exhibited a set of very intriguing flaring and eruptive activities between 04:30 UT and 06:00 UT which can be nicely followed in the GOES SXR time profiles shown in Figure 5.3. A major flare of class M6.2 occurred in the active region between 05:17 and 06:00 UT. It is remarkable to observe significant activities in the active region that started several minute before the onset of the M-class flare that continued until the flare's impulsive phase. The GOES light curves (Figure 5.3) clearly recognize these pre-flare activities in the form of multiple small peaks at ∼04:41 UT, ∼05:06 UT and ∼05:16 UT before the onset of the impulsive phase of the flare at ∼05:17 UT. Thereafter, the flare attains its peak at ∼05:23 UT and gradually ends by 06:00 UT. We mark pre-flare GOES peaks as I, II, and III in Figure 5.3. These activities correspond to the localized and discrete brightenings at low-lying loops at the site of the main flare and simultaneous contraction of large overlying coronal loops. The detailed imaging analysis of X-ray and EUV data presented in the next section clearly shows that the pre-flare activity corresponds to phases of episodic energy release at the earliest stages of restructuring of magnetic fields. It is further noteworthy that multiple peaks at pre-flare phases are more pronounced in the high energy GOES channel (i.e., in 0.5–4.0 Å band). Based on GOES and TRACE observations, we consider the following phases of flare evolution (1) pre-flare activity which includes large-scale loop contraction and brightenings in the core region; and (2)

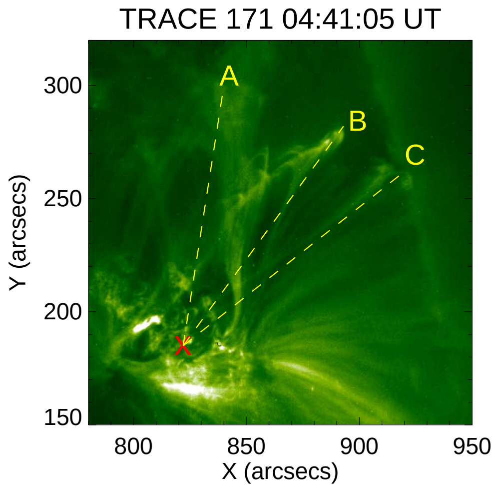

Figure 5.5: TRACE 171 Å image showing a set of coronal loops associated with the active region NOAA 10646. Three system of distinct sets of loops can be recognized and are named as A, B, and C. Their heights from the source region are estimated as ∼92 Mm, 88 Mm, and 93 Mm. Only the loop system 'B' exhibited a large-scale contraction between 04:47 and 05:18 UT.

M6.2 flare, which is accompanied by a failed eruption of a filament. Here we note that although the loop contraction proceeds during the whole pre-flare activity, we describe loop contraction and core region brightenings separately in the next section to provide a clear understanding of these two phenomena. We should note that the contraction was observed in higher overlying coronal loops that are spatially separated from the regions of pre-flare brightenings. It is, however, quite possible that the two phenomena (localized brightenings and contraction of overlying loop system) are physically interconnected.

In Figure 5.2, we further show the locations of a pair of HXR and MW emission centroids observed during the early impulsive phase of M6.2 flare by star (★) and filled circle (●) symbols, respectively. It is apparent that the flare occurred close to the neutral line of photospheric magnetic field. We mark locations of HXR and MW emission centroids as S1 and S2. Following the main impulsive phase, we note another prominent MW source appeared at a distant location, marked as S3 in Figure 5.2, which does not have any HXR counterpart.

Our analysis involves the identification of X-ray and MW source locations during the dynamical evolution of the filament and coronal loops observed by TRACE at EUV channel. For a proper alignment of EUV images with X-ray and MW sources, we need to re-register TRACE images (see section 2.3). Here, we corrected TRACE pointing by a cross-correlation alignment between a TRACE white light (WL) and a SOHO/MDI WL image taken at 04:45:20 UT and 04:47:32 UT respectively using the method described in Gallagher et al. (2002)[1].

5.3 Pre-flare activity

5.3.1 Large-scale contraction of coronal loops

Active region NOAA 10646 was enveloped by a set of large coronal loops with different orientations, which presents a peculiar structure of active region corona (see Figure 5.5). We have estimated the height of three prominent overlying loop systems (which are indicated in Figure 5.5 by A, B, and C) from the source region (shown by "×"). The projected heights of these three systems of loops were estimated as ∼92, 88, and 93 Mm. We found significant activities occurring in the coronal as well as source regions by examining 171 Å images available from 04:30 UT onward. From the sequence of EUV images, it is evident that the higher coronal loops began to collapse from ∼04:47 UT (see Figures 5.6 and 5.7). We find that only one loop system "B" underwent contraction. This large-scale contraction continued until the impulsive rise of the M6.2 flare at 05:18 UT.

We note some important observational characteristics of the loop contraction. (1) Before and at the beginning of loop contraction (i.e., 04:42–04:51 UT) the top of the loop system exhibited intense emission, which gives evidence for localized heating in the higher corona (indicated by the arrow in Figure 5.6(f)). (2) From 04:51 UT onward, this LT brightening started getting dispersed and the brightening mostly dissolves by ∼05:02 UT. (3) From 04:54 UT, we observe intermittent brightenings in a set of low-lying loops at the source region besides contraction of higher loops (Figure 5.6(h)).

In Figure 5.7(a), we present a height-time plot of the collapsing coronal loops.

[1]https://www.tcd.ie/Physics/people/Peter.Gallagher/trace-align/index.html

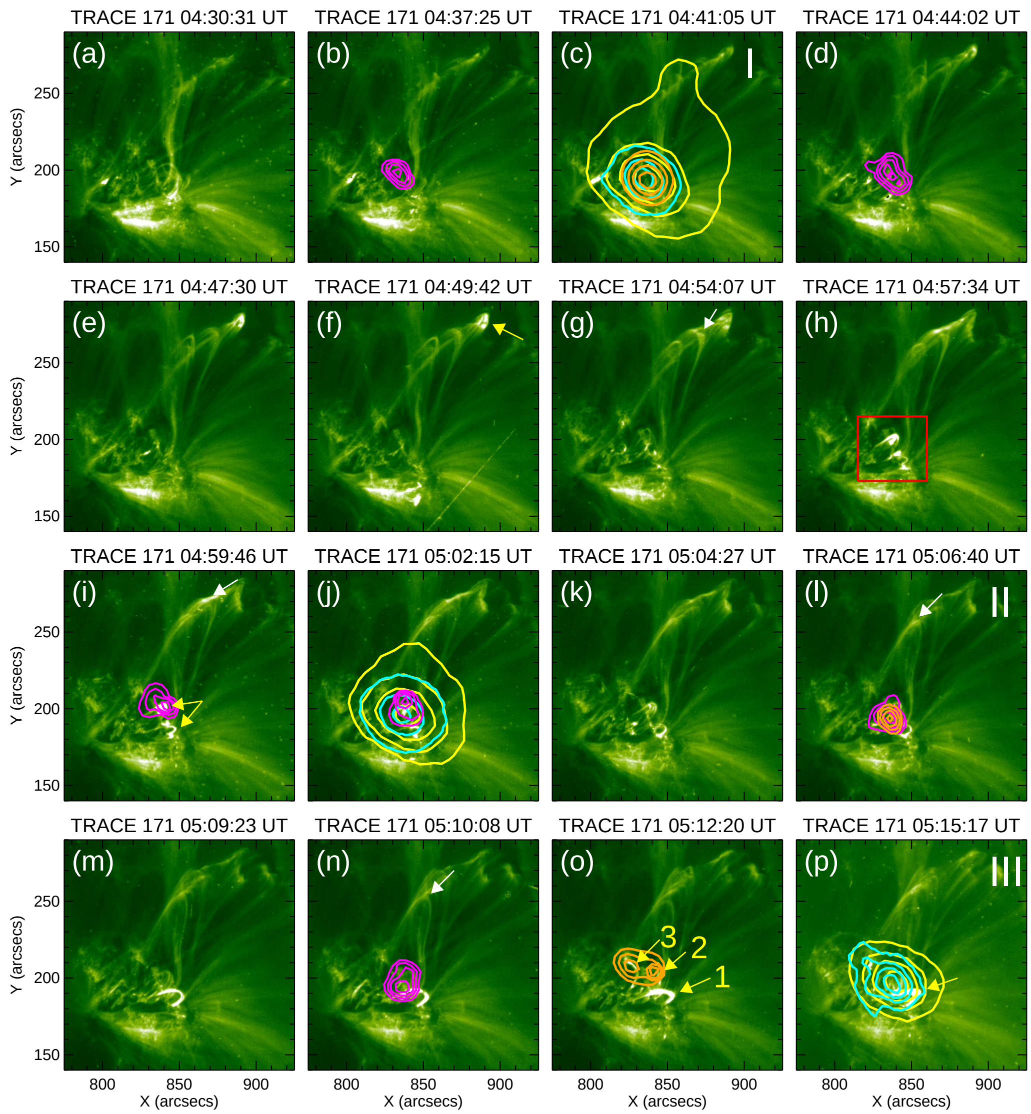

Figure 5.6: Series of TRACE 171 Å images during the pre-flare phase of the M6.2 flare showing the contraction of coronal loops as well as localized brightening at the source region. We have marked I, II and III in panels (c), (l), and (p) respectively to show EUV brightenings at the events of GOES flux enhancement (see Figure 5.3) before the M6.2 flare onset. We indicated the contracting loops by the white arrows in a few panels. An intense brightening is noted in the high corona and indicated in panel (f). The sequential brightenings in the low-lying coronal loops are enclosed within a box in panel (h) and their evolution during later stages are indicated by arrows in panels (i) and (o). Co-temporal X-ray (6−12 keV: magenta, 12−25 keV: orange) and MW (17 GHz: yellow, 34 GHz: sky) contours are over plotted on a few selected panels. The contour levels are set as 15%, 30%, 50%, and 80% of the peak flux for both X-ray and MW images.

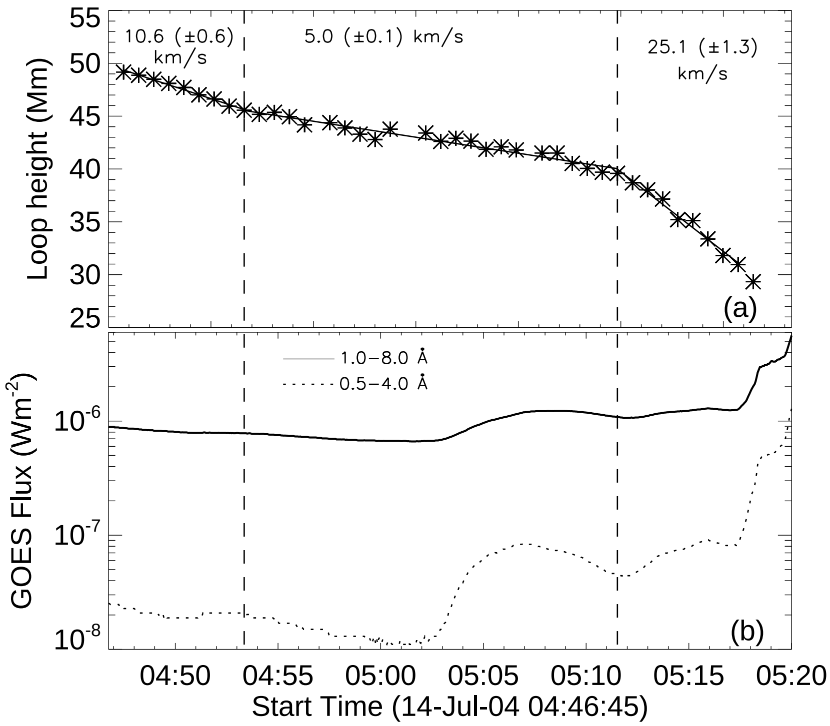

Figure 5.7: Height-time plot of the coronal loop system presenting contraction motion between 04:47 UT and 05:18 UT (panel (a)). The speed of downward motion of the contracting loops during different phases are also indicated with their respective uncertainty in the measurements. To compare the evolutionary phases of loop contraction with the flare evolution, we plotted the GOES flux profile for the same time interval in the panel (b).

Due to mingling of several loops which altogether evolve dynamically, the estimation of loop height was a tedious exercise. We took utmost care in distinguishing one of the loop systems undergoing the contraction by carefully identifying its legs. We find that the loop contraction proceeds with varying speed. In order to compare the phases of loop contraction with the thermal emission from the flaring region, we have also plotted the co-temporal GOES flux profiles in both channels in Figure 5.7(b). We find that in terms of contraction speed, the collapsing loop system undergoes three phases of evolution. In the beginning, the loops contract with relatively higher speed of $\sim$11 km s^{-1} that were sustained for $\sim$6 minutes.

This is followed by a prolonged phase of ∼19 minutes during which the contractions slowed down to ∼5 km s^{-1}. As shown in Figure 5.3, the pre-flare activity is characterized by three episodes of flux enhancement (marked as I, II, and III). We note that the loop contraction continued during all three stages (Figure 5.7) but there is a drastic increase in the speed of contraction from ∼5 to ∼25 km s^{-1} at 05:12 UT which marks the third episode of flux enhancement. The loop contraction halts at 05:18 UT with the beginning of the flare impulsive phase after which the expansion predominates over the implosion.

5.3.2 Localized brightenings at the core region

The sequence of images during the pre-flare phase clearly indicates that the large-scale contraction of EUV coronal loops is accompanied by localized brightenings at the core of active region loops. In Figure 5.6, we show EUV images showing pre-flare activity and mark the three events of GOES flux enhancement (see Figure 5.3) as I, II, and III in panels (c), (l), and (p), respectively. Here it is important to note that the core region exhibited pre-flare emission even before the onset of contraction in the form of X-ray (6–12 and 12–25 keV) and MW (17 and 34 GHz) emissions, which are co-spatial (Figures 5.6(b)–(d)). However, at this time EUV images do not show any significant bright structures associated with X-ray and MW emitting regions. The X-ray and MW sources in the pre-flare phase clearly indicate distinct events of energy release at the core of active region loops that precede the large-scale contraction of overlying loops.

We observe localized, distinct bright EUV sources at the core region from 04:54 UT onward, i.e., after the initiation of the contraction of the loop system. The location of EUV brightening is shown inside a box in Figure 5.6(h). Although brightenings at three locations were observed in the beginning (∼04:57 UT), we can clearly recognize two of the three bright structures as low-lying loops at some later stages (∼05:02 UT). The intensity of bright loops rapidly decreased

(∼05:07 UT) and we observe the formation of a relatively large system of low-lying loops thereafter (i.e., 05:08 UT onward). In fact three new bright loops formed sequentially, appearing in coincidence for a brief interval (around 05:12 UT). These three loops are marked as 1, 2, and 3 in order of their occurrences. We also note that the loop-1 became very intense in the later stages (marked in Figure 5.6(p) at 05:15:17 UT) and lasted until the impulsive phase of M6.2 flare. The comparison of pre-flare EUV brightening with the co-temporal RHESSI images clearly reveals X-ray sources at the top of low-lying loops. It is interesting to see that although in EUV images loop-1 appeared the most intense, the HXR emission in 12–25 keV energy band is essentially associated with loops 2 and 3. We further note that MW emission at 17 and 34 GHz is observed in the form of a single source that shows clear association with the bright low-lying EUV loops (Figure 5.6(p)).

5.4 The M6.2 flare

5.4.1 High energy emission and stages of prominence eruption

In Figure 5.8, we present the RHESSI and NoRH light curves along with the GOES time profiles for the M6.2 flare. We find that the HXR light curves >25 keV show a rapid increase in count rates from 05:17 UT onward, indicating the onset of the impulsive phase of the flare. The non-thermal HXR emission continued until ∼05:25 UT which can be recognized in 25–40 keV light curve and further confirmed by HXR spectroscopy (see Section 5.4.2). Therefore, we have considered the period from 05:17 to 05:25 UT as the impulsive phase of the flare, which is indicated in Figure 5.8 by the gray shaded area. The MW light curves clearly show that the impulsive phase is characterized by three distinct events of flux enhancements (marked as events ‘a’, ‘b’, and ‘c’ in Figure 5.8) with the first

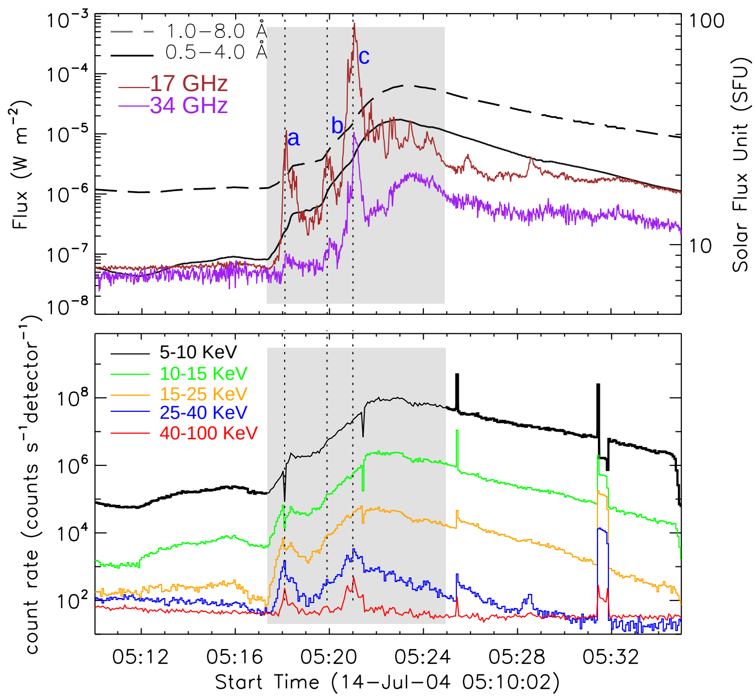

Figure 5.8: Top panel: GOES soft X-ray flux profiles in the 0.5–4 Å and 1–8 Å chanels between 05:10 UT and 05:36 UT. The figure also presents time evolution of microwave emission at 17 GHz and 34 GHz frequencies, obtained from NoRH. Bottom panel: The temporal variations of RHESSI X-ray fluxes in five different energy bands. For the clarity in presentation, we have scaled RHESSI count rates by factor of 1, 1, 1/2, 1/5, and 1/40 for 5–10, 10–15, 15–25, 25–40, and 40–100 keV energy bands respectively. Note that the impulsive phase of the the flare is indicated by gray shaded area during which MW emission exhibits three events of flux enhancement ‘a’, ‘b’, and ‘c’. The events ‘a’ and ‘c’ are common in HXR and MW profiles (above 25 keV) while event ‘b’ does not appear prominent in HXR observations.

and third peaks at 05:18 UT and 05:21 UT also being common in HXR profiles. During MW peak ‘b’ at 05:19:54 UT, the HXR profiles above 25 keV also exhibit flux enhancement but a distinct peak structure as in MW light curves can not be recognized. Furthermore, these MW peaks are much more distinguishable at 17 GHz than 34 GHz observations. After the peak ‘c’, MW flux profiles (mainly at 17 GHz) exhibit significant fluctuations during the impulsive phase.

In Figure 5.9, we present combined imaging observations of the M6.2 flare in EUV, HXR, and MW to show the crucial phases of the flare evolution. Following

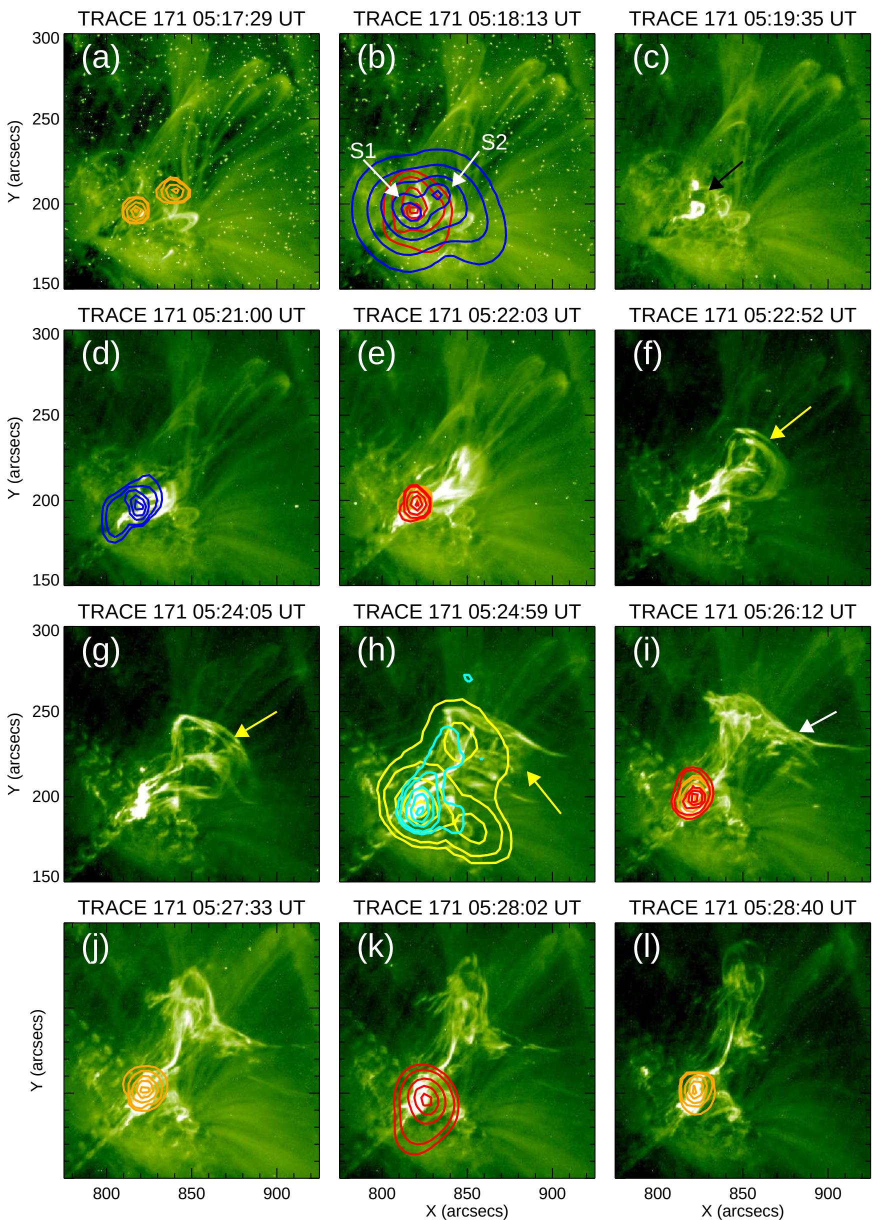

Figure 5.9: Sequence of TRACE 171 Å images showing the activation, expansion and eruption of the prominence and associated flaring activity. The X-ray contours in different energy bands (12–25: orange, 25–40: red, 40–100 keV: blue) are overplotted on some of the co-temporal EUV images. The conjugate emission centroids of HXR source at the 40–100 keV are marked by S1 and S2 in panel (b). For a comparison of the spatial location of HXR and MW emissions, we plot NoRH microwave images at 17 GHz (yellow) and 34 GHz (sky) in panel (h). The contour levels for RHESSI and NoRH images are set as 5%, 10%, 30%, 60%, and 90% of the peak flux of the each images.

the impulsive onset of HXR and MW emissions (event 'a'), we observe the rise of the prominence at the source region and intense EUV brightening beneath it (Figures 5.9(a)–(c)). In subsequent EUV images, we observe the evolution of filament in the corona with distinct appearance of its outermost structure (shown by arrow in Figures 5.9(f), (g) and (i)) which we term as the "eruption front". The eruption front likely represents a part of the magnetic structure associated with the erupting filament. In Figure 5.10, we provide a height-time plot of the eruption front. The eruption front underwent its fastest expansion between 05:21 and 05:23 UT with the speed of $\sim$242 km s^{-1}. The eruption speed rapidly decreases after 05:23 UT. We note that there is a further decrease in the speed of the eruption front as it moves to higher altitudes; the speed of the eruption front was $\sim$65 km s^{-1} between $\sim$05:23–05:24 UT which decreased to $\sim$26 km s^{-1} between 05:24–05:26 UT. The eruption front was intact and symmetrical until $\sim$05:24 UT while attaining a height of 4.8×10^4 km (from the source region) at 05:25 UT. Thereafter, the eruption front got disrupted (Figure 5.9(h)) while its major portion (right segment; marked by arrow in Figure 5.9(i)) descended which we could track/identify until $\sim$05:29 UT. In this interval, the downward speed of the eruption front was estimated as $\sim$95 km s^{-1}. The remaining portion of the eruption front narrowed down while moving further upward and eventually disrupted. In Figure 5.11, we present a series of MW sources at 17 and 34 GHz over co-temporal EUV 171 Å images to study the spatial evolution of MW emission in relation to the phases of the prominence activity.

Large Angle Spectroscopic Coronograph (LASCO; Brueckner et al. 1995) on board SOHO did not detect any CME associated with this flare. The absence of CME suggests that all the erupted material either fell down on the source region or arrested within overlying coronal loops.

EUV images from $\sim$05:21–05:23 UT showed a very important phase of eruption that requires more attention. We present an enlarged view of EUV images in Figure 5.12 to emphasize some interesting morphological structures during the

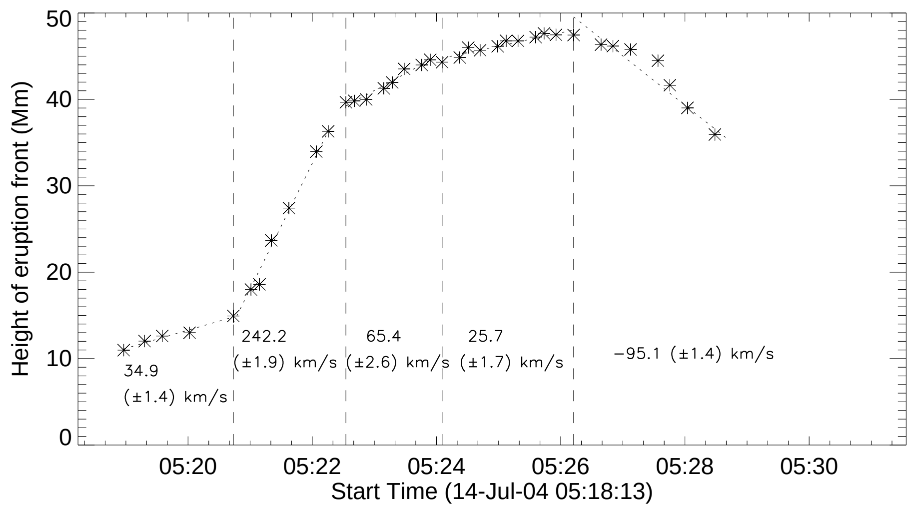

Figure 5.10: Height-time plot of the eruption front during the main flare phase from 05:19 UT to 05:29 UT. The expansion of the eruption front shows different behavior during different stages of eruption. In the early stage, the prominence started to rise with a constant velocity of ~35 km s^{-1} till 05:20:40 UT. Thereafter, it suddenly accelerate to attain its maximum rising velocity of ~242 km s^{-1} between 05:20:40 and 05:22:30 UT. After that the rising speed started slowed down from 242 to 65 and further, 65 to 26 km s^{-1}. Finally, the eruption front has completely halted at 05:26:10 UT after attaining a height of ~48 Mm above the solar surface and started downward motion with a speed of ~95 km s^{-1}.

early evolution of the erupting system. We observe a system of twisted loops at the western side (leading side of eruption) that undergoes fast expansion (marked by yellow arrows), which conceivably could be the projection of the helically twisted loops. To understand the associated high energy emission, we present co-temporal HXR images at 12–25 keV (orange) and 25–40 keV (red) in Figure 5.12(c).

5.4.2 RHESSI X-ray spectroscopy

We have studied the evolution of RHESSI X-ray spectra during the flare over consecutive 20 s intervals from 05:17 UT to 05:25 UT. Furthermore, we have analyzed spectra for a few selected intervals during the pre-flare peaks. The time

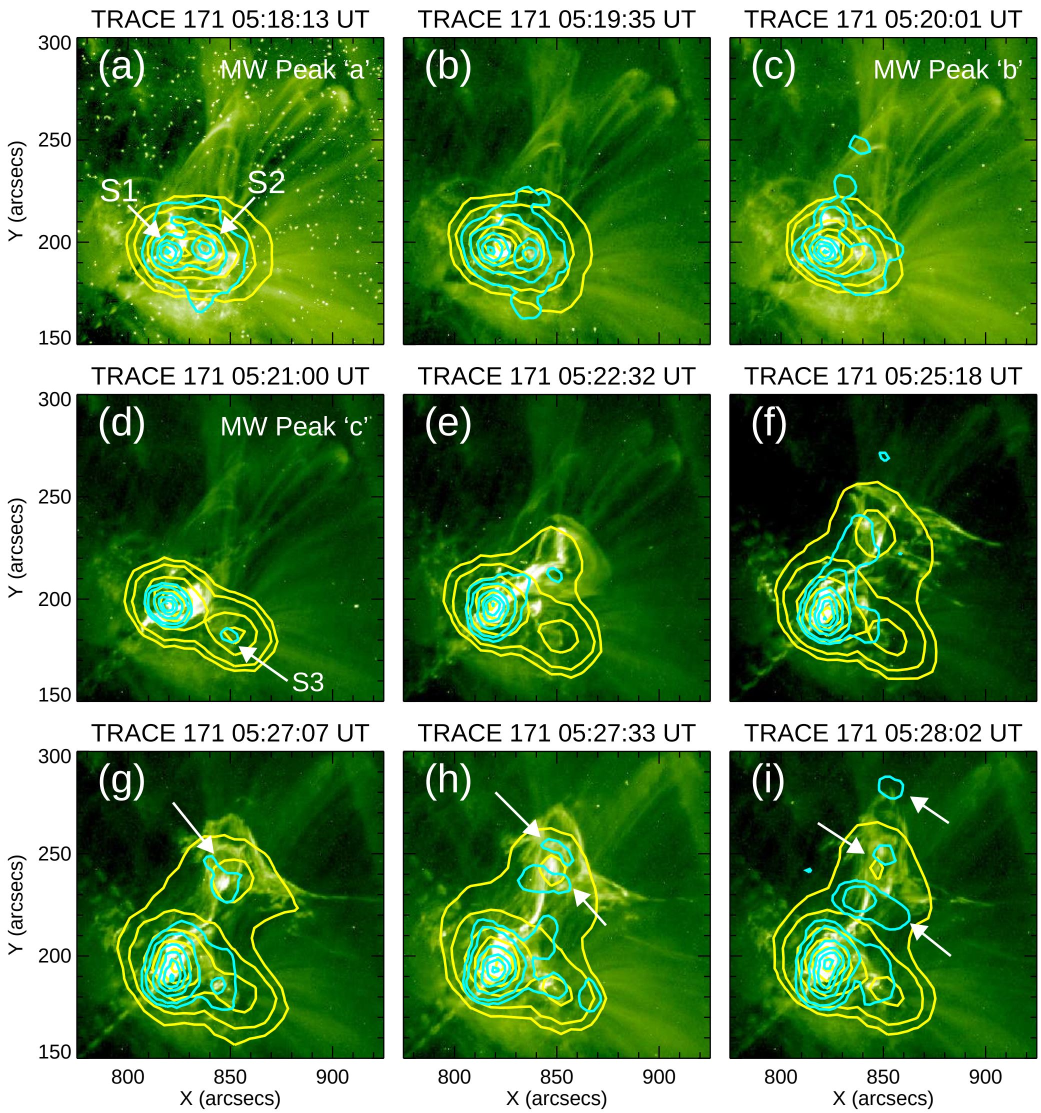

Figure 5.11: Series of TRACE 171 Å images overlaid by co-temporal NoRH MW contours in 17 GHz (yellow) and 34 GHz (sky). The conjugate emission centroids of MW source at 34 GHz during early impulsive phase are marked by S1 and S2 in panel (a). We further indicate a relatively distant MW source by S3 in panel (d) which is more prominent at 17 GHz. The source S3 appeared during main impulsive peak (05:21 UT) and prevailed till the end of the flare (∼05:30 UT). The contour levels for MW images are set as 5%, 10%, 30%, 55%, 75%, and 95% of the peak flux of the each images. We note multiple coronal MW sources at both 17 GHz and 34 GHz and indicated them with arrows (white) in the panels (g), (h) and (i).

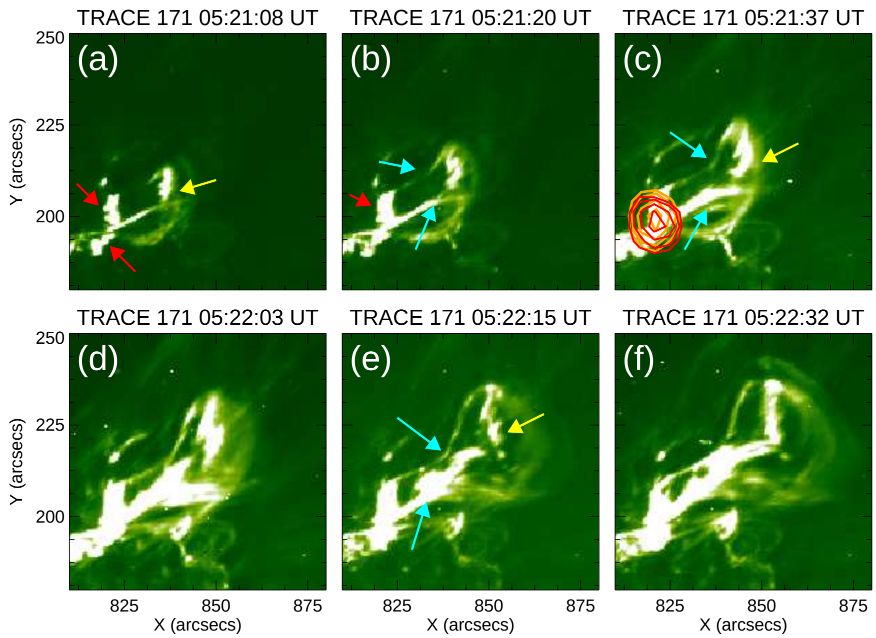

Figure 5.12: Sequence of TRACE EUV images from 05:21–05:23 UT showing the fast expanding phase of the eruption. The X-ray contours in 12–25 keV (orange) and 25–40 keV (red) are shown in panel (c). The bending of magnetic field lines toward bright central region due to stretching by rising prominence-flux rope is indicated by arrows (sky) in panels (b), (c) and (e).

intervals for spectral analysis are carefully chosen to avoid the bad intervals due to changes in the attenuator states. In this particular case, there were two bad intervals during 05:18:04–05:18:08 UT (change in attenuator state from A0 to A1, i.e., the thin shutter comes in) and 05:21:24–05:21:28 UT (change in attenuator state from A1 to A3, i.e., thin+thick (both) shutters are in).

In Figure 5.13, we illustrate spatially integrated, background subtracted RHESSI spectra along with their respective residuals for few selected intervals. Spectral fits were obtained using a forward-fitting method implemented in the OSPEX code. The HXR emission during pre-flare peaks was observed only up to 20 keV and can be well fitted with an isothermal model (see Figure 5.13(a)). During the impulsive phase, we note HXR emission up to 100 keV. For this phase, the spectral fittings were obtained using the bremsstrahlung and line spectrum of an isothermal plasma and a non-thermal thick-target bremsstrahlung model (i.e., combination of Vth and thick2 models; see Figures 5.13(b)–(f)). Also, we have chosen different time intervals for fitting during pre-flare peaks (1 minute) and impulsive phase (20 s) for better count statics. In Figure 5.14, we plot various spectroscopic parameters derived from spectral fittings: temperature (T) and emission measure (EM) from thermal fits; low-energy cutoff (E_{LC}) and electron spectral index (δ) from non-thermal thick target fits. RHESSI observations reveal a very high plasma temperature (T $\sim$32 MK) at the time of first HXR peak at 05:18 UT (see Figure 5.14(a)) while EM remains at lower values, which suggest intense heating within localized regions. Later on both, the T and EM exhibit smooth variations (see Figure 5.14(a) and (b)).

From the thermal parameters, we have further estimated the density (n) and the pressure (P) of the flaring region (see Figure 5.14(c)). The density of thermal plasma is inferred by the formula, $n = \sqrt{EM/(f \cdot V)}$, where EM is the emission measure, V is the source volume, and f is the volume filling factor. The volume has been estimated by the relation, $V = A^{3/2}$, where A is the area of X-ray sources at 50% contour level of the corresponding 6–15 keV RHESSI images reconstructed with the CLEAN algorithm. The filling factor (f), ratio of the volume filled by hot X-ray emitting plasma to the total source volume, is often assumed to be unity (see, e.g., Sui et al. 2005a). The pressure of the plasma in thermal emission has been estimated by the formula, $P = 2nk_BT$, where k_B is Boltzmann's constant. It is noticeable that the density and pressure show a slow yet steady rise until the second HXR peak at $\sim$05:21 UT, but exhibit rather oscillatory behavior in the later stages (see Figure 5.14(c)).

The evolution of low-energy cutoff (E_{LC}) is shown in Figure 5.14(d). The E_{LC} values derived are the upper estimates due to the dominance of the hot thermal contribution, and thus yield lower limits to the number of non-thermal electrons and their energies derived (Holman et al. 2003). The temporal evolution of electron spectral index (δ) clearly indicates spectral hardening at the two HXR peaks

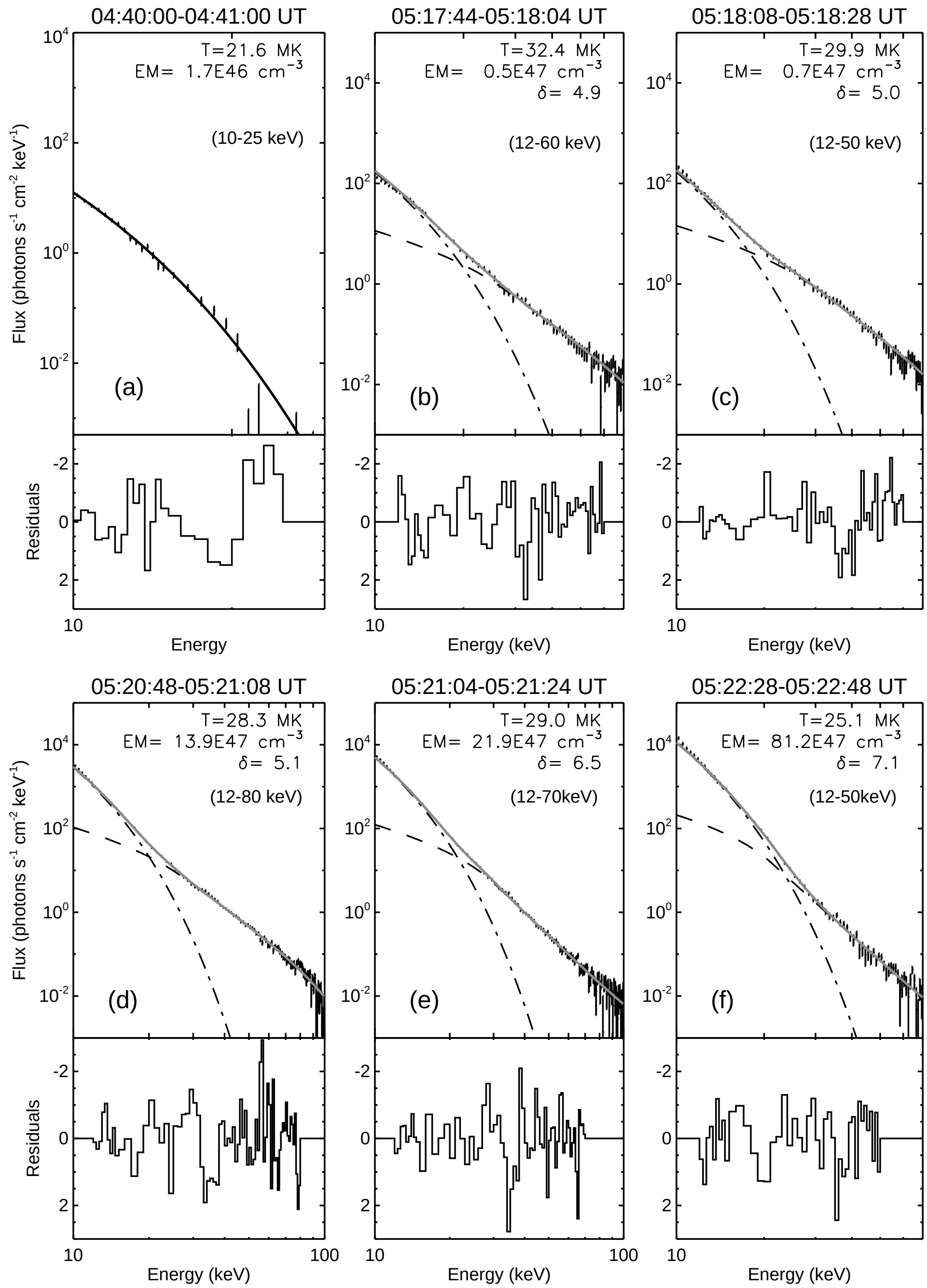

Figure 5.13: RHESSI X-ray spectra along with their residuals derived during various time intervals before and during the M6.2 flare event on 2004 July 14. Panel (a) presents the spectrum which is fitted with an isothermal model during pre-flare peak I (defined in Figure 5.3). Panels (b)–(f) display a set of spectra that are fitted with a combination of isothermal model (dashed-dotted line) and thick-target bremsstrahlung model (dashed line). The gray (solid) line indicates the sum of the two components. The energy ranges chosen for fitting are shown on each panels.

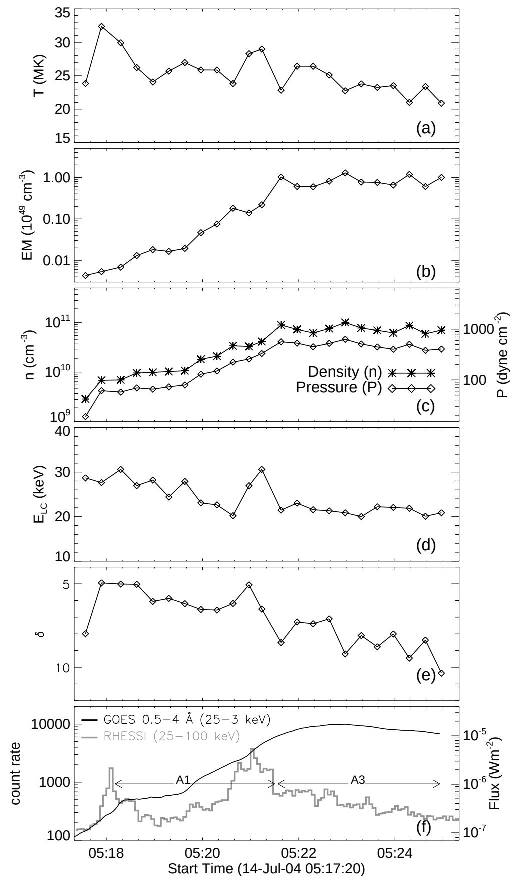

Figure 5.14: Temporal evolution of various spectroscopic quantities derived from X-ray spectral analysis during the impulsive phase of the M6.2 flare. Panels (a)–(e): Temperature (T), emission measure (EM), density (n) along with pressure (P), low-cutoff energy (E_{LC}), and electron spectral index (δ). To compare these parameters with respect to the flare evolution, we have plotted GOES high energy flux (0.4–5 Å) and RHESSI 25–100 keV count rates in panel (f). We also indicated the time-duration in which the attenuators A1 and A3 were present in front of the RHESSI detectors.

(at 05:18 and 05:21 UT) with electron spectral index (δ ∼5; see Figure 5.14(e) and spectra in Figures 5.13(b) and 5.13(d)) which suggest stronger acceleration of high energy particles at these epochs.

5.4.3 Estimations of thermal and non-thermal energies

In the preceding subsection (5.4.2), we have estimated various spectroscopic parameters (EM, T, δ, F_e, and E_{LC}) which are used to evaluate thermal and non-thermal energies associated with the flare.

Using instantaneous values for T and EM, the total thermal energy content can be estimated by following expressions,

$$E_{th} = 3k_B TnV = 3k_B T\sqrt{EM \cdot f \cdot V} \text{ [erg]}, \tag{5.1}$$

where k_B, T, EM, V, and f are the Boltzmann constant, the plasma temperature (K), the emission measure (cm^{-3}), the source volume (cm^3) and volume filling factor, respectively. In accordance with previous RHESSI studies (e.g., Holman et al. 2003; Veronig et al. 2005; Warmuth and Mann 2013), we assume unity for the filling factor (f). Recently Guo et al. (2012) determined from RHESSI imaging spectroscopy for a number of extended loop flares that the filling factor lies within the range 0.1 and 1 which they interpret as somewhat less than, but consistent with unity.

The evolution of E_{th} is shown in Figure 5.15(a). We find that E_{th} gradually builds up till the second HXR peak (05:21 UT) and remain roughly constant till the end of impulsive phase. E_{th} maximizes ∼2 minutes after peak HXR flux and resembles the GOES SXR profiles (see Figure 5.15(a)).

In collisional thick-target model, the HXRs are produced by collisional bremsstrahlung during the passage of non-thermal electrons through denser plasma regions, in which the electrons are stopped completely by Coulomb collisions (Brown 1971; Brown et al. 2009; Kontar et al. 2011). Using the electrons distribution parameters derived from RHESSI spectroscopy, the power delivered by non-thermal electrons above low-energy cutoff (E_{LC}) can be calculated by the following expression,

$$P_{nth}(E > E_{LC}) = \frac{\delta - 1}{\delta - 2} F_e E_{LC} 10^{35} \text{ [erg s}^{-1}\text{]}, \tag{5.2}$$

where E_{LC} is the low-energy cutoff, F_e is the total number of electrons per second above E_{LC} in units of 10^{35} electrons s^{-1}, and δ is the electron spectral index (Fletcher et al. 2013). An accurate determination of the low-energy cutoff to non-thermal electron distributions is crucial for the calculation of power and consequently non-thermal energy in solar flares (Sui et al. 2005b; Veronig et al. 2005). In general flares are thought to have low-energy cutoffs close to or in the region where the emission is dominated by thermal bremsstrahlung (Ireland et al.

2013). We further emphasize that in flares with multiple HXR sub-peaks during the impulsive phase (like the present one), the determination of E_{LC} is rather illusive during the peak emission as it is difficult to distinguish the signals of flare accelerated electrons against dominant thermal bremsstrahlung. This often results in the overestimation of E_{LC} during HXR peak phases. For this event, we find that E_{LC} varies in the range of 20–32 keV with relatively higher values (~32 keV) during the second peak (see Figure 5.14(d)). Therefore, in order to get an estimation of power (and consequently energy) of the non-thermal electrons, we have taken E_{LC} as 25 keV which is the average of E_{LC} over the flare time interval. The estimated non-thermal electron flux (F_e) above 25 keV is plotted in Figure 5.15(b). In Figure 5.15(c), we have plotted the power (P_{nth}) and energy (E_{nth}) contained in non-thermal electron beams. The plots of F_e and P_{nth} clearly indicate noticeable enhancement in the particle rate and consequently power of flare-accelerated electrons during the two HXR peaks.

5.5 Results and discussion

5.5.1 Contraction of coronal loops and pre-flare emission

Although the active region NOAA 10646 had a relatively simple bipolar magnetic structure in the photosphere, it exhibited very complex structures of overlying loops in the corona (see Figure 5.5). The EUV images at 171 Å clearly show large-scale contraction of a system of higher coronal loops that started ~30 minutes prior to the M6.2 flare. It is important to note that the loop contraction was observed throughout the pre-flare phase and ceased with the onset of the flare impulsive phase. We observed three small events during the pre-flare phase (events I, II, and III; Figures 5.3 and 5.6) which are characterized by localized brightenings in the core region of the overlying loops. The speed of loop contraction increased drastically (from ~5 to ~25 km s^{-1}; Figure 5.7) just ~5 minute prior to the impulsive phase of the M class flare, i.e., during the pre-flare event III. RHESSI measurements during the pre-flare events reveal HXR emission up to 20 keV. From the X-ray spectra, we find that the X-ray emission was predominantly thermal during this phase with plasma temperature >20 MK during pre-flare peaks (see e.g., Figure 5.13(a)). These observations indicate that the flaring site was already enveloped by hot plasma before the onset of filament activation and associated M6.2 flare.

Table 5.1: Summary of various stages of flare evolution from pre-flare to decay phase.

Phases	Time (UT)	Observations
Pre-flare activity	04:30–05:17	Three small GOES flare events, EUV loop contraction for $\sim$30 min, drastic change in speed of contraction during third peak of pre-flare phase, pre-flare events showing localized brightenings in EUV 171 Å, MW and X-ray sources at the core region underneath the contracting coronal loops.
Contraction phase	04:47–05:17	Large overlying coronal loops observed at EUV 171 Å undergo contraction by $\sim$20 Mm (40% of original height), loop contraction continues through all three episodes of pre-flare activity.
Flare impulsive phase and rapid activation of flux rope	05:17–05:25	Peak HXR emission up to 100 keV with electron spectral index δ $\sim$5, multiple peaks in HXR and MW (17 and 34 GHz) emission, rapid rise of flux rope by $\sim$40 Mm.
Decay phase and confinement of eruption	05:25–05:35	Braking and successive disruption of eruption front, multiple MW sources from footpoint and coronal regions, compact HXR footpoint source.

It is worth emphasizing that the M6.2 flare occurred at the location of pre-flare brightenings which were enveloped by the large contracting coronal loop system.

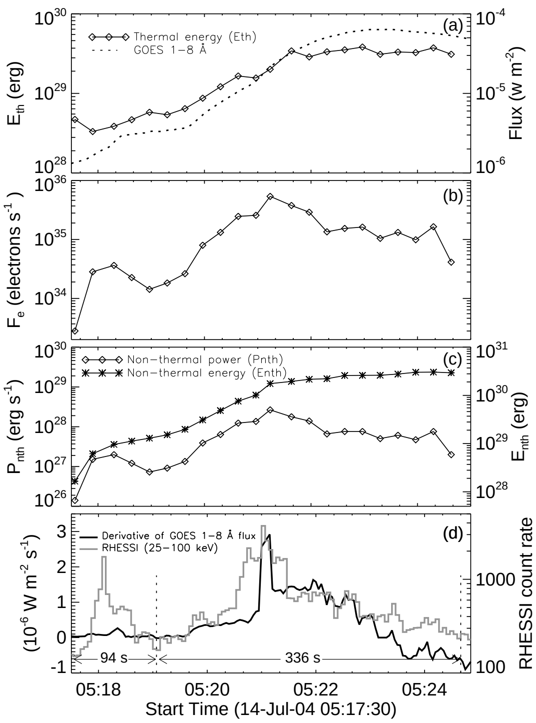

Figure 5.15: Temporal evolution of (a) thermal energy (E_{th}) along with GOES SXR flux at 1–8 Å, (b) electron flux above 25 keV energy (F_e), (c) non-thermal power (P_{nth}) and cumulative non-thermal energy (E_{nth}) during the M6.2 flare. We have also shown the comparison of RHESSI HXR flux profile at 25–100 keV (gray) with derivative of GOES 1–8 Å flux (black) in panel (d).

Although the phenomena of loop contraction has been observed in several recent studies, the contraction reported here is remarkable in several aspects. First, the contraction was observed in overlying coronal loops at large-scales both at spatial and temporal domains during which the loop height decreased by ~20 Mm (40% of original height). The total duration of loop contraction is ~30 minutes, which is the longest period of loop contraction reported so far. Further, the contraction phase ends with the onset of the impulsive phase of the M6.2 flare, i.e., the the onset of impulsive phase can be treated as the transition from inward to outward motion of coronal loops.

The investigations of loop contraction have emerged as a very important aspect of solar eruptions in recent times. These studies are essentially inspired by the RHESSI discovery of altitude decrease in the HXR LT source during the early impulsive phase in SOL2002-04-15 of class M1.2 (Sui and Holman 2003). This phenomena of downward motion of the HXR LT source was established by many subsequent RHESSI observations in flares of different intensity classes (i.e., from

Table 5.2: Important characteristics of impulsive phase of the M6.2 flare derived from RHESSI spectroscopy (refer to Figure 5.15).

Flare characteristics	Parameters
Total duration of HXR peaks	430 s
No. of HXR peaks	2
	94 s and 336 s
Total non-thermal energy ($(E_{nth})_{tot}$)	3.03 $\times 10^{30}$erg
Thermal energy (E_{th})	
–$(E_{th})_{max}$	3.89 $\times 10^{29}$ erg
–$(E_{th})_{min}$	0.33 $\times 10^{29}$ erg
$(E_{nth})_{tot}/(E_{th})_{max}$	∼7.5

C to X) during their earliest stages of the impulsive phase (Liu et al. 2004, 2009b; Sui et al. 2004; Veronig et al. 2006; Joshi et al. 2007, 2009).

Motivated by the RHESSI observations, the dynamics of complex coronal loop system over the flaring core was extensively investigated in EUV images. These studies reveal a significant contraction of coronal loops that envelop the flaring region before and during the flare (e.g., Li and Gan 2006; Joshi et al. 2009; Gosain 2012) which was attributed to "magnetic implosion" (Hudson 2000) by many authors (Liu et al. 2009b; Simões et al. 2013). Li and Gan (2006) provided the first evidence for the contraction of EUV coronal loops that lasted for ∼5 minutes from TRACE 195 Å images that was temporarily and spatially correlated with the shrinkage in the RHESSI 12–25 keV LT source during the early impulsive phase of SOL2002-04-16 flare of class M2.5. The study of a long duration M7.6 event (SOL2003-10-24), characterized by a prolonged rise phase of ∼20 minutes, provided one of the best examples for the contraction of coronal loops (Joshi et al. 2009). In this event, TRACE 195 Å loops and HXR LT sources underwent a shrinkage of ∼35% of initial height during ∼11 minutes. More importantly, the downward motion was observed simultaneously with a speed of ∼15 km s^{-1} in EUV loops as well as HXR LT sources in different energy bands, viz., 6–12, 12–25, and 25–50 keV.

Due to observational limitations, it is usually not possible to probe the motions of flare associated LT and FP sources simultaneously. Nevertheless some uniquely observed events have given us the opportunity to examine the relationship between the dynamics of LT and FP sources in the early flare phases (Ji et al. 2007; Liu and Wang 2009; Liu et al. 2009b). These studies indicate that the shrinkage in LT sources are associated with converging FP motions, making us predict that simultaneity of the two phenomena could be the part of the coronal implosion. Liu et al. (2009b) presented observations of contraction of large coronal loops during the early impulsive phase of SOL2005-07-30 of class C8.9. This contraction was found in three clusters of EUV loops observed at 171 Å that sustained for a longer interval with relatively slower speed ($\sim$10 minutes with an average speed of $\sim$5 km s^{-1}). In an other study by Simões et al. (2013), loop contraction was seen in EUV 171 Å images during impulsive phase of an M6.4 flare (SOL2012-03-09) which were associated with loop oscillations.

It is widely believed that coronal transients derive their energy from the energy stored locally in the coronal magnetic fields. Hudson (2000) conjectured that the energy conversion process during transient events would involve a magnetic implosion when the following assumptions hold: (1) the energy required for the event must come from the corona directly; (2) gravitational potential energy plays no significant role; and (3) low plasma β in the corona. With these assumptions, the conversion of energy implies that magnetic energy decreases between the static states before and after the energy release. The reduction of magnetic energy, $\int B^2/8\pi$ dV, and consequently the reduction of the magnetic pressure, B$^2/8\pi$, would inevitably result in the contraction of overlying field lines so as to achieve a new force balance. The observations of the contraction of overlying coronal loops during and before the impulsive phase of flares by high temporal cadence images from TRACE and SDO support the predictions of the conjecture by (Hudson 2000). However, the observational evidences for the contraction in coronal loops are uncommon for the majority of flares that exhibit explosive rather than implosive behavior.

We note that in our observations prolonged coronal implosion displays three distinct stages with varying speed of loop contraction (Figure 5.7(a)). Here it is important to focus on the brief and localized X-ray and MW emissions that were observed from the core region of the overlying loop system a few minutes before the onset of contraction (Figures 5.6(b)–(d)). Later on this region brightened up in EUV images also with the localized brightening of multiple low-lying loops. More importantly, the contraction speed rapidly increased $\sim$5 minutes before the flare onset and this phase is co-temporal with the sequential brightenings of low-lying coronal loops at the core region during which X-ray and MW emissions intensified (Figure 5.6). The observations of sequential and localized brightenings during the pre-flare phase imply episodic release of small amount of energy which can be considered as the signature of magnetic reconnection at relatively small-scales (in contrast to large-scale reconnection during the flare impulsive phase) (Chifor et al. 2007; Joshi et al. 2011, 2013; Awasthi et al. 2014). RHESSI observations of this phase further indicate that this interval is mostly dominated by the thermal emission. The slow and gradual energy release over the prolonged pre-flare phase will cause the magnetic pressure of the coronal loop system to decrease. It is likely that during this slow preheating phase, the increase of the thermal pressure is mainly due to localized heating and gentle evaporation which is not enough to compensate for the decrease of the magnetic pressure (Liu et al. 2009b). This will result in the implosion of the surrounding flaring region consisting of EUV coronal loops. We therefore conjecture that multiple small-scale, localized events of energy release at the core region over the prolonged preheating phase favorably contributed to sustain a large-scale contraction of coronal loops. With the onset of the “standard flare reconnection” during the impulsive energy release, the implosion becomes insignificant as the large-scale magnetic reconnection proceeds successively in the higher coronal loops stretched by the eruption of the prominence or magnetic flux rope.

5.5.2 Multi-wavelength flare emissions and confinement of erupting prominence

We examine the temporal and morphological evolution of MW and HXR emission during the impulsive phase (i.e., shaded area in Figure 5.8) and their associations with the prominence activation. The comparisons of spatial and temporal structures of HXR and MW emission offer us crucial information on different aspects of conditions in the solar atmosphere where the flare occurs as both type of emissions are produced by highly energetic electrons but with different emission mechanisms. The HXR emission most likely arises from bremsstrahlung produced when energetic electrons are decelerated by Coulomb forces in collisions with the ambient ions, either in the chromosphere or in the corona. Bremsstrahlung HXR emission is proportional to the product of the non-thermal electron density and the ambient ion density. On the other hand, non-thermal MW emission is produced by the gyrosynchrotron mechanism which depends on the magnetic field intensity and its direction. The gyrosynchrotron production mechanism is very efficient and allows us to detect electrons at energies of hundreds of keV, even when their numbers are very low. MW emission can also be produced by thermal electrons through bremsstrahlung in sufficiently dense thermal plasma (for a review see White et al. 2011).

The impulsive phase is characterized by three events of flux enhancements in MW emission denoted by “a,” “b” and “c”. It is worth noting that events “a” and “c” occurred simultaneously in MW and HXR profiles while “b” is largely missing in HXR measurements. The spatial evolution of HXR emission with respect to EUV images (see Figure 5.9) provides some important insights for understanding the relationship between flare emission and phases of prominence activity. We find that at the very beginning of the impulsive phase (∼05:17 UT;

Figure 5.9(a)), two distinct 12–25 keV HXR sources are observed and at this time the flare related EUV brightening at HXR source locations is insignificant. Soon afterwards, non-thermal high energy HXR emission (at 40–100 keV energy band) was observed from the same location with two distinct, well separated emission centroids (see Figure 5.9(b)). This phase corresponds to the first peak of the impulsive phase (i.e., event "a" marked in Figure 5.8). At this time, plasma temperature (estimated from RHESSI spectra; Figure 5.13(b)) increased to $\sim$32 MK which also corresponds to the maximum temperature during the flare (Figure 5.14(a)). The high temperature and low emission measure (Figures 5.14(a) and (b)) indicate impulsive heating of plasma within a small volume, which is also consistent with corresponding EUV images that show localized brightening.

We also note that this very epoch is associated with significant non-thermal characteristics with an electron spectral index $\delta \sim 5$ (Figures 5.13 and 5.14). It is further noteworthy that during event "a," a high energy HXR source at 40–100 keV resembles the MW source at 34 GHz; both show emission from an extended region with the appearance of two distinct well separated emission centroids (see also Figures 5.9(b) and 5.11(a)). In Figure 5.2, these conjugate emission centroids are indicated on a combined WL/magnetogram image as S1 and S2. The associations of S1 and S2 with opposite polarity magnetic regions suggest that they probably represent emissions from the FPs of a flaring loop. On the other hand, the 17 GHz source resembles the HXR emitting structure at relatively lower energies (<40 keV). We also note that event "a" is followed by the rise and subsequent eruption of the prominence.

The peak of the impulsive phase (i.e., event "c") occurred simultaneously in HXR and MW emission. At this time, HXR sources at energies >25 keV exhibit a single structure (Figure 5.9(d)). The non-thermal HXR emission is generally believed to originate from FP locations of coronal loops by thick-target bremsstrahlung, thus observations of pairs of HXR sources are expected. The single HXR source implies that the two FPs are very close indicating energy release in small low-lying loops (e.g., Kushwaha et al. 2014). Here it should be noted that the present event occurred close to the limb, so due to projection effects the FP sources may appear much closer than their actual separation. Although this HXR peak (event "c") is much broader and intense than the first peak (event "a"), the non-thermal electron spectral indices during the two peaks are comparable ($\sim$5; see Figures 5.13 and 5.14).

In table 5.2, we summarize various aspects of energy release during the impulsive phase of the flare (see also Figure 5.15). The total duration of HXR impulsive phase (as revealed by HXR flux profile >25 keV) is 430 s which is composed of two peaks of 94 s and 336 s durations (see Figure 5.15(d)). We find that the power delivered by the non-thermal electrons (P_{nth}) was maximum during the peak of HXR impulsive phase (event 'c') while the thermal energy E_{th} maximized $\sim$2 min later which nearly coincides with the peak of thermal SXR emission (Figures 5.15(a) and (c)). The total non-thermal energy ($(E_{nth})_{tot}$) emitted during this whole impulsive phase was $\sim 3.0 \times 10^{30}$ erg while the maximum thermal energy ($(E_{th})_{max}$) was noted at the end of impulsive phase as $\sim 3.9 \times 10^{29}$ergs, yielding a ratio of $(E_{nth})_{tot}/(E_{th})_{max} \sim 7.5$. Saint-Hilaire and Benz (2005) examined the ratio of non-thermal to thermal energies for a set of C- and M- class flares and found that this ratio varies in the range of $\sim$1.5–6. It was also noted the flares with longer HXR peaks (>200 s) display larger ratios of non-thermal to thermal energy. Considering that the present event displays a longer HXR impulsive phase of 430 s with two sequential HXR peaks, the ratio of $\sim$7.5 is in good agreement with the results of Saint-Hilaire and Benz (2005).

In order to understand the relationship between the flare-accelerated electron beam and the flare-associated emission from thermal plasma, we compare the HXR profile (RHESSI 25–100 keV) with the derivative of SXR flux (GOES 1–8 Å) in Figure 5.15(d). We obtained a good temporal consistency between the two curves which suggests that this flare, associated with confined eruption, follows the Neupert effect (Hudson 1991; Dennis and Zarro 1993; Veronig et al. 2005).

The consistency with the Neupert effect is further complemented by the fact that the curve showing the evolution of cumulative non-thermal energy (Figure 5.15(c)) exhibits a good temporal correspondence with the evolution of thermal energy (Figure 5.15(a)) indicating that the non-thermal energy is eventually converted into the thermal energy (Saint-Hilaire and Benz 2005). The validity of the Neupert effect implies that the energetic electrons responsible for the HXR emission by thick-target collisional bremsstrahlung (imaged as high energy HXR sources) are the main source of heating and mass supply of the SXR emitting hot coronal plasma (Veronig et al. 2005). We also note that with the onset of prominence activation and increase of flare emission after event 'a,' there is an enhancement in the density and pressure of the thermal plasma (Figure 5.14(c)).

With the onset of event 'c,' we observe a rapid increase in the speed of the erupting prominence (Figure 5.10). It is important to note that HXR images at high energies (>25 keV) do not show significant changes in the location and structure of the HXR source, i.e., a single compact source is observed that remained at the same location. We note that the eruption proceeded symmetrically till ∼05:24 UT with the distinct appearance of an intact eruption front (shown by arrow in Figure 5.9(f) and (g)). Thereafter, the eruption front evolved into an asymmetrical structure (first seen in EUV image at 05:24:30 UT) with the disruption of the south-west part of the eruption front (marked by arrow in Figure 5.9(h)). In the successive images, we clearly observe the downfall of the erupted material which eventually leads to the complete failure of the filament eruption without any CME. Mrozek (2011) and Netzel et al. (2012) have carried out detailed investigations to understand the reason for the confinement of the prominence for this event. They found strong evidence that the interaction between overlying coronal magnetic fields with the erupting prominence was capable to suppress the eruption completely.

We have recognized some interesting morphological structures associated with the erupting prominence that overlap the flare's impulsive phase (∼05:21–05:23 UT) and highlighted in EUV 171 Å images in Figure 5.12. Here we emphasize that this phase corresponds to the interval when the erupting prominence attained the maximum speed of $\sim$242 km s^{-1} (Figure 5.10). These structures consists of rapidly expanding bright twisted loops at the front and spiky patterns at the following part which very likely represent the helically twisted loops associated with the erupting prominence. These structures can be attributed to the portions of the heated prominence within the flux rope. The HXR source at 25–40 keV along with corresponding spectrum (Figure 5.13(f)) presents evidence for non-thermal emission from accelerated electrons in that region in addition to hot plasma. Further, from the EUV images, it is apparent that the magnetic field lines underwent curving toward the bright central region after being stretched by the erupting prominence-flux rope system (shown by arrows in Figures 5.12(b), (c), and (e)).

Flux ropes are considered to be an important structural component in the models of solar eruptions. Many recent studies validate the existence of flux ropes in the lower corona in EUV observations, mostly in hot EUV channels (Li et al. 2005; Cheng et al. 2011; Kumar et al. 2012; Patsourakos et al. 2013; Joshi et al. 2014; Vemareddy and Zhang 2014). Here we emphasize that evidence for a flux rope was found just after the peak 'c' (the largest peak) of the flare impulsive phase (Figure 5.8). It is probable that the flux rope was formed following this most violent episode of energy release. Li et al. (2005) presented a very clear example of formation and rise of an EUV flux rope structure during the impulsive phase of an X-class flare. These observations suggest that a flux rope has a multi-temperature structure that possesses several structural components, such as, sigmoid, hot plasma blob or plasmoid, leading edge, etc. In our observations, the flux rope structure was seen in EUV 171 Å (which represents plasma at a temperature of $\sim$1 MK) presumably due to the heating of the prominence that lies within the flux rope. Gilbert et al. (2007) illustrated three kinds of magnetic topology that can lead to the diversity of eruptive phenomena: full, partial and nil (Gilbert et al. 2001). According to this study, magnetic reconnection can occur completely above the system of a prominence and its supporting flux rope or within it leading to nil or partial eruption of the filament. We believe that the eruption of bright prominence material along with the helically twisted loops represents the case of magnetic reconnection occurring within the system of prominence and supporting magnetic flux rope. However, we believe that this is just a part of the flux rope which contain the prominence body. It is very likely that the remaining part of the flux rope, devoided of the prominence, might exist at a very high temperature which is not visible in 171 Å EUV images.

MW sources at 17 and 34 GHz show an interesting evolution from lower as well as higher coronal regions (Figure 5.11). In general, we note significant differences in the morphology of MW and HXR sources although one of the MW sources (which appeared at the early impulsive phase; see Figure 5.9(h)) exhibits spatial correlation with the HXR source throughout the flare. During event ‘a’ (i.e., between 05:18–05:19 UT), we observe a 34 GHz MW source with two distinct centroids having a separation of $\sim 18''$ (see Figure 5.11(a) and (b)). On the other hand, 17 GHz images (note that 17 GHz images have lower spatial resolution than 34 GHz images) show a relatively extended single source. As discussed earlier, the conjugate centroids (S1 and S2; Figures 5.2 and 5.11(a)), observed at high energy HXR (40−100 keV) and 34 GHz MW emissions, exhibit structural similarities and co-spatiality during event ‘a’. At the second peak (event ‘b’; see Figure 5.8), images at both MW frequencies present similar source structures with a single centroid (see Figure 5.11(c)). During the third MW burst at 05:21 UT (event ‘c’; Figure 5.8), a new MW source originated at a distance of $\sim 33''$ toward the south-west of the pre-existing source (see Figure 5.11(d)–(i)). We mark the newly developed source as S3 (Figure 5.11(d)) and show its location on WL/magnetogram in Figure 5.2. This new source S3 prevailed till the end of the flare ($\sim$05:30 UT) with more prominent appearance at 17 GHz over 34 GHz. We also note the source S3 never appeared in HXRs. The temporal and spatial associations of HXR and MW sources (also see Figure 5.2) indicate that the main energy release site lies in coronal loops close to the magnetic neutral line, probably formed by connecting footpoints S1 and S2. It is also likely that the distant MW source S3 resulted from the injection of flare accelerated electrons onto an overlying coronal loop (which probably connects S1 and S3 regions) as the rising flux rope interacted with overlying loop systems. We note that NoRH has much better dynamic range than RHESSI and therefore it is capable of detecting secondary sources (White et al. 2011).

More importantly, we find multiple MW sources from higher coronal regions that intermittently appear at several locations after ∼05:22 UT (Figures 5.11(e)–(i)). It is also important to note that the whole flaring region (i.e., footpoint and coronal regions associated with the prominence eruption and its subsequent confinement) brightened up in 17 GHz MW emission following the impulsive phase of the flare. In particular, distinct MW sources appeared along the narrow, bright region seen in EUV images where bright blobs of plasma were observed following the confinement of the eruption (marked by arrows in Figures 5.11(g)–(i)). These multiple coronal MW sources were observed after the beginning of disruption of the eruption front, i.e., when the ejected prominence and its supporting flux rope were subjected to confinement by the overlying field lines. In view of this, we conclude that the distinct MW sources in the corona presumably represent emission from hot plasma blobs formed within the collapsing magnetic flux rope.

5.6 Summary and conclusions

In this chapter, we present study of coronal events that occurred in active region NOAA 10646 on 2004 July 14. We observed large-scale contraction of higher active region loops for a time span of ∼30 minutes which was followed by an M6.2 flare and associated failed eruption of a flux rope. The availability of a wide range of multi-wavelength data (EUV, MW, X-ray) from the beginning of the pre-flare to the end of the impulsive phase of the event provided us with a unique opportunity to probe several flare associated phenomena in detail: large-scale loop contraction, small-scale loop brightenings, eruption of prominence-flux rope system and its subsequent confinement. Table 5.1 presents a summary of the different phases of flare evolution and associated phenomena. In the following, we summarize the important results of this study:

1. We have reported implosion of overlying coronal loops that continued over 30 minute during which overlying loops underwent contraction by $\sim$20 Mm (40 % of their original height) during the pre-flare phase. Such a large-scale contraction has been reported for the first time. We observe episodic and localized events of energy release in low-lying loops at the core of the large overlying loops. By synthesizing the multi-wavelength data, we propose that prolonged loop contraction is a manifestation of localized events of energy release that occurred intermittently during the pre-flare phase of the M6.2 flare.

2. The pre-flare phase was dominated by thermal emission with temperatures beyond 20 MK. This indicates that the plasma was already substantially preheated at the flare core before the onset of impulsive phase. We believe that the strong preheating at the flare core will contribute favorably toward efficient particle acceleration during the subsequent impulsive phase of the event.

3. The impulsive phase of the flare is characterized by multiple non-thermal peaks. After the first impulsive peak, associated with strong HXR emission up to 40–100 keV, we observe the activation of the prominence and its supporting flux rope. Our observations imply that the onset of impulsive flare emission (which probably corresponds to large-scale magnetic reconnection) has triggered the eruption of the flux rope.

4. RHESSI spectroscopy reveals high plasma temperatures ($\sim$30 MK) and substantial non-thermal characteristics with electron spectral index (δ $\sim$5) during the impulsive phase of the flare. During this phase, characterized by two sequential HXR peaks, the ratio of total non-thermal energy to maximum thermal energy was found to be ∼7.6 which is consistent with earlier studies. More importantly, the time-evolution of thermal energy nicely correlates with the variations of the cumulative non-thermal energy throughout the impulsive phase of the flare. This can be interpreted in terms of conversion of the energy of accelerated particles to hot flare plasma and is well consistent with the Neupert effect.

5. The prominence along with its supporting flux rope could not have a successful escape through the overlying coronal loops and therefore leads to a confined eruption. The observations of the confinement process of the flux rope are remarkable; we detect multiple coronal MW sources along the trajectory of the eruption. The EUV images show hot plasma blobs on the location of these coronal sources. In our opinion, the coronal MW sources represent emission from hot plasma blobs which are formed within the collapsing magnetic flux rope as a result of its interaction with the overlying and surrounding magnetic field lines.

Our observations highlight the importance of studying the pre-flare activity. This study also underlines that confined eruptions form a very interesting category of solar eruptive phenomena. Their investigations provide a unique opportunity to probe the interaction among different magnetic field systems in the corona besides exploring the triggering mechanisms and energy releases processes.

Chapter 6

Multi-wavelength study of sigmoid-to-arcade evolution in AR 11719

6.1 Introduction

Coronal mass ejections (CMEs) immensely affect space weather phenomena. Thus a major objective of research in solar physics in recent times has been to explore the source region characteristics of CMEs. Through these efforts, some conditions have been recognized that are favorable for eruptions. In this regard, “sigmoid” has been considered an important precursor of a CME. Sigmoids were first identified by the Yohkoh Soft X-ray Telescope (SXT) as large regions producing enhanced soft X-ray emission having S-shaped (or inverse S-shaped) morphology (Rust and Kumar 1996; Manoharan et al. 1996; Pevtsov et al. 1996; Sterling and Hudson 1997). Using SXT data, Hudson et al. (1998) studied the source region of several halo CMEs and found that, for majority of events, the source regions exhibited a characteristic pattern in which pre-eruption sigmoids turned into loop arcades following the passage of CME (see also Sterling et al. 2000; Moore et al.

2001). Sigmoids are typically interpreted as evidence of strong shear or twist in active regions, i.e., source regions of non-potential "free" energy. Using a large data set of SXT images, Canfield et al. (1999) classified solar active regions in sigmoidal and non-sigmoidal categories and found that the former type of activity centers are more likely to be eruptive than the other ones. Moore et al. (2001) analyzed six sigmoidal single-bipole eruptive events using Yohkoh/SXT data. Out of six events, four were ejective explosions and two were confined eruptions. In their sample, each event was a magnetic explosion that occurred in an initially closed single bipole in which the core field was sheared and twisted in the form of sigmoid, having an oppositely curved elbow on each end (see Figure 1 of Moore et al. 2001). All the explosions begin with brightening and expansion of two elbows together with the appearance of short bright sheared loops low over the neutral line. Further, they found that all six events are single-bipole events in that during the onset and early development of the explosion they show no evidence for reconnection between the exploding bipole and any surrounding magnetic fields. They concluded that in each of their event the magnetic explosion was unleashed by runaway tether-cutting via implosive/explosive reconnection in the middle of sigmoid, as in the standard model.

Underneath the twisted coronal SXR structures, filament channels are frequently found in Hα observations (Pevtsov et al. 1996; Pevtsov 2002; Gibson et al. 2002). Although the *sigmoid-to-arcade* evolution is quite dramatic, the underlying filament may not show significant changes with the sigmoid eruption (Pevtsov 2002). Sigmoid can also develop over decayed active regions that exhibit weak and dispersed distribution of magnetic flux (Glover et al. 2001). We believe that sigmoids and filaments are magnetically coupled structures although they exist at different heights in the solar atmosphere and correspond to the hottest and coldest material associated with active region corona. Therefore, it is essential to probe what happens in-between these two layers and temperatures regions during the formation and disruption stages of the sigmoids. This objective can

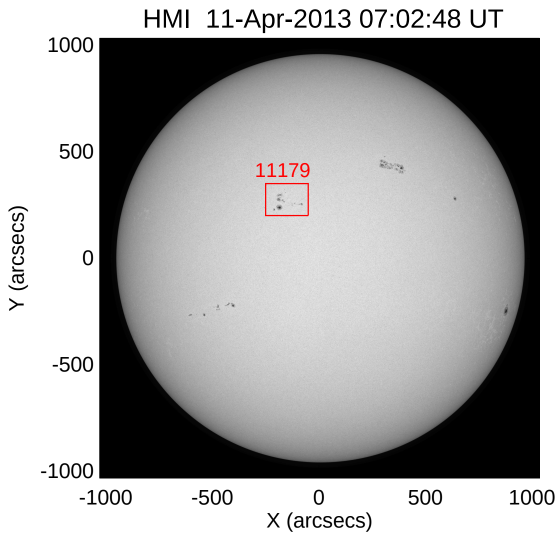

Figure 6.1: White light image of the full Sun taken by HMI/SDO on the day of event reported in this chapter. The active region 11719 is enclosed in a rectangular box.

be accomplished by the analysis of suitable multi-wavelength data sets. Recent studies indicate that sigmoidal structures are visible in a wide range of temperature (Liu et al. 2007). Finally, we need to understand how the overlying coronal and chromospheric structures are related to underlying magnetic field evolution through the photosphere.

In this chapter, we present a comprehensive multi-wavelength analysis of sigmoidal active region NOAA 11719 on 2013 April 11. The location of active region on solar disk is illustrated in Figure 6.1. We discuss the evolution of this active region over a period of ten hours (00:00–10:00 UT) during which EUV sigmoid structure was formed by the interaction of coronal loops system. With the expansion of twisted flux ropes, the sigmoid underwent an activation phase and subsequently erupted. The evolution of sigmoid was observed at AIA 94 Å images which implies that the structure comprised of very high temperature plasma (∼6 MK). During the eruption, we observed a large M6.5 flare (SOL2013-04-11) which is characterized by a prolonged rise phase of ∼21 min. We present an observational overview of activities in Section 6.2. The results are presented in Section 6.3 which are derived from X-ray, E(UV) and radio observations. We discuss our results and emphasize the new findings of this work in Section 6.4. A few concluding remarks are given in section 6.5.

6.2 Overview of observations

In Figure 6.2, we present multi-wavelength view of active region NOAA 11719 at white light (WL), 94 Å and Hα wavelengths. The WL image clearly indicates that the active region consists of several small-to-intermediate sized sunspots with the largest one possessing negative polarity (cf. figures 6.1(a) and (b)). It is interesting to note that most of the visibly prominent sunspots are of negative polarity. Further, there is scarcity of sunspots exhibiting positive polarity while the positive flux region is dispersed over a relatively larger region (Figure 6.1(b)). The overall photospheric flux distribution suggests $\beta\gamma$ magnetic configuration of the AR. An inverse S-shaped structure (i.e., a sigmoid) is observed in 94 Å image which consists of a set of highly sheared coronal loops (Figure 6.1(c)). From Hα filtergram of the active region, we find that a long filament channel existed under the coronal sigmoid which is indicated by arrows in Figure 6.1(d).

We observed significant variations of line-of-sight (LOS) photospheric magnetic flux in AR 11719 from ∼5 hrs prior to the eruption till the post-eruption phase (∼00:00–10:00 UT). During the eruption of the flux rope, a large M6.5 two-ribbon flare was observed in the source region (∼06:45–07:45 UT) and a halo CME was recorded in the solar corona[1].

6.3 Analysis and results

6.3.1 Pre-eruption activities

Formation and evolution of EUV sigmoid

Pre-eruption activities refer to the processes leading to formation, activation, and expansion of an EUV sigmoid that subsequently erupts during M6.5 eruptive flare. The evolution of sigmoid in pre-eruption phase is illustrated in Figure 6.3 by a

[1]http://cdaw.gsfc.nasa.gov/CME_list/UNIVERSAL/2013_04/univ2013_04.html

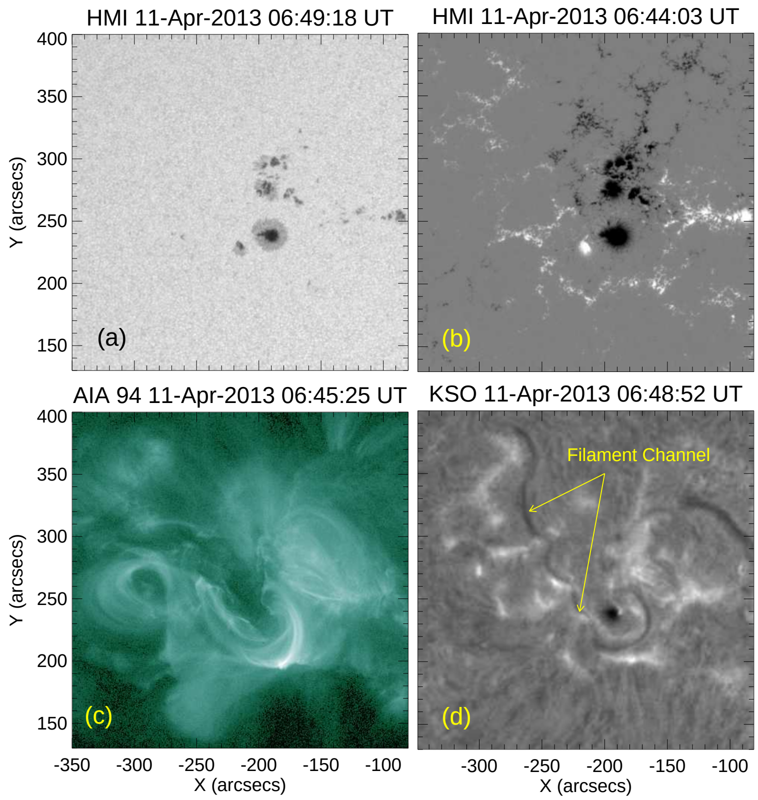

Figure 6.2: Multi-wavelength view of active region 11719 on 2013 April 11. Panel (a): White light picture of the active region showing the distribution of sunspots. Panel (b): HMI line-of-sight magnetogram presenting magnetic polarity distribution of active region. Panel (c): AIA 94 Å image of pre-flare phase showing sigmoidal structure. Panel (d): KSO Hα image showing a long filament channel (marked with arrows) along the polarity inversion line.

sequence of AIA 94 Å images. In the beginning (∼00:00 UT), two closely situated bundles of coronal loops are identified (marked by arrow in Figure 6.3(a)). At this stage, we cannot clearly identify connectivity between these loops. From ∼01:40 UT, the intensity of two loop systems increases and we clearly notice establishment of connectivity between them in a sequential manner. This phase (∼01:40–02:00 UT) is characterized by build-up of bright, diffuse emission in the region that lies between the two loop systems. The coupled loop system undergoes further expansion and the whole region evolves into a large coronal sigmoid (see Figure 6.3(h)). The examination of this sigmoid during the whole pre-eruption

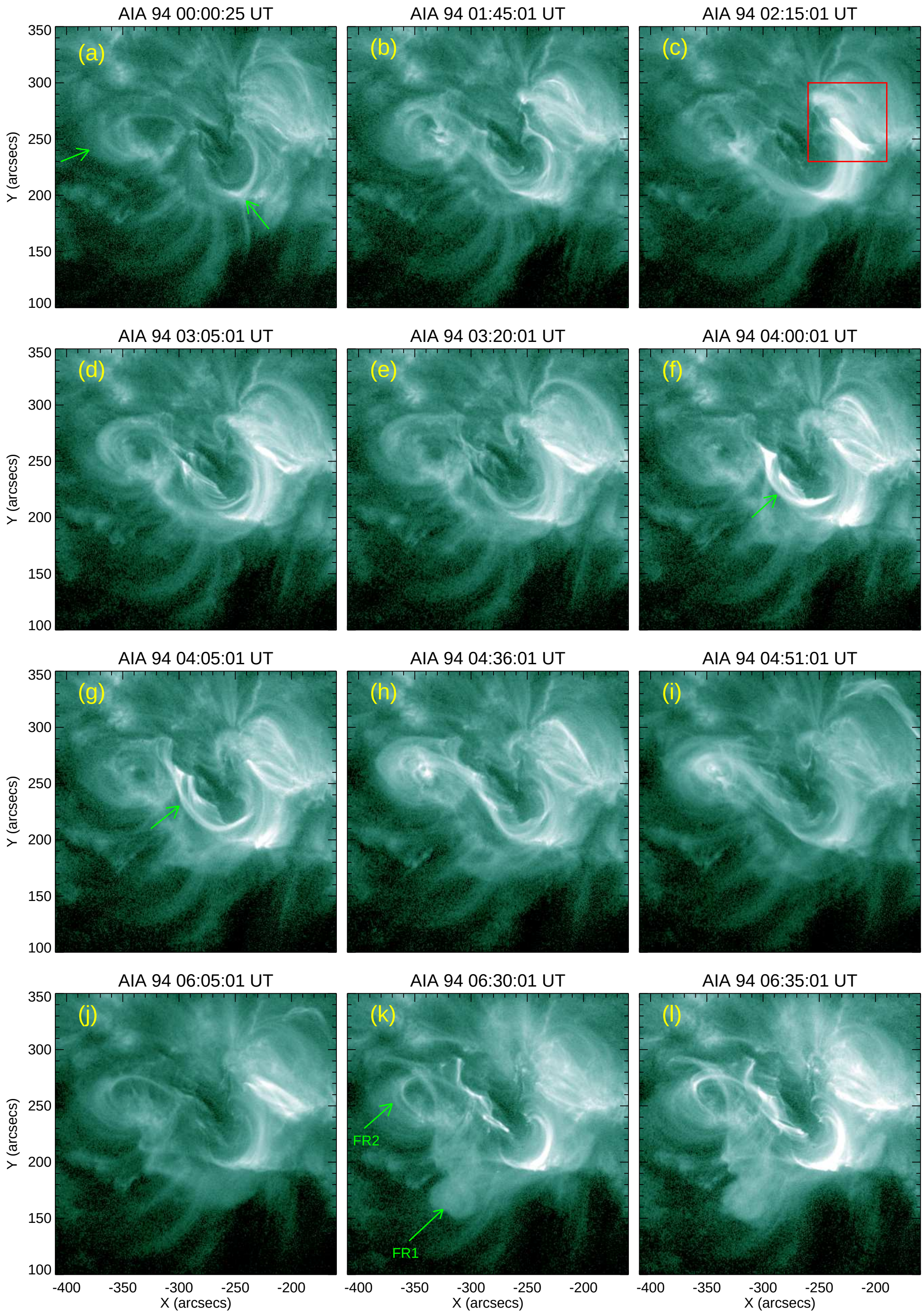

Figure 6.3: Series of AIA 94 Å images showing the development of sigmoidal structure in active region NOAA 11719 during pre-eruption phase. Two evolving flux ropes (FR1 and FR2) are indicated by arrows in panel (k).

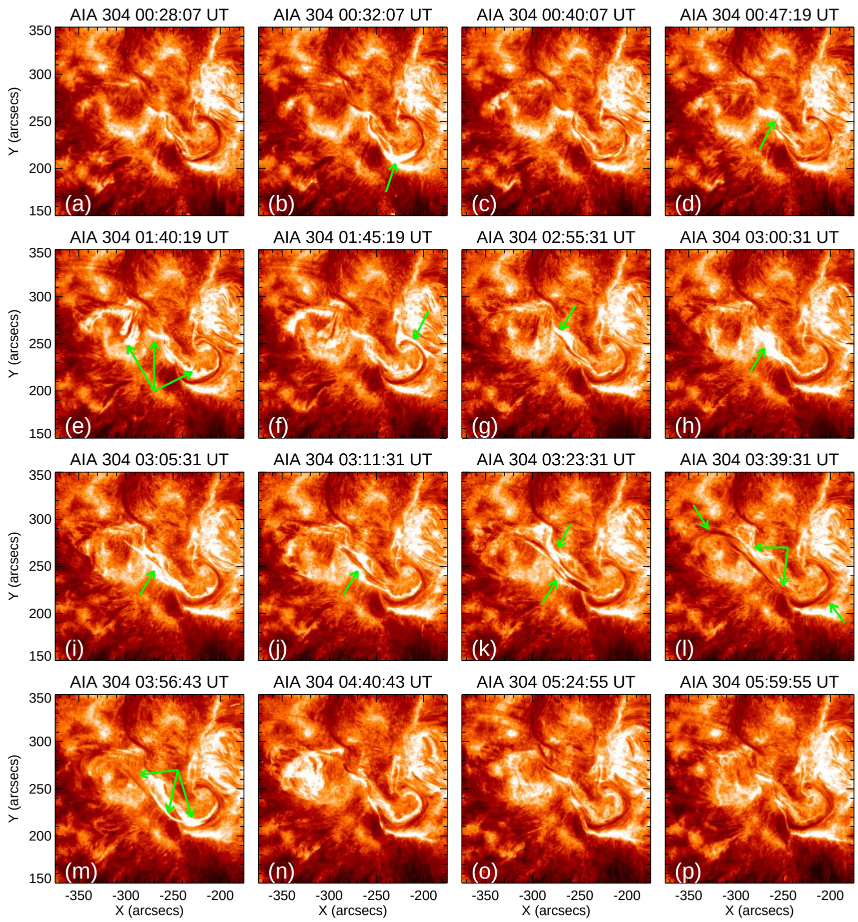

Figure 6.4: Series of AIA 304 Å images showing the occurrence of sequential brightenings (indicated by arrows) from different locations of a long filament channel. In addition to the several brightenings, the formation, activation, and destabilization of the eastern part of the filament channel can also be seen in panels (g) and (i)–(l).

phase (i.e., before the onset of M6.5 flare at 06:55 UT) reveals several important activities that suggest activation of the sigmoid (i.e., the flux rope) several hours (∼5 hrs) prior to its total loss of equilibrium.

It is noteworthy that the western leg of the sigmoid (shown within the box in Figure 6.3(c)) exhibited multiple incidences of localized brightenings during the pre-eruption phase (note structured emission in EUV 94 Å images from this region at ∼02:10–02:25 UT, ∼03:05–03:35 UT, ∼04:30 UT, and ∼06:00–06:10 UT). We further emphasize that the region close to western leg of the sigmoid

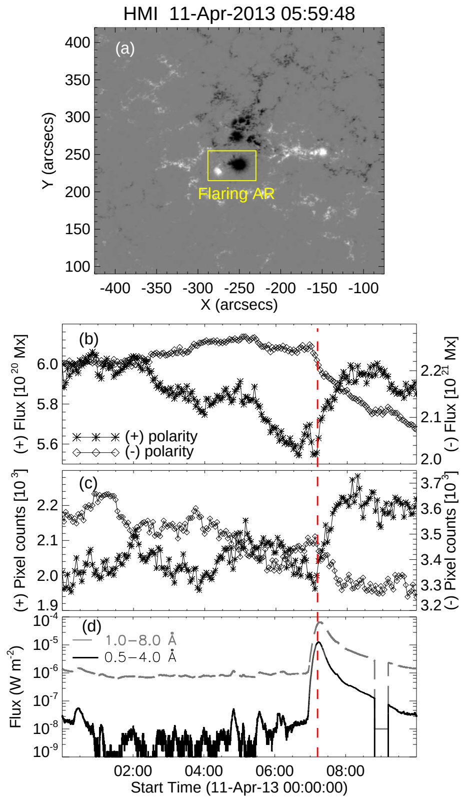

Figure 6.5: Panel (a): A representative magnetogram showing magnetic field distribution in AR NOAA 11719. The flaring area is enclosed with a rectangular box. Panels (b) and (c): The temporal evolution of magnetic flux and pixel counts of positive and negative polarities from the flaring region. Panel (d): Plots of GOES SXR fluxes at 0.5–4 and 1–8 Å channels. The vertical dashed line marks the peak time of the M6.5 flare.

is densely occupied with a cluster of low-lying loops. It is very likely that the multiple localized brightenings imply episodes of magnetic reconnection between the western part of expanding flux rope associated with the sigmoid and the adjacent low-lying loop systems. Another striking evidence of sigmoid activation comes from the observations of its middle portion (i.e., flux rope suspended in the corona) where we notice lift-up of the flux rope in multiple steps which are accompanied with loop-like structured emission (note EUV images of the middle portion of sigmoid at ∼03:00–03:15 UT, ∼03:55–04:10 UT, ∼04:30–04:40 UT, ∼06:30–06:40 UT; e.g., Figure 6.3(g) where loop brightening is indicated by an arrow). We further observe rise of the dark (cool) filament along with the hot flux rope at the earlier stages (∼03:00–03:20 UT) which is well consistent with observations of filament activation seen in low temperature channel (e.g., 304 Å) of AIA (refer to section 6.3.1). Finally, we highlight the fast rise of a large bundle of flux rope that evolved into a kinked structure toward the south-east side of

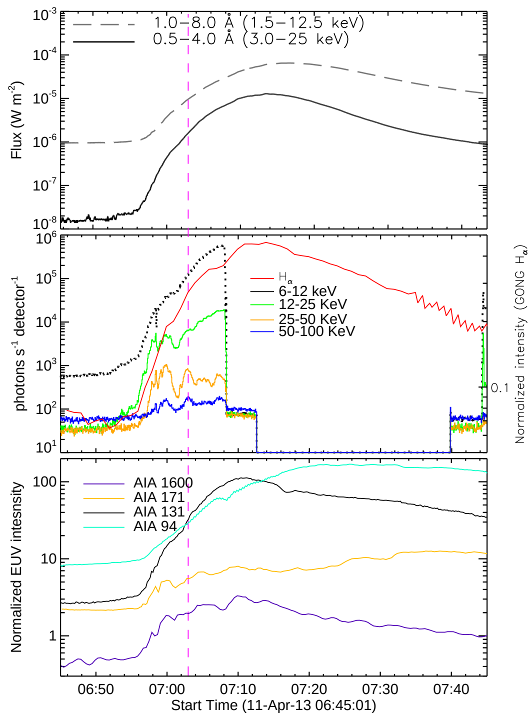

Figure 6.6: X-ray and EUV lightcurves of M6.5 flare on 2013 April 11. Top panel: GOES SXR profiles at both 0.5–4 and 1–8 Å energy channels. Middle panel: HXR lightcurves in 4 different energy bands along with GONG Hα intensity profile of flaring region. Bottom panel: EUV lightcurves at 1600, 171, 131, and 94 Å channels. A vertical dashed line (at 07:03 UT) is drawn to differentiate between early rise phase and late rise phase of the flare.

the sigmoid. We have marked this structure as FR1 in Figure 6.3(k). We clearly notice twisting at the top portion of FR1 and simultaneous expansion of its legs during which the core of sigmoid brightens up at multiple locations (06:30 UT; see Figure 6.3(k)). We further mention the rise of flux rope from the eastern leg of the sigmoid in conjunction with the rise of FR1. Although both rising structures have originated from the same sigmoid, for the convenience of our description, we mark them with different terms (FR1 and FR2 as indicated in Figure 6.3(k)).

Episodic energy release in the vicinity of the filament channel

In Figure 6.4, we present sequence of AIA 304 Å images showing the incidences of episodic brightenings in the vicinity of a long filament channel during pre-eruption phase (i.e., between 00:30 UT and 06:00 UT). This filament channel is embedded within the coronal sigmoid as discussed in Section 6.2. At the very beginning (i.e., at 00:28 UT), we observed a U-shaped filament at the south-west part of the AR with localized brightening at its southern side (see Figures 6.4(a) and (b)). Thereafter, we note episodic brightenings from different portions of the filament channel (marked by arrows in Figures 6.4(d)–(h)) and simultaneous extension in the length of filament toward the north-east part of the AR. A partial eruption of the newly developed filament from northern side is observed along with intense EUV brightenings at ∼03:05 UT which is marked by arrow in Figure 6.4(i). In the subsequent images, we observe rapidly evolving ribbon-like brightenings that appear to move in opposite directions along the length of filament. These fast evolving ribbon-like structures probably represent oppositely directed parallel flows of plasma. We further note extension in the length of filament for next ∼20–30 minutes. At around 03:40 UT, the filament channel has attained its maximum length and a clear inverse S-shaped structure emerged (see Figure 6.4(l)) which is the chromospheric counterpart of the coronal sigmoid seen in AIA 94 Å images (cf. Figures 6.3 and 6.4). After complete development of the filament, its eastern portion started lifting up and partially disrupted in next few minutes. At this stage, we observed ribbon-like brightenings below the rising portion of the filament (rising filament and ribbon like brightenings are indicated by arrows in Figure 6.4(m)). However, the south-west portion of the filament has remained quiet.

Magnetic flux evolution

It is now well established that coronal transients are driven by the solar magnetic fields. Therefore, it is crucial to examine the evolution of photospheric magnetic fluxes prior to the solar eruptions. We have estimated the positive and negative magnetic fluxes through the central flaring region (shown within the rectangular box in Figure 6.5(a)) above ±10 Gauss, and present their temporal evolution between 00:00 UT and 10:00 UT in Figure 6.5(b). In order to ascertain whether the flux evolution occurs from the pre-existing sunspots regions or new locations, we have also plotted the temporal variations in pixel counts of positive and negative polarities in Figure 6.5(c). From Figure 6.5(b), it is evident that the magnetic fluxes from flaring region exhibit evolutionary phases. In the first phase (∼00:00 to 02:30 UT), the magnetic fluxes of positive and negative polarities do not show any significant variations. During the second phase (∼02:30 to 06:30 UT), the positive flux shows a prominent decrease while negative flux do not show appreciable changes. The third phase of flux evolution (∼06:30 to 09:00 UT) is accompanied by M6.5 eruptive flare. During this phase, we observe sudden changes in the photospheric magnetic fluxes that continued till the decay of the flare. The peak time of flare emission is marked with a dashed vertical line in Figure 6.5(b)–(d). These sudden changes in photospheric magnetic fields accompanying the flare are also reflected in the temporal variations of pixel counts.

6.3.2 Sigmoid-to-arcade evolution and eruptive M6.5 flare

Flare light curves

After a significant pre-eruption activities in the forms of photospheric magnetic changes, formation, evolution and activation of a long filament channel, and localized brightenings from various locations close to filament channel, a large M6.5 flare occurred in AR 11719 which is associated with a halo CME. In Figure 6.6, we present the flare light curves at multiple energy channels from 06:45 to 07:45 UT on 2013 April 11. GOES SXR profiles presented at the top panel indicate that the flare emission started at ∼06:55 UT, peaked at ∼7:16 UT and gradually ended by ∼07:45 UT. GOES light curves suggest that the flare is characterized by a rather prolonged rise phase of ∼21 minute. RHESSI observed rise phase of the flare while missing subsequent phases (from ∼07:06 to 07:45 UT) due to satellite night-time. In Figure 6.6 (middle panel), we provide RHESSI light curves in different energy bands (6–12, 12–25, 25–50, and 50–100 keV) along with the normalized Hα intensity profile (red) of localized flaring region from Global Oscillation Network Group (GONG) data. The comparison of GOES and RHESSI light curves indicate that the multiple HXR peaks (>25 keV) occurred during the

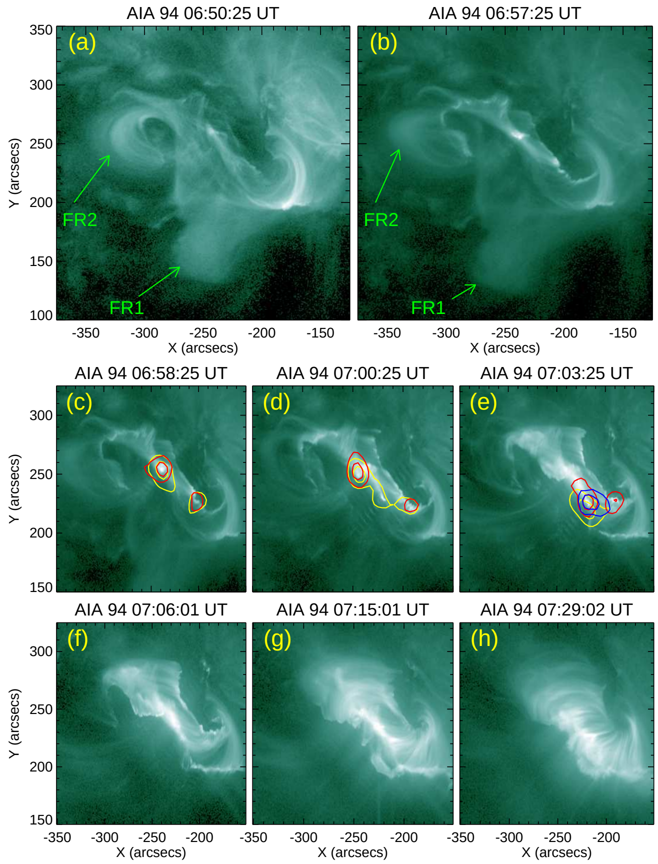

Figure 6.7: Sequence of AIA 94 Å images showing expansion and eruption of flux ropes during M6.5 flare. We have marked the expanding fronts as FR1 and FR2 in panels (a) and (b). Co-temporal HXR sources in 12–25 keV (yellow), 25–50 keV (red), and 50–100 keV (blue) are also overplotted on the representative AIA 94 Å images (panels (c)–(e)). A bright post-flare loop arcade is formed after eruption of the flux rope (see panels (f)–(h)).

prolonged SXR rise phase. At the bottom panel of Figure 6.6, EUV light curves at 94, 131, 171, and 1600 Å passbands are shown. These flux profiles represent the mean intensity of flaring region normalized by the mean intensity of quiet region for each image.

Sigmoid-to-arcade development

In Figure 6.7, we present series of AIA 94 Å images to show sequential evolution of the sigmoid into the post-flare arcade during various phases of energy release in

M6.5 flare. The HXR contours in different energy bands (12–25 keV: yellow, 25–50 keV: red, and 50–100 keV: blue) are also over plotted on a few EUV images. We note that the sigmoid exhibited the signs of activation several hours (∼5 hrs) before the onset of eruption (Section 6.3.1) in the form of multiple episodes of localized energy release and expansion of two flux ropes (FR1 and FR2) at middle and eastern part of sigmoid respectively. We note that activated flux ropes (FR1 and FR2) remained in a quasi-stationary state for several minutes (∼06:40–06:55 UT). The examination of sequence of images clearly reveal that FR1 and FR2 undergo rapid expansion from ∼06:55 UT, marking the onset of rise phase of M6.5 flare (Figures 6.6 and 6.7). With the rapid eruption of FR1 and FR2, we observe intense brightening in the source region which subsequently evolved into two distinct flare ribbons that separate from each other with flare progression. The co-temporal AIA 94 Å and RHESSI HXR images reveal that the high energy emission is entirely associated with the middle portion of the EUV sigmoid. Further HXR emission originates in the form of kernels that lie over conjugate EUV flare ribbons. Following the peak phase of SXR emission (∼07:16 UT; Figure 6.6), a system of post-flare arcades envelop the flaring region that was occupied with sigmoid in the pre-eruption phase (Figure 6.7(h)). In Figure 6.8, we present a few representative images taken by AIA at 131 Å channel. Here, we note a cusp structure above the post-flare loop arcade which is indicated by an arrow in Figure 6.8(c). The rapid expansion and eruption of FR1 is clearly observed in AIA 131 Å images also while the FR2 is not visible at this temperature (see Figure 6.8(a) and (b)).

6.3.3 Dynamical evolution of flare ribbons

According to kinematic and morphological properties of the flare ribbons, we divide evolution of flare ribbons in the following two parts:

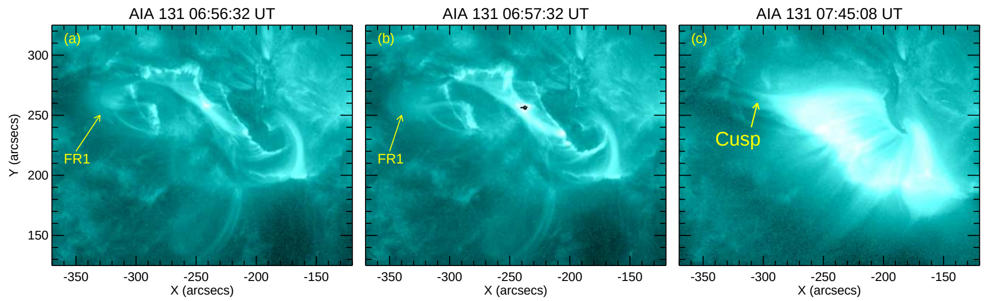

Figure 6.8: Sequence of AIA 131 Å images showing the important stages of the eruption. The expanding flux rope is clearly recognized which subsequently evolved into a bright loop arcade. We also note a cusp at the northern end of the loop arcade (indicated in panel (c)).

Converging motion of flare ribbons during early rise phase

From the X-ray and EUV flux profiles, it is clear that the event under study belongs to the category of long duration events (LDE) which are marked by typical evolution of long, parallel flare ribbons in the chromosphere. However, during the prolonged rise phase of this flare of ∼21 minute duration (Figure 6.6), the flare ribbons and associated HXR sources exhibit a complicated dynamical evolution. For the detailed study of the evolution of flare ribbons, we have presented a sequence of Kanzelhöhe Solar Observatory (KSO) Hα and AIA 1600 Å images in Figure 6.9. The KSO Hα telescope is a refractor with an aperture ratio of d/f = 100/2000 and a Lyot band-pass filter centered at 6563 Å with a FWHM of 0.7 Å. It provide Hα images at a very high cadence of 6 s and a spatial resolution of 1″/pixel. The co-temporal HXR contours in 25–50 keV (red) are also overplotted on a few representative Hα images (Figures 6.9(c), (e)–(g)). The early Hα flare emissions are originated in the form of bright patches (see Figures 6.9(a) and (b)). It is important to note that the eastern flare ribbon presents semicircular morphology during the early stages (i.e., ∼06:55–07:00 UT; see Figure 6.9(b)–(f)). A comparison of Hα filtergrams with the evolution of sigmoid seen in AIA 94 Å images (cf. Figures 6.9 and 6.7) suggests that the formation of semicircular flare ribbon is associated and probably physically linked with the eruption of overlying

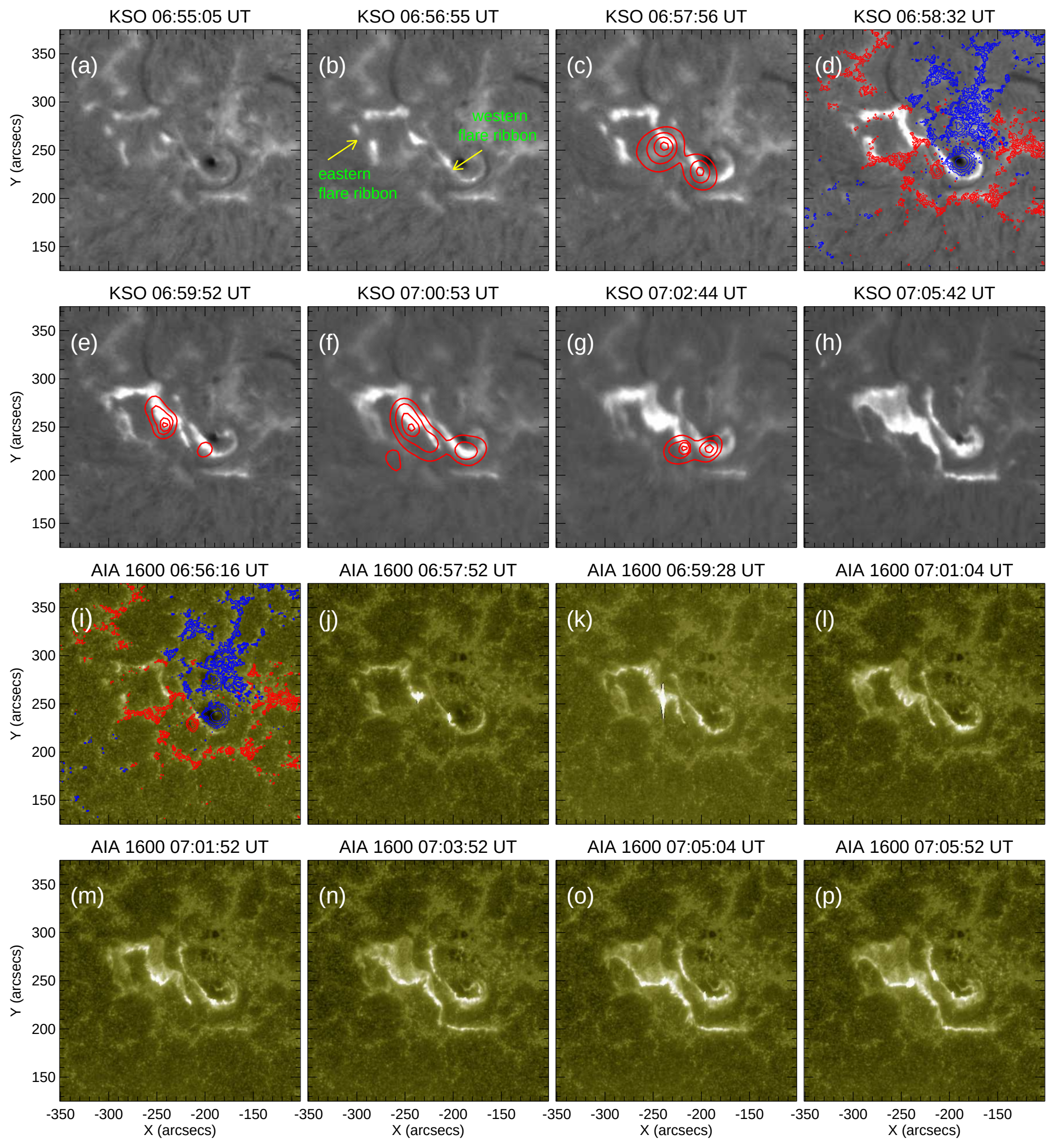

Figure 6.9: KSO Hα (panels (a)-(h)) and AIA 1600 Å (panels (i)-(p)) images showing the temporal evolution of flare brightenings/ribbons during early rise phase (i.e., 06:55–07:03 UT; see Figure 6.6). During this early phase, the flare ribbons present a semicircular morphology and show lateral extension toward each other. Note that after this early phase ($\sim$07:05 UT), flare ribbons become parallel to each other and exhibits "standard" morphology and spatial evolution. The eastern and western ribbons are indicated by arrows in panel (b). The co-temporal HXR contours in 25–50 keV (red) energy band are overplotted on a few representative Hα images (panels (c), (e)–(g)). In panels (d) and (i), the contours represent the magnetic polarity distribution (blue: negative, red: positive) over Hα and AIA 1600 Å images respectively.

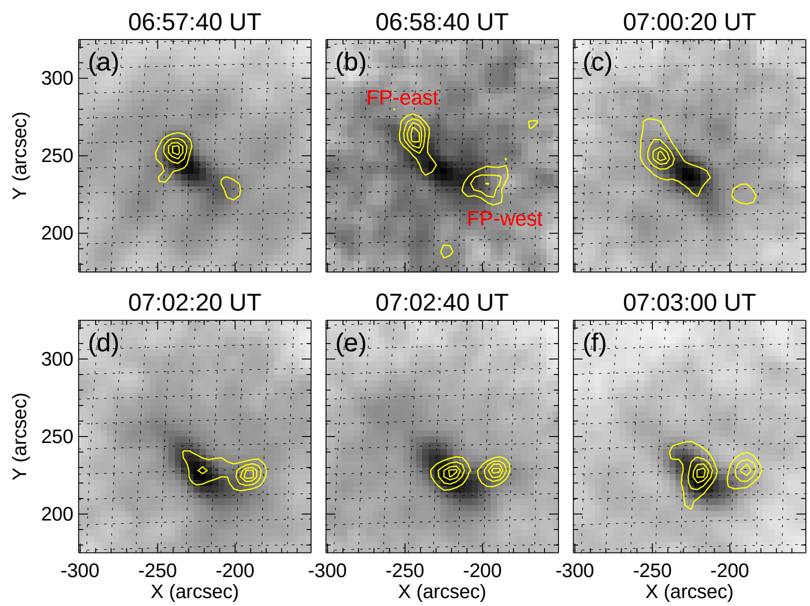

Figure 6.10: Sequence of RHESSI images in 6–12 keV (background images) overlaid by co-temporal contours of 25–50 keV HXR sources. We note the converging motion of HXR foot-point sources at 25–50 keV during prolonged rise phase of the flare. In panel (b), we named the conjugate FP sources as FP-east and FP-west.

flux rope (FR1). On the other hand, western flare ribbon is shorter and presents a simple morphology. We note that the HXR conjugate sources in 25–50 keV energy bands nicely correlates with the brightest part of the respective Hα flare ribbons (see Figures 6.9(c), (e)–(g)). Further, we note that eastern flare ribbon extends toward south-west direction, parallel to the polarity inversion line (PIL) until ∼07:05 UT while the western flare ribbon evolves in the opposite sense. The lateral extension of eastern flare ribbon is more noticeable in AIA 1600 Å images (Figure 6.9(i)–(p)). The morphology and spatial evolution of flare ribbons during this early rise phase is not consistent with the canonical picture of eruptive two-ribbon flares. In particular, the conjugate Hα flare ribbons apparently move toward each other parallel to polarity inversion line (PIL).

The converging motion of flare ribbons is further supported by the spatial motion of HXR footpoint sources, especially in 25–50 keV (see Figure 6.10). In all the images, we observed two distinct HXR sources annotated as FP-east

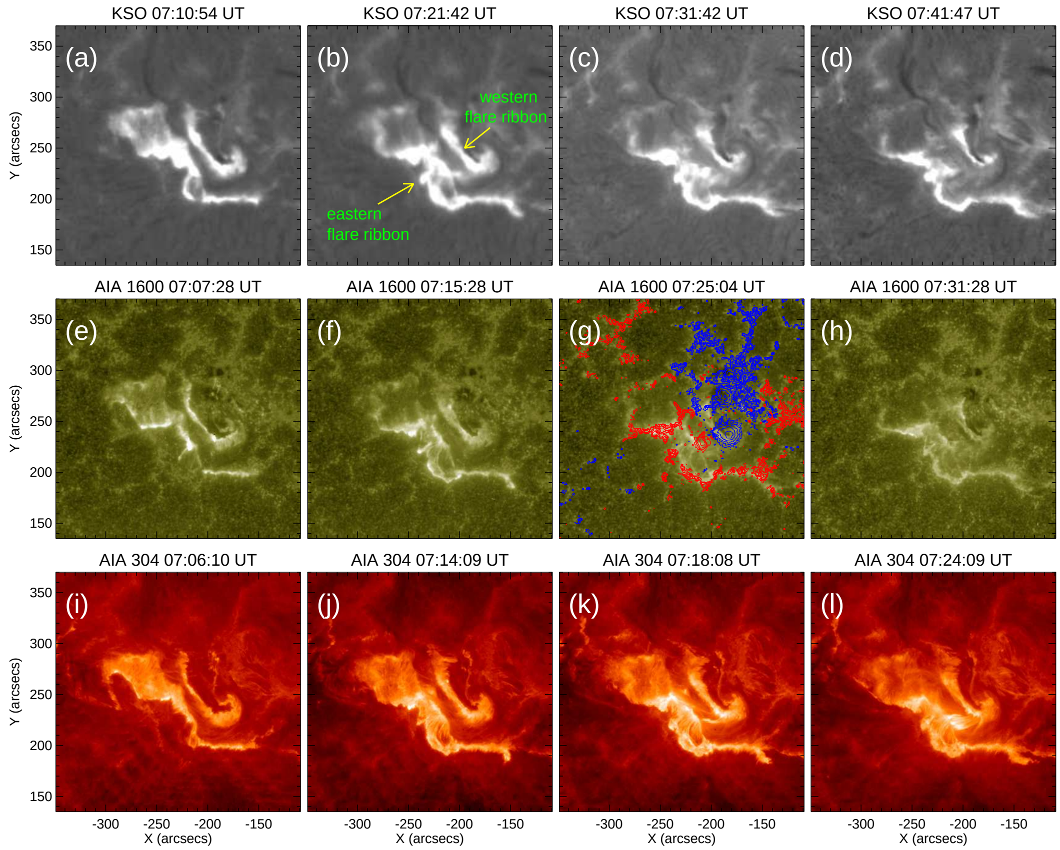

Figure 6.11: The flare evolution during main phase is shown by a sequence of images taken in KSO Hα (top row), AIA 1600 Å (middle row) and 304 Å (bottom row). The eastern and western ribbons are indicated by arrows in panel (b). The co-temporal magnetogram is also overplotted on a AIA 1600 Å image in panel (g). The blue and red contours represent the negative polarity and positive polarity magnetic fluxes, respectively.

and FP-west respectively (Figure 6.10). Due to the limited observations from RHESSI, we could investigate the motion of HXR sources only for the first $\sim$6 minutes of the rise phase. We find that the separation between conjugate HXR sources decreases in the beginning, further confirming the observed converging motions of flare ribbons. To compare the evolution of low and high energy X-ray emitting regions, we have also shown the sequence of RHESSI 6–12 keV images as gray background along with co-temporal 25–50 keV images in Figure 6.10. We find that initially the FP-west is relatively weak and does not show much spatial

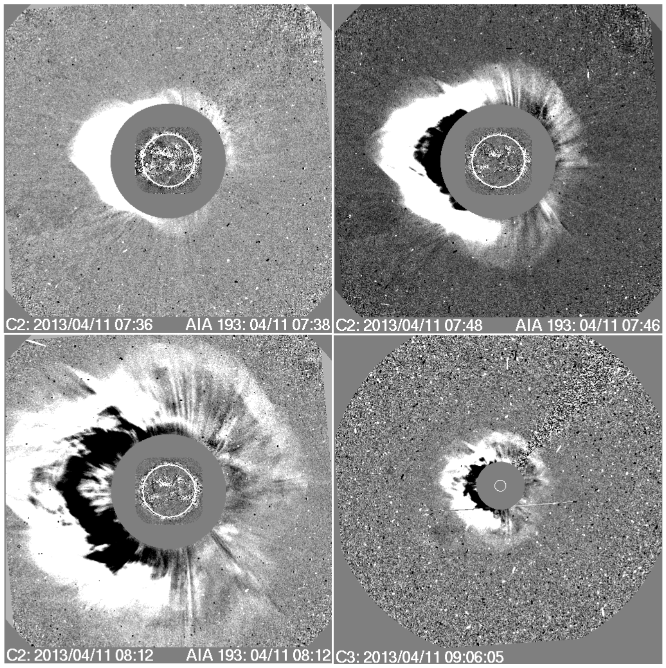

Figure 6.12: Running difference images derived from LASCO C2 and C3 showing the propagation of the CME associated with M6.5 flare.

variations. On the other hand, FP-east is stronger and rapidly moves towards the FP-west. More importantly, the intensity of FP-west is significantly enhanced by the end of rise phase (see Figures 6.10(e) and (f)) when both the FP sources are closest to each other and their respective flare ribbons became almost parallel at ∼07:05 UT (see Figures 6.9(h) and (p)).

Standard motion of flare ribbons and flare's gradual phase

During the early rise phase (06:55–07:03 UT; see previous section), the flare ribbons approach each other parallel to PIL that eventually form two classical parallel ribbons. In the subsequent phases of the flare, we note 'standard' evolution of flare ribbons in which they start moving away from each other in the perpendicular direction to the PIL (Figure 6.11). Out of the two ribbons, the eastern ribbon undergoes much dynamic expansion compared to the western flare ribbon (Figure 6.11). The eastern ribbon exhibits a continuous lateral expansion from

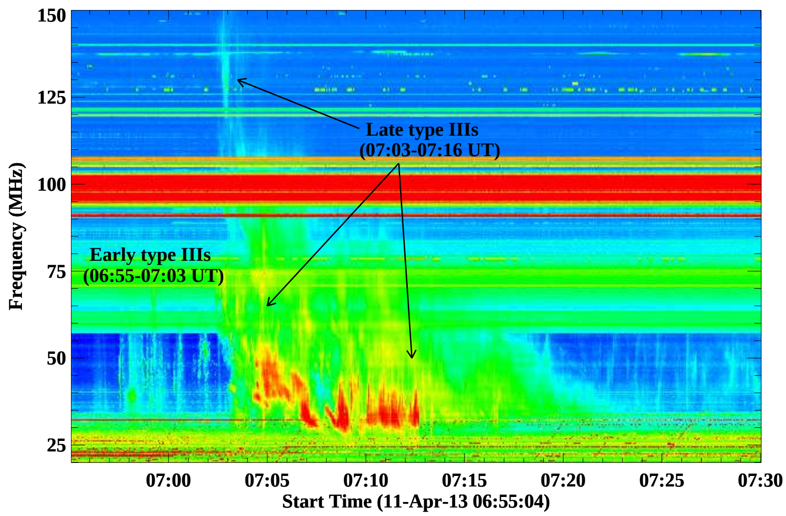

Figure 6.13: Radio dynamic spectra observed by Culgoora Solar Radio Spectrograph during M6.5 flare. We have marked 'Early type IIIs' and 'Late type IIIs' in the dynamic spectra as they observed in early and late rise phase of the flare, respectively.

the north-east to the south-west part of the active region (Figure 6.11). Figure 6.11 clearly reveals that the eastern flare ribbon remains prolonged and bright by late gradual phase of the event while the western flare ribbon appreciably decays in length and intensity. In this context, we emphasize that the western ribbon is associated with stronger magnetic field (negative polarity) while the eastern ribbon forms over the weaker and dispersed flux regions (positive polarity) in the photosphere (Figure 6.2). These observations provide evidence for the asymmetric distribution in the injection of accelerated particles in the post-flare loop systems.

6.3.4 CME observations

The eruption of the flux rope eventually led to an Earth-directed (halo) CME. In Figure 6.12, we show a few representative white-light images observed by LASCO on board SOHO. The CME was first seen in C2 field-of-view (FOV) at 07:24 UT at the position angle of 85°. The halo structure of CME emerged after

07:46 UT in C2 coronagraph which was tracked by C3 coronagraph till 12:00 UT up to the height of 24 $R_\odot$. The height-time plot available at the SOHO LASCO CME catalog[2] shows that the linear speed of CME is ∼861 km s^{-1}. A second-order fit to the height-data indicates a deceleration of ∼8 m s^{-2} in the propagation of CME. Here it is worth to mention that the COR1 coronagraph on board SECCHI/STEREO-B, which observe the inner corona with better temporal resolution (5 min), detected this CME at ∼07:10 UT when the M6.5 flare was still going through its rise phase (Figure 6.6). The early detection of CME could be due to different viewing angle of STEREO-B with the separation angle of 142° from Earth (in heliocentric coordinates) on the day of observation.

6.3.5 Radio bursts (dynamic spectrum)

The Culgoora Solar Radio Spectrograph operating at Narrabri, New South Wales, Australia, sweeps through a frequency range of 18–1800 MHz every 3 seconds to monitor solar radio bursts[3]. In Figure 6.13, we present the dynamic radio spectrum from 06:55 UT to 07:30 UT covering the flaring interval from early rise phase till its gradual phase. The observing summary of spectrograph events provided by Culgoora Observatory suggests complex radio activities comprising type III, type II and type IV emissions during the observing period[4]. During the early rise phase (i.e., 06:55 UT to 07:03 UT) significant radio emissions were observed in the form of group of type III radio bursts (marked as early type IIIs) which are observed in the frequency range of ∼60–30 MHz. This phase corresponds to the period of fast expansion of flux ropes (FR1 and FR2; see Figure 6.7 and Section 6.3.1). It is likely that the expansion of flux ropes will initiate reconnection in the corona as the rising flux ropes will interact with overlying coronal loops. Another group of Type IIIs (marked as late type IIIs) started

[2] http://*cdaw.gsfc.nasa.gov/CME_list/UNIVERSAL/*2013_04/*univ*2013_04.*html*
[3] http: //*www.sws.bom.gov.au/Solar*/2/2
[4] http: //*www.sws.bom.gov.au/World*$_D$*ata*$_C$*entre*/1/9/10

to appear from very high frequency (∼150 MHz) at ∼07:03 UT which extends down to almost lower frequency range of the spectrum (∼30 MHz). These type III bursts likely suggest the beams of electrons thrown out from the reconnection region along the open field lines.

During the late rise phase of the flare (07:04–07:16 UT), we observed a group of strong type III burst that remain intense till ∼07:13 UT, although their traces can be seen till ∼07:16 UT. Further, as typically observed, the type IIIs tend to be more prominent (in intensity as well as width) at the lower end of the frequency range. A close inspection of the radio emission from 07:04–07:09 UT reveal complex structures. Here we recognize a slow drifting component of radio emission from ∼100 to ∼30 MHz which is overlapped with type III spikes. This complex structures probably suggest the "spine" of a type II burst is straddled with type III bursts over much of its length. Finally, we emphasize a temporal correlation between multiple HXR peaks in RHESSI light curves above 25 keV (see Figure 6.6) with bunch of intense type III bursts over the extended period. This correlation between HXR and type III radio emissions along with the fine structures of these group of type IIIs likely suggests successive increase in the site of particle acceleration as a result of the fast expansion of the flux rope in the corona that would result in the opening of field lines at increasing coronal heights by magnetic reconnection.

6.4 Discussions

In this chapter, we present a multi-wavelength investigation of a sigmoid-to-arcade development in AR 11719 on 2013 April 11. The study aims to explore several crucial aspects involved during the processes of solar eruption right from the formation stage of coronal EUV sigmoid to the post-eruption phase of the source region. We investigate the sequence of activities simultaneously at different layers of solar atmosphere during successive transformation of overlying hot active region loops (e.g., coronal structures at 94 Å) into the sigmoid that continued over several hours (∼9 hrs) prior to the eruption. The CME initiation was accompanied with a large two-ribbon M6.5 flare (SOL2013-04-11).

6.4.1 Multi-step process of sigmoid formation

The comprehensive analysis of AIA E(UV) images and HMI magnetograms of ∼ 10 hrs duration was undertaken to explore the formation and eruption processes of sigmoid and its association with the underlying process of magnetic flux evolution through the photosphere. The simultaneous observations of the active region in hot (94 Å; T: 6 MK) and cool (304 Å; T: 50,000 K) channels clearly reveal that formation of sigmoid occurred in multiple steps. The EUV observations at 94 Å reveal that the interaction between pre-existing system of loops finally evolved into a large sigmoid structure. The coronal sigmoids were discovered in soft X-ray emission as a precursor to CMEs. However, many recent studies have confirmed that sigmoid structures can be observed at different EUV channels which provide evidence that sigmoids exist at wider range of temperatures (Liu et al. 2007; Cheng et al. 2014). Our study reveals that transient and localized brightening occurred when the closely situated footpoints of coronal loop systems join together (Figure 6.3) evidencing the role of magnetic reconnection toward the formation of sigmoid. With the complete development of sigmoid, its central part, extended in a large region, showed intense emission at 94 Å images. This implies that the twisted structure is at a higher temperature (T ∼6 MK) than that of the ambient volume. It is likely that the localized, multiple reconnection events occurring within the region have not only changed its magnetic topology toward the formation of the large sigmoid but also contributed in sustaining its temperature at a higher level.

The phase of sigmoid formation in corona is associated with dynamical activities at lower layers of solar atmosphere, viz., chromosphere and transition region.

We observe multiple brightenings at different locations of filament channel which was observed at 304 Å images. Following these localized events of energy release at multiple locations, an S-shaped long filament channel emerged which obviously represent the core of large overlying EUV sigmoid. The study reveals a simultaneous changes in the magnetic configuration of overlying as well as core regions during the formation of sigmoid. The association between the twisted filament structures and overlying coronal sigmoid has been recognized in several papers (Pevtsov et al. 1996; Gibson and Low 2000; Gibson et al. 2002; Pevtsov 2002). In all these studies, the filament was studied in Hα. Pevtsov (2002) studied a set of active region filaments associated with X-ray sigmoid. This study reveals that as the eruption proceeds, sigmoid gets replaced by a cusp or arcade while the underlying Hα filament does not show significant changes. However, unlike to the study of Pevtsov (2002) in which the filament evolution was studied following the onset of eruption, we analyze the filament during the formation stage of sigmoid. Further, in our study, filament evolution is studied in EUV images at 304 Å that observes structures in transition region and chromosphere which are formed at higher temperatures than Hα features. Our observations reveal that the filament and nearby regions underwent a fast morphological and dynamical evolution as the overlying sigmoid was taking its shape. From these observational results, we infer that the upper layers of chromosphere and its overlying transition region were highly dynamic when various coronal activities occurred (observed at 94 Å channel) during the development phase of the sigmoid. This also suggests that perhaps multiple, localized brightenings in corona and lower layers are associated with magnetic reconnection at chromospheric and/or transition region heights. We wish to emphasize that the rapidly evolving ribbon-like brightenings observed in 304 Å images can have important implications. A careful examinations of movie of high-time resolution images at 304 Å indicate that the bright ribbons, appearing both sides of filament, move in the opposite directions. We interpret these rapidly evolving features as oppositely directed plasma flows (see section 6.3.1 and Figure 6.4). Such flows may cause footpoints of coronal loops to move, enhancing the shear of coronal magnetic fields during the pre-eruption phase.

Significant variations in photospheric magnetic flux were observed from the active region during the whole process of sigmoid formation. The active region possessed an interesting magnetic structure in which a stronger field region of negative polarity was surrounded by weaker, dispersed region of positive polarity. We find very interesting phases of flux evolution from the flaring region right from the stages of sigmoid formation to its eruption (Figure 6.5). In the beginning, the flux variations were small. During the coronal and chromospheric activities in the pre-eruption phase, noted in the forms of localized brightenings associated with the interaction/merging of loop systems and filaments, the positive flux exhibited a decrease while negative flux almost maintains its level. The phase of decrease/cancellation of positive flux is associated with the localized brightenings at different segments of the sigmoid. The evolution of photospheric flux through the active region has been observed in earlier observations prior to the sigmoid eruption (e.g., Cheng et al. 2014). The synthesis of multi-channel EUV and magnetogram observations presents a complex picture in which the interaction between the coronal loops, oppositely directed plasma flows at the chromosphere and transition region, and flux cancellation at the photosphere occur simultaneously during the build-up phase of the sigmoid.

The flux evolution after the onset of M6.5 flare is rather drastic and requires a careful interpretation. During this phase, the positive flux exhibited a rapid increase in the beginning and achieved the higher level after the impulsive phase of the flare (Figure 6.5(b) and (c)). On the other hand, negative flux underwent a continuous decrease from the flare onset to its decay (Figure 6.5(b)). Such abrupt, significant, and persistent changes in photospheric magnetic fields accompanying the flare is now a well observed phenomena (Wang et al. 2004; Yurchyshyn et al. 2004; Sudol and Harvey 2005; Petrie and Sudol 2010; Wang et al. 2012) although its physical understanding is still not clear. Recently, Wang et al. (2012) presented concrete evidence of a rapid (in about 30 minutes) and irreversible enhancement in the horizontal magnetic field at the flaring magnetic polarity inversion line (PIL) by a magnitude of 30% during a large X2.2 flare occurred in sigmoidal active region. It has been suggested that the flare-induced changes in the photospheric magnetic fields can also occur as the response of restructuring of coronal field lines by magnetic reconnection which turns the magnetic field lines near the PIL to a more horizontal state (Wang and Liu 2010; Wang et al. 2012).

The sigmoid studied here was a fast evolving structure. As noted in earlier studies, the sigmoid can sustain a stable phase for a long period (even days or weeks). However, the present sigmoid started showing eruptive activities soon after its formation. A similar SXR sigmoid was studied by Pevtsov et al. (1996) which underwent even more rapid evolution. Their study reveals that formation of a sigmoid initiated several minutes before the eruptive flare by the emergence of short loops between two pre-existing fishhook-shaped, large SXR loops. We therefore conclude that the fast evolving sigmoids may not be uncommon structures and require more investigations.

6.4.2 Sigmoid eruption and M6.5 flare

The early phase

The M6.5 flare underwent a very prolonged rise phase of ∼21 minutes during which SXR flux showed a gradual rise (06:55–07:16 UT; Figure 6.6). A careful analysis of imaging observations at E(UV), Hα and HXR channels reveal this phase to exhibit complex dynamical evolution of flare ribbons and HXR footpoints during the early stages. In view of this, we have divided the rise phase in two parts: early rise phase (06:55–07:03 UT) and late rise phase (07:03–07:16 UT). The fundamental difference of these phases lie in the fact that the emission signatures of early rise phase do not comply with the description of standard flare model while the late rise phase correlates well with the criteria of standard model (see e.g., Joshi et al. 2012). Although a flare with prolonged rise phase is a subject of interest in itself, it is not an uncommon phenomena (Bąk-Stęślicka et al. 2011).

Converging motion of flare ribbons is the most crucial aspect of the early rise phase. It is noteworthy that the ribbons appeared (i.e., brightening in chromosphere started) as the flux rope FR1 and FR2 started rising upward (Figures 6.7(a) and (b)). In several recent papers, the flux ropes have been identified in images taken at hot EUV channels, viz., 94, 131, 171 Å (Cheng et al. 2011; Patsourakos et al. 2013; Kumar and Cho 2014; Kushwaha et al. 2015). As typically observed, we note flux ropes as bundle of hot coronal loops in EUV displaying extended, diffuse emission. At this interval, we find type III radio bursts at relatively lower frequencies (annotated as 'early type IIIs' in Figure 6.13). It is very likely that the eruptive expansion of flux ropes caused successive opening of overlying field lines which will set discrete events of magnetic reconnection. The early type III bursts then represent beams of electrons pushed away from the reconnection regions. The coronagraphic observations provide the first detection of the CME associated with this flare at ∼07:10 UT, i.e., during the rise phase of the flare. The eruptive expansion of flux ropes therefore provides the earliest signature of this CME in the source region. The association of type III radio bursts at early stages of CMEs have been observed in earlier studies (see e.g., Joshi et al. 2007).

The converging motion of flare ribbons is observed for ∼4 min. During this period, flare ribbons expanded parallel to polarity inversion line (PIL). Further, ribbons expanded laterally in opposite directions which means that although their vertical separation remains almost constant, they appear to move toward each other. It is noteworthy that this kind of motion is just opposite to the flow patterns noted in 304 Å images during the formation phase of the overlying sigmoid (03:06–03:30 UT; Figures 6.4(i)–(k)). Also we emphasize that both phenomena (oppositely directed parallel flows and ribbon convergence) occurred at approximately same region. These observations indicate that magnetic shear developed in the corona during the sigmoid formation by parallel flows while shear relaxation occurred during the early rise phase. Our interpretations are consistent with the predictions of *rainbow reconnection model* proposed by Somov (1986) (see also Joshi et al. 2009). The converging motion of flare ribbons is confirmed by several recent observations (Bogachev et al. 2005; Ji et al. 2006, 2007; Liu et al. 2008; Joshi et al. 2009) indicating this to be a crucial phenomena of flare evolution. In particular, Liu et al. (2008) noted that during SOL2002-04-30, the two conjugate HXR footpoints first move toward and then away from each other, mainly parallel and perpendicular to the magnetic inversion line, respectively. Further, they found that the transition of these two phases of footpoint motions coincides with the direction reversal of the motion of looptop source.

Moore et al. (2001) investigated the eruption of six bipole sigmoid structures in the context of standard flare model. Their study reveals that during the early stage of explosion, the upward release of flux rope is accompanied with the compact brightening under the middle of the sigmoid. In our case, we clearly observed expansion of flux ropes FR1 and FR2 to be temporarily associated with intense emission observed at AIA 94 Å and RHESSI X-ray images. Thus in the light of model given by Moore et al. (2001) (see their Figure 1), we believe that the eruption of this sigmoid active region NOAA 11719 is likely initiated by internal tether-cutting process.

The standard phase

After early rise phase (>07:03 UT), the flare exhibited the features of a "standard" large eruptive flare as described by the standard flare model. Here the main observational characteristics of standard flare is recognized in the form of increase in the separation of parallel flare ribbons while they move perpendicular to the PIL (Figure 6.11). Following the eruption of flux ropes, we observed the development of arcade of coronal loops over the source region previously occupied by the coronal sigmoid. This phenomena, called *sigmoid-to-arcade* transformation, is well established and theoretically studied in relation to eruptive dynamics of CMEs (Gibson et al. 2002, 2004). The study of associated flare emission originated at the source region of such sigmoid eruptions has important implications toward exploring the complicated processes of thermal and non-thermal energy release (see e.g., Liu et al. 2007). We, therefore, conclude that the standard flare model is well applicable to the late phase of this flare. The consistency with the standard flare model implies that during this phase, the main driver of energy release process is the magnetic reconnection driven by the erupting flux rope.

6.5 Concluding remarks

Sigmoid-to-arcade development is now considered as an important aspect of solar eruptive phenomena. Although the association of sigmoids with eruption is well recognized, we do not have clear idea about the formation of these structures over the active region. In this detailed multi-wavelength study, we have focused on the evolutionary stages of sigmoid formation as well as its eruption. The observations of active region in hot EUV channel (94 Å) reveal the formation of S-shaped flux rope through a sequence of multiple, localized brightenings involving two large pre-existing coronal loops. Considering the fact that the bright emission at 94 Å images corresponds to very hot plasma (T $\sim$6 MK), we attribute multiple localized brightenings during the loop interactions as repetitive magnetic reconnections. Simultaneous to the formation to large sigmoid structure in the corona, we observe fast morphological evolution of a filament channel in the underlying layers of chromosphere and transition region. Our analysis also suggests that the repetitive magnetic reconnections during the pre-eruption phase are likely driven by the magnetic flux evolution through the photosphere. In future studies, we would like to extend this work to more EUV sigmoids to probe the formation stages of sigmoid and its association with phenomena occurring at underlying layers.

The eruption of the sigmoid is accompanied with M6.5 two-ribbon flare. The rise phase of this flare is characterized by converging motions of Hα/UV flare ribbons and decrease in the separation of HXR footpoints. The flare exhibits features of the standard flare model from the late rise phase till its decay. These observations validate recent findings of unusual motions of flare sources during the early rise phase which are formed at chromospheric region (i.e., ribbons or footpoints) and corona (i.e., looptop source). These new results obviously contradict with the standard flare model. We propose to undertake more studies to understand the multi-wavelength aspects of rise phase of solar flares.

Chapter 7

Summary and prospects

In this thesis, I have studied some important issues pertaining to the multi-wavelength aspects of solar eruptive phenomena at temporal, spatial, and spectral domains. In the first chapter, I have introduced the topic of my research and outlined the objectives of this thesis. We have described the solar observing instruments in chapter 2 whose data are analyzed to carry out the work presented in this thesis. In this chapter, I briefly summarize the results presented from chapters 3–6 and discuss the scope for future work which I would like to pursue in this area.

7.1 Summary

Chapter 3 – In this chapter, I have presented comprehensive multi-wavelength studies of two active region prominences occurred in active regions NOAA 10656 on 2004 August 18 and NOAA 11548 on 2012 August 18. Both the prominences were located close to the solar limb. For both events, we have analyzed EUV and X-ray measurements of extended period covering quasi-static, slowly evolving and eruptive phases of the prominences. A major objective of this study is to identify the process of prominence destabilization through the observations of pre-eruption phase of the active region and pre-flare activity. The violent eruption of the prominences is accompanied by major solar flares. We have synthesized multi-wavelength measurements during the eruptive phase of prominences to explore the signatures of magnetic reconnection in the corona and discuss the thermal and non-thermal effects driven by the prominence eruption.

The prominence eruption in active region NOAA 10656 on 2004 August 18 was associated with multiple flare activity over a period of 2 hr. Out of four successive flares, three were class C events, and the final event was a large X1.8 flare. The activities during the pre-eruption phase, i.e., before X1.8 flare are characterized by three localized episodes of energy release occurring in the vicinity of a filament that produces intense heating along with non-thermal emission. A few minutes before the eruption, the filament undergoes an activation phase during which it slowly rises with a speed of $\sim$12 km s^{-1}. The filament eruption was accompanied with an X1.8 flare during which multiple HXR bursts are observed up to 100–300 keV energies. We observe a bright and elongated coronal structure simultaneously in E(UV) and 50–100 keV HXR images underneath the expanding filament during the period of HXR bursts, which provides strong evidence for ongoing magnetic reconnection. This phase is accompanied by very high plasma temperatures of $\sim$31 MK, followed by the detachment of the prominence from the solar source region. From the location, timing, strength and spectrum of HXR emission, we conclude that the prominence eruption is driven by the distinct events of magnetic reconnection occurring in the current sheet below the erupting prominence. These multi-wavelength observations also suggest that the localized magnetic reconnections associated with different evolutionary stages of the filament in the pre-eruption phase play an important role in destabilizing the active region filament through the *tether-cutting* process, leading to large-scale eruption and X-class flare.

The prominence eruption in active region NOAA 11548 on 2012 August 18 was associated with an M1.8 flare. Prior to the activation of the prominence, we observed multitude of coronal activities in the form of a blowout jet, rapid evolution of a flux rope, and events of episodic energy release. Out of these activities, the flux rope exhibited the most dramatic evolution, characterized by splitting and rotation along with localized brightenings during its outward expansion. These coronal activities are followed by the prominence activation during which it slowly rises with a speed of $\sim$12 km s^{-1}. We note a gradual increase of thermal X-ray and EUV emissions under the activated prominence, suggesting precursor emission due to the onset of magnetic reconnection at the flare current sheet formed below the slowly rising prominence. We suggest that the coronal activities prior to the prominence activation provide observational evidence of *breakout* reconnection at higher corona that would result in the weakening of constraining magnetic configuration thus allowing slow rise of the large, dense prominence. The prominence underwent catastrophic loss of equilibrium with the onset of impulsive phase of M1.8 flare suggesting large-scale energy release by magnetic reconnection. At this stage, a plasmoid eruption was observed below the apex of erupting prominence at multiple EUV channels. The temporal, spatial and kinematic correlations between erupting prominence and plasmoid imply that the magnetic reconnection supported the fast ejection of prominence in the lower corona.

Chapter 4 – Confined flares are largely characterized by very rapid temporal and morphological evolution within a compact region. Unlike the eruptive flares, where the large-scale reconnection is driven by flux ropes or filament eruptions, we do not have clear idea about the triggering of reconnection in confined flares. Now with the availability of solar observations from SDO and RHESSI with unprecedented resolutions, we have made an effort to investigate the triggering mechanism and magnetic reconnection scenario in a confined M4.0 flare. This confined flare occurred in active region NOAA 11302 on 2011 September 26. The flare light curves exhibit an abrupt rise of non-thermal emission with co-temporal

HXR and MW bursts that peaked instantly without any precursor emission. This stage was associated with HXR emission up to 200 keV that followed a power law with photon spectral index (γ) $\sim$3. Another non-thermal peak was observed after 32 s from the first one which was more pronounced in MW light curves than HXR profiles. Dual peaked structure in the MW and HXR light curves suggest a two-step magnetic reconnection process. EUV images exhibit a sequential evolution of the inner and outer core regions of magnetic loop systems while the overlying loop configuration remained unaltered. Combined observations in HXR, E(UV), and Hα provide support for flare models involving the interaction of coronal loops. The magnetograms obtained by the HMI/SDO reveal emergence of magnetic flux that began $\sim$5 hr before the flare. However, the crucial changes in the photospheric magnetic flux occurred about one minute prior to the flare onset with opposite polarity magnetic transients appearing at the early flare location within the inner core region. The spectral, temporal and spatial properties of magnetic transients suggest that the sudden changes in the small-scale magnetic field have likely triggered the flare by destabilizing the highly sheared pre-flare magnetic configuration.

Chapter 5 – Confined eruption (or failed eruption) forms a special category of solar eruptive phenomena. Such kind of eruptions occur less frequently and therefore form a less studied topic in solar physics. In such cases, one needs to closely examine the state of overlying coronal loops of the active region that likely suppress the rapid ejection of the flux rope.

In this chapter, we have presented a comprehensive study of the flaring and eruptive activities observed in active region NOAA 10646 on 2004 July 14 over a span of one and half hours. After the pre-flare phase, we observe a major M6.2 flare during which a large flux rope and associated prominence material underwent confined eruption. A major highlight of this study lies in the striking observation of implosion of overlying coronal loops that continued over 30 minutes during which overlying loops underwent contraction by 20 Mm (∼40% of their initial height) during the pre-flare phase. Such a large-scale contraction has been reported for the first time. We observe episodic and localized events of energy release in low-lying loops at the core of the large overlying loops. By synthesizing the multi-wavelength data, we propose that prolonged loop contraction is a manifestation of localized events of energy release that occurred intermittently during the pre-flare phase of the M6.2 flare. Our observational results are in good agreement with Hudson's conjecture (Hudson 2000) of coronal implosion.

The impulsive phase of the flare is characterized by multiple non-thermal peaks. After the first impulsive peak, associated with strong HXR emission up to 40–100 keV, we observe the activation of the prominence and its supporting flux rope. Our observations imply that the onset of impulsive flare emission (which probably corresponds to large-scale magnetic reconnection) has triggered the eruption of the flux rope. RHESSI spectroscopy reveals high plasma temperatures (∼30 MK) and substantial non-thermal characteristics ($\delta \sim 5$) during the impulsive phase of the flare. During this phase, characterized by sequential HXR peaks, we found that the total non-thermal energy and maximum thermal energy are of the same order with a ratio of ∼7.6. More importantly, the time evolution of thermal energy correlates with the variations of the cumulative non-thermal energy throughout the impulsive phase of the flare. This can be interpreted in terms of efficient conversion of the energy of accelerated particles to hot flare plasma implying validation of the Neupert effect in terms of flare energetics.

Chapter 6 – *Sigmoid-to-arcade* development has been recognized as an important aspect of solar eruptive phenomena. Although several earlier studies underline the association of sigmoids with eruptions, our knowledge is still limited regarding the formation of these structures over the active region. It is therefore desirable to examine sigmoids in multi-channel EUV images and probe the underlying changes in photospheric magnetic flux for insightful understanding of these important signatures of CME. With this motivation, we analyze the multi-wavelength data of an eruptive event that encompasses the *sigmoid-to-arcade* development.

The observations presented in this chapter correspond to *sigmoid-to-arcade* transformation observed in active region NOAA 11719 on 2013 April 11. The evolution and eruption of sigmoid was studied over the duration of ∼10 hrs. The disruption of sigmoid caused a major two-ribbon flare of M6.5 class. The observations in hot EUV channel (94 Å) reveal the formation of inverse S-shaped flux rope over the active region through a sequence of multiple, localized brightenings involving two large pre-existing coronal loops. Considering the fact that the bright emission at 94 Å images corresponds to very hot plasma (∼6 MK), we attribute multiple localized brightenings during the loop interactions as repetitive magnetic reconnections. Simultaneous to the formation of large sigmoid structure in the corona, we observe fast morphological evolution of a filament channel in the underlying layers of chromosphere and transition region. The synthesis of multi-channel EUV and magnetogram observations presents a complex picture in which the interaction between the coronal loops, oppositely directed plasma flows at the chromosphere and transition region, and flux cancellation at the photosphere occur simultaneously during the build-up phase of the sigmoid.

The sigmoid eruption led to an M6.5 eruptive flare and a halo CME. The rise phase of this flare is marked by converging motions of Hα/UV flare ribbons and decrease in the separation of HXR footpoints. The flare displays the features of the standard flare model from the late rise phase till its decay. These observations support recent findings of unusual motions of flare sources during the early rise phase which are formed at chromospheric region (i.e., ribbons or footpoints) and corona (i.e., looptop source). These new results obviously contradict with the standard flare model. Therefore, we believe that it would be promising to undertake more studies in future to explore the multi-wavelength aspects of rise phase of solar flares.

7.2 Future work

My future research would include further studies on the lines of investigations we have been carrying out. We would like to advance with new tools and techniques to understand the eruptive phenomena on the Sun. Some of the studies which may be pursued in future are briefly listed below.

- We plan to carry out extensive study of a large data set of solar flares to understand the unusual motions of HXR looptop and footpoint sources. For this study, limb and disk flares will be investigated separately. This exercise is expected to bring clarity about the complex dynamical evolution of X-ray sources during the early rise phase of solar flares.

- The imaging spectroscopy is a unique tool which allows us to perform spectroscopic study of the looptop and footpoint HXR sources independently. We plan to explore imaging-spectroscopic capabilities of RHESSI for an in-depth analysis of HXR coronal sources.

- The dynamic evolution of chromospheric flare ribbons are believed to be a proxy for the progression of magnetic reconnection in the corona. In view of this, we plan to carry out precise quantitative estimations of energy release rate by exploiting high resolution Hα observations from recently installed state-of-the-art Multi Application Solar Telescope (MAST) at Udaipur Solar Observatory (USO). These estimations will further be compared with HXR measurements.

- Solar radio bursts are very effective probes of the physical state of the flaring atmosphere, providing an important diagnostic tool for magnetic structures, and displaying signatures of electrons accelerated with very high speed. In future studies, we would like to analyze radio dynamic spectrum in the range of decimetric-metric emissions to infer the state of flare accelerated electrons and magnetized flaring atmosphere.

- The detailed investigations of Earth-directed CMEs are crucial in view of their space-weather effects. We propose to undertake extensive studies of such events by probing radiative signatures of solar flares, source region characteristics of the eruptions, evolution of CMEs in the near-Sun region as well as their propagation effects in the interplanetary medium. These investigations will employ multi-instrument observations of solar transients near the Sun and in the interplanetary medium along with associated in situ measurements of magnetic fields and plasma parameters.

References

Alexander, D., Liu, R., and Gilbert, H. R.: 2006, *Astrophys. J.* **653**, 719

Ali, S. S., Uddin, W., Chandra, R., Mary, D. L., and Vršnak, B.: 2007, *Solar Phys.* **240**, 89

Amari, T., Luciani, J. F., Aly, J. J., and Tagger, M.: 1996, *Astron. Astrophys.* **306**, 913

Ambastha, A.: 2007, *Sun and Geosphere* **2**, 13

Antiochos, S. K., DeVore, C. R., and Klimchuk, J. A.: 1999, *Astrophys. J.* **510**, 485

Antiochos, S. K. and Sturrock, P. A.: 1978, *Astrophys. J.* **220**, 1137

Aschwanden, M. J., Metcalf, T. R., Krucker, S., Sato, J., Conway, A. J., Hurford, G. J., and Schmahl, E. J.: 2004, *Solar Phys.* **219**, 149

Awasthi, A. K., Jain, R., Gadhiya, P. D., Aschwanden, M. J., Uddin, W., Srivastava, A. K., Chandra, R., Gopalswamy, N., Nitta, N. V., Yashiro, S., Manoharan, P. K., Choudhary, D. P., Joshi, N. C., Dwivedi, V. C., and Mahalakshmi, K.: 2014, *Mon. Not. Roy. Astron. Soc.* **437**, 2249

Battaglia, M., Fletcher, L., and Benz, A. O.: 2009, *Astron. Astrophys.* **498**, 891

Bąk-Stęślicka, U., Mrozek, T., and Kołomański, S.: 2011, *Solar Phys.* **271**, 75

Benz, A. O.: 1977, *Astrophys. J.* **211**, 270

Benz, A. O.: 2008, *Living Reviews in Solar Physics* **5**, 1

Berger, T.: 2014, in B. Schmieder, J.-M. Malherbe, and S. T. Wu (eds.), *IAU Symposium*, Vol. 300 of *IAU Symposium*, pp 15–29

Berger, T. E., Shine, R. A., Slater, G. L., Tarbell, T. D., Title, A. M., Okamoto, T. J., Ichimoto, K., Katsukawa, Y., Suematsu, Y., Tsuneta, S., Lites, B. W., and Shimizu, T.: 2008, *Astrophys. J. Lett.* **676**, L89

Bogachev, S. A., Somov, B. V., Kosugi, T., and Sakao, T.: 2005, *Astrophys. J.* **630**, 561

Brown, J. C.: 1971, *Solar Phys.* **18**, 489

Brown, J. C., Turkmani, R., Kontar, E. P., MacKinnon, A. L., and Vlahos, L.: 2009, *Astron. Astrophys.* **508**, 993

Brueckner, G. E., Howard, R. A., Koomen, M. J., Korendyke, C. M., Michels, D. J., Moses, J. D., Socker, D. G., Dere, K. P., Lamy, P. L., Llebaria, A., Bout, M. V., Schwenn, R., Simnett, G. M., Bedford, D. K., and Eyles, C. J.: 1995, *Solar Phys.* **162**, 357

Canfield, R. C., Hudson, H. S., and McKenzie, D. E.: 1999, *Geophys. Res. Lett.* **26**, 627

Carmichael, H.: 1964, *NASA Special Publication* **50**, 451

Carrington, R. C.: 1859, *Mon. Not. Roy. Astron. Soc.* **20**, 13

Chandra, R., Schmieder, B., Aulanier, G., and Malherbe, J. M.: 2009, *Solar Phys.* **258**, 53

Cheng, X., Ding, M. D., Guo, Y., Zhang, J., Vourlidas, A., Liu, Y. D., Olmedo, O., Sun, J. Q., and Li, C.: 2014, *Astrophys. J.* **780**, 28

Cheng, X., Zhang, J., Liu, Y., and Ding, M. D.: 2011, *Astrophys. J. Lett.* **732**, L25

Chifor, C., Mason, H. E., Tripathi, D., Isobe, H., and Asai, A.: 2006, *Astron. Astrophys.* **458**, 965

Chifor, C., Tripathi, D., Mason, H. E., and Dennis, B. R.: 2007, *Astron. Astrophys.* **472**, 967

Choe, G. S. and Lee, L. C.: 1996, *Astrophys. J.* **472**, 372

Chou, Y.-P. and Charbonneau, P.: 1996, *Solar Phys.* **166**, 333

Cliver, E. W., Dennis, B. R., Kiplinger, A. L., Kane, S. R., Neidig, D. F., Sheeley, Jr., N. R., and Koomen, M. J.: 1986, *Astrophys. J.* **305**, 920

Couvidat, S., Schou, J., Shine, R. A., Bush, R. I., Miles, J. W., Scherrer, P. H., and Rairden, R. L.: 2012, *Solar Phys.* **275**, 285

Dennis, B. R. and Zarro, D. M.: 1993, *Solar Phys.* **146**, 177

Dere, K. P., Brueckner, G. E., Howard, R. A., Michels, D. J., and Delaboudiniere, J. P.: 1999, *Astrophys. J.* **516**, 465

Ding, M. D., Chen, Q. R., Li, J. P., and Chen, P. F.: 2003, *Astrophys. J.* **598**, 683

Fárník, F., Hudson, H., and Watanabe, T.: 1996, *Solar Phys.* **165**, 169

Fárník, F., Hudson, H. S., Karlický, M., and Kosugi, T.: 2003, *Astron. Astrophys.* **399**, 1159

Fárník, F. and Savy, S. K.: 1998, *Solar Phys.* **183**, 339

Filippov, B. and Koutchmy, S.: 2002, *Solar Phys.* **208**, 283

Filippov, B. P. and Den, O. G.: 2001, *J. Geophys. Res.* **106**, 25177

Fletcher, L., Dennis, B. R., Hudson, H. S., Krucker, S., Phillips, K., Veronig, A., Battaglia, M., Bone, L., Caspi, A., Chen, Q., Gallagher, P., Grigis, P. T., Ji, H., Liu, W., Milligan, R. O., and Temmer, M.: 2011, *Space Sci. Rev.* **159**, 19

Fletcher, L., Hannah, I. G., Hudson, H. S., and Innes, D. E.: 2013, *Astrophys. J.* **771**, 104

Fletcher, L., Metcalf, T. R., Alexander, D., Brown, D. S., and Ryder, L. A.: 2001, *Astrophys. J.* **554**, 451

Forbes, T. G.: 2000, *J. Geophys. Res.* **105**, 23153

Forbes, T. G. and Acton, L. W.: 1996, *Astrophys. J.* **459**, 330

Forbes, T. G. and Isenberg, P. A.: 1991, *Astrophys. J.* **373**, 294

Forbes, T. G. and Priest, E. R.: 1995, *Astrophys. J.* **446**, 377

Gallagher, P. T., Dennis, B. R., Krucker, S., Schwartz, R. A., and Tolbert, A. K.: 2002, *Solar Phys.* **210**, 341

Gary, G. A. and Moore, R. L.: 2004, *Astrophys. J.* **611**, 545

Gibson, S. E., Fan, Y., Mandrini, C., Fisher, G., and Demoulin, P.: 2004, *Astrophys. J.* **617**, 600

Gibson, S. E., Fletcher, L., Del Zanna, G., Pike, C. D., Mason, H. E., Mandrini, C. H., Démoulin, P., Gilbert, H., Burkepile, J., Holzer, T., Alexander, D., Liu, Y., Nitta, N., Qiu, J., Schmieder, B., and Thompson, B. J.: 2002, *Astrophys. J.* **574**, 1021

Gibson, S. E. and Low, B. C.: 2000, *J. Geophys. Res.* **105**, 18187

Gilbert, H. R., Alexander, D., and Liu, R.: 2007, *Solar Phys.* **245**, 287

Gilbert, H. R., Holzer, T. E., and Burkepile, J. T.: 2001, *Astrophys. J.* **549**, 1221

Gilbert, H. R., Holzer, T. E., Burkepile, J. T., and Hundhausen, A. J.: 2000, *Astrophys. J.* **537**, 503

Glover, A., Harra, L. K., Matthews, S. A., Hori, K., and Culhane, J. L.: 2001, *Astron. Astrophys.* **378**, 239

Gopalswamy, N.: 2006, *Journal of Astrophysics and Astronomy* **27**, 243

Gosain, S.: 2012, *Astrophys. J.* **749**, 85

Gosling, J. T.: 1990, *Washington DC American Geophysical Union Geophysical Monograph Series* **58**, 343

Grigis, P. C. and Benz, A. O.: 2004, *Astron. Astrophys.* **426**, 1093

Guo, W. P. and Wu, S. T.: 1998, *Astrophys. J.* **494**, 419

Guo, Y., Giavalisco, M., Ferguson, H. C., Cassata, P., and Koekemoer, A. M.: 2012, *Astrophys. J.* **757**, 120

Hanaoka, Y.: 1996, *Solar Phys.* **165**, 275

Hanaoka, Y.: 1997, *Solar Phys.* **173**, 319

Hanaoka, Y., Kurokawa, H., Enome, S., Nakajima, H., Shibasaki, K., Nishio, M., Takano, T., Torii, C., Sekiguchi, H., Kawashima, S., Bushimata, T., Shinohara, N., Irimajiri, Y., Koshiishi, H., Shiomi, Y., Nakai, Y., Funakoshi, Y., Kitai, R., Ishiura, K., and Kimura, G.: 1994, *Pub. Astron. Soc. Japan* **46**, 205

Handy, B. N., Acton, L. W., Kankelborg, C. C., Wolfson, C. J., Akin, D. J., Bruner, M. E., Caravalho, R., Catura, R. C., Chevalier, R., Duncan, D. W., Edwards, C. G., Feinstein, C. N., Freeland, S. L., Friedlaender, F. M., Hoffmann, C. H., Hurlburt, N. E., Jurcevich, B. K., Katz, N. L., Kelly, G. A., Lemen, J. R., Levay, M., Lindgren, R. W., Mathur, D. P., Meyer, S. B., Morrison, S. J., Morrison, M. D., Nightingale, R. W., Pope, T. P., Rehse, R. A., Schrijver, C. J., Shine, R. A., Shing, L., Strong, K. T., Tarbell, T. D., Title, A. M., Torgerson, D. D., Golub, L., Bookbinder, J. A., Caldwell, D., Cheimets, P. N., Davis, W. N., Deluca, E. E., McMullen, R. A., Warren, H. P., Amato, D., Fisher, R., Maldonado, H., and Parkinson, C.: 1999, *Solar Phys.* **187**, 229

Handy, B. N., Bruner, M. E., Tarbell, T. D., Title, A. M., Wolfson, C. J., Laforge, M. J., and Oliver, J. J.: 1998, *Solar Phys.* **183**, 29

Harker, B. J. and Pevtsov, A. A.: 2013, *Astrophys. J.* **778**, 175

Harrison, R. A.: 2001, *From Encyclopedia of Astronomy and Astrophysics, by P. Murdin* **ISBN:0333750888**, 1

Hirayama, T.: 1974, *Solar Phys.* **34**, 323

Hodgson, R.: 1859, *Mon. Not. Roy. Astron. Soc.* **20**, 15

Holman, G. D., Sui, L., Schwartz, R. A., and Emslie, A. G.: 2003, *Astrophys. J. Lett.* **595**, L97

Howard, R. A., Moses, J. D., Vourlidas, A., Newmark, J. S., Socker, D. G., Wang, D., Plunkett, S. P., Baugh, R., McMullin, D. R., Davila, J. M., Thompson, W. T., Lemen, J. R., Wuelser, J., Harrison, R. A., Waltham, N. R., Davis, C. J., Eyles, C. J., Defise, J., Halain, J., Bothmer, V., Delaboudiniere, J., Auchere, F., Mercier, R., and Ravet, M. F.: 2007, *AGU Spring Meeting Abstracts* p. A1

Hudson, H. S.: 1991, in *Bulletin of the American Astronomical Society*, Vol. 23 of *Bulletin of the American Astronomical Society*, p. 1064

Hudson, H. S.: 2000, *Astrophys. J. Lett.* **531**, L75

Hudson, H. S., Bougeret, J.-L., and Burkepile, J.: 2006, *Space Sci. Rev.* **123**, 13

Hudson, H. S., Lemen, J. R., St. Cyr, O. C., Sterling, A. C., and Webb, D. F.: 1998, *Geophys. Res. Lett.* **25**, 2481

Hudson, H. S. and Webb, D. F.: 1997, in N. Crooker, J. A. Joselyn, and J. Feynman (eds.), *Coronal Mass Ejections*, Vol. 99 of *Geophysical Monograph*, pp 27–38, American Geophysical Union, Washington, DC

Hundhausen, A.: 1999, in K. T. Strong, J. L. R. Saba, B. M. Haisch, and J. T. Schmelz (eds.), *The many faces of the sun: a summary of the results from NASA's Solar Maximum Mission.*, p. 143

Hurford, G. J., Schmahl, E. J., Schwartz, R. A., Conway, A. J., Aschwanden, M. J., Csillaghy, A., Dennis, B. R., Johns-Krull, C., Krucker, S., Lin, R. P., McTiernan, J., Metcalf, T. R., Sato, J., and Smith, D. M.: 2002, *Solar Phys.* **210**, 61

Ireland, J., Tolbert, A. K., Schwartz, R. A., Holman, G. D., and Dennis, B. R.: 2013, *Astrophys. J.* **769**, 89

Isenberg, P. A., Forbes, T. G., and Demoulin, P.: 1993, *Astrophys. J.* **417**, 368

Ji, H., Huang, G., and Wang, H.: 2007, *Astrophys. J.* **660**, 893

Ji, H., Huang, G., Wang, H., Zhou, T., Li, Y., Zhang, Y., and Song, M.: 2006, *Astrophys. J. Lett.* **636**, L173

Ji, H., Wang, H., Schmahl, E. J., Moon, Y.-J., and Jiang, Y.: 2003, *Astrophys. J. Lett.* **595**, L135

Joshi, B., Kushwaha, U., Cho, K.-S., and Veronig, A. M.: 2013, *Astrophys. J.* **771**, 1

Joshi, B., Manoharan, P. K., Veronig, A. M., Pant, P., and Pandey, K.: 2007, *Solar Phys.* **242**, 143

Joshi, B., Veronig, A., Cho, K.-S., Bong, S.-C., Somov, B. V., Moon, Y.-J., Lee, J., Manoharan, P. K., and Kim, Y.-H.: 2009, *Astrophys. J.* **706**, 1438

Joshi, B., Veronig, A., Manoharan, P. K., and Somov, B. V.: 2012, *Astrophysics and Space Science Proceedings* **33**, 29

Joshi, B., Veronig, A. M., Lee, J., Bong, S.-C., Tiwari, S. K., and Cho, K.-S.: 2011, *Astrophys. J.* **743**, 195

Joshi, N. C., Magara, T., and Inoue, S.: 2014, *Astrophys. J.* **795**, 4

Kahler, S. W.: 1992, *Annual Rev. in Astron. & Astrophys.* **30**, 113

Kane, S. R., Kreplin, R. W., Martres, M. J., Pick, M., and Soru-Escaut, I.: 1974, in G. A. Newkirk (ed.), *Coronal Disturbances*, Vol. 57 of *IAU Symposium*, p. 147

Karlický, M.: 2014, *Research in Astronomy and Astrophysics* **14**, 753

Karpen, J. T., Antiochos, S. K., and DeVore, C. R.: 2012, *Astrophys. J.* **760**, 81

Kim, S., Moon, Y.-J., Kim, Y.-H., Park, Y.-D., Kim, K.-S., Choe, G. S., and Kim, K.-H.: 2008, *Astrophys. J.* **683**, 510

Klimchuk, J. A.: 2001, *Washington DC American Geophysical Union Geophysical Monograph Series* **125**, 143

Kontar, E. P., Brown, J. C., Emslie, A. G., Hajdas, W., Holman, G. D., Hurford, G. J., Kašparová, J., Mallik, P. C. V., Massone, A. M., McConnell, M. L., Piana, M., Prato, M., Schmahl, E. J., and Suarez-Garcia, E.: 2011, *Space Sci. Rev.* **159**, 301

Kopp, R. A. and Pneuman, G. W.: 1976, *Solar Phys.* **50**, 85

Krucker, S., Saint-Hilaire, P., Christe, S., White, S. M., Chavier, A. D., Bale, S. D., and Lin, R. P.: 2008, *Astrophys. J.* **681**, 644

Kumar, P. and Cho, K.-S.: 2013, *Astron. Astrophys.* **557**, A115

Kumar, P. and Cho, K.-S.: 2014, *Astron. Astrophys.* **572**, A83

Kumar, P., Cho, K.-S., Bong, S.-C., Park, S.-H., and Kim, Y. H.: 2012, *Astrophys. J.* **746**, 67

Kumar, P., Srivastava, A. K., Filippov, B., Erdélyi, R., and Uddin, W.: 2011, *Solar Phys.* **272**, 301

Kundu, M. R., Garaimov, V. I., White, S. M., and Krucker, S.: 2004, *Astrophys. J.* **600**, 1052

Kundu, M. R., Grechnev, V. V., Garaimov, V. I., and White, S. M.: 2001, *Astrophys. J.* **563**, 389

Kundu, M. R., Grechnev, V. V., White, S. M., Schmahl, E. J., Meshalkina, N. S., and Kashapova, L. K.: 2009, *Solar Phys.* **260**, 135

Kusano, K., Bamba, Y., Yamamoto, T. T., Iida, Y., Toriumi, S., and Asai, A.: 2012, *Astrophys. J.* **760**, 31

Kushwaha, U., Joshi, B., Cho, K.-S., Veronig, A., Tiwari, S. K., and Mathew, S. K.: 2014, *Astrophys. J.* **791**, 23

Kushwaha, U., Joshi, B., Veronig, A. M., and Moon, Y.-J.: 2015, *Astrophys. J.* **807**, 101

Lee, J., Gallagher, P. T., Gary, D. E., Nita, G. M., Choe, G. S., Bong, S.-C., and Yun, H. S.: 2003, *Astrophys. J.* **585**, 524

Lemen, J. R., Title, A. M., Akin, D. J., Boerner, P. F., Chou, C., Drake, J. F., Duncan, D. W., Edwards, C. G., Friedlaender, F. M., Heyman, G. F., Hurlburt,

N. E., Katz, N. L., Kushner, G. D., Levay, M., Lindgren, R. W., Mathur, D. P., McFeaters, E. L., Mitchell, S., Rehse, R. A., Schrijver, C. J., Springer, L. A., Stern, R. A., Tarbell, T. D., Wuelser, J.-P., Wolfson, C. J., Yanari, C., Bookbinder, J. A., Cheimets, P. N., Caldwell, D., Deluca, E. E., Gates, R., Golub, L., Park, S., Podgorski, W. A., Bush, R. I., Scherrer, P. H., Gummin, M. A., Smith, P., Auker, G., Jerram, P., Pool, P., Soufli, R., Windt, D. L., Beardsley, S., Clapp, M., Lang, J., and Waltham, N.: 2012, *Solar Phys.* **275**, 17

Li, J., Mickey, D. L., and LaBonte, B. J.: 2005, *Astrophys. J.* **620**, 1092

Li, Y. P. and Gan, W. Q.: 2005, *Astrophys. J. Lett.* **629**, L137

Li, Y. P. and Gan, W. Q.: 2006, *Astrophys. J. Lett.* **652**, L61

Lin, C.-H., Gallagher, P. T., and Raftery, C. L.: 2010, *Astron. Astrophys.* **516**, A44

Lin, J. and Forbes, T. G.: 2000, *J. Geophys. Res.* **105**, 2375

Lin, J., Forbes, T. G., Isenberg, P. A., and Démoulin, P.: 1998, *Astrophys. J.* **504**, 1006

Lin, J., Ko, Y.-K., Sui, L., Raymond, J. C., Stenborg, G. A., Jiang, Y., Zhao, S., and Mancuso, S.: 2005, *Astrophys. J.* **622**, 1251

Lin, J., Soon, W., and Baliunas, S. L.: 2003, *New Astronomy Review* **47**, 53

Lin, R. P., Dennis, B. R., Hurford, G. J., Smith, D. M., Zehnder, A., Harvey, P. R., Curtis, D. W., Pankow, D., Turin, P., Bester, M., Csillaghy, A., Lewis, M., Madden, N., van Beek, H. F., Appleby, M., Raudorf, T., McTiernan, J., Ramaty, R., Schmahl, E., Schwartz, R., Krucker, S., Abiad, R., Quinn, T., Berg, P., Hashii, M., Sterling, R., Jackson, R., Pratt, R., Campbell, R. D., Malone, D., Landis, D., Barrington-Leigh, C. P., Slassi-Sennou, S., Cork, C., Clark, D., Amato, D., Orwig, L., Boyle, R., Banks, I. S., Shirey, K., Tolbert, A. K., Zarro, D., Snow, F., Thomsen, K., Henneck, R., McHedlishvili, A., Ming, P., Fivian, M., Jordan, J., Wanner, R., Crubb, J., Preble, J., Matranga, M., Benz, A., Hudson, H., Canfield, R. C., Holman, G. D., Crannell, C., Kosugi, T., Emslie, A. G., Vilmer, N., Brown, J. C., Johns-Krull, C., Aschwanden, M., Metcalf, T., and Conway, A.: 2002, *Solar Phys.* **210**, 3

Lin, R. P. and Hudson, H. S.: 1976, *Solar Phys.* **50**, 153

Linker, J. A., Mikic, Z., Lionello, R., Riley, P., and Amari, T.: 2003, *AGU Fall Meeting Abstracts* p. A4

Liu, C., Lee, J., Yurchyshyn, V., Deng, N., Cho, K.-s., Karlický, M., and Wang, H.: 2007, *Astrophys. J.* **669**, 1372

Liu, R. and Alexander, D.: 2009, *Astrophys. J.* **697**, 999

Liu, R., Alexander, D., and Gilbert, H. R.: 2009a, *Astrophys. J.* **691**, 1079

Liu, R., Gilbert, H. R., Alexander, D., and Su, Y.: 2008, *Astrophys. J.* **680**, 1508

Liu, R. and Wang, H.: 2009, *Astrophys. J. Lett.* **703**, L23

Liu, R., Wang, H., and Alexander, D.: 2009b, *Astrophys. J.* **696**, 121

Liu, W., Jiang, Y. W., Liu, S., and Petrosian, V.: 2004, *Astrophys. J. Lett.* **611**, L53

Liu, W., Wang, T.-J., Dennis, B. R., and Holman, G. D.: 2009c, *Astrophys. J.* **698**, 632

Low, B. C.: 1981, *Astrophys. J.* **251**, 352

Low, B. C.: 1996, *Solar Phys.* **167**, 217

Low, B. C.: 1999, in S. R. Habbal, R. Esser, J. V. Hollweg, and P. A. Isenberg (eds.), *American Institute of Physics Conference Series*, Vol. 471 of *American Institute of Physics Conference Series*, pp 109–114

Low, B. C.: 2001, *J. Geophys. Res.* **106**, 25141

Magara, T. and Shibata, K.: 1999, *Astrophys. J.* **514**, 456

Mandrini, C. H., Demoulin, P., Schmieder, B., Deluca, E. E., Pariat, E., and Uddin, W.: 2006, *Solar Phys.* **238**, 293

Manoharan, P. K. and Kundu, M. R.: 2003, *Astrophys. J.* **592**, 597

Manoharan, P. K., van Driel-Gesztelyi, L., Pick, M., and Demoulin, P.: 1996, *Astrophys. J. Lett.* **468**, L73

Martin, S. F.: 1998, *Solar Phys.* **182**, 107

Maurya, R. A., Vemareddy, P., and Ambastha, A.: 2012, *Astrophys. J.* **747**, 134

Metcalf, T. R., Alexander, D., Hudson, H. S., and Longcope, D. W.: 2003, *Astrophys. J.* **595**, 483

Metcalf, T. R., Hudson, H. S., Kosugi, T., Puetter, R. C., and Pina, R. K.: 1996, *Astrophys. J.* **466**, 585

Mikic, Z. and Linker, J. A.: 1994, *Astrophys. J.* **430**, 898

Milligan, R. O., Gallagher, P. T., Mathioudakis, M., Bloomfield, D. S., Keenan, F. P., and Schwartz, R. A.: 2006a, *Astrophys. J. Lett.* **638**, L117

Milligan, R. O., Gallagher, P. T., Mathioudakis, M., and Keenan, F. P.: 2006b, *Astrophys. J. Lett.* **642**, L169

Moon, Y.-J., Cho, K. S., Smith, Z., Fry, C. D., Dryer, M., and Park, Y. D.: 2004, *Astrophys. J.* **615**, 1011

Moore, R. L., Cirtain, J. W., Sterling, A. C., and Falconer, D. A.: 2010, *Astrophys. J.* **720**, 757

Moore, R. L. and Roumeliotis, G.: 1992, in Z. Svestka, B. V. Jackson, and M. E. Machado (eds.), *IAU Colloq. 133: Eruptive Solar Flares*, Vol. 399 of *Lecture Notes in Physics, Berlin Springer Verlag*, p. 69

Moore, R. L., Sterling, A. C., Falconer, D. A., and Robe, D.: 2013, *Astrophys. J.* **769**, 134

Moore, R. L., Sterling, A. C., Hudson, H. S., and Lemen, J. R.: 2001, *Astrophys. J.* **552**, 833

Mrozek, T.: 2011, *Solar Phys.* **270**, 191

Nakajima, H., Nishio, M., Enome, S., Shibasaki, K., Takano, T., Hanaoka, Y., Torii, C., Sekiguchi, H., Bushimata, T., Kawashima, S., Shinohara, N., Irimajiri, Y., Koshiishi, H., Kosugi, T., Shiomi, Y., Sawa, M., and Kai, K.: 1994, *IEEE Proceedings* **82**, 705

Netzel, A., Mrozek, T., Kołomański, S., and Gburek, S.: 2012, *Astron. Astrophys.* **548**, A89

Neupert, W. M.: 1968, *Astrophys. J. Lett.* **153**, L59

Nishizuka, N., Takasaki, H., Asai, A., and Shibata, K.: 2010, *Astrophys. J.* **711**, 1062

Nitta, S., Imada, S., and Yamamoto, T. T.: 2012, *Solar Phys.* **276**, 183

Ohyama, M. and Shibata, K.: 1997, *Pub. Astron. Soc. Japan* **49**, 249

Ohyama, M. and Shibata, K.: 1998, *Astrophys. J.* **499**, 934

Okamoto, T. J., Tsuneta, S., Berger, T. E., Ichimoto, K., Katsukawa, Y., Lites, B. W., Nagata, S., Shibata, K., Shimizu, T., Shine, R. A., Suematsu, Y., Tarbell, T. D., and Title, A. M.: 2007, *Science* **318**, 1577

Pallavicini, R., Serio, S., and Vaiana, G. S.: 1977, *Astrophys. J.* **216**, 108

Pariat, E., Dalmasse, K., DeVore, C. R., Antiochos, S. K., and Karpen, J. T.: 2015, *Astron. Astrophys.* **573**, A130

Patsourakos, S., Vourlidas, A., and Stenborg, G.: 2013, *Astrophys. J.* **764**, 125

Pesnell, W. D., Thompson, B. J., and Chamberlin, P. C.: 2012, *Solar Phys.* **275**, 3

Petrie, G. J. D. and Sudol, J. J.: 2010, *Astrophys. J.* **724**, 1218

Pevtsov, A. A.: 2002, *Solar Phys.* **207**, 111

Pevtsov, A. A., Canfield, R. C., and Zirin, H.: 1996, *Astrophys. J.* **473**, 533

Plunkett, S. P., Vourlidas, A., Šimberová, S., Karlický, M., Kotrč, P., Heinzel, P., Kupryakov, Y. A., Guo, W. P., and Wu, S. T.: 2000, *Solar Phys.* **194**, 371

Priest, E. and Forbes, T.: 2000, *Magnetic Reconnection*

Priest, E. R. and Forbes, T. G.: 2002, *Astron. Astrophys. Rev.* **10**, 313

Qiu, J. and Gary, D. E.: 2003, *Astrophys. J.* **599**, 615

Raadu, M. A., Malherbe, J. M., Schmieder, B., and Mein, P.: 1987, *Solar Phys.* **109**, 59

Riley, P., Lionello, R., Mikić, Z., and Linker, J.: 2008, *Astrophys. J.* **672**, 1221

Rust, D. M.: 2003, *Advances in Space Research* **32**, 1895

Rust, D. M. and Kumar, A.: 1996, *Astrophys. J. Lett.* **464**, L199

Saint-Hilaire, P. and Benz, A. O.: 2005, *Astron. Astrophys.* **435**, 743

Scherrer, P. H., Bogart, R. S., Bush, R. I., Hoeksema, J. T., Kosovichev, A. G., Schou, J., Rosenberg, W., Springer, L., Tarbell, T. D., Title, A., Wolfson, C. J., Zayer, I., and MDI Engineering Team: 1995, *Solar Phys.* **162**, 129

Schmieder, B., Guo, Y., Moreno-Insertis, F., Aulanier, G., Yelles Chaouche, L., Nishizuka, N., Harra, L. K., Thalmann, J. K., Vargas Dominguez, S., and Liu, Y.: 2013, *Astron. Astrophys.* **559**, A1

Schou, J., Borrero, J. M., Norton, A. A., Tomczyk, S., Elmore, D., and Card, G. L.: 2012, *Solar Phys.* **275**, 327

Shibata, K.: 1996, *Advances in Space Research* **17**, 9

Shibata, K.: 1997, in A. Wilson (ed.), *Fifth SOHO Workshop: The Corona and Solar Wind Near Minimum Activity*, Vol. 404 of *ESA Special Publication*, p. 103

Shibata, K.: 1999a, *Astrophys. Space Sci.* **264**, 129

Shibata, K.: 1999b, in T. S. Bastian, N. Gopalswamy, and K. Shibasaki (eds.), *Proceedings of the Nobeyama Symposium*, pp 381–389

Shibata, K., Masuda, S., Shimojo, M., Hara, H., Yokoyama, T., Tsuneta, S., Kosugi, T., and Ogawara, Y.: 1995, *Astrophys. J. Lett.* **451**, L83

Shimojo, M. and Shibata, K.: 2000, *Advances in Space Research* **26**, 449

Siarkowski, M., Falewicz, R., and Rudawy, P.: 2009, *Astrophys. J. Lett.* **705**, L143

Simões, P. J. A., Fletcher, L., Hudson, H. S., and Russell, A. J. B.: 2013, *Astrophys. J.* **777**, 152

Smith, D. M., Lin, R. P., Turin, P., Curtis, D. W., Primbsch, J. H., Campbell, R. D., Abiad, R., Schroeder, P., Cork, C. P., Hull, E. L., Landis, D. A., Madden, N. W., Malone, D., Pehl, R. H., Raudorf, T., Sangsingkeow, P., Boyle, R., Banks, I. S., Shirey, K., and Schwartz, R.: 2002, *Solar Phys.* **210**, 33

Somov, B. V.: 1986, *Astron. Astrophys.* **163**, 210

Srivastava, N., Ambastha, A., and Bhatnagar, A.: 1991, *Solar Phys.* **133**, 339

Sterling, A. C. and Hudson, H. S.: 1997, *Astrophys. J. Lett.* **491**, L55

Sterling, A. C., Hudson, H. S., Thompson, B. J., and Zarro, D. M.: 2000, *Astrophys. J.* **532**, 628

Sterling, A. C. and Moore, R. L.: 2004, *Astrophys. J.* **602**, 1024

Sterling, A. C. and Moore, R. L.: 2005, *Astrophys. J.* **630**, 1148

Sterling, A. C., Moore, R. L., and Freeland, S. L.: 2011, *Astrophys. J. Lett.* **731**, L3

Sterling, A. C., Moore, R. L., Qiu, J., and Wang, H.: 2001, *Astrophys. J.* **561**, 1116

Sturrock, P. A.: 1966, *Nature* **211**, 695

Sturrock, P. A.: 1972, *Solar Phys.* **23**, 438

Su, Y., Veronig, A. M., Holman, G. D., Dennis, B. R., Wang, T., Temmer, M., and Gan, W.: 2013, *Nature Physics* **9**, 489

Subramanian, P., Ananthakrishnan, S., Janardhan, P., Kundu, M. R., White, S. M., and Garaimov, V. I.: 2003, *Solar Phys.* **218**, 247

Sudol, J. J. and Harvey, J. W.: 2005, *Astrophys. J.* **635**, 647

Sui, L. and Holman, G. D.: 2003, *Astrophys. J. Lett.* **596**, L251

Sui, L., Holman, G. D., and Dennis, B. R.: 2004, *Astrophys. J.* **612**, 546

Sui, L., Holman, G. D., and Dennis, B. R.: 2005a, *Astrophys. J.* **626**, 1102

Sui, L., Holman, G. D., and Dennis, B. R.: 2006a, *Astrophys. J.* **646**, 605

Sui, L., Holman, G. D., and Dennis, B. R.: 2006b, *Astrophys. J.* **646**, 605

Sui, L., Holman, G. D., White, S. M., and Zhang, J.: 2005b, *Astrophys. J.* **633**, 1175

Syrovatskii, S. I. and Shmeleva, O. P.: 1972, *Sov. Astron.* **16**, 273

Takano, T., Nakajima, H., Enome, S., Shibasaki, K., Nishio, M., Hanaoka, Y., Shiomi, Y., Sekiguchi, H., Kawashima, S., Bushimata, T., Shinohara, N., Torii, C., Fujiki, K., and Irimajiri, Y.: 1997, in G. Trottet (ed.), *Coronal Physics from Radio and Space Observations*, Vol. 483 of *Lecture Notes in Physics, Berlin Springer Verlag*, p. 183

Takasao, S., Asai, A., Isobe, H., and Shibata, K.: 2012, *Astrophys. J. Lett.* **745**, L6

Tang, F.: 1986, *Solar Phys.* **105**, 399

Tappin, S. J.: 1991, *Astron. Astrophys. Suppl.* **87**, 277

Temmer, M., Veronig, A. M., Kontar, E. P., Krucker, S., and Vršnak, B.: 2010, *Astrophys. J.* **712**, 1410

Temmer, M., Veronig, A. M., Vršnak, B., Rybák, J., Gömöry, P., Stoiser, S., and Maričić, D.: 2008, *Astrophys. J. Lett.* **673**, L95

Thalmann, J. K., Su, Y., Temmer, M., and Veronig, A. M.: 2015, *Astrophys. J. Lett.* **801**, L23

Thompson, B. J., Gurman, J. B., Neupert, W. M., Newmark, J. S., Delaboudinière, J.-P., Cyr, O. C. S., Stezelberger, S., Dere, K. P., Howard, R. A., and Michels, D. J.: 1999, *Astrophys. J. Lett.* **517**, L151

Tiwari, S. K., Venkatakrishnan, P., and Gosain, S.: 2010, *Astrophys. J.* **721**, 622

Tiwari, S. K., Venkatakrishnan, P., and Sankarasubramanian, K.: 2009, *Astrophys. J. Lett.* **702**, L133

Török, T. and Kliem, B.: 2005, *Astrophys. J. Lett.* **630**, L97

Török, T., Kliem, B., and Titov, V. S.: 2004, *Astron. Astrophys.* **413**, L27

Tripathi, D., Gibson, S. E., Qiu, J., Fletcher, L., Liu, R., Gilbert, H., and Mason, H. E.: 2009, *Astron. Astrophys.* **498**, 295

van Ballegooijen, A. A. and Martens, P. C. H.: 1989, *Astrophys. J.* **343**, 971

van Driel-Gesztelyi, L. and Culhane, J. L.: 2009, *Space Sci. Rev.* **144**, 351

Vemareddy, P., Maurya, R. A., and Ambastha, A.: 2012, *Solar Phys.* **277**, 337

Vemareddy, P. and Zhang, J.: 2014, *Astrophys. J.* **797**, 80

Veronig, A. M. and Brown, J. C.: 2004, *Astrophys. J. Lett.* **603**, L117

Veronig, A. M., Brown, J. C., Dennis, B. R., Schwartz, R. A., Sui, L., and Tolbert, A. K.: 2005, *Astrophys. J.* **621**, 482

Veronig, A. M., Karlický, M., Vršnak, B., Temmer, M., Magdalenić, J., Dennis, B. R., Otruba, W., and Pötzi, W.: 2006, *Astron. Astrophys.* **446**, 675

Veronig, A. M., Rybák, J., Gömöry, P., Berkebile-Stoiser, S., Temmer, M., Otruba, W., Vršnak, B., Pötzi, W., and Baumgartner, D.: 2010, *Astrophys. J.* **719**, 655

Vrsnak, B., Ruzdjak, V., Brajsa, R., and Dzubur, A.: 1988, *Solar Phys.* **116**, 45

Vrsnak, B., Ruzdjak, V., and Rompolt, B.: 1991, *Solar Phys.* **136**, 151

Wang, H., Ji, H., Schmahl, E. J., Qiu, J., Liu, C., and Deng, N.: 2002, *Astrophys. J. Lett.* **580**, L177

Wang, H. and Liu, C.: 2010, *Astrophys. J. Lett.* **716**, L195

Wang, H., Qiu, J., Jing, J., Spirock, T. J., Yurchyshyn, V., Abramenko, V., Ji, H., and Goode, P. R.: 2004, *Astrophys. J.* **605**, 931

Wang, S., Liu, C., Liu, R., Deng, N., Liu, Y., and Wang, H.: 2012, *Astrophys. J. Lett.* **745**, L17

Wang, Y. and Zhang, J.: 2007, *Astrophys. J.* **665**, 1428

Warmuth, A. and Mann, G.: 2013, *Astron. Astrophys.* **552**, A87

Warren, H. P. and Warshall, A. D.: 2001, *Astrophys. J. Lett.* **560**, L87

White, S. M., Benz, A. O., Christe, S., Fárník, F., Kundu, M. R., Mann, G., Ning, Z., Raulin, J.-P., Silva-Válio, A. V. R., Saint-Hilaire, P., Vilmer, N., and Warmuth, A.: 2011, *Space Sci. Rev.* **159**, 225

Wu, S. T., Guo, W. P., and Wang, J. F.: 1995, *Solar Phys.* **157**, 325

Wu, S. T., Wang, A. H., Plunkett, S. P., and Michels, D. J.: 2000, *Astrophys. J.* **545**, 1101

Wuelser, J.-P., Lemen, J. R., Tarbell, T. D., Wolfson, C. J., Cannon, J. C., Carpenter, B. A., Duncan, D. W., Gradwohl, G. S., Meyer, S. B., Moore, A. S., Navarro, R. L., Pearson, J. D., Rossi, G. R., Springer, L. A., Howard, R. A., Moses, J. D., Newmark, J. S., Delaboudiniere, J.-P., Artzner, G. E., Auchere, F., Bougnet, M., Bouyries, P., Bridou, F., Clotaire, J.-Y., Colas, G., Delmotte, F., Jerome, A., Lamare, M., Mercier, R., Mullot, M., Ravet, M.-F., Song, X., Bothmer, V., and Deutsch, W.: 2004, in S. Fineschi and M. A. Gummin (eds.), *Telescopes and Instrumentation for Solar Astrophysics*, Vol. 5171 of *Society of Photo-Optical Instrumentation Engineers (SPIE) Conference Series*, pp 111–122

Yashiro, S., Gopalswamy, N., Michalek, G., St. Cyr, O. C., Plunkett, S. P., Rich, N. B., and Howard, R. A.: 2004, *Journal of Geophysical Research (Space Physics)* **109**, 7105

Yurchyshyn, V., Wang, H., Abramenko, V., Spirock, T. J., and Krucker, S.: 2004, *Astrophys. J.* **605**, 546

Zarro, D. M., Sterling, A. C., Thompson, B. J., Hudson, H. S., and Nitta, N.: 1999, *Astrophys. J. Lett.* **520**, L139

Zhang, J., Dere, K. P., Howard, R. A., Kundu, M. R., and White, S. M.: 2001, *Astrophys. J.* **559**, 452

Zhang, Y., Tan, B., Karlický, M., Mészárosová, H., Huang, J., Tan, C., and Simões, P. J. A.: 2015, *Astrophys. J.* **799**, 30

Zheng, R., Jiang, Y., Yang, J., Bi, Y., Hong, J., Yang, B., and Yang, D.: 2012, *Astrophys. J.* **747**, 67

Zhou, G. P., Wang, J. X., Zhang, J., Chen, P. F., Ji, H. S., and Dere, K.: 2006, *Astrophys. J.* **651**, 1238

Zirin, H.: 1988, *Astrophysics of the sun*

List of Publications

Publications in Journals

1. Joshi, B., **Kushwaha, U.**, Cho, K.-S., and Veronig, A., 2013, *RHESSI and TRACE Observations of Multiple Flare Activity in AR 10656 and Associated Filament Eruption,* ***Astrophys. J.,*** *771*, 1.

2. **Kushwaha, U.**, Joshi, B., Cho K.-S., Veronig A., Tiwari, S. K., and Mathew, S. K., 2014, *Impulsive Energy Release and Non-Thermal Emission in a Confined M4.0 Flare Triggered by Rapidly Evolving Magnetic Structures,* ***Astrophys. J.,*** *791*, 23.

3. **Kushwaha, U.**, Joshi, B., Veronig A. M., Moon Y. J., 2015, *Large-scale Contraction and Subsequent Disruption of Coronal Loops During Various Phases of the M6.2 Flare Associated with the Confined Flux Rope Eruption,* ***Astrophys. J.,*** *807*, 101.

Conference Proceedings

1. Joshi, B., **Kushwaha, U.**, Cho, K., Veronig, A., 2014, *Signatures of Magnetic Reconnection During the Evolutionary Phases of a Prominence Eruption and Associated X1.8 Flare,* ***IAU Symposium 300,*** 424.

2. **Kushwaha, U** and Joshi, B., 2012, *Intense HXR Emission and Magnetic Restructuring Associated with an Unusual Impulsive Flare: RHESSI and SDO Observations,* ***I^{st} PSSI Plasma Scholars' Colloquium,*** 96.

Publications attached with thesis

1. **Kushwaha, U.**, Joshi, B., Veronig A. M., Moon Y. J., 2015, *Large-scale Contraction and Subsequent Disruption of Coronal Loops During Various Phases of the M6.2 Flare Associated with the Confined Flux Rope Eruption,* ***Astrophys. J.,*** *807*, 101.

2. **Kushwaha, U.**, Joshi, B., Cho K.-S., Veronig A., Tiwari, S. K., and Mathew, S. K., 2014, *Impulsive Energy Release and Non-thermal Emission in a Confined M4.0 Flare Triggered by Rapidly Evolving Magnetic Structures,* ***Astrophys. J.,*** *791*, 23.